

به نام خدا



# مرکز دانلود رایگان مهندسی متالورژی و مواد

[www.Iran-mavad.com](http://www.Iran-mavad.com)



---

# Thermomechanical Processing of High-strength Low-alloy Steels

---

**Imao Tamura**, Kyoto University

**Hiroshi Sekine**, Nippon Steel Corporation

**Tomo Tanaka**, Kawasaki Steel Corporation

**Chiaki Ouchi**, Nippon Kokan Corporation

**Butterworths**

London Boston Singapore Sydney Toronto Wellington

[www.iran-mavad.com](http://www.iran-mavad.com)

مرجع دانشجویان و مهندسين مواد

All rights reserved. No part of this publication may be reproduced or transmitted in any form or by any means, including photocopying and recording, without the written permission of the copyright holder, application for which should be addressed to the Publishers. Such written permission must also be obtained before any part of this publication is stored in a retrieval system of any nature.

This book is sold subject to the Standard Conditions of Sale of Net Books and may not be re-sold in the UK below the net price given by the Publishers in their current price list.

First published 1988

© Butterworth & Co. (Publishers) Ltd, 1988

**British Library Cataloguing in Publication Data**

Thermomechanical processing of high strength  
low-alloy steel

1. Steel—Heating 2. Rolling (metal-  
work)

I. Tamura, Imao  
671.3'2 TS325

ISBN 0-408-11034-1

**Library of Congress Cataloging-in-Publication Data**

Thermomechanical processing of high-strength  
low-alloy steels / Imao Tamura . . . [et al.].

p. cm.

Includes bibliographies and index.

ISBN 0-408-11034-1

1. Steel—Thermomechanical treatment.

I. Tamura, Imao, 1923—

TN752.T54T49 1988

672'.3—dc19 87-29994

CIP

---

## Preface

---

Since about 1950, much research has been carried out in the field of thermomechanical treatment of steels, and many methods have been proposed. Among such treatments, controlled-rolling and deformation-quenching (direct quenching, forge quenching, etc.) have achieved practical success. Controlled-rolling especially has played an important role in the development of the as-rolled high-strength low-alloy (HSLA) steels. The early development of controlled-rolling in the 1960s owes much to the research done in the UK which was of very considerable value. Since the 1970s, developments in this field owe much to the research done by several steelmaking companies in Japan.

Controlled-rolling is a technique which produces strong and tough steel by refining the ferrite ( $\alpha$ ) grains. In controlled-rolling, recrystallization during or immediately after hot-rolling is controlled by the rolling conditions and by the addition of microalloying elements such as niobium, titanium and vanadium. During cooling after controlled-rolling, the transformation of the austenite ( $\gamma$ ) produces fine  $\alpha$ -grains. Furthermore, the precipitation of carbonitrides of the microalloying elements contributes to the strengthening to some degree. Controlled-cooling processes to produce smaller  $\alpha$  grains or more strengthened structures have also been developed.

Although there have been many publications on various aspects of controlled-rolling, including a number of excellent summaries and overviews, the techniques and metallurgical bases for the processes involved have not formed the subject of a book. This book is aimed to fulfil such a need. The authors have been intimately and significantly involved in the field of controlled-rolling at the research centres of major steel-making companies in Japan for many years and established some of the most recent controlled-rolling techniques. This book aims to provide essential information to the metallurgists and engineers working in this field throughout the world.

The book considers some of the most advanced techniques, and the metallurgical bases for controlled-rolling. Readers are expected to have some knowledge of metallurgy, and consequently introductory explanations are omitted. In Chapter 1, the purpose of thermomechanical processing and a historical survey is described. In Chapter 2, fundamental issues such as the kinetics of phase transformations and the refinement of grain size in steels are considered. In Chapters 3, 4 and 5, the techniques and the metallurgical bases for controlled-rolling in the recrystallization, nonrecrystallization and ( $\alpha + \gamma$ ) regions are described. In Chapters 6 and 7, deformation resistance during hot-rolling and the restoration processes which will occur during or immediately after rolling are discussed. In Chapter 8, phase transformations during cooling following hot-rolling are mentioned. In Chapter 9, the effects of alloying elements, which play an important role throughout reheating, rolling and cooling are summarized. The mechanical properties of controlled-rolled steel are dealt with in Chapter 10, whilst the prediction and control of microstructure and properties by thermomechan-

ical processes is covered in Chapter 11. The problems faced at present and the possibility for future developments are stated in Chapter 12.

I. Tamura  
H. Sekine  
T. Tanaka  
C. Ouchi

# Introduction

---

## 1.1 What is thermomechanical processing?

For most commercial products in the steel industry, their external shapes are the result of hot-deformation, such as hot-rolling, whilst the necessary mechanical properties are obtained from the alloy design and by heat treatment after hot-deformation. Improvements in the mechanical properties by virtue of the effects of alloying elements are frequently realized by means of heat treatment.

In processing steel materials for machinery, forgings sometimes show improved mechanical properties compared with mechanically processed and normalized material. Furthermore, the properties of material directly quenched after forging and then tempered are sometimes improved compared with material aircooled after forging and then quenched and tempered. In these cases, the hot-deformation itself becomes a necessary constituent of the heat treatment and metallurgical changes caused by the hot-deformation results in additional beneficial effects on the properties of steels after cooling or after final heat treatment.

Thermomechanical processing is a technique designed to improve the mechanical properties of materials by controlling the hot-deformation processes which originally were designed to produce the required external shape of the product. Controlled-rolling, controlled-cooling and direct-quenching are typical examples of thermomechanical processing. Such processing saves energy in steel manufacture by minimizing or even eliminating the heat treatment after hot-deformation, thus increasing the productivity for high-grade steels. It generally demands a change in alloy design and frequently reduces the productivity of the hot-deformation process itself, but nevertheless makes it possible to reduce the total amount of alloying additions and to improve weldability, whilst sometimes producing new and beneficial characteristics in the steel.

## 1.2 Historical survey

### 1.2.1 Controlled low-temperature hot-rolling of ships' plates

The first introduction of thermomechanical processing into commercial production was controlled rolling of carbon-manganese steel plates of 40 kgf/mm<sup>2</sup> grade for ship-building in the 1950s.<sup>1</sup> During the Second World War, a number of transport ships

were built as welded structures to reduce the construction time. These 'Liberty' ships suffered from the occurrence of brittle fractures initiated at welded joints. This stimulated, after 1945, the concept of toughness as distinct from the concept of ductility, and notch toughness became a requirement for shipbuilding and other structural steel plates. In the 1950s, an increase in the manganese : carbon ratio, deoxidization by the addition of aluminium and the normalizing of aluminium-killed steels were all adopted to improve notch toughness. At that time also the concept that the ductile  $\rightarrow$  brittle transition temperature can be reduced by refinement of ferrite ( $\alpha$ ) grain size was established.<sup>2,3</sup> Normalizing of aluminium-killed steels is one of the effective methods to refine  $\alpha$  grains. Instead of normalizing, however, controlled low-temperature hot-rolling was being practised on plates of a restricted thickness range in some European plate-mills in order to refine the  $\alpha$  grains and to provide increased notch toughness. ( $\alpha$  refinement also increases the yield stress.) Though there were considerable differences in detail of the practice of controlled-rolling in different mills, the following features were generally applied (Figure 1.1(a) and (b)):

- (1) Interrupting the hot-rolling operation when the slab had been reduced to the prescribed thickness, e.g. 1.65 times the product thickness.
- (2) Recommencing hot-working when the slab had cooled to the prescribed temperature, e.g. 890° C, and finishing at temperatures in the austenite ( $\gamma$ ) range, i.e. above the  $A_{r3}$  but lower than the normal or conventional finishing temperature, e.g. down to 800° C.

The low-temperature finish-rolling practice for carbon–manganese steels is apparently quite similar to that for controlled-rolling niobium-containing high-strength steels, but the metallurgical basis is completely different. As will be described in detail later, the low-temperature rolling refines the recrystallized  $\gamma$  grains in the controlled-rolling of carbon–manganese steels, but it elongates unrecrystallized  $\gamma$  grains in the niobium-containing steels (Figure 1.1(c)). The smallest required reductions per pass were also defined for some powerful mills,<sup>1</sup> but such a control is not necessary in modern low-temperature rolling of niobium-containing steels. It was reported that an improvement (decrease) of about 10–15° C in the 20 J transition temperature was possible by the controlled low-temperature hot-rolling process. The interrupting of the rolling operation and holding in order to decrease the temperature of the slab necessarily resulted in some decrease in rolling productivity, and for plates thicker than the prescribed thickness, e.g. greater than 38 mm, normalizing was usually adopted to guarantee the toughness.<sup>1</sup>

It has been known for many years that the mechanical properties of rolled products can be improved when they are rolled to low finishing temperatures.<sup>4</sup> In 1925, Hanemann and Lucke found that the  $\alpha$  grains in steels (slowly cooled after forging in one reduction and subsequently holding in the  $\gamma$  region) were coarsened with small forging reductions but were refined by an increase in the amount of forging reduction, and they were also refined with a decrease in the austenitizing or deformation temperature whether forging was applied or not.<sup>5</sup> Hanemann and Lucke interpreted this behaviour in terms of recrystallization of  $\gamma$  after hot-deformation and discussed the possibility of grain refinement of steels by hot-rolling or forging only without additional heat treatment. These research results seem to be accepted as showing that  $\alpha$  grain refinement could be attained just by decreasing the temperature of the final hot-working reduc-

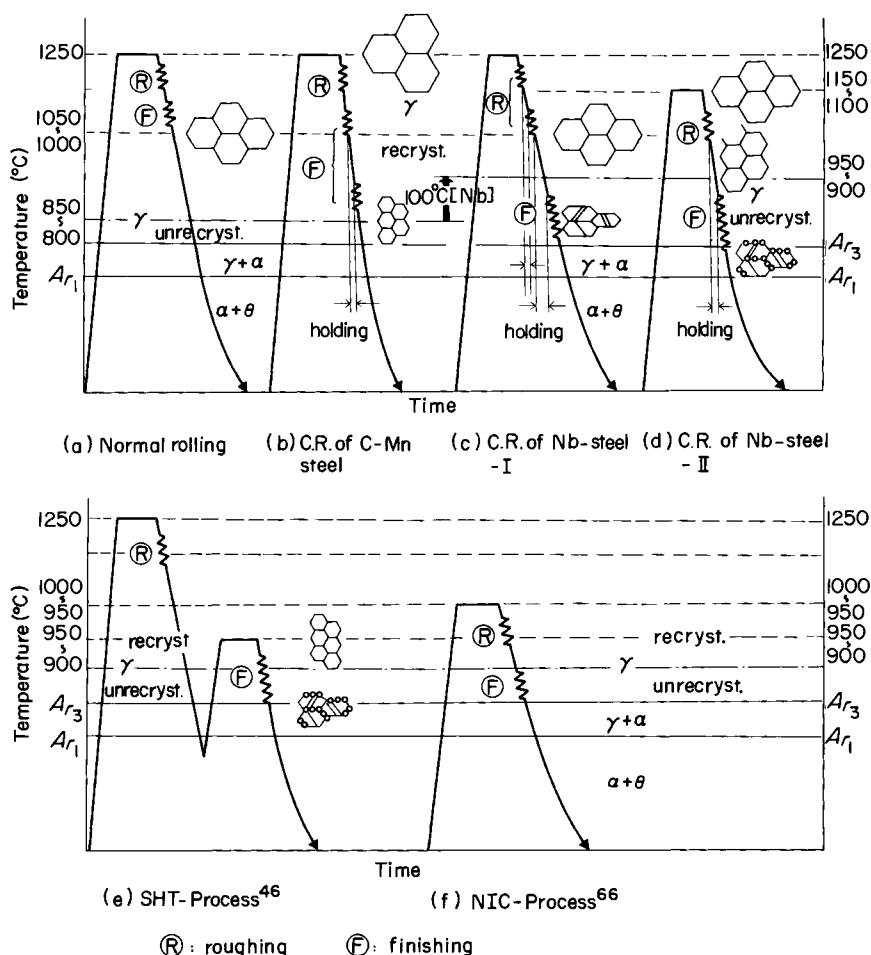


Figure 1.1 Development of controlled-rolling: (a) normal-rolling; (b) controlled-rolling of carbon-manganese steels; (c) controlled-rolling of niobium steel (I); (d) controlled-rolling of niobium steel (II); (e) Sumitomo high-toughness process;<sup>46</sup> (f) Nippon steel intercritical control process<sup>66</sup>

tion. After 1945 it became clear that notch ductility, a newly defined requirement of steel plates, and yield strength can both be improved by  $\alpha$  grain refinement.<sup>2,3</sup>

In the commercial controlled-rolling of carbon-manganese steels already being practised in Europe, experimental rolling studies were carried out by decreasing just the temperatures of the final one or two reductions,<sup>6,7</sup> or by changing the temperature during one-pass rolling.<sup>8</sup> It was not always possible to obtain consistent results for the relation between the rolling temperature and notch toughness.

When thinner plates are normally hot-rolled, the reductions are extended to lower temperatures, and so the finish-rolling temperatures are also reduced. With reducing plate thickness, the  $\alpha$  grains become finer and the yield strength and toughness are further improved. In the controlled-rolling practice for carbon-manganese steels described above, the conditions of the later stages of the rolling of thicker plates are controlled similarly to those in the normal rolling of thinner plates.



In 1964, about 40 years after Hanemann and Lucke's report<sup>5</sup> Grange<sup>9</sup> combined experimentally the mechanism of  $\alpha$  grain refinement by low-temperature finish-rolling with the recrystallization behaviour of the  $\gamma$  grains after hot-deformation. By delineating prior  $\gamma$  grain boundaries of specimens aircooled after hot-rolling or forging, he found that the larger the  $\gamma$  grain size prior to deformation the slower the rate of recrystallization and the coarser the recrystallized grains, the lower the deformation temperature, the slower the rate of recrystallization and the finer the recrystallized grains. These results strongly suggest that only repeated hot-deformation down to lower temperatures may effectively refine the recrystallized  $\gamma$  grains.

### 1.2.2 Controlled-rolling of low-carbon niobium-containing steels

In 1958, the first niobium-containing high-strength steel plates were produced.<sup>10</sup> Then, in 1959, Beiser carried out detailed experiments on niobium-containing steels and reported as follows:<sup>11</sup>

- (1) By a small addition of niobium, (up to 0.06%) the strength was increased by 10 kgf/mm<sup>2</sup> but the transition temperature was raised by 40° C in as-hot-rolled steels. A decrease in the temperature of just the final pass down to 870° C had almost no effect on the mechanical properties.
- (2) By normalizing, the tensile strength was decreased to the same level but the yield strength and the transition temperature were improved by 5–8 kgf/mm<sup>2</sup> and 25–70° C respectively, compared with normalized niobium-free steels.

The improvements in mechanical properties by a small addition of niobium, especially the marked increase of 10 kgf/mm<sup>2</sup> in tensile strength in the as-rolled state, was quite remarkable. In order to minimize the deterioration in notch toughness in as-rolled steels, studies on the application of controlled-rolling to niobium-containing steels were undertaken in many countries.

In the first half of the 1960s, the following measures were reported to improve the notch toughness of as-rolled niobium-containing steels:

- (1) An increase in the additional manganese.<sup>11,12</sup>
- (2) Lower reheating temperatures of slabs down to 1200° C<sup>8</sup> or less.<sup>12</sup>
- (3) Lower finish-rolling temperatures down to 800° C,<sup>13</sup> an increase in total percentage reduction below 900° C of up to 30%<sup>13</sup> or below 830° C to more than 20%.<sup>14</sup> Low-temperature finish-rolling was more effective in niobium-containing, than in plain carbon–manganese, steels.<sup>13</sup>

In 1963, very tough niobium-containing semi-killed steels were developed with yield strengths of 36 kgf/mm<sup>2</sup> (X-52 grade) in the as-rolled condition after reheating the slabs at 1170° C,<sup>12</sup> which was the first introduction of low-temperature reheating into commercial production by controlled-rolling. Swedish<sup>8</sup> and Japanese researchers<sup>12</sup> both showed that this was effective in improving toughness by refining the  $\alpha$  grains and by suppressing the appearance of upper bainite, which was liable to be produced in as-rolled niobium-containing steels. In the controlled-rolling of IN-steels developed in Japan, rolling temperatures were required in the range 1200–700° C and a total percen-

tage reduction of more than 20% was required at temperatures below 1000°C<sup>15</sup> in order to guarantee notch toughness comparable with that of normalized steels, whether niobium was used or not. The low-temperature reheating of slabs was favourable for the starting temperature of such low-temperature controlled-rolling,<sup>15</sup> and has been one of the necessary technical requirements of present-day controlled-rolling, because it is metallurgically important in order to commence hot-reduction from temperatures where the slabs have fine  $\gamma$  grains, and to decrease the rolling temperatures at least in the early stages of rolling.

Research on precipitation hardening in the as-rolled or normalized condition, and in controlled-rolled niobium- or vanadium-containing steels carried out in the UK and Japan in the 1960s, and the following results, fundamental to the development of the current controlled-rolled, low-carbon, low-alloy, precipitation-hardened, high-toughness, high-strength steels, were obtained.

- (1) A remarkable strengthening by niobium or vanadium additions was caused by precipitation of fine planar niobium carbonitrides<sup>16</sup> or vanadium nitride,<sup>17,18</sup> coherent with the  $\alpha$  matrix,<sup>16,19</sup> these carbides and nitrides having been in solution in the  $\gamma$  grains at the reheating temperature of the slabs. The precipitates formed on  $\langle 100 \rangle$  planes of the  $\alpha$  matrix during and after transformation. The solubility of niobium carbonitrides in  $\gamma$  is small,<sup>9,16</sup> so the strength of as-rolled niobium-containing steels becomes constant with more than a critical amount of niobium, e.g. 0.05% in 0.10% C steels, and decreases after normalizing or with low-temperature reheating of slabs prior to hot-rolling, because a considerable amount of the added niobium has not been in solution in the  $\gamma$  prior to the transformation to  $\alpha$  and therefore is ineffective in strengthening the  $\alpha$  matrix. Vanadium nitride and vanadium carbide are more soluble in  $\gamma$  and  $\alpha$  than niobium carbide and niobium nitride.<sup>20</sup> Therefore, the strength of vanadium-containing steels can increase with larger amounts of vanadium, i.e. does not show such a pronounced saturation effect, and does not decrease after normalizing or low-temperature reheating of slabs, although the strength increment per unit addition of vanadium is smaller than that of niobium.<sup>21</sup>
- (2) A decrease in the pearlite fraction by reducing the carbon content lowers the ultimate tensile strength while not changing the yield strength, but does improve the notch toughness and weldability in carbon-manganese steels.<sup>22</sup> Duckworth, Phillips and Chapman<sup>23</sup> proposed that a very attractive combination of properties could be obtained in extra-low-carbon steels, when the strength was increased by niobium and/or vanadium additions and the notch toughness was guaranteed by low-temperature finish-rolling with heavy draughting (pearlite-free steel<sup>18</sup> and pearlite-reduced steel<sup>23</sup>).

The strength increment by an increase in manganese content up to 1.5% is much larger in niobium-containing steels than in carbon-manganese steels.<sup>23</sup> A reduction in carbon content in niobium-containing steels, however, increased the amount of precipitated niobium carbide but did not increase the strength.<sup>21</sup> This can be explained by the change in the  $A_{r3}$  temperatures and the very low solubility of niobium carbonitrides in  $\alpha$ .<sup>21</sup> The increase of  $A_{r3}$  temperatures resulting from the decrease in carbon content causes overageing of niobium carbonitrides precipitated in  $\alpha$  matrix, and a coarser grain size, and the manganese addition reduces

$A_{r3}$  temperatures and is effective for suppressing their overageing. Some comment is required as to why the lower carbon increases the amount of precipitated niobium carbonitrides. It is due to the extension of the  $\alpha$  range having poorer solubility of niobium carbonitride to the higher temperature side where diffusion of niobium is the more accelerated. The carbon and nitrogen consumed by their growth are not those in  $\gamma$ , the amount of which is determined by the steel composition, but by those in  $\alpha$  whose amount is determined only by temperature independent to the steel composition. The effect of the  $A_{r3}$  temperature on precipitation hardening becomes more pronounced in vanadium-containing steels, i.e. vanadium nitride and vanadium carbide have larger solubilities in  $\alpha$  than niobium carbonitrides and thus do not exhibit sufficient supersaturation to precipitate in the  $\alpha$  matrix which has transformed at higher temperatures,<sup>21</sup> so that a considerable decrease in the carbon equivalent is not possible without a decrease in strength.<sup>17,21</sup>

- (3) The addition of niobium retards recrystallization of the  $\gamma$  grains during hot-rolling.<sup>24-28</sup> Recrystallization of coarse-grained  $\gamma$  in steels containing 0.02–0.05% of niobium can occur after one or a few reductions at temperatures down to from 1050<sup>25</sup> to 1100°C,<sup>26</sup> but it takes more than 100 s to complete the recrystallization at these temperatures.<sup>25</sup> A similar but weaker effect is also observed by the addition of vanadium.<sup>27,28</sup> Kubota *et al.*<sup>28</sup> pointed out that these effects were also caused by niobium or vanadium in solution at least at the reheating temperatures of slabs.<sup>27,28</sup>

An important observation was made by Phillips, Duckworth and Copley,<sup>24</sup> on the controlled-rolling of niobium-containing steels, namely that there might be a correlation between the transformation from unrecrystallized  $\gamma$  and the improvement in notch toughness by the low-temperature finish-rolling.

Steel plates thinner than 12.7 mm controlled-rolled to 850°C, showed a satisfactory combination of strength and impact properties in industrial trials.<sup>26</sup> At this stage it was believed that the most important factor in the controlled-rolling operation was the attainment of a low finishing temperature such as occurs in thinner plates. It becomes necessary therefore to define a delay time (or holding time) in successive rolling reductions to carry out properly the effective low-temperature finish-rolling for thicker plates.

In mill trials of thicker plates, however, the lowering of the temperature of just the final reduction<sup>28</sup> and the introduction of a holding period at approximately 1050–900°C between roughing and finishing<sup>26</sup> caused mixed grain structures and gave poor impact properties. The thicker plates held at temperatures above 1050°C showed improved toughness.<sup>26</sup> These results were interpreted as follows. The improper selection of the holding temperature range would produce a partly recrystallized structure during holding<sup>29</sup> or during the time between the recommenced successive rolling reductions,<sup>30</sup> which would not be eliminated but rather be reproduced and intensified by the subsequent reductions and would finally transform into the mixed grain structure containing coarse upper bainite.<sup>26</sup> Heavy reductions at fairly equally spaced intervals over the whole temperature range after a reduced reheating temperature, if possible,<sup>26,29</sup> or holding in the temperature range either above 1100° or below 950°C<sup>26</sup> were recommended.

Kubota *et al.*<sup>28</sup> also reported that improvements in notch ductility and  $\alpha$  grain refinement were progressive with increasing total reduction below 950–900° C, where  $\gamma$  recrystallization could not start during intervals between reductions. At the same time, they found that plates in which roughing reductions were completed at higher temperatures followed by delayed cooling had very poor toughness compared with the values expected from their amount of total reduction in the lower temperature range. Such plates also exhibited mixed grain structures.<sup>28</sup> It was supposed that  $\gamma$  grain refinement by recrystallization might occur by reductions at temperatures down to 950° C and be effective in minimizing mixed grain structure.

In 1969, research was carried out into the commercial production of 14.3-mm thick plates and 11.7-mm thick coiled strip for API 5-LX-X-65 and API 5-LS-X-65 line-pipes for Alaska by controlled-rolling of niobium- and/or vanadium-containing steels having C + (Mn/6) smaller than 0.40%. The various combinations of the basic techniques for controlled-rolling – such as low-temperature reheating of slabs, controlled-rolling for the refinement of recrystallized  $\gamma$ , a holding period in an appropriate temperature range, a sufficient amount of reductions below the recrystallization temperature, finish-rolling at intercritical temperatures, rapid cooling on runout tables and low-temperature coiling – were adopted according to the steel compositions and their rolling-mill characteristics. Examples of the compositions and the rolling conditions used at that time are shown in Table 1.1 and Figure 1.1(c), in which low-temperature

TABLE 1.1 Chemistries and production conditions of controlled-rolled plates for API X-65 line-pipes for Alaska (1969)

|                                 | Plate-mill                                    | Hot-strip mill                                 |
|---------------------------------|---|--|
| Standard                        | API 5-LX-X-65                                 | API 5-LS-X-65                                  |
| Plate thickness (mm)            | 14.3  | 11.7   |
| Chemistry                       | 0.10% C–0.25% Si–1.4% Mn<br>–0.04% Nb–0.06% V | 0.10% C–0.25% Si–1.35% Mn<br>–0.04% Nb–0.04% V |
| Mn<br>C + $\frac{\text{Mn}}{6}$ | 0.33  | 0.32   |
| Slab reheating (° C)            | 1250° C                                       | 1250° C  |
| Final roughing (° C)            | 1050–1000° C                                  | 1000° C  |
| Transfer thickness              | 3.1   | 2.8  |
| Plate thickness                 |   |  |
| First finishing (° C)           | 910   | 980  |
| Final finishing (° C)           | (720)   | (830)  |
| Coiling (° C)                   | —   | 630  |

reheating and the intercritical-temperature rolling were not adopted. In the plate-rolling typified in Table 1.1, the reductions in the roughing and the finishing stands were carried out in the recrystallization and the nonrecrystallization temperature ranges respectively. The prototype conditions for controlled-rolling low-carbon, HSLA steels were virtually established by this development. The research results and the experience accumulated during these developments were reported in the 1970s, and can be summarized as follows:

- (1) The notch toughness was always better in niobium-containing, than in vanadium-containing, steels when compared at the same strength level for steels continuously

rolled down to 900° C.<sup>31,32</sup> An addition of nitrogen can improve the strength and toughness of vanadium-containing steels but reduce the weldability.<sup>32</sup> An addition of niobium above 0.05% becomes effective in terms of strengthening by the reduction of carbon content, but it reduces weldability.<sup>32,33</sup> Simultaneous additions of niobium and vanadium were favourable to obtain higher strengths and better weldability.<sup>31-33</sup>

- (2) The improvement of toughness as well as of strength in pearlite-reduced steels by the manganese addition<sup>1,23</sup> can also be explained by the effect of lowering the  $A_{r3}$  temperature.<sup>32</sup> The decreased  $A_{r3}$  temperatures mitigate the embrittlement which accompanies precipitation hardening, by refining the niobium carbonitrides and vanadium nitrides precipitated in the  $\alpha$  matrix<sup>32,34</sup> and by refining the  $\alpha$  grains more effectively after the same rolling conditions<sup>32,34</sup> and also by making it possible to intensify controlled-rolling at nonrecrystallization temperatures in the  $\gamma$ .<sup>35</sup> Similar effects can be expected by nickel and copper additions, by rapid cooling after rolling and by low-temperature coiling.<sup>32</sup>
- (3) The recrystallization temperatures of niobium-containing steels during successive rolling reductions were reported to be lowered to 950–900° C by Sekine and Maruyama<sup>32</sup> and Yamaguchi *et al.*<sup>36</sup> This is caused by the fact that recrystallization can occur down to the lower reduction temperature when the  $\gamma$  grains prior to hot-deformation are finer,<sup>9</sup> these being achieved by the preceding reductions from the reheating temperature down to the temperatures in question.<sup>32,36</sup> This explains why the hold time in the temperature range below 950° C<sup>26,28</sup> and the increase in the total reduction at temperatures below 950–900° C<sup>13,28</sup> are effective in improving notch toughness, and shows that the holding period should occur between the recrystallization and nonrecrystallization temperature ranges,<sup>26,28</sup> and should be in the temperature range 1000–950° C<sup>32</sup> instead of above 1100° C.<sup>26</sup>

Recrystallization of  $\gamma$  in silicon–manganese steels not containing niobium during successive reductions can occur after deformation at 850–800° C.<sup>32,36</sup> Precipitation of niobium carbonitrides in the  $\gamma$  matrix is accelerated by hot-deformation<sup>37</sup> and the increase in recrystallization temperatures by the niobium addition is mainly caused by fine niobium carbonitrides which have been in solution at the reheating temperature<sup>28</sup> and reprecipitated during hot-deformation.<sup>37</sup>

- (4) In the nonrecrystallized  $\gamma$  grains which are elongated in the rolling direction, there are deformation bands.\*  $\alpha$  grains nucleate on these hot-deformation and their twin bands as well as on  $\gamma$  grain boundaries, giving an increased surface area for the  $\gamma \rightarrow \alpha$  transformation.<sup>37</sup> This is the reason for the  $\alpha$  grain refinement in niobium-containing steels finish-rolled with heavy reductions below 900° C.<sup>13,18,28</sup>
- (5) Some of the nonrecrystallized elongated grains do not contain deformation bands\* or twins, and these result in a mixed  $\alpha$  grain structure after transformation.<sup>32,36</sup> The preliminary refinement of the recrystallized  $\gamma$  grains by controlling the rolling at higher temperatures<sup>32,39</sup> or with an increase in total reduction at nonrecrystallization temperatures<sup>32,39,40</sup> is necessary to obtain the uniform and fine transformed structure, which possesses good toughness. These two methods can both obtain the same transition temperature<sup>32,39</sup> but the Charpy shelf energy in the

\* It is now known that almost all the deformation bands were actually deformed annealing twins (Inagaki<sup>38</sup>).

transverse (T) direction is always higher when the controlled-rolling to intensify the preliminary refinement of  $\gamma$  grains is carried out.<sup>32</sup>  $\gamma$  grain refinement by controlling during roughing is more effective in hot-strip mills,<sup>32</sup> where heavier reductions per pass can be applied and the finishing rolling conditions are much restricted. Many nonmetallic inclusions, especially manganese sulphide, are elongated to the rolling direction by hot-deformation at lower temperatures, and this causes a deterioration of the toughness in the T direction. This tendency, which is fatal to line-pipes, can be alleviated also by reducing the sulphide content of steels<sup>31,41</sup> and by cross-rolling.<sup>31</sup>

- (6) Whether niobium is added<sup>39</sup> or not,<sup>9,32</sup> the lower the hot-deformation temperature, the heavier the draught and the finer the starting grain size during hot-working in the recrystallization temperature range, the finer the recrystallized  $\gamma$  grains which can give the smaller the  $\alpha$  grain size after transformation. These are the reasons for the improvement in toughness by low-temperature finish-rolling in carbon–manganese steels, by low-temperature slab reheating,<sup>8,12,26,40,42</sup> and by low-temperature roughing<sup>26,28,32</sup> in niobium and/or vanadium-containing steels.
- (7) The extension of finish-rolling down into the ( $\gamma + \alpha$ ) two-phase region improves the strength and transition temperature due to dislocation hardening and some further  $\alpha$  grain refinement.<sup>40,42</sup> However, due to the deformation of the developing  $\alpha$  phase, the shelf energy is reduced and the intensity of a  $\langle 100 \rangle$  texture and the number of separations in the fractured surface increased.<sup>42</sup>

### 1.2.3 Outline of controlled-rolling

The role of controlled-rolling is to introduce a high density of nucleation sites for  $\alpha$  grains in the  $\gamma$  matrix during transformation by controlling the hot-rolling conditions and so to refine the structure of the steel after transformation. With respect to  $\alpha$  nucleation sites,  $\gamma$  grain boundaries, interfaces of the annealing twins activated by hot-deformation and the deformation bands should be considered.

The most crucial factor in rolling conditions to control the  $\gamma$  structure is the hot-deformation temperature. Normal rolling, which does not involve any control of the rolling conditions, usually finishes at 1050–900° C according to the plate thickness, as shown in Figure 1.1(a). In the controlled-rolling of simple silicon–manganese steels which do not contain any element retarding the recrystallization of  $\gamma$ , recrystallized  $\gamma$  grains are refined by performing the several hot-deformations in the final stage of rolling at the lowest temperature (950–800° C) in the range where recrystallization of  $\gamma$  grains can occur; the refinement of the  $\alpha$  grains is achieved by the transformation from the fine-grained  $\gamma$  structure (Figure 1.1(b)). Further refinement of the transformed structure is also possible by continuing the rolling reductions down into the nonrecrystallization temperature range, but the temperature range between the critical temperature for  $\gamma$  recrystallization and the  $A_{r3}$  temperature is not so wide so that a large effect cannot be expected.

The addition of niobium raises the recrystallization temperature by about 100° C. The types of  $\alpha$  nucleation sites other than  $\gamma$  grain boundaries, which are introduced by reductions in the nonrecrystallization temperature range are activated twin boundaries and the deformation bands. The density of these interfaces and their activity as  $\alpha$  nucleation sites including elongated  $\gamma$ -grain boundaries are increased by increasing the



total reduction in the nonrecrystallization temperature range. In the controlled-rolling of niobium-containing steels, a certain amount of the  $\gamma$  grain refinement by recrystallization can occur during the reductions in the temperature range above 1000–950° C, and after the holding period further reductions are applied in the temperature range below 950–900° C where no recrystallization can occur (Figure 1.1.(c) and (d)). The  $\alpha$  grain refinement above that which occurs in controlled-rolled silicon–manganese steels is achieved by transformation from the unrecrystallized and elongated  $\gamma$  grains. When improved notch ductility is demanded, greater deformations should be used in this temperature range. The roughing reductions preceding holding ordinarily finish at temperatures comparably higher than 1000–950° C. An improvement in notch ductility can also be achieved by applying the final roughing passes towards 1000–950° C.

The controlled-rolling practices for silicon–manganese, and niobium-containing, steels are apparently very similar, but the metallurgical phenomena occurring during the low-temperature finish-rolling are intrinsically different as described above.

In both cases, lowering the reheating temperature of the slabs (Figure 1.1.(d)) is effective in increasing the rolling productivity by shortening the holding time and this can also improve the ductility of rolled products by refining the recrystallized  $\gamma$  grains after finishing or roughing. The strength of niobium-containing steels is apt to be reduced by low-temperature reheating because of the incomplete solution of niobium carbonitrides in the  $\gamma$  which consequently decreases the intensity of precipitation strengthening.

Whether the steel contains niobium<sup>40,42</sup> or not,<sup>43,44</sup> the extension of finish rolling into the ( $\gamma + \alpha$ ) two-phase region raises the strength and improves the ductile→brittle transition temperature and crack arrestability,<sup>33,45,46</sup> but deteriorates the through-thickness (Z) properties<sup>47</sup> and the Charpy shelf energy particularly in the T direction.<sup>42,47</sup> It is attempted to reach a compromise between strength and the  $C_{eq}$  of steels, especially in the low-temperature reheating, niobium- or vanadium-containing steels<sup>40,48,49</sup> (Figure 1.1.(d)).

The various operational factors described are occasionally cumulative but generally counteract each other in simultaneously improving the characteristics of steels, the productivity and the prime cost. Their selection is also largely restricted by the capacities of the rolling equipment and its layout.<sup>32,39,46</sup> Details of the practices used differ widely in many rolling mills, and it is rarely possible to transfer a specific controlled-rolling schedule from one mill to another. Table 1.1 also shows the conditions for controlled-rolling of steel coils having a similar compositional specification in a hot-strip mill, as an extreme example.

#### 1.2.4 Further developments of controlled-rolling: bainitic steels and extra-low-temperature reheating

Control-rolled high-strength steels had been almost exclusively used for line-pipes in the early 1970s. The demands for plates, however, have moved toward higher strength, greater toughness and larger thickness without detriment to weldability. Projects of the construction of pipelines for natural gas transportation require higher transverse Charpy shelf-energy. The fracture appearance transition temperature in the drop weight tear test (DWTT), which corresponds to the resistance to crack propagation,<sup>50</sup> became a requirement in addition to the transverse Charpy energy at the service tem-

perature, which indicates the resistance to crack initiation. This new measure of toughness has been improved by increasing the total hot-rolling deformation below the recrystallization temperature.<sup>45,46</sup>

The increase in the plate thickness and the intensification of low-temperature finish-rolling both increased the transfer thickness of slabs at which holding was carried out. Longer holding times were required and, consequently, larger rolling forces, so that the rolling mills suffered from a decrease in productivity and limitations of mill capacities.<sup>46,51</sup>

Finish-rolling at intercritical temperatures could improve both strength and the ductile→brittle transition temperature without increases in the  $C_{eq}$  and the mill loading.<sup>48</sup> It also raised crack arrestability<sup>33,45,46</sup> but required a longer holding time. More careful attention to steelmaking has been necessary to reduce the sulphur content and to change the shapes of sulphides by additions of rare earth metals<sup>47,48</sup> zirconium, titanium or calcium<sup>52</sup>, in order to meet the transverse impact shelf-energy and the Z direction property requirements.

The low-temperature reheating of slabs became more popular<sup>53</sup> and the carbon contents of steels were further reduced to ensure that both the required amount of niobium was in solid solution at the lower reheating temperature and the demand for high toughness was met. The additions of manganese were increased, and also nickel and/or copper were added. The  $\alpha$  grain refinement and the decrease in the pearlite fraction caused an increase in yield ratio (LYP : UTS) of rolled products. This tendency led to a decrease in yield strength of tensile specimens taken after pipeforming due to the Bauschinger effect,<sup>49</sup> which meant a reduction of the plastic stability of rolled plates as materials for high-strength pipes. The small difference between the stress for the start of deformation and the fracture stress was not favourable if the materials were to be used for other structures. Intercritical rolling also increased the yield ratio.<sup>47</sup>

In the process of reducing the carbon content and increasing the manganese content in controlled-rolled niobium-containing steels, the developments of low-carbon (0.06%), high-manganese transformation-strengthened steels named low-carbon bainitic steel<sup>54</sup> and acicular  $\alpha$  steel<sup>55</sup> were announced in 1972 by Terazawa, Higashiyama and Sekino<sup>54</sup> and Smith, Coldren and Cryderman<sup>55</sup> respectively. These steels showed continuous yielding and increased ultimate tensile strengths compared with conventional  $\alpha$ -pearlite steels and increase in proof stress after pipeforming in spite of their low-carbon compositions.<sup>56</sup> In the materials having lower yield ratios, rapid work-hardening can exceed any drop in yield strength due to the Bauschinger effect.<sup>56</sup> The structure of the steels is typically acicular  $\alpha$  or low-carbon bainite, retaining a distinct boundary for the prior  $\gamma$  grains after normalizing or normal rolling, i.e. after the transformation from the polygonal  $\gamma$  grains.<sup>54,55</sup>

The transformation from the heavily deformed  $\gamma$  grains after controlled-rolling changes the main structure of the steels into fine nonequiaxed and 'blocky'  $\alpha$  dispersed with martensite islands<sup>54</sup> and bainite islands<sup>54</sup> showing no indication of the location of the prior  $\gamma$  grain boundaries.<sup>55</sup> The strength of the controlled-rolled steels increased abruptly at 2% manganese, corresponding to the change in  $\alpha$  microstructure from polygonal  $\alpha$ -pearlite to the upper fine nonequiaxed and blocky  $\alpha$  structures.<sup>54</sup> The manganese content can be reduced by using additions of boron and titanium,<sup>54</sup> or by an addition of a small amount of molybdenum.<sup>55</sup> Niobium in solid solution is also effective in promoting the above microstructural changes as well as manganese<sup>54,55</sup>



and molybdenum.<sup>55</sup> In the typical bainitic steels, the effective grain size is nearly equal to the prior  $\gamma$  grain size, whereas in these steels the effective grain size of the transformation products from the unrecrystallized and elongated  $\gamma$  grains becomes much smaller, which decreases the transition temperature.<sup>54,55</sup> Increases in the amount of hot-deformation below the recrystallization temperature introduce fine polygonal  $\alpha$  grains into the matrix, and the best combination of strength and toughness can be obtained with the appropriate amount of polygonal  $\alpha$ .<sup>55,57</sup> In the low-carbon–manganese–molybdenum–niobium steels, the strength and the toughness are less sensitive to variation of the reheating temperature of the slabs.<sup>55</sup> Later, it was shown that molybdenum in solid solution retarded recrystallization of  $\gamma$ , although the effect was not so strong as that of niobium,<sup>58–60</sup> and molybdenum (or it) also refined the recrystallized  $\gamma$  grains.<sup>59</sup> Molybdenum does not precipitate as carbides or nitrides in  $\gamma$  with the additions used and its effects are substantially insensitive to the reheating temperature, i.e. different from those of niobium. The appearance of the molybdenum-containing acicular  $\alpha$  steels has greatly facilitated the controlled-rolling of plates having larger thickness and higher toughness, and removed the unwanted high-yield ratio typical of the controlled-rolled, low-carbon,  $\alpha$ –pearlite steels.

The  $\gamma$  grains in aluminium-killed steels start to coarsen at 1000–1050°C during the reheating of slabs, and additions of niobium raise this temperature by about 50°C.<sup>8,61</sup> When a large amount of strengthening by niobium additions is not expected, and/or vanadium is added as a strengthening element, or in the case of conventional structural steels not containing these elements, the use of reheating temperatures below the grain-coarsening temperatures makes it possible to start the hot-deformation process from the fine-grained  $\gamma$  condition.<sup>62</sup> This is effective in improving the toughness.<sup>62</sup> Controlled-rolling of niobium-containing steels after reheating to 1050°C<sup>53</sup> corresponds to rolling from the fine-grained  $\gamma$  condition. In 1975, a process was developed for extra-low-temperature reheating in conjunction with a two-stand rolling line, and this began commercial production of silicon–manganese steels for low-temperature service and for thicker line-pipe steels, namely the Sumitomo high-toughness (SHT) process described by Nozaki and Fukuda<sup>45</sup> and Takeuchi *et al.*<sup>46</sup> Its characteristic is 'double reheating – double rolling' (Figure 1.1(e)). The rough-rolled slabs are water-cooled down to a temperature below  $A_{r1}$  and secondary rolling is carried out after reheating of the slabs to the normalizing temperature. Satisfactory rolling efficiency, comparable to that of ordinary rolling, has been obtained by interspersing one slab for SHT rolling and one or two slabs for normal rolling on the production line which includes the SHT reheating furnace.<sup>46</sup> The hot-rolling from the normalizing temperature has made it possible to reduce the delay time and made it unnecessary to use conventional controlled-rolling for the preliminary refinement of the recrystallized  $\gamma$  grains.

Since the oil crisis of 1973, low-temperature reheating of slabs has been further applied to conventional steels not containing niobium or vanadium, in order to save energy because it was shown that the increase in the cost of electric power to the rolling mill by decreasing the rolling temperatures was smaller than the decrease in the cost of fuel produced by lowering the temperatures of the reheating furnaces. The use of controlled-rolling practices, the appearance of the new characteristics of controlled-rolled steels and the demand for saving energy have combined to stimulate study on the elimination of normalizing and the reduction in carbon equivalent and alloying ad-

ditions in conventional steels by the extensive application of these technical concepts of controlled-rolling. Double reheating in the SHT process is, however, unfavourable from the viewpoint of saving energy.

Additions of very small amounts of titanium (0.005–0.02%) can improve the toughness of the heat-affected zone of welds by suppressing the growth of the  $\gamma$  grains because of the presence of fine dispersed titanium nitride which pins the  $\gamma$  grain boundaries.<sup>63</sup> In such steels the grain coarsening temperature is higher than for other steels and the  $\gamma$  grains remain finer at all reheating temperatures. The grain coarsening temperature is increased to 1150–1250°C especially in continuously cast slabs.<sup>64</sup> Such small additions of titanium to niobium-containing steels make it possible to start hot-deformations after once reheating slabs at temperatures at which there is no  $\gamma$  grain coarsening, and yet to dissolve sufficient niobium to retard recrystallization and also introduce precipitation strengthening. This has led to the development of new acicular steel as titanium-microalloyed manganese–molybdenum–niobium–vanadium steel<sup>64</sup> and successively ultra low-carbon bainitic steel<sup>65</sup> for line-pipes. In ultra-low-carbon bainitic steel, bainite has been added to reduce or eliminate the molybdenum addition in the manganese–molybdenum–niobium–titanium steel,<sup>64</sup> and the best combination of strength and toughness has been obtained by controlled-rolling after reheating to 1000–1050°C, with the bainitic structure containing fine polygonal  $\alpha$  grains and martensite islands.<sup>65</sup> In both steels, the decrease in the reheating temperature of slabs down to 950–960°C, made it possible to extend the finish-rolling down into the intercritical range without holding, so changing the structure into finer and deformed polygonal  $\alpha$  and elongated martensite. This produced a lower transition temperature in the Charpy and DWTT tests. The strength was lower in the ultra-low-carbon bainitic steel but increased in the vanadium-containing new acicular  $\alpha$  steel due to the extra-low-temperature reheating. The  $\alpha$ -martensite dual-phase steel having the manganese–molybdenum–vanadium–titanium composition is favourable for the materials of pipes such as that in pumping stations, in which heavier wall thickness, stress-relief annealing after welding and heat-affected zone toughness at extremely low temperatures are required. The reheating temperature of continuously cast slabs of titanium-microalloyed steels giving the most improved heat-affected zone toughness is about 1000°C.<sup>66</sup> In 1980, a new reheating furnace was developed, permitting extra-low-temperature reheating together with conventional-temperature reheating, which led to the production of ultra-low carbon bainitic steel, the  $\alpha$ -martensite dual-phase steel and the titanium–vanadium  $\alpha$ -pearlite steel for the low-temperature service having improved weldability by the low-temperature once-reheating of slabs called the Nippon steel intercritical control (NIC) process<sup>66</sup> (Figure 1.1(f)).

### 1.2.5 Accelerated cooling in plate-rolling mills

Engineers in plate-mills have long known that accelerated cooling after rolling increases the strength equally as well as ‘off-line’ heat treatment. Studies of direct quenching accompanied by off-line tempering have been carried out by many workers, and the applications have been widely reported.<sup>67</sup> Furthermore, investigations on the introduction of accelerated cooling after rolling during the processing of the more average plate products which are generally offered as aircooled products after rolling, have promised an increase in strength or a reduction of  $C_{eq}$ , e.g. by changing from the

$\alpha$ -pearlite, to the  $\alpha$ -bainite, structure. However, these trials have not been commercially successful because of the difficulty in guaranteeing dimensional accuracy, uniformity of properties in the Z direction, toughness and ductility.

Coils having high strength and improved toughness for spiral pipes and electric welded pipes<sup>32,40,68,69</sup> and in the dual-phase sheet steel having high strength and a low-yield ratio for motor vehicles,<sup>70</sup> have both been produced by the combination of controlled-rolling and the control of the cooling and the coiling conditions in hot-strip mills.<sup>32,40,69,70</sup> The run-out table and the coiler, which had been originally installed to reduce the spatial length requirements of rolling mills, began to function as the equipment for 'on-line heat treatment', and the control of the processing conditions made it possible to produce coils with a more extensive range of properties and characteristics than those of controlled-rolled and aircooled heavy plates.

Furthermore, it became clear in plate-rolling that the strengthening due to controlled-rolling can reduce the hardenability of the hot-rolled  $\gamma$ , refine the transformed structure, and improve even the toughness and the ductility of bainitic steels. Thus, the new controlled-rolled transformation-strengthened steels were developed.<sup>54,55</sup> These have more attractive characteristics than the precipitation-strengthened  $\alpha$ -pearlite steels,<sup>56</sup> but their compositions are made expensive because of the need to provide sufficient hardenability for the aircooled condition. Accelerated cooling after controlled-rolling can reduce not only the amounts of molybdenum and manganese in these bainitic steels<sup>68</sup> but also the  $C_{eq}$  of the conventional-tonnage structural steels which also have improved toughness and ductility. The spread of the practices of controlled-rolling, and the accumulated knowledge on the transformation behaviour after controlled-rolling, provided the possibility of a guarantee of the properties of accelerated-cooled plates. Thus, the development of the plant and processes for controlled-cooling for the production of plates of good appearance has become a major subject for investigation in heavy-plate mills.<sup>71</sup>

## References

1. VANDERBECK, R.W. *Weld. J.*, **37**, 114-S (1958)
2. BARR, W. and TIPPER, C.F. *J. Iron and Steel Inst.*, **157**, 223 (1947)
3. HESLOP, J. and PETCH, N.J. *Phil. Mag.*, **3**, 1128 (1958)
4. BERRY, W.J. *Iron Coal Trade Rev.*, **66**, 900 (1928)
5. HANEMANN, H. and LUCKE, F. *Stahl u. Eisen*, **45**, 1117 (1925)
6. FRAZIER, R.H., BOULGER, F.W. and LORIG, C.H. *Iron and Steel Engr.*, **33**, 10, 67 (1956)
7. WIESTER, H.-J., DAHL, W. and HENGSTENBERG, H. *Stahl u. Eisen*, **82**, 1176 (1962)
8. DE KAZINCZY, F., AXNÄS, A and PACHLEITNER, P. *Jernkont. Ann.*, **147**, 408 (1963)
9. GRANGE, R.A. *Fundamentals of deformation processing*, ed. W.A. Backofen, Syracuse University Press, p.229 (1964)
10. Great Lakes Steel Corp., *Steel*, **116**, 102 (1960)
11. BEISER, C.A., *Preprint* 138, Annual conference, American Society of Metals (1959)
12. GONDOH, H., GOHDA, S. and KIMURA, I. *International Institute of Welding Document No. TX 416-64* (1964); *Tetsu-to-Hagané*, **53**, 629 (1967)
13. NOREN, T.M. *Ship Structure Committee Special Report No. SSC-154, PB181539* (1964)
14. JONAS, E.A. *Blast furnace and steel plant*, **53**, 706 (1965)
15. NAKAMURA, H. Japanese Patent No. Sho-41-9283 (1966)
16. MORRISON, W.B. *J. Iron and Steel Inst.*, **201**, 317 (1964)
17. STEPHENSON, E.T., CARCHNER, G.H. and STARK, P. *Trans Am. Soc. Metals*, **57**, 208 (1964)
18. DUCKWORTH, W.E. *Iron and steel*, **37**, 585 (1964)

19. TANINO, M., NISHIDA, T., OOKA, T. and YOSHIKAWA, K. *J. Japan Inst. Metals*, **29**, 734 (1965)
20. SEKINE, H., INOUE, T. and OGASAWARSA, M. *Trans Iron and Steel Inst. Japan*, **8**, 101 (1968)
21. SEKINE, H., MARUYAMA, T., SEKIGUCHI, S. and OHNO, T. *Tetsu-to-Hagané*, **56**, 569 (1970)
22. PICKERING, F.B. and GLADMAN, T. *Iron and Steel Institute Special Report No. 81*, p.10 (1963)
23. DUCKWORTH, W.E., PHILLIPS, R. and CHAPMAN, J.A. *J. Iron and Steel Inst.*, **203**, 1198 (1965)
24. PHILLIPS, R., DUCKWORTH, W.E. and COPLEY, P.E.L. *J. Iron and Steel Inst.*, **201** 593 (1964)
25. OHMORI, Y. *J. Japan. Inst. Metals*, **30**, 1164 (1966)
26. IRANI, J.J., BURTON, D., JONES, J.D. and ROTHWELL, A.B. *Iron and Steel Institute Special Report No. 104*, 10 (1967); Iron and Steel Institute, *Strong tough structural steels*, p.110 (1967)
27. KOZASU, I., SHIMIZU, T. and KUBOTA, H. *Trans Iron and Steel Inst. Japan*, **11**, 71 (1971)
28. KUBOTA, H., KOZASU, I., SHIMIZU, T., MURAI, S. and KANEKO, Y., *Nippon Kokan Technical Report No. 46*, p.205 (1969); *Nippon Kokan Technical Report-Overseas* p.23 (1971)
29. JONES, J.D. and ROTHWELL, A.B. *International Steel Institute Special Report No. 108*, p.78 (1968); Iron and Steel Institute *Deformation under hot-working conditions*, p.78 (1968)
30. IRANI, J.J., BURTON, D. and LATHUM, D.J. *British Iron and Steel Research Association Open Report No. Mg/C/31/68* (1968)
31. MATSUBARA, H., OSUKA, T., KOZASU, I. and TSUKADA, K. *Trans Iron and Steel Inst. Japan*, **12**, 435 (1972)
32. SEKINE, H. and MARUYAMA, T. *Seitetsu Kenkyu* **43**, 289 (1976)
33. YAMAGUCHI, T., OSUKA, T., TAIRA, T. and IWASAKI, N. *Microalloying 75*, Union Carbide Corp. p.415 (1977)
34. SEKINE, H., MARUYAMA, T. and SEKIGUCHI, S. *Tetsu-to-Hagané*, **58**, S224 (1972)
35. KOZASU, I., SHIMIZU, T. and TSUKADA, K. *Trans Iron and Steel Inst. Japan*, **12**, 305 (1972)
36. SEKINE, H. and MARUYAMA, T. *The microstructure and design of alloys*, Vol. I, Metals Society, p.85 (1973)
37. SEKINE, H. and MARUYAMA, T. *Tetsu-to-Hagané*, **58**, 1424 (1972); *Trans Iron and Steel Inst. Japan*, **16**, 427 (1976)
38. INAGAKI, H. *Trans Iron and Steel Inst. Japan*, **23**, 1059 (1983)
39. KOZASU, I., OUCHI, C., SAMPEI, T. and OKITA, T. *Microalloying 75*, Union Carbide Corp., p.120 (1977)
40. FUKUDA, M., HASHIMOTO, T. and KUNISHIGE, K. *Microalloying 75*, Union Carbide Corp., p.136 (1977)
41. GONDOH, H. and NAKASUGI, H. *Processing and properties of low-carbon steel*, Metallurgical Society of the American Institute of Engineers, p.47 (1973)
42. TANAKA, T., TABATA, N., HATOMURA, T. and SHIGA, C. *Microalloying 75*, Union Carbide Corp., p.107 (1977)
43. GOHDA, S., WATANABE, K. and HASHIMOTO, Y. *Tetsu-to-Hagané*, **65**, 1400 (1979)
44. HASHIMOTO, T., SAWAMURA, T. and OHTANI, H. *Tetsu-to-Hagané*, **65**, 1425 (1979)
45. NOZAKI, N. and FUKUDA, M. *Pressure Engrg.*, **16**, 8 (1978); IKESHIMA, T. *Tetsu-to-Hagané*, **65**, 1644 (1979)
46. TAKEUCHI, H., SUZUKI, T., HASHIMOTO, T. and YOKOI, T. *Steel rolling*, Vol. II, Iron and Steel Institute of Japan, p.957 (1980)
47. COLEMAN, T., DULIEU, D. and GOUCH, A. *The microstructure and design of alloys*, Vol. I, The Metal Society, p.70 (1973)
48. LITTLE, J.H., CHAPMAN, J.A., MORRISON, W.B. and MINTZ, B. *The microstructure and design of alloys*, Vol. I, The Metal Society, p.80 (1973)
49. TANAKA, T., FUNAKOSHI, T., UEDA, M., YASUDA, T., TSUBOI, J. and UTAHASHI, C. *Microalloying 75*, Union Carbide Corp., p.399 (1977)
50. EIBER, R.J. *Oil and Gas J.*, 158 (September 1963)
51. LAFRANCE, M.L., CARON, F.A., LAMENT, G.R. and LECLERC, J. *Microalloying 75*, Union Carbide Corp., p.367 (1977)
52. NAKAI, Y., HAIDA, O., SAKURAYA, T. and EMI, T. *Kawasaki Steel Giho.*, **11**, 44 (1979)
53. CIVALLERO, M., and PARRINI, C. *Scientific techniques for iron and steel*, Vol. II, p.758 (1971)
54. TERAZAWA, T., HIGASHIYAMA, H. and SEKINO, S. *Toward improved ductility and toughness*, Climax Molybdenum Co. (Japan), p.101 (1972)
55. SMITH, Y.E., COLDREN, A.P. and CRYDERMAN, R.L. *Toward improved ductility and toughness*, Climax Molybdenum Co. (Japan), p.119 (1972)
56. TITHER, G. and LAVITE, M. *J. Metals*, **27**, 15 (1975)
57. TABATA, N., SHIGA, C., KAMADA, A. and TANAKA, T. *Tetsu-to-Hagané*, **63**, S797 (1977)
58. MAEHARA, Y., KUNITAKE, T. and FUJINO, N. *Tetsu-to-Hagané*, **67**, 138 (1981)
59. SEKINE, H., MARUYAMA, T., KAGEYAMA, H. and KAWASHIMA, Y. *Thermomechanical processing of micro-alloyed austenite*, The Metallurgical Society of the American Institute of Metallurgical Engineers, p.141 (1981)
60. BACROIX, B., AKBEN, M.G. and JONAS, J.J. *Thermomechanical processing of microalloyed austenite*, The

- Metallurgical Society of the American Institute of Metallurgical Engineers, p.293 (1981)
61. GLADMAN, T. and PICKERING, F.B. *J. Iron and Steel Inst.*, **205**, 653 (1967)
  62. MAEKAWA, S., MIYANO, K. and SHIMAZAKI, M. *Tetsu-to-Hagané*, **58**, 1861 (1972)
  63. KANAZAWA, S., NAKASHIMA, A., OKAMOTO, K. and KANAYA, K. *Trans Iron and Steel Institute Japan*, **16**, 486 (1976)
  64. GONDOH, H., NAKASUGI, H. MATSUDA, H., TAMEHIRO, H. and CHINO, H. *Nippon Steel Technical Report No. 14*, p.55 (1979)
  65. NAKASUGI, H., MATSUDA, H. and TAMEHIRO, H. *Steel rolling*, Vol. II, Iron and Steel Institute of Japan, p.1028 (1980)
  66. MATSUDA, H., TAMEHIRO, H., CHUJIWA, R., MASUI, H. and SOGO, Y. *Seitetsu Kenkyu*, 309, 35 (1982)
  67. PARRINI, C. and PIZZIMENTI, N. *Microalloying 75*, Union Carbide Corp., p.288 (1977)
  68. HAMRE, E.C. and GILROY-SCOTT, A.M. *Microalloying 75*, Union Carbide Corp., p.375 (1977)
  69. TAEFFNER, K.D., GORGES, G. and RECKNAGEL, W. TH. *Microalloying 75*, Union Carbide Corp., p.425 (1977)
  70. FURUKAWA, T., MORIKAWA, H., TAKECHI, H. and KOYAMA, K. *Structure and properties of dual-phase steels*. The Metallurgical Society of the American Institute of Engineers, p.281 (1979)
  71. OKITA, T., OUCHI, C. and KOZASU, I. *Tetsu-to-Hagané*, **63**, S798 (1977)

---

## Austenite to ferrite transformation and refinement of ferrite grain size

---

### 2.1 $\gamma \rightarrow \alpha$ phase transformation

#### 2.1.1 Classification of phase transformation

The transformation from austenite ( $\gamma$ ) can be classified into two groups: (1) the diffusional transformation of, for example, ferrite ( $\alpha$ ) or pearlite, which proceeds with nucleation and growth mechanism; and (2) the martensitic transformation which proceeds with shear mechanism. When a steel is cooled faster than its critical cooling rate, martensite transformation occurs. In low-carbon and low-alloy steels, the morphology of martensite is usually lath martensite. The characteristics of lath martensite are mentioned by Maki, Tsuzaki and Tamura<sup>1</sup> and the reader is referred to that work. The bainite transformation, which is similar to martensite transformation, will also be omitted, the main emphasis being given to  $\alpha$  transformation.

The following three phenomena usually occur simultaneously during diffusional phase transformation: (1) lattice change; (2) compositional change; and (3) recrystallization. When  $\alpha$  forms from  $\gamma$ ,  $\alpha$  nucleates mainly at the  $\gamma$  grain boundaries. When the supercooling is small, polygonal  $\alpha$  forms and some of the adjacent  $\alpha$  grains with similar orientation coalesce into one grain. However, one  $\gamma$  grain is usually divided into several  $\alpha$  grains by transformation, and the smaller the  $\gamma$  grain the smaller the  $\alpha$  grains become. When the cooling rate is fast (accelerated cooling) and the supercooling is large, many fine  $\alpha$  grains form. However, when the supercooling is sufficiently large, acicular  $\alpha$  with the Widmanstätten structure forms.

The orientation relationship between the  $\gamma$  and  $\alpha$  phases is the K-S relationship similar to lath martensite, i.e.:

$$\langle 111 \rangle_{\gamma} // \langle 011 \rangle_{\alpha}, [\bar{1}01]_{\gamma} // [\bar{1}1\bar{1}]_{\alpha} \quad (2.1)$$

There are 24 variants satisfying this orientation relationship. When the  $\alpha$  grain is nucleated at the  $\gamma$  grain boundary, the  $\alpha$  grain satisfies the K-S orientation relationship with one of the adjacent  $\gamma$  grains. The incoherent  $\alpha$ - $\gamma$  interface without the K-S orientation relationship grows faster than the other boundary with the K-S relationship. When supercooling is low, the incoherent  $\alpha$ - $\gamma$  interface grows so that a grain becomes polygonal. After the completion of transformation the orientation relationship be-

tween the  $\gamma$  and  $\alpha$  phases is hardly detected. When Widmanstätten  $\alpha$  forms, its side plane (habit plane) is coherent and close to  $(111)_\gamma$  and satisfies the K-S orientation relationship with  $\gamma$ . The Widmanstätten  $\alpha$  grows sideways with the ledge mechanism as will be described below.

### 2.1.2 Effect of alloying elements on $\gamma \rightarrow \alpha$ transformation

Among the alloying elements in low-alloy steels, nickel, manganese, cobalt, copper, carbon and nitrogen are the  $\gamma$  formers, which stabilize  $\gamma$  by lowering the  $A_{r3}$  temperature and retard the decomposition of  $\gamma$ . The alloying elements such as silicon, aluminium, phosphorus, chromium, vanadium, molybdenum, tungsten, titanium, tantalum, niobium and zirconium are  $\alpha$  formers which raise the  $A_{r3}$  temperature but retard decomposition of  $\gamma$  by slowing down the diffusivity of carbon in  $\gamma$  and some other reasons such as grain boundary enrichment. Furthermore, among the  $\alpha$ -forming elements, chromium, vanadium, molybdenum, tungsten, titanium, tantalum, niobium and zirconium are the strong carbide formers and precipitate alloy carbides independently. Furthermore, the above elements (except molybdenum and tungsten) can also form nitrides in steels, and if both carbon and nitrogen exist, they can form carbonitrides. Carbonitrides can be precipitated in the  $\gamma$  phase according to the solubility product of the alloying element and the carbon or nitrogen. Of course, carbonitrides precipitate more in the  $\alpha$  phase because of the low solubility.

When the polygonal  $\alpha$  forms from  $\gamma$  during slow-cooling,  $\alpha$ -forming elements enrich in  $\alpha$  and  $\gamma$ -forming elements enrich in  $\gamma$ , i.e. alloy partitioning occurs. Local equilibrium conditions are considered usually to exist at  $\alpha$ - $\gamma$  interface. Orthoequilibrium is the condition at which alloying elements are partitioned into both phases to equilibrate chemical potentials of alloying elements in both phases. However, when a cooling with a usual rate is applied, partition of the carbon is easy to achieve, but partition of the alloying element is harder. Such a condition is called 'paraequilibrium'.

As  $\alpha$  transformation progresses, carbon is enriched in the retained  $\gamma$  and pearlite transformation begins. When the carbide-forming element exists in steel, either one of the following three things can happen:

- (1) Alloy carbides of niobium ( $\text{NbC}$ ), vanadium ( $\text{V}_4\text{C}_3$ ) and titanium ( $\text{TiC}$ ), etc. precipitate during  $\gamma \rightarrow \alpha$  transformation.
- (2) Once carbide-forming elements come into  $\alpha$  (because these elements are  $\alpha$  formers) carbon precipitates as iron carbide; iron carbide then changes to alloy carbide in  $\alpha$  because these elements are stronger carbide formers than iron, but diffusion is difficult. Iron is always neighbors.
- (3) Carbide-forming elements come into  $\alpha$  after transformation and then alloy carbides precipitate in  $\alpha$  directly, not through iron carbide.

In case of (1), it is often observed that alloy carbides form as rows of very fine particles at the  $\alpha$ - $\gamma$  interface during the growth of  $\alpha$ . This can occur both during isothermal holding and continuous cooling with appropriate cooling rate. As is shown in Figure 2.1, at the  $\gamma$  side of  $\alpha$ - $\gamma$  coherent interface ( $\{111\}_\gamma // \{\bar{1}10\}_\alpha$ ) carbon enriches the local equilibrium condition, and alloy carbide precipitates as rows of very fine particles. The carbon concentration is decreased by this precipitation and the incoherent interface of ledge (close to  $\{112\}_\alpha$ ) grows rapidly. By the movement of a large number of ledges, the



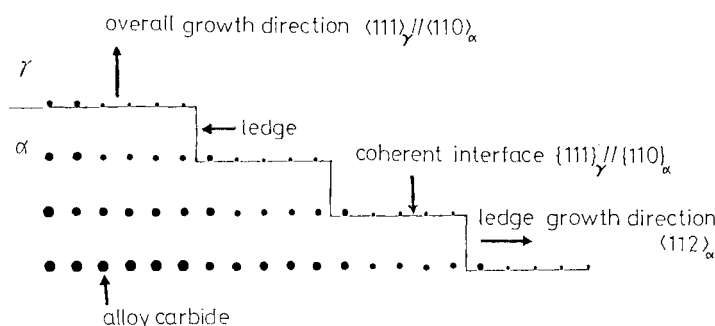


Figure 2.1 Schematic illustration of ledge mechanism of growth during  $\gamma \rightarrow \alpha$  transformation

macroscopic  $\alpha$  interface appears to grow in the direction of  $\langle 111 \rangle_\gamma$  ( $\parallel \langle 110 \rangle_\alpha$ ). Such growth is called the 'ledge mechanism of growth', and the precipitation which occurs accompanying this growth is called the 'interphase precipitation'.<sup>2</sup> Figure 2.2 shows an example of such precipitation.

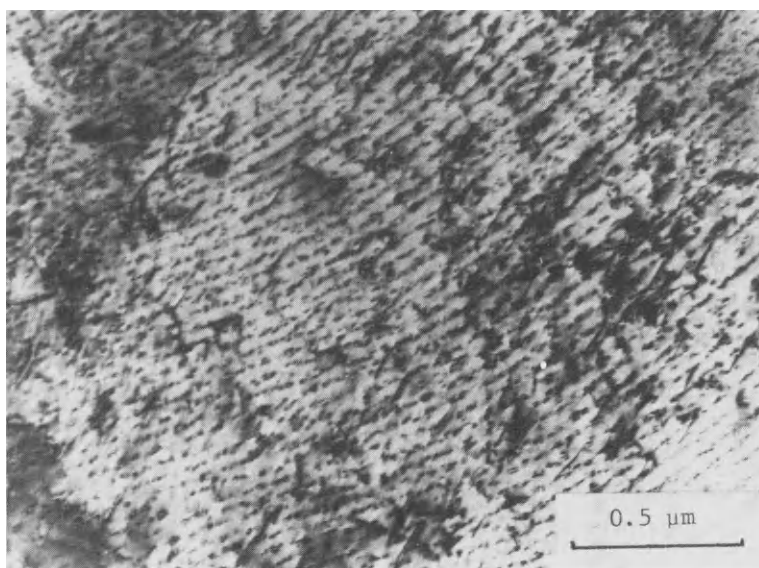


Figure 2.2 The interphase precipitation of niobium carbide particles observed in Fe-0.036% Nb-0.09% C-0.003% B alloy, isothermally transformed at 800°C for 2 min after austenitization at 1100°C for 10 min. (Courtesy of T. Sakuma and R.W.K. Honeycombe)

### 2.1.3 Precipitation of alloy carbide from $\alpha$

The carbide-forming elements are also the  $\alpha$  formers. Thus, when steel is cooled rapidly and diffusion of such elements is prevented, they stay in  $\alpha$  in solution. In this case, carbon exists either as iron carbide ( $\text{Fe}_3\text{C}$ ) or in solution similar to the case of the martensite phase. If such materials are heated, carbon precipitates firstly as the carbide  $\text{Fe}_3\text{C}$ . Above 450°C, carbides of vanadium ( $\text{V}_4\text{C}_3$ ), molybdenum ( $\text{Mo}_2\text{C}$ ), titanium



(TiC), niobium (NbC), etc. gradually precipitate and  $\text{Fe}_3\text{C}$  decreases. The equilibrium partition coefficient (the ratio of alloying element in  $\text{Fe}_3\text{C}$  over in  $\alpha$ ) is chromium, 23; manganese, 10.5; vanadium, 9; molybdenum, 7.5; tantalum, 2 and less than unity for titanium, niobium and zirconium. For instance, chromium sufficiently solves in  $\text{Fe}_3\text{C}$  and enriches in  $\text{Fe}_3\text{C}$ . Thus nuclei of  $\text{Cr}_7\text{C}_3$  form in  $\text{Fe}_3\text{C}$  or in contact with  $\text{Fe}_3\text{C}$ . This is called *in situ* nucleation. On the other hand, some elements like niobium are hardly solved in  $\text{Fe}_3\text{C}$ . Thus, nuclei of niobium carbide form on mainly dislocations in the  $\alpha$  matrix. Coherent precipitation of such carbides contributes markedly to the strengthening. This is called 'separate nucleation', while vanadium and molybdenum solve in  $\text{Fe}_3\text{C}$  in some degree and the precipitation of  $\text{V}_4\text{C}_3$  and  $\text{Mo}_2\text{C}$  occurs partly by *in situ* nucleation although mostly by separate nucleation.

## 2.2 Transformation kinetics

### 2.2.1 Transformation kinetics of $\gamma$ (isothermal)

When the  $\alpha$  or pearlite forms from  $\gamma$  by isothermal holding below the transformation temperature, these nuclei form preferentially at the prior  $\gamma$  grain boundaries. Thus, their transformation kinetics can usually be expressed<sup>3</sup> by including the effect of  $\gamma$  grain size as:

$$X = 1 - \exp \left[ -k(T) \left( \frac{t^n}{d^m} \right) \right] \quad (2.2)$$

where  $X$  is the transformed fraction,  $t$  is isothermal holding time,  $d$  is diameter of  $\gamma$  grain and  $k(T)$  is the rate constant which depends only on transformation temperature and corresponds directly to the C-curve of the *TTT* isothermal transformation diagram. The values of the exponent  $m$  and  $n$  are listed in Table 2.1.

TABLE 2.1 The values of  $n$  and  $m$  in Equation (2.2) for various transformation conditions.

$$X = 1 - \exp \left[ -k(T) \left( \frac{t^n}{d^m} \right) \right]$$

| Mechanism     | Site saturation |     | Nucleation and growth |     |
|---------------|-----------------|-----|-----------------------|-----|
| site          | $n$             | $m$ | $n$                   | $m$ |
| Grain surface | 1               | 1   | 4                     | 1   |
| Grain edge    | 2               | 2   | 4                     | 2   |
| Grain corner  | 3               | 3   | 4                     | 3   |

These values depend on both the transformation mechanism and type of nucleation site. Here the transformation, especially nucleation, which progresses over almost the entire range of transformation is called 'nucleation and growth'. The transformation where all the nuclei are nucleated at an early stage in the reaction and where the

progress of transformation is controlled mostly by their growth is called 'site saturation'. An  $\gamma$  grain is assumed to be a tetrakaidecahedra, and the nucleation sites at the  $\gamma$  grain boundary can be classified into surfaces, edges and corners as shown in Figure 2.3.<sup>4</sup> Of course, the actual nucleation sites are not limited to any one of such types, and the value of  $m$  would be the weighted average of the various nucleation sites and would not always be an integer.

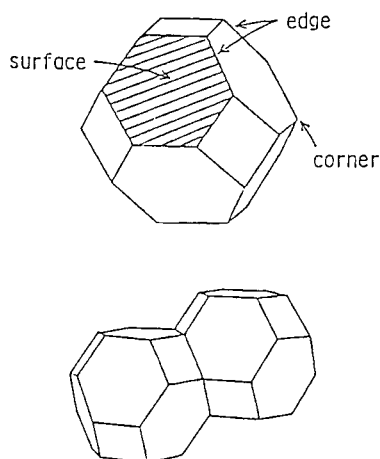


Figure 2.3 Schematic diagram of a  $\gamma$  grain as a tetrakaidecahedra and showing three types of nucleation sites of  $\alpha$

According to Umemoto and Tamura,<sup>3</sup> the values of  $n$  and  $m$  and transformation modes were shown experimentally as in Table 2.2. It is mentioned in Table 2.2 that the mode of  $\gamma \rightarrow \alpha$  transformation is site saturation, but it means that the large extent of nucleation of  $\alpha$  would occur at the beginning of transformation, which would not be real 'site saturation'. Sometimes, the nucleation site is varied by supercooling (accelerated cooling). It seems that the nucleation site of  $\alpha$  is moved gradually from edge to surface by the decrease in transformation temperature with cooling rate.

TABLE 2.2 The values of  $n$  and  $m$  for various transformation modes

| Transformation | $n$ | $m$ | Nucleation  |
|----------------|-----|-----|---|
| Pearlite       | 4   | 2   | Edge nucleation, nucleation and growth              |
| Ferrite        | 1   | 1   | Surface nucleation near site saturation             |
| Bainite        | 4   | 0.6 | Grain boundary, inside grain, nucleation and growth |

## 2.2.2 Continuous cooling transformation kinetics of $\gamma$

Scheil<sup>5</sup> considered the case where the  $\gamma$  is cooled continuously through its transformation temperature. He assumed that  $\gamma$  consumes its fractional nucleation time and when the sum of a number of such fractions equals unity the transformation starts, i.e.:

$$\int_{t=0}^{t=t_n} \frac{dt}{\tau(T)} = \int_{T_e}^T \frac{dt}{dT} \cdot \frac{dT}{\tau(T)} = 1 \quad (2.3)$$

Now extend this Scheil's additivity rule to the entire range of transformation. In this case the incubation time ( $\tau_{(T)}$ ) is extended to the time required for the reaction to reach a certain fractional completion  $X$  by isothermal holding at temperature  $T$ . If we combine Equations (2.3) and (2.2):

$$X_{(T)} = 1 - \exp \left( - \frac{1}{d^m} \left\{ \int_T^{T_e} \frac{K_{(T)}^{1/n}}{Q_{(T)}} dT \right\}^n \right) \quad (2.4)$$

where  $Q_{(T)} = -dT/dt$  and is a cooling rate. This equation expresses the transformed fraction at temperature  $T$  during cooling from the  $\gamma$  condition with a cooling rate  $Q_{(T)}$ .<sup>3,6</sup> Furthermore, from Equations (2.2) and (2.4) we obtain:

$$t_{(T)} = \frac{1}{K_{(T)}^{1/n}} \int_T^{T_e} \frac{K_{(T')^{1/n}}}{Q_{(T')}} dT' = t_{eq} \quad (2.5)$$

This equation tells us that the fraction transformed by cooling from  $T_e$  to  $T$  with cooling rate  $Q_{(T)}$  is equal to that obtained by the isothermal holding at temperature  $T$  for time  $t_{(T)}$ . Thus, we call  $t_{(T)}$  an equivalent cooling time,  $t_{eq}$  is the isothermal holding time which gives the equivalent transformed fraction with continuous cooling. The curve produced by the successive plot of such  $t_{eq}$  at each temperature during cooling with cooling rate  $Q_{(T)}$  will be called an equivalent cooling curve.<sup>7</sup> The transformation behaviour for a given cooling curve can be predicted from the  $TTT$  diagram by plotting such curve on a  $TTT$  diagram.

## 2.3 $\alpha$ grain size transformed from $\gamma$

### 2.3.1 Major purpose of controlled-rolling

The major purpose of controlled-rolling is to refine the structure of steels and, thereby, to enhance both strength and toughness. The controlled-rolling process is usually divided into three stages.<sup>8,9</sup> Figure 2.4 illustrates these three stages, the microstructural change accompanying deformation in each stage:

- (1) The deformation at recrystallization temperature range. The  $\gamma$  grain is refined by repeated static recrystallization. A small  $\gamma$  grain size obtained by recrystallization at this stage leads to a refinement of  $\alpha$  grains. In general, recrystallized  $\gamma$  grain size decreases rapidly with an increase in the amount of rolling reduction and reaches a limiting value,<sup>9-18</sup> which limits the degree of  $\alpha$  grain refinement achieved by  $\gamma$  recrystallization.
- (2) The deformation at the unrecrystallized temperature range. The  $\gamma$  grains are elongated and deformation structures are introduced within the grains.<sup>19-23</sup> The deformation in this stage substantially increases the nucleation rate at  $\gamma$  grain boundaries and within  $\gamma$  grains. This intragranular nucleation of  $\alpha$  is one of the most important aspects of controlled-rolling. Microalloying elements such as niobium and titanium, etc. can increase the recrystallization temperature of  $\gamma$ .

- (3) The deformation in the  $(\alpha + \gamma)$  two-phase region. The  $\gamma$  is further work-hardened and deformation of  $\alpha$  produces substructures.

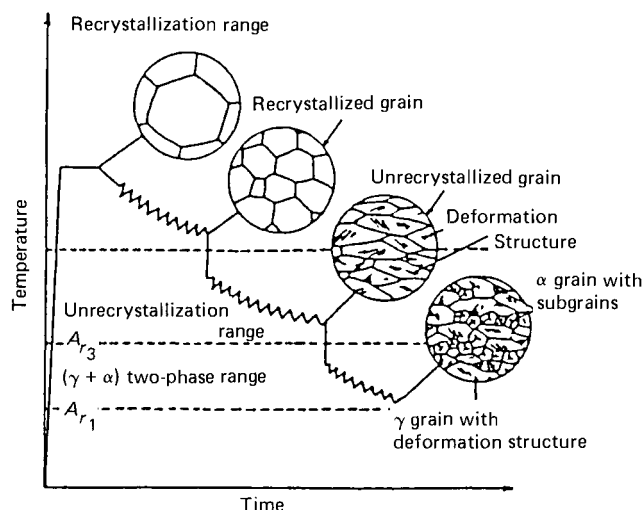


Figure 2.4 Three stages of the controlled-rolling process and the change in microstructure accompanying deformation in each stage

Accelerated cooling after hot-rolling is currently being recognized as a further advanced thermomechanical treatment in the hot-rolling process.<sup>24,25</sup> This cooling process is characterized by accelerated cooling in a  $\gamma \rightarrow \alpha$  transformation range just after controlled-rolling. It has been shown that the accelerated cooling refines the  $\alpha$  grain size and thus further improves both the strength and toughness.

This section reviews our current understanding of the mechanisms of  $\alpha$  grain refinement by hot-rolling and accelerated cooling. The expression for  $\alpha$  grain size on a basis of transformation is first introduced. The fundamental mechanism of  $\alpha$  grain refinement by  $\gamma$  grain refinement, work-hardening of  $\gamma$  and accelerated cooling are discussed.

### 2.3.2 Expression for $\alpha$ grain size (isothermal)

Figure 2.5 schematically shows the progress of  $\alpha$  transformation. In general, ferrites nucleate at  $\gamma$  grain boundaries and grow into  $\gamma$  grains. The grain size of  $\alpha$  formed from  $\gamma$  is directly related to the process of transformation.<sup>26</sup> The nominal  $\alpha$  grain diameter  $D_\alpha$

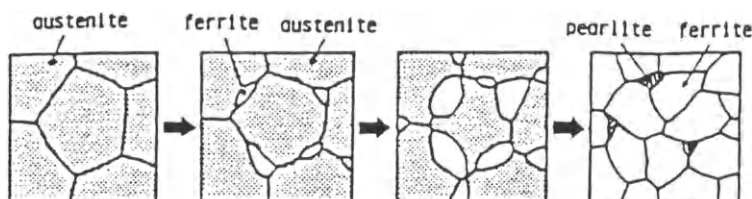


Figure 2.5 Schematic drawings showing the process of transformation in an HSLA steel

can be expressed with the total number of  $\alpha$  grains nucleated throughout transformation per unit volume of  $\gamma$   $n_v$  as:<sup>27</sup>

$$n_v = \int_0^\infty I(1-X)dt \quad (2.6)$$

$$D_\alpha = \left( \frac{2}{3n_v} \right)^{\frac{1}{3}} \quad (2.7)$$

Thus, the problem of obtaining the expression for  $\alpha$  grain size is the problem of how to express  $n_v$ .

When ferrites nucleate at the  $\gamma$  grain boundary surfaces, they grow as ellipsoid with the aspect ratio of 3:1<sup>28</sup> as shown in Figure 2.6. The total number of  $\alpha$  grains nucleated per unit area of  $\gamma$  grain boundary surface is:

$$n_s = I_s \int_0^\infty \exp \left( -\frac{9}{2} \pi \alpha^2 I_s t^2 \right) dt = 1/(3\sqrt{2}) (\sqrt{I_s/\alpha}) \quad (2.8)$$

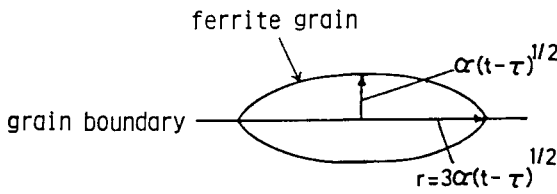


Figure 2.6 Schematic drawing of a  $\alpha$  grain nucleated at a  $\gamma$  grain boundary

where  $I_s$  is the nucleation rate per unit area of  $\gamma$  grain surface and  $\alpha$  the parabolic rate constant for thickness. The  $\alpha$  grain size  $D_\alpha$  is given as:

$$D_\alpha = \left( \frac{2}{3n_s S_{gb}} \right)^{\frac{1}{3}} \quad (2.9)$$

where  $S_{gb}$  is the  $\gamma$  grain surface area per unit volume, and can be expressed by  $\gamma$  grain diameter  $D_\gamma$  as:

$$S_{gb} = 4/(\sqrt{\pi} D_\gamma) \quad (2.10)$$

Substituting Equations (2.8) and (2.10) into Equation (2.9), the  $\alpha$  grain size and the  $\gamma \rightarrow \alpha$  transformation ratio can be expressed as:

$$D_\alpha = (2/\pi)^{-\frac{1}{6}} (\sqrt{I_s/\alpha})^{-\frac{1}{3}} D^{\frac{1}{3}} \quad (2.11)$$

and

$$\frac{D_\gamma}{D_\alpha} = \left( \frac{S_{gb}}{2\sqrt{2}} \frac{\sqrt{I_s}}{\alpha} \right)^{\frac{1}{3}} \cdot D_\gamma = \left( \frac{2}{\pi} \right)^{\frac{1}{3}} \left( \frac{\sqrt{I_s}}{\alpha} \right)^{\frac{1}{3}} \cdot D_\gamma^{\frac{2}{3}} \quad (2.12)$$

In the above derivation it is assumed that the nucleation rate and the parabolic rate constant of growth are time-independent and that one nuclei grows and forms one grain.

Similarly, the  $D_\alpha$  and  $\gamma \rightarrow \alpha$  transformation ratio in the case of homogeneous and grain edge nucleation has been obtained as:<sup>26</sup>

$$\left. \begin{aligned} D_\alpha &= 0.974 \left( \frac{\sqrt{I_h}}{\alpha} \right)^{-\frac{2}{3}} \\ \frac{D_\gamma}{D_\alpha} &= 1.027 \left( \frac{\sqrt{I_h}}{\alpha} \right)^{\frac{2}{3}} \cdot D_\gamma \end{aligned} \right\} \quad (\text{homogeneous}) \quad (2.13)$$

$$\left. \begin{aligned} D_\alpha &= 0.784 \left( \frac{\sqrt{I_e}}{\alpha} \right)^{-\frac{2}{3}} \cdot D_\gamma^{\frac{2}{3}} \\ \frac{D_\gamma}{D_\alpha} &= 1.275 \left( \frac{\sqrt{I_e}}{\alpha} \right)^{\frac{2}{3}} \cdot D_\gamma^{\frac{1}{3}} \end{aligned} \right\} \quad (\text{grain edge})$$

where  $I_h$  and  $I_e$  are the homogeneous nucleation rate per unit volume and nucleation rate per unit length of  $\gamma$  grain edge respectively.

It should be noted that the Equations (2.11)–(2.13) indicate that  $\alpha$  grain size and the  $\gamma \rightarrow \alpha$  transformation ratio depend on the ratio of the square root of the nucleation rate to the parabolic rate constant in all three types of nucleation sites. Furthermore, for grain boundary nucleation, a small  $\gamma$  grain leads to a small  $\alpha$  one. The effect of  $\gamma$  grain size on  $\alpha$  grain size depends on the type of nucleation site, and it becomes large in the following ascending order: (1) homogeneous; (2) grain surfaces; and (3) grain edges.

The  $\gamma$  grain is refined by the repeated static recrystallization during mutipass rolling in the first stage of controlled-rolling. The relations of recrystallized  $\gamma$  grain size and the rolling parameters such as temperature, pass reduction and rolling speed have been studied extensively.<sup>12–15, 17, 29</sup> Table 2.3 is a summary of the phenomenological equations reported for recrystallized  $\gamma$  grain size. In most of the equations the recrystallized grain size is expressed in terms of the initial grain size ( $D_0$ ), strain ( $\epsilon$ ), and the Zener–Hollomon parameter ( $Z$ ) [ $Z = \dot{\epsilon} \exp(Q/RT)$ ] or flow stress ( $\sigma$ ). In general, the  $\gamma$  grain size is refined by increasing the value of  $Z$  or  $\epsilon$ , i.e. by increasing the flow stress. It should be noted that the grain refinement in  $\gamma$  turns out to be less effective in  $\alpha$  grain refinement, e.g. in the case of grain surface nucleation  $D_\alpha$  is proportional to  $D_\gamma^{\frac{2}{3}}$ . This means that when  $D_\gamma$  is reduced to one-eighth of the initial,  $D_\alpha$  would be reduced only to one-half.

The type of predominant nucleation site of  $\alpha$  depends on the site density and the nucleation frequency at each given site. In more fundamental terms it is determined by the  $\alpha$ – $\gamma$  interfacial energy, degree of supercooling, and  $\gamma$  grain size.<sup>4</sup> An experiment by

TABLE 2.3 Relationship between recrystallized  $\gamma$  grain size ( $D_R$ ) and various parameters<sup>30</sup>

|   |  |
|---|--|
| $D_R = 25 \left( \frac{1}{\beta} \ln \frac{Z}{A} \right)^{-\frac{1}{3}} \varepsilon^{-1} D_0^{\frac{1}{3}}$                     | Carbon-manganese steel <sup>13</sup>       |
| $D_R = \frac{BZ^{-0.1} D_0^{0.5}}{1.15 - \exp \left\{ -2.5 \left( \frac{\varepsilon_p - 0.08}{\varepsilon_p} \right) \right\}}$ | 18-8 stainless steel <sup>12</sup>         |
| $D_R \propto \varepsilon^{-0.5} D_0 Z^{-0.06}$  | 18-8 stainless steel <sup>17</sup>         |
| $D_R = 1368 \varepsilon^{-0.29} Z^{-0.19}$  | 17% ferritic stainless steel <sup>29</sup> |
| $D_R = \left( \frac{623}{\sigma} \right)^{2.9} \quad (\sigma \text{ in kilogram force per square millimetre})$                  | Niobium steel <sup>14</sup>                |
| $*N_R = -8.3\varepsilon^{-\frac{1}{3}} + \frac{1}{3}N_{i0} + \frac{1}{100}(1200 - T) + 8.8$                                     | Niobium steel <sup>15</sup>                |

\* $N_R$  and  $N_{i0}$  are recrystallized and initial grain size number respectively

the present authors<sup>31</sup> showed that the dominant nucleation site changes from grain edges to surfaces by lowering the transformation temperature. In a typical controlled-rolling where the ferrites transform with fairly high supercooling,  $\gamma$  grain surfaces are considered to be the dominant nucleation site of  $\alpha$ .

### 2.3.3 Estimation of $\alpha$ grain size formed by continuous cooling transformation

It can be assumed that  $\alpha$  nucleates preferentially at  $\gamma$  grain surfaces. A continuous cooling transformation can be considered as the sum of short-time isothermal holdings at successive temperatures as is schematically shown in the Figure 2.7.

During cooling,  $\alpha$  grains are nucleated and grow at each temperature with the corresponding nucleation and growth rates, as is schematically shown in the Figure 2.7 (bottom). During  $\alpha$  transformation, carbon enriches in retained  $\gamma$  and influences the nucleation and growth rates of  $\alpha$ . However, since  $\alpha$  nucleation occurs mostly in the early stages of transformation, it can be assumed that both the nucleation and growth rates of  $\alpha$  are a function of an instantaneous temperature only and not a function of thermal history.

Based on this assumption, the number of  $\alpha$  nuclei ( $N_a$ ) nucleated at temperature  $T_a$  during cooling, is given in Equation (2.14):

$$N_a = I_{s(T_a)} dt_a = - \frac{I_{s(T_a)}}{Q_{(T_a)}} dT_a \quad (2.14)$$

where  $Q_{(T)} (= -dT/dt)$  is a cooling rate.

$\alpha$  grains, once nucleated, grow thereafter with a corresponding growth rate at each temperature during cooling. Thus, at temperature  $T$ , the radius of a  $\alpha$  grain on an  $\gamma$

grain surface nucleated at temperature  $T_a$  is given in Equation (2.15):

$$r_a = 3 \left( \int_T^{T_a} \frac{\alpha^2(T')}{Q(T')} dT' \right)^{\frac{1}{3}} \quad (2.15)$$

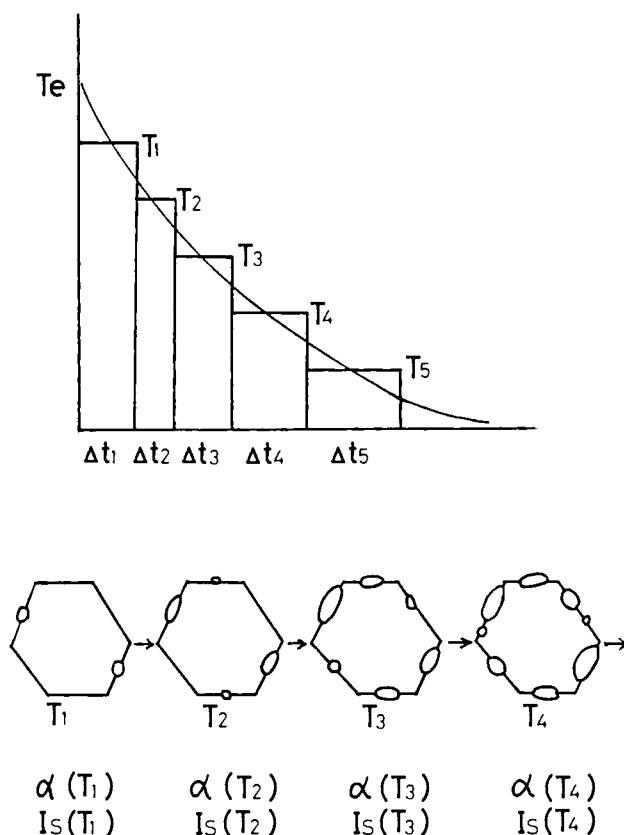


Figure 2.7 Diagrams to explain the relation between isothermal and continuous cooling transformation and schematic drawing showing the formation process of  $\alpha$  during continuous cooling

The  $\gamma$  grain boundary area occupied at temperature  $T$  by a  $\alpha$  grain nucleated at temperature  $T_a$  is given as Equation (2.16):

$$\pi r_a^2 = 9\pi \int_T^{T_a} \frac{\alpha^2(T')}{Q(T')} dT' \quad (2.16)$$

It will be convenient to use the concept of extended area which is the sum of the areas of  $\gamma$  grain surface occupied by  $\alpha$  grains, assuming that  $\alpha$  grains never stop growing and keep nucleating at the same rate during transformation as well as on untransformed  $\gamma$  grain surfaces. The extended grain boundary area occupied by all the  $\alpha$  grains nucleated at  $T_a$  during cooling is given in Equation (2.17):



$$Y^{\text{ex}}_{(T_a)} = N_a \pi r_a^2 = -\frac{I_s(T_a)}{Q_{(T_a)}} d(Ta) \cdot 9\pi \int_T^{T_a} \frac{\alpha^2_{(T')}}{Q_{(T')}} \cdot dT' \quad (2.17)$$

Thus, the grain boundary area function occupied by the  $\alpha$  grains nucleated during cooling from  $A_{r3}$  ( $T_e$ ) to  $T$  is given by Equation (2.18):

$$Y = 1 - \exp \left( -9\pi \int_T^{T_e} \frac{I_s(T_a)}{Q_{(T_a)}} \left\{ \int_T^{T_a} \frac{\alpha^2_{(T')}}{Q_{(T')}} dT' \right\} dTa \right) \quad (2.18)$$

The total number of  $\alpha$  grains nucleated per unit area of  $\gamma$  grain boundary surface is given in Equation (2.19):

$$\begin{aligned} n_\alpha &= \int_T^{T_e} \frac{I_s(T')}{Q_{(T')}} (1 - Y) dT' \\ &= \int_T^{T_e} \frac{I_s(T')}{Q_{(T')}} \cdot \exp \left( -9\pi \int_T^{T_e} \frac{I_s(T_a)}{Q_{(T_a)}} \left\{ \int_T^{T_a} \frac{\alpha^2_{(T'')}}{Q_{(T'')}} dT'' \right\} dTa \right) dT' \end{aligned} \quad (2.19)$$

$\alpha$  grain size is given in Equation (2.20).

$$D_\alpha = \left( \frac{2}{3S_{g.b} \cdot n_\alpha} \right)^{\frac{1}{3}} \quad (2.20)$$

where  $S_{g.b} [= 4/(\sqrt{\pi} D_\gamma)]$  is the  $\gamma$  grain surface area per unit volume.

From these equations,  $\alpha$  grain size can be calculated.

The growth rate of  $\alpha$  as a function of temperature can be obtained as follows. It is well established<sup>4</sup> that the parabolic rate constant  $\alpha$  for thickening is given as:<sup>32</sup>

$$\alpha = \frac{D^{\frac{1}{2}} (C_\gamma^e - C_0)}{(C_\gamma^e - C_\alpha^e)^{\frac{1}{2}} (C_0 - C_\alpha^e)^{\frac{1}{2}}} \quad (2.21)$$

where  $D$  is the diffusivity of carbon in  $\gamma$ ,  $C_0$  the initial carbon content and  $C_\gamma^e$  and  $C_\alpha^e$  the equilibrium carbon content in  $\gamma$  and  $\alpha$  respectively.

$C_\gamma^e$  and  $C_\alpha^e$  can be calculated by the regular solution–sublattice model proposed by Hillert and Staffanson.<sup>33</sup> For an example,  $C_\gamma^e$  and  $C_\alpha^e$  for the steel such as Fe 0.15–C 0.4 Mn were calculated under the paraequilibrium condition, since the partitioning of manganese between  $\gamma$  and  $\alpha$  occurs only at relatively high transformation temperatures.<sup>34</sup> About  $D$ , the data of Wells, Batz and Mehl<sup>35</sup> indicate that the amount of manganese present in the steel has an insignificant effect on  $D$ . Therefore, the following  $D$  in iron–carbon alloys reported by Kaufman, Radcliffe and Cohen<sup>36</sup> are used:

$$D = 0.5 \exp(-30C_\gamma) \exp\left(-\frac{38\,300 - 190\,000C_\gamma + 550\,000C_\gamma^2}{1.987T}\right) \text{ (centimetres per second)} \quad (2.22)$$

where  $C_\gamma$  is the carbon content in  $\gamma$ .

Following the Wagner<sup>37</sup> approximation, the value of  $D$  corresponds to the equilibrium carbon content in  $\gamma$ .

The nucleation rate of  $\alpha$  can be expressed as:<sup>38</sup>

$$I_s = \frac{K_1 D}{(K \cdot T)^{\frac{1}{2}}} \exp\left(-\frac{K_2}{(\Delta G_v)^2 K \cdot T}\right) \quad (2.23)$$

where  $K_1$  is a constant mostly related to nucleation site density,  $K_2$  is a constant related with the  $\gamma$ - $\alpha$  interfacial energy and  $\Delta G_v$  is the driving force for the nucleation of  $\alpha$ .

$\Delta G_v$  can be obtained by a thermodynamical calculation; however, the  $K_1$  and  $K_2$  constants are difficult to obtain theoretically at the present.<sup>39</sup> In the present case,  $K_1$  and  $K_2$  are estimated indirectly as follows. In the early stage of  $\alpha$  transformation, the fraction transformed can be expressed as:<sup>40</sup>

$$X = 1 - \exp\left(-\frac{4}{15}\pi\alpha^3 I_s \cdot S_{g \cdot b} t^{\frac{1}{2}}\right) \quad (2.24)$$

Thus, the nucleation rate of  $\alpha$ ,  $I_s$ , can be expressed as:

$$I_s = \frac{15}{4\pi\alpha^3 t^{\frac{1}{2}} S_{g \cdot b}} \ln \frac{1}{1-X} \quad (2.25)$$

From this equation,  $I_s$  can be estimated for a temperature at which the time  $t$  to reach a certain transformed fraction is measured. An isothermal transformation experiment was carried out using the automatic quench dilatometer (Formaster F). The times to reach a 10%  $\gamma$  fraction transformed to  $\alpha$  were measured at various temperatures and  $I_s$  was calculated for various temperatures from Equation (2.25). The constants  $K_1$  and  $K_2$  in Equation (2.23) were then determined so as to obtain the best fit between the  $I_s$  values calculated from Equations (2.25) and (2.23) as functions of temperature. The obtained  $K_1$  and  $K_2$  values are  $2.07 \times 10^3 \text{ J}^{\frac{1}{2}} \text{ cm}^{-4}$  and  $6.33 \times 10^{-15} \text{ J}^3 \text{ mol}^{-2}$ , respectively.

Figure 2.8 shows the calculated parabolic rate constant  $\alpha$  as a function of temperature for the steel used in the present case (approximately Fe-0.15 C-0.4 Mn alloy). It is seen that the growth rate of  $\alpha$  of this steel reaches a maximum at around 873° K (600° C). The calculated  $I_s$  is also shown as a function of temperature in Figure 2.8 together with  $\alpha$ . It is seen that  $I_s$  is very sensitive to temperature and has a maximum of 913° K (640° C). In the temperature range of interest, the change in  $I_s$  is 5 orders of magnitude larger than that for  $\alpha$ . This suggests that, in  $\alpha$  transformation, the nucleation rate mostly controls the grain size of  $\alpha$ .

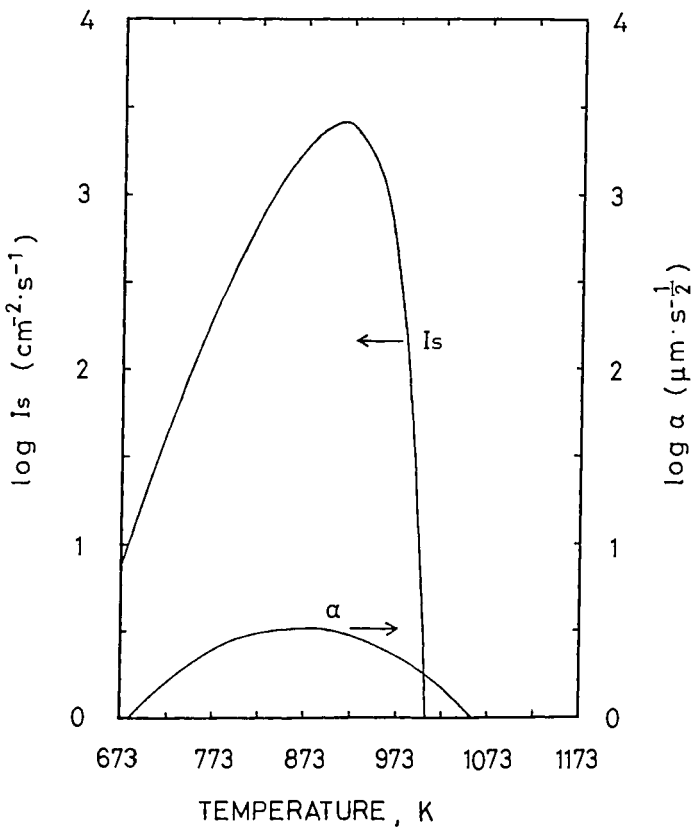


Figure 2.8 Calculated parabolic rate constant  $\alpha$  and nucleation rate  $I_s$  as a function of temperature for the steel studied

The  $\alpha$  grain size formed during cooling was calculated in Equation (2.20) using  $\alpha$  and  $I_s$  estimated above. Figure 2.9 shows the calculated  $D_\alpha$  as a function of cooling rate  $q$ . It is seen that the calculated  $D_\alpha$  is nearly proportional to  $q^{-0.17}$ .

As is discussed in the previous section,  $\gamma$  grain size is proportional to  $D_\gamma^\dagger$  when  $\gamma$  grain surfaces are the dominant nucleation site of  $\alpha$ . Thus, the theoretically estimated  $\alpha$  grain size can be expressed as a function of cooling rate  $q$  and  $\gamma$  grain size as:

$$D_\alpha = 1.0q^{-0.17} (D_\gamma)^\dagger \quad (2.26)$$

This is an example of theoretical calculation. An experimental example will be shown in Equation (2.38) for the experimental plots in Figure 2.9.

## 2.4 Deformation behaviour of steels at elevated temperatures

### 2.4.1 Restoration during hot-deformation

Steels are usually deformed by slip at room temperature, and work-hardened by the

increase in dislocation density. On the other hand, both slip deformation and grain boundary sliding occur when steels are deformed at elevated temperatures at low strain rate (creep deformation). Grain boundary sliding depends markedly on the temperature  $T$  and strain rate  $\dot{\epsilon}$ . Slip in the creep deformation arises from the movement of dislocations accompanying the dragging of solute atoms and, hence, shows the large temperature and strain-rate dependence.

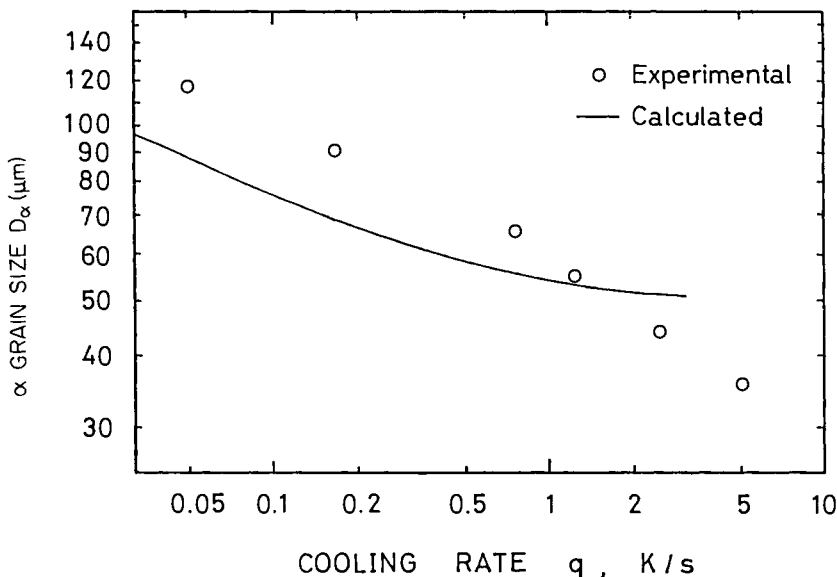


Figure 2.9  $\alpha$  grain size as a function of cooling rate for the specimens of  $D_\gamma = 151 \mu\text{m}$ . Circles represent experimental data and the solid line is calculated

In the case of deformation at high strain rates – such as hot-rolling of  $\gamma$  – the grain-boundary sliding hardly occurs even at high temperatures, and only the slip takes place by the movement of dislocations without the dragging effect of solute atoms. However, even then, the recovery occurs to some extent during work-hardening. When the dislocation density is increased to a certain value, the recrystallization can take place during deformation. Recovery and recrystallization occurring during deformation are called ‘dynamic recovery’ and ‘dynamic recrystallization’ respectively.

When aluminium is tensile-deformed at around  $300^\circ\text{C}$  at a strain rate of about  $10^{-4}/\text{s}$ , the steady-state deformation occurs after the initial work-hardening and the true-stress–true-strain curve, such as that shown in Figure 2.10(a), is obtained. In the stage of steady-state deformation, the work-hardening and the softening due to dynamic recovery are balanced; hence, the true stress is maintained as a constant. This restoration process is called the ‘dynamic recovery’ type. Aluminium has a high stacking fault energy of about  $180 \text{ erg/cm}^2$  and is therefore the representative metal to belong to this type.

In the case of copper, which has a fairly low stacking fault energy (about  $60 \text{ erg/cm}^2$ ), the rate of softening due to recovery is slow in comparison with aluminium. The work-hardening of copper cannot, therefore, be balanced only by dynamic recovery, even at

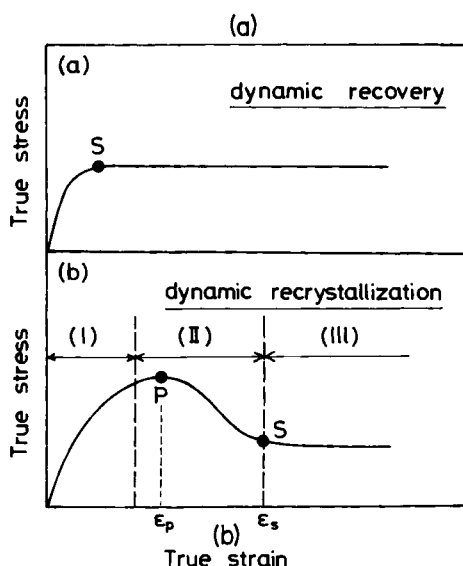


Figure 2.10 Schematic illustrations of two types of true-stress-true-strain curves accompanying the steady-state deformation at elevated temperatures

high temperatures (500–600°C). The dislocation density is gradually increased and, finally, the recrystallization starts to occur during deformation. The true stress is lowered beyond the peak stress by dynamic recrystallization and reaches a certain steady-state stress level at which the work-hardening and softening (due to recrystallization occurring repeatedly) are balanced. The schematic true-stress-true-strain curve is shown in Figure 2.10(b). The dynamic recrystallization starts at a strain of around  $0.7\varepsilon_p$  ( $\varepsilon_p$  is the strain showing the peak stress). In Figure 2.10(b), the range of strain values up to about  $0.7\varepsilon_p$  forms the work-hardening region, the strain range between about  $0.7\varepsilon_p$  and  $\varepsilon_s$  (the strain at which the steady-state deformation starts) forms the range of partially dynamic recrystallization, and the strain range after  $\varepsilon_s$  is the range of steady dynamic recrystallization. This type of restoration process is called the 'dynamic recrystallization' type.  $\gamma$  in steels belongs to this type. In  $\alpha$ , the restoration is performed mainly by dynamic recovery, since the recovery occurs very quickly. However, the dynamic recrystallization occurs under certain deformation conditions even in ferritic steels.<sup>41</sup> The peak stress ( $\sigma_p$ ) and the steady-state stress ( $\sigma_s$ ) in the dynamic recrystallization type change with the Zener–Hollomon parameter  $Z$ .  $Z$  is expressed by:

$$Z = \dot{\varepsilon} \exp(Q/RT) \quad (2.27)$$

where  $\dot{\varepsilon}$  is the strain rate ( $s^{-1}$ ),  $Q$  is the activation energy for deformation in joules per mole,  $R$  is a gas constant in joules per mole and  $T$  is temperature in degrees Kelvin.

$\sigma_p$ ,  $\varepsilon_p$ ,  $\sigma_s$  and  $\varepsilon_s$  are increased with increase in  $Z$ , i.e. with increase in  $\dot{\varepsilon}$  or decrease in  $T$ .

Figure 2.11 shows the change in optical microstructure with strain in Fe–31% Ni–0.3% C austenitic alloy which was tensile-deformed at 1000°C at a strain rate of  $1.7 \times 10^{-2}/s$ . Figure 2.11(a) shows the  $\gamma$  structure before deformation.  $\gamma$  grains are equi-axed and their boundaries are smoother and planer. Many annealing twins exist in  $\gamma$  grains. When deformed slightly ( $\varepsilon=0.08$ ), as shown in Figure 2.11 (b), the grain

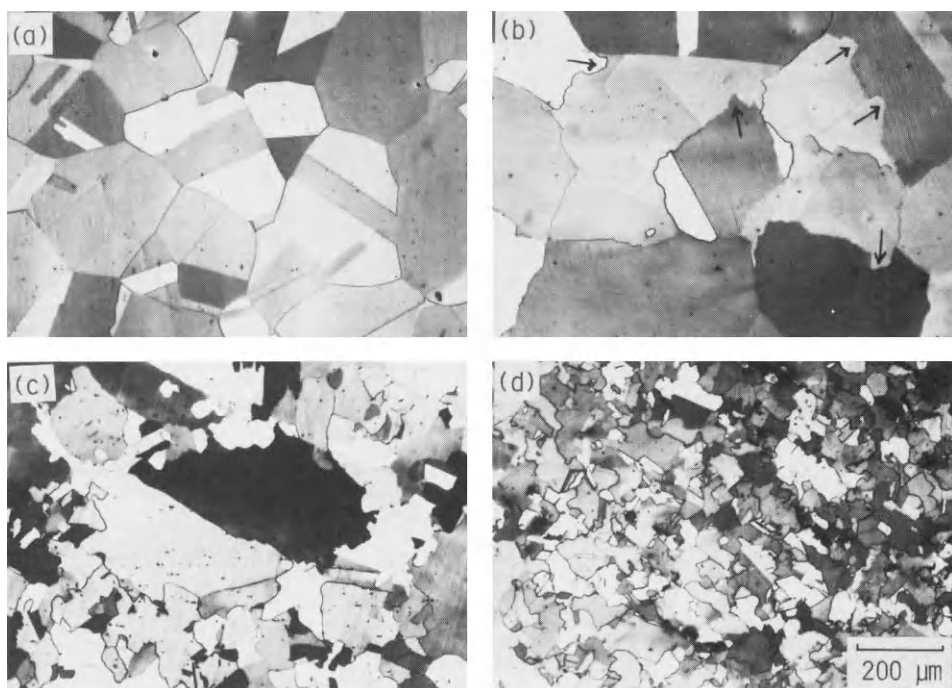


Figure 2.11 Optical micrographs showing the formation process of dynamically recrystallized  $\gamma$  in Fe-31Ni-0.3C austenitic alloy deformed at 1000°C,  $1.7 \times 10^{-2}$ /s: (a) before testing ( $\epsilon = 0$ ); (b)  $\epsilon = 0.08$ ; (c)  $\epsilon = 0.24$ ; (d)  $\epsilon = 0.40$

boundaries become finely serrated and the bulgings of grain boundary are observed as indicated by the arrows. At the strain slightly after  $\epsilon_p$ , many small grains are newly formed along the  $\gamma$  boundaries as shown in Figure 2.11(c). It is characteristic that these newly formed grains seldom contain annealing twins. Furthermore, some of the initial  $\gamma$  grains become larger by the strain-enhanced coarsening. Figure 2.11(d) shows the structure in the range of steady-state deformation at which the work-hardening and the recrystallization softening are balanced. This structure consists of several grains corresponding to various stages of recrystallization, i.e. from small grains which have just started to recrystallize to fairly large ones which have been subjected to deformation after the finishing of recrystallization and are in the work-hardened state just before the next recrystallization. In the stage of steady-state deformation, the recrystallization occurs repeatedly during deformation. Dynamic recrystallized grains contain a few annealing twins at low  $Z$  but scarcely contain them when  $Z$  is high.

As in the static recrystallization,<sup>42</sup> there are two main mechanisms for dynamic recrystallization: (1) the bulging mechanism; and (2) the nucleation-growth mechanism. Generally, the former operates predominantly at small strain and the latter occurs at high strain. The bulging mechanism seems to occur at a very early stage of deformation, e.g. at a strain above 0.05. The nucleation-growth mechanism becomes dominant at a strain more than about 0.2. However, even in the range of steady-state deformation at which the strain is usually more than 0.2, the actual strain in each grain is estimated to be fairly small since the recrystallization occurs repeatedly. Therefore,

even in the steady-state deformation, there might be the case in which the bulging mechanism is predominant.

In the case of hot-rolling, when the strain (reduction) is fixed to a certain value, the work-hardening structure is obtained under higher  $Z$  conditions and the dynamically recrystallized structure is obtained under lower  $Z$  conditions. Therefore, in order to know the  $\gamma$  structure immediately after hot-rolling, both factors of strain and  $Z$  must be considered. Furthermore, it must be borne in mind that both strain and strain rate (and hence  $Z$ ) are increased with an increase in the amount of reduction of one pass in hot-rolling.

Dynamic recrystallization becomes easier when the initial grain size  $\bar{d}_0$  of  $\gamma$  is smaller. Therefore, in the case of fine initial grain size,  $\varepsilon_p$  and  $\varepsilon_s$  become small even at deformation under the same  $Z$  condition. However,  $\sigma_p$  and  $\sigma_s$  are independent of  $\bar{d}_0$ . The average size  $\bar{d}$  of dynamically recrystallized grains is the only function of  $Z$  and is expressed by the following equation:

$$\bar{d} = AZ^{-p} \quad (2.28)$$

where  $A$  and  $p$  are material constants such as those shown in Table 2.4.

It should be noted that  $\bar{d}$  is independent of  $\bar{d}_0$ .

TABLE 2.4 Approximate values of  $A$  and  $p$  in Equation (2.28)

|                      | $A$                    | $p$       | $Q$ (kJ/mol) |
|----------------------|------------------------|-----------|--------------|
| Carbon steel         | $5 \times 10^{-4}$     | 0.30–0.35 | 230–280      |
| low alloy steel      |                        |           |              |
| Niobium steel        | $2 \times 10^{-6}$     | 0.41      | 330          |
| High alloy steel     | $10^{-5} \sim 10^{-6}$ | 0.35–0.40 | 330–370      |
| 18-8 stainless steel | $4 \times 10^{-7}$     | 0.40      | 435          |

## 2.4.2 Static restoration during holding right after hot-deformation

When the hot-deformation is finished at the work-hardening stage (Figure 2.10(b)), the work-hardened  $\gamma$  is then softened by the usual static recrystallization during isothermal holding after deformation. However, if the strain is too small, the recrystallization cannot occur and only the recovery takes place. On the other hand, when specimens are isothermally held after hot-deformation to the range of the steady-state deformation, in which the dynamic recrystallization has occurred, the recrystallization and the grain growth can occur continuously during holding after hot-deformation. Such a recrystallization is called a metadynamic or post-dynamic recrystallization, i.e. the dynamically recrystallized structure is further softened by the metadynamic recrystallization. When specimens are deformed to the range of (II) in Figure 2.10(b), in which the work-hardened  $\gamma$  and dynamically recrystallized  $\gamma$  have coexisted, the static recrystallization occurs in work-hardened  $\gamma$  and the metadynamic recrystallization occurs simultaneously in dynamically recrystallized  $\gamma$ .

In the case of rolling by hot-strip in which slabs are rolled through several passes, the

static restoration process occurring during interval between each rolling pass has a great influence on the deformation behaviour of each subsequent pass. If the softening due to the static restoration is not completed in the interval between each rolling pass, the work-hardening is successively accumulated by subsequent passes.

Fractional softening  $X$  occurring during isothermal holding right after hot-deformation can be evaluated by the two-step deformation test from Equation (2.29) and will be described in Chapter 7:

$$X = \frac{\sigma_m - \sigma_{y_2}}{\sigma_m - \sigma_{y_1}} \quad (2.29)$$

where  $\sigma_m$  is the flow stress immediately before unloading,  $\sigma_{y_2}$  is the yield stress on reloading after holding the specimen for various periods of time and  $\sigma_{y_1}$  is the initial yield stress

As an example, the change in the fractional softening  $X$  with the holding time ( $\Delta t$ ) in Fe-31% Ni-0.3% C austenitic alloy is shown in Figure 2.12. Specimens were tensile-deformed at 1100° C at a strain rate of  $4 \times 10^{-2}$ /s to  $\varepsilon = 0.18$  (work-hardened  $\gamma$ ) and  $\varepsilon = 1.0$  (completely dynamically recrystallized  $\gamma$ ) respectively, and then isothermally

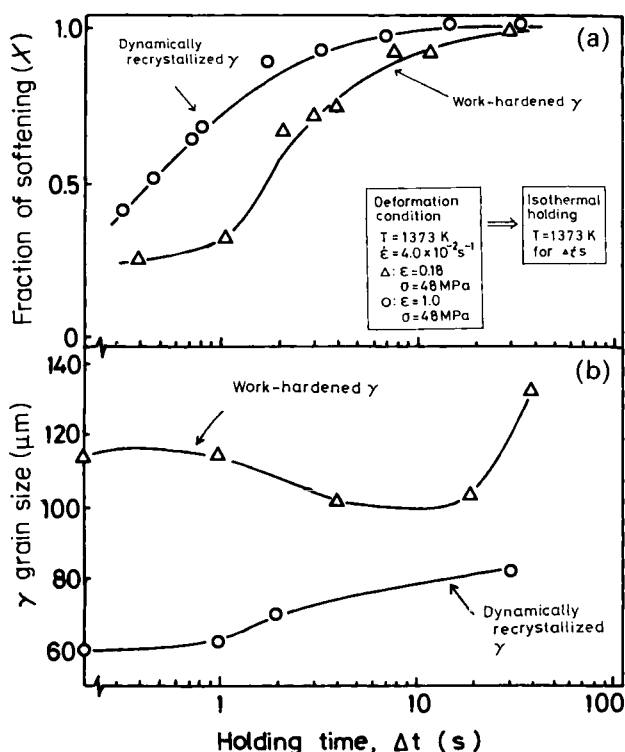


Figure 2.12 Change in fraction of softening: (a)  $\gamma$  grain size; (b) with the isothermal holding time of work-hardened  $\gamma$  and dynamically recrystallized  $\gamma$  in Fe-31 Ni-0.3 C austenitic alloy



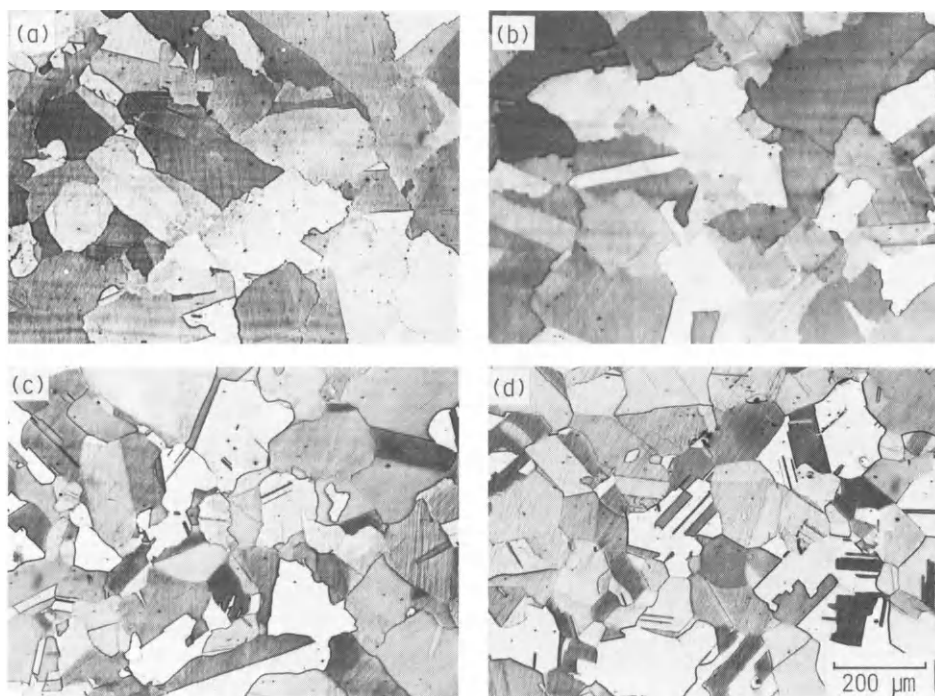


Figure 2.13 Change in optical microstructure of work-hardened  $\gamma$  (deformed at  $1100^\circ\text{C}$ ,  $\dot{\epsilon} = 4.0 \times 10^{-2}/\text{s}$ ,  $\epsilon = 0.18$ ) during isothermal holding at  $1100^\circ\text{C}$  for  $\Delta t$  in Fe-31 Ni-0.3 C austenitic alloy: (a) as deformed ( $\Delta t = 0\text{ s}$ ); (b)  $\Delta t = 1\text{ s}$ ; (c)  $\Delta t = 4\text{ s}$ ; (d)  $\Delta t = 15\text{ s}$

held for various periods of time. The change in average  $\gamma$  grain size with  $\Delta t$  is also plotted in Figure 2.12. Microstructural changes during isothermal holding at  $1100^\circ\text{C}$  are shown in Figures 2.13 and 2.14. As shown in Figure 2.13 ( $\epsilon = 0.18$ ), work-hardened austenites are slightly elongated along the tensile direction (Figure 2.13(a)). The  $\gamma$  structure hardly changes by holding for 1s (Figure 2.13(b)), although the softening occurs to some extent by the static recovery as can be seen in Figure 2.12. However, when specimens were isothermally held for 4 s (Figure 2.13(c)), fine  $\gamma$  grains – which are formed by static recrystallization – are partly formed mainly along the deformed  $\gamma$  grain boundaries and the static recrystallization is completed by the holding of 15 s (Figure 2.13(d)). Annealing twins in static recrystallized austenites are gradually developed as the holding time increases. By holding for 40 s, recrystallized  $\gamma$  grains are coarsened (Figure 2.12). When the  $\gamma$  was much more heavily deformed under higher  $Z$  conditions (work-hardened), the static recrystallized  $\gamma$  grains become much finer as shown in Figure 2.15. As shown in Figure 2.14 ( $\epsilon = 1.0$ ), dynamically recrystallized austenites are characterized by irregular grain boundaries, a low density of annealing twins and the mixed grain size. With an increase in holding time,  $\gamma$  grain boundaries become fairly straight and the  $\gamma$  structure becomes almost of equiaxed grains; furthermore, the density of annealing twins is increased. This is the typical microstructural change occurring during the metadynamic recrystallization process. Metadynamic recrystallization is completed by holding for about 30 s in the case of

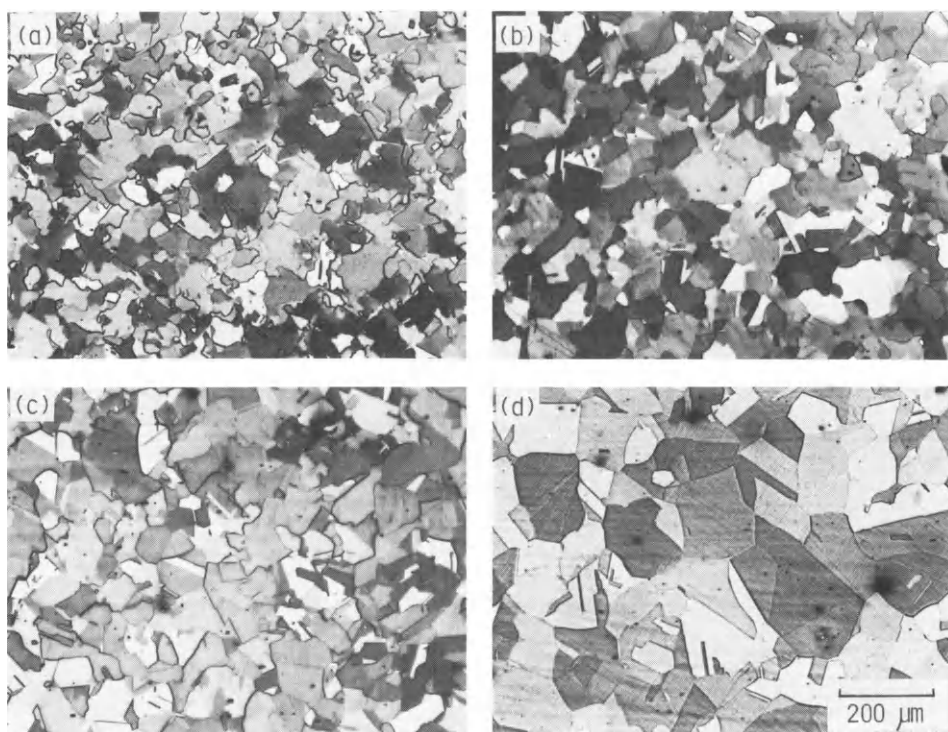


Figure 2.14 Change in optical microstructure of dynamically recrystallized  $\gamma$  (deformed at  $1100^\circ\text{C}$ ,  $\dot{\epsilon} = 4.0 \times 10^{-2}/\text{s}$ ,  $\epsilon = 1.0$ ) during isothermal holding at  $1100^\circ\text{C}$  for  $\Delta t$  in Fe-31 Ni-0.3 C austenitic alloy: (a) as deformed ( $\Delta t = 0$  s); (b)  $\Delta t = 1$  s; (c)  $\Delta t = 2$  s; (d)  $\Delta t = 30$  s

Figure 2.14, and the usual grain coarsening occurs by further holding. The grain size right after the completion of metadynamic recrystallization is smaller, as the grain size of dynamically recrystallized  $\gamma$  is smaller. However, as can be seen in Figure 2.12,  $\gamma$  grains are not refined and only increased by the metadynamic recrystallization, unlike the static recrystallization in which  $\gamma$  grains are once refined.

### 2.4.3 Effect of alloying elements on the retardation of recrystallization

The effect of alloying elements on the restoration process during or after hot-deformation is very important. Microaddition of niobium and titanium causes a remarkable retardation effect on recrystallization due to the suppression of grain boundary migration. The suppression of grain boundary migration due to microalloying is caused by either: (1) the solute dragging effect due to segregation of alloying elements to the boundaries; or (2) the pinning effect due to precipitates of carbonitride of alloying elements at grain boundaries. For example, molybdenum to the  $\gamma$  grain boundaries, resulting in the suppression of grain boundary migration. Niobium and titanium are precipitated as fine carbonitride particles and these precipitates suppress the grain boundary migration by the pinning effect.

Carbonitride particles are gradually coarsened with the holding time by the Ostwald ripening and their size can be expressed for spherical particles by Equation (2.30):<sup>43</sup>



Figure 2.15 Optical micrographs showing the static recrystallization occurring during isothermal holding of heavily work-hardened  $\gamma$  in Fe–31 Ni–0.3 C austenitic alloy: (a) work-hardened  $\gamma$  (deformed at 900° C,  $\dot{\epsilon} = 3/s$ ,  $\epsilon = 1.0$ ); (b) static recrystallized  $\gamma$  (isothermally held at 900° C for 50 s of structure (a))

$$\bar{r}^3 - \bar{r}_0^3 = k_0 \cdot t, \quad k_0 = \frac{8(a+b)\sigma V^\theta D X_M}{9a \cdot R \cdot T(X_M^\theta - X_M)} \quad (2.30)$$

where  $\bar{r}_0$  and  $\bar{r}$  are the mean particle radii at time 0 and at time  $t$  respectively,  $\sigma$  is the interfacial energy of the particle–matrix interface,  $V^\theta$  is the molar volume of carbide of  $M_aC_b$ ,  $D$  is the diffusion coefficient of solute in matrix,  $X_M$  is the content of solute atom in matrix, i.e. the solubility limit of solute atoms and  $X_M^\theta$  is the content of solute atom in  $M_aC_b$ ,  $R$  is the gas constant and  $T$  is the temperature in degrees Kelvin.

The following relation between the average radius ( $\bar{r}$ ) of dispersed or precipitated particles and the average radius ( $\bar{R}$ ) of grains (Zener's relation) has been observed.<sup>44</sup>

$$\bar{R} = 4\bar{r}/9f \quad (2.31)$$

where  $f$  is the volume fraction of dispersed particles

From Equations (2.30), (2.31) and others, Equation (2.32) is derived:

[www.iran-mavad.com](http://www.iran-mavad.com)

مرجع دانشجویان و مهندسين مواد

$$\bar{R}^3 - \bar{R}_0^3 = \left(\frac{4}{9f}\right)^3 k_0 \cdot t \quad (2.32)$$

These equations indicate that the pinning effect on grain boundary migration is effective because the particle size is small. If the average particle size is the same, the larger fraction  $f$ , i.e. the larger amount, of particles is effective for pinning. Furthermore, the smaller  $k_0$  is also effective for pinning.  $k_0$  is smaller as the solubility  $X_M$  of  $M_aC_b$  is smaller. Since the solubility of niobium or titanium carbonitrides is very small, their pinning effect is very effective. This will be described in Chapter 9. These carbonitrides are formed by strain-induced precipitation during hot-rolling or formed by strain-enhanced precipitation during holding after hot-rolling. The most effective suppression of recrystallization is obtained by the precipitation of fine carbonitrides formed during or after hot-rolling at 850–1000°C, after the solution treatment at higher temperatures at which alloying elements such as niobium or titanium are in solution.

#### 2.4.4 Texture due to hot-deformation

When the later stage of hot-rolling in the range of work-hardened  $\gamma$  is done in steels containing molybdenum, niobium or titanium, the work-hardened  $\gamma$  shows a fairly strong texture and, hence, the ferrites formed from such a deformed  $\gamma$  also exhibit a texture. Textures of  $\{110\}_\gamma \langle 112 \rangle_\gamma$  and  $\{112\}_\gamma \langle 111 \rangle_\gamma$  are strongly developed by the deformation of  $\gamma$ . These  $\gamma$  textures are inherited by  $\alpha$  as textures of  $\{332\}_\alpha \langle 113 \rangle_\alpha$  and  $\{311\}_\alpha \langle 011 \rangle_\alpha$ , respectively.<sup>45</sup> When the rolling temperature is lowered to the  $(\alpha + \gamma)$  two-phase region in addition to above textures such as  $\{332\}_\alpha \langle 113 \rangle_\alpha \sim \{554\}_\alpha \langle 225 \rangle_\alpha$  and  $\{112\}_\alpha \langle 110 \rangle_\alpha \sim \{113\}_\alpha \langle 110 \rangle_\alpha$ , the texture of  $\{100\}_\alpha \langle 011 \rangle_\alpha$  is strongly developed by the deformation of  $\alpha$ . These textures influence the strength and toughness and their anisotropy of steel.<sup>45,46</sup> These are also mentioned in detail in Chapter 5.

## 2.5 $\alpha$ grain refinement by the work-hardening of $\gamma$

### 2.5.1 $\alpha$ nucleation in deformed $\gamma$ (isothermal)

Figure 2.16 shows typical micrographs of the effect of  $\gamma$  deformation on the progress of  $\alpha$  transformation.<sup>47</sup> Specimens of an Fe–0.12 C–0.04 Nb–0.04 V steel were austenitized at 1200°C for 30 min, rolled 30 or 50% in reduction by a single pass at 840°C (in the unrecrystallized temperature range) and held at 680°C for 15, 30 and 180 s. The  $\alpha$  transformation is clearly accelerated by the deformation of  $\gamma$ . In the nondeformed specimen,  $\gamma$  grain boundaries are the predominant nucleation sites of  $\alpha$ , but in the deformed specimens nucleation occurs not only on  $\gamma$  grain boundaries but also within grains. Moreover, the nucleation rate on grain boundaries is accelerated substantially.

Figure 2.17 shows various types of nucleation sites of  $\alpha$  observed in deformed specimens.<sup>47</sup> Figure 2.17(a) shows  $\alpha$  grains nucleated at  $\gamma$  grain boundaries. The  $\alpha$  grains grow into both sides of  $\gamma$  grains, and the prior  $\gamma$  grain boundaries disappear once ferrites are nucleated. Figure 2.17(b) shows the  $\alpha$  grains nucleated at the annealing twin boundaries. In contrast to the nondeformed specimens, the annealing twin boundaries



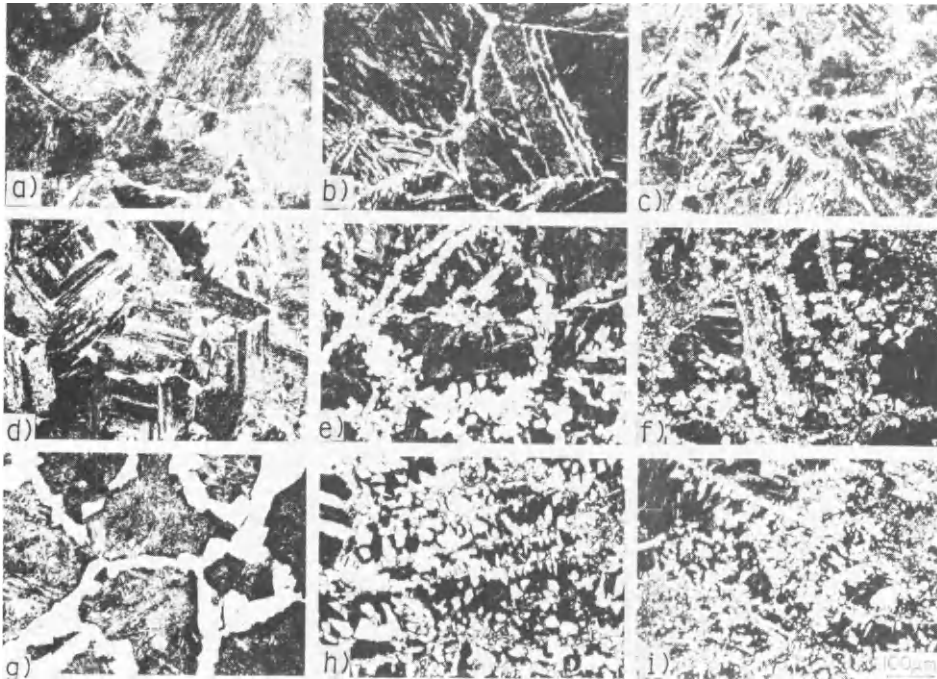


Figure 2.16 Optical micrograph showing the effect of  $\gamma$  deformation on the process of  $\alpha$  transformation at 680°C in Fe-0.12C-0.04Nb-0.04V steel: (a) nondeformed, 15 s; (b) 30%-rolled, 15 s; (c) 50%-rolled, 15 s; (d) nondeformed, 30 s; (e) 30%-rolled, 30 s; (f) 50%-rolled, 30 s; (g) nondeformed, 3 min; (h) 30%-rolled, 3 min; (i) 50%-rolled, 3 min

in the deformed specimens are the preferential nucleation sites of  $\alpha$ . The  $\alpha$  grains nucleated at annealing twin boundaries grow mostly into one side, and the traces of prior annealing twin boundaries remain after transformation. Figure 2.17(c) shows  $\alpha$  grains nucleated intragranularly. These ferrites were considered to be nucleated on the dislocations at the cell wall inside the grains. Figure 2.17(d) shows the  $\alpha$  grains nucleated at deformation bands.

The increase in the  $\alpha$  nucleation rate per unit volume of  $\gamma$  by deformation is attributed: (1) to the increase in the  $\gamma$  grain surface by elongation of grains; (2) to the increase in the nucleation rate *per se* per unit area of grain surface; and (3) to the formation of additional nucleation sites such as annealing twin boundaries, deformation bands, etc.

The grain boundary surface area of  $\gamma$  per unit volume of a specimen increases by deformation. A spherical  $\gamma$  grain (Figure 2.18(a)) becomes an ellipsoid as shown in Figure 2.18(b) by applying the rolling with reduction  $p$ . The surface area of a grain with a unit radius before rolling is given as:

$$S_{g,b}^0 = 4\pi \quad (2.33)$$

The surface area of the grain after rolling with reduction  $p$  is given as:<sup>48</sup>

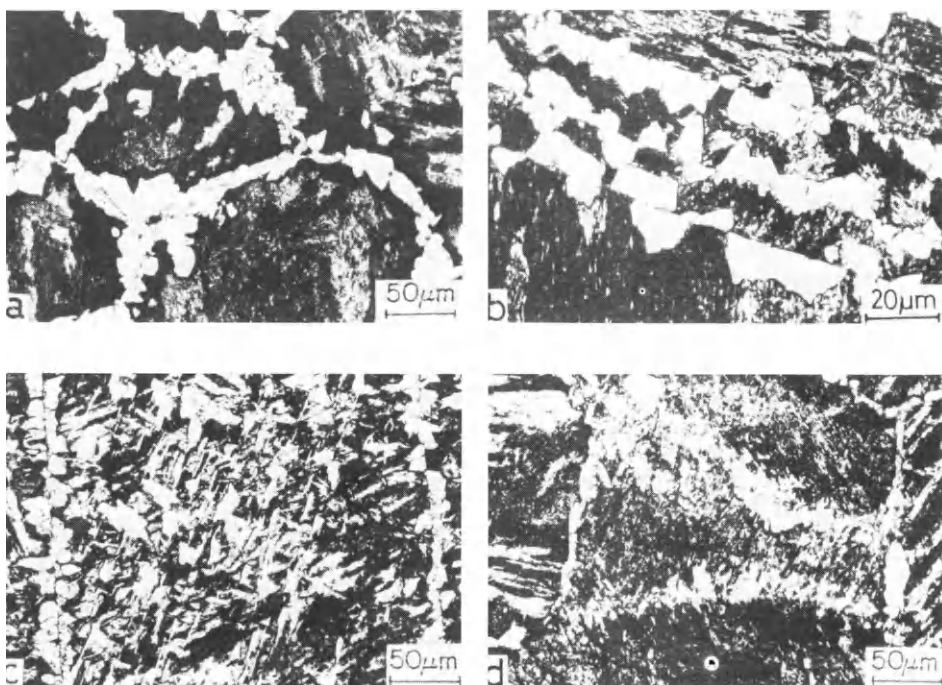


Figure 2.17 Optical micrographs showing the various types of nucleation sites of  $\alpha$  observed in deformed specimens: (a) nucleation at grain boundaries; (b) nucleation on annealing twin boundaries; (c) nucleation inside grains; (d) nucleation on deformation bands

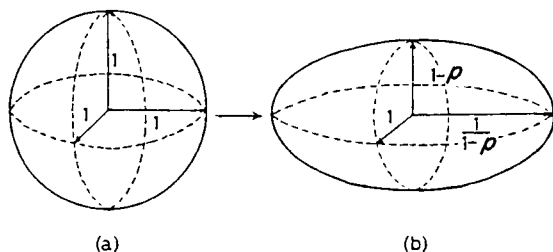


Figure 2.18 The shape change of an  $\gamma$  grain by the rolling with reduction  $p$ : (a) before rolling (sphere); (b) after rolling (ellipsoid)

$$S_{g \cdot b}(p) = \int_{-1/(1-p)}^{1/(1-p)} \left( \left\{ 4x \int_0^{\pi/2} \sqrt{1 - (2p - p^2) \sin^2 \theta} \cdot d\theta \right\} \times \sqrt{\frac{x^2(1-p)^6}{1 - x^2(1-p)^2} + 1} \right) dx \quad (2.34)$$

The ratio of the surface areas before : after rolling  $q (= S_{g \cdot b}/S_g^0)$ , is plotted in Figure 2.19 as a function of rolling reduction  $p$ . Since the volume of the sphere shown in Figure 2.18(a) is equal to that of the ellipsoid shown in Figure 2.18(b), the ratio  $q$  in Figure 2.19 is equal to that obtaining to grain surface areas per unit volume before and after rolling. It is seen that the increase in the grain surface area per unit volume with the increase in  $p$  is quite small when  $p$  is small, e.g. a 50% reduction by rolling increases the

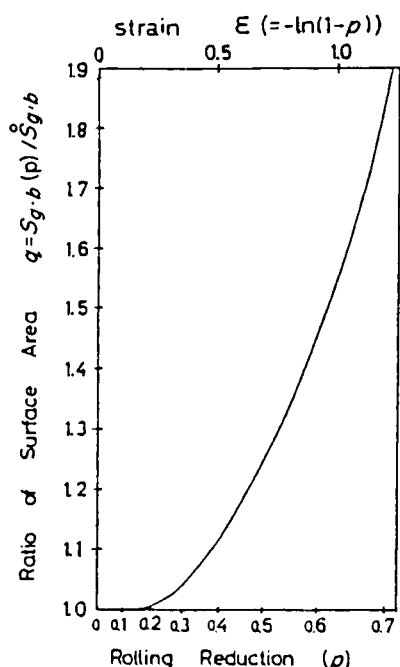


Figure 2.19 The ratio of  $\gamma$  grain surface area before rolling to that of after rolling as a function of rolling reduction  $p$

surface area by 25%. This increase is equivalent to that obtained by only a 20% reduction in  $\gamma$  grain size by recrystallization.

The number of  $\alpha$  grains nucleated on  $\gamma$  grain boundaries is substantially increased by deformation. Figure 2.20 (a), (b) and (c)<sup>47</sup> shows the  $\alpha$  grains nucleated on the  $\gamma$  grain boundaries in nondeformed 30%-rolled, and 50%-rolled specimens respectively; accordingly, the acceleration of  $\alpha$  nucleation rate on  $\gamma$  grain boundaries by deformation can be estimated. The number of  $\alpha$  grains intersecting per 1 mm of  $\gamma$  grain boundaries were counted as 41, 214 and 330 for nondeformed, 30%-rolled and 50%-rolled specimens respectively. The numbers of  $\alpha$  grains nucleated per unit area of  $\gamma$  grain boundary surface are proportional to the squares of these numbers. Furthermore, the number of  $\alpha$  grains nucleated per unit area of  $\gamma$  grain surface,  $n_s$ , is proportional to the square root of  $I_s$  as is shown in Equation (2.8). Since  $\alpha$  (parabolic rate constant) is not much changed by deformation, the  $\alpha$  nucleation rate per unit area of  $\gamma$  grain boundary surface is estimated to be increased by 740  $(214/41)^2$  and 4200  $((330/41)^2)$  times faster by 30%- and 50%-rolling respectively.

As is shown above, the nucleation of  $\alpha$  on  $\gamma$  grain boundaries is substantially accelerated by deformation. The mechanism of enhanced nucleation is considered to be as follows. The deformed  $\gamma$  grain boundaries may have many ledges (or steps) shown schematically in Figure 2.21(a). If  $\alpha$  nucleates at the corner of such a ledge, as is shown in Figure 2.21(b), the activation energy for nucleation becomes  $\theta/\pi$  times less than that for nucleation on a planar grain boundary (if the surface energy is assumed to be equal for all kinds of interfaces). Thus, if numerous ledges are produced on grain boundaries by deformation, considerable increases in the nucleation rates can be expected. As is shown in Figure 2.17(b) the annealing twin boundaries in work-hardened  $\gamma$  also act as the preferential nucleation sites of  $\alpha$ . The reasons for this can be considered to be as

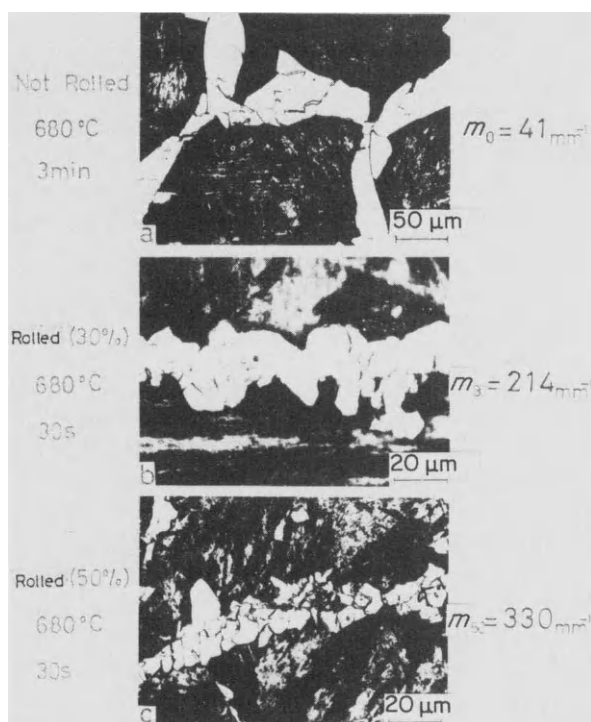


Figure 2.20 Optical micrographs showing the effect of deformation on the number of ferrites formed on  $\gamma$  grain boundaries: (a) nondeformed, 3 min at 680° C; (b) 30%-rolled, 30 s at 680° C; (c) 50%-rolled, 30 s at 680° C

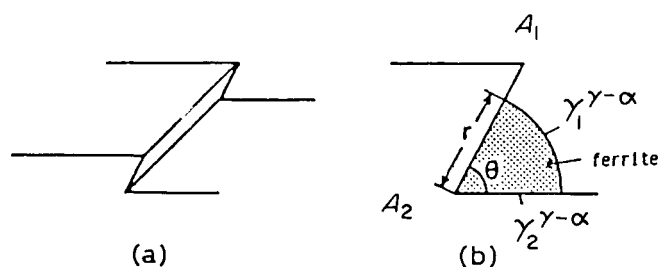


Figure 2.21 Schematic drawing showing  $\alpha$  nucleation at a ledge on deformed  $\gamma$  grain boundaries: (a) a ledge on a grain boundary; (b)  $\alpha$  nucleation at a ledge

follows. The coherent twin boundaries before deformation lose coherency and at the same time a large number of ledges are produced on the twin boundaries by deformation. Thus, deformed twin boundaries have similar structures to those of  $\gamma$  grain boundaries and act as the preferential nucleation sites of  $\alpha$ .

Similar mechanisms have been proposed for the enhanced nucleation on deformed  $\gamma$  grain boundaries by several researchers. Sandberg and Roberts<sup>49</sup> have suggested that deformation leads to the formation of grain boundary serrations or bulges, and these act as nucleation sites. Amin and Pickering<sup>50</sup> proposed that deformed  $\gamma$  grain boundaries appear to exhibit greater lattice mismatch, possibly because of greater lattice



distortion and a higher dislocation density near deformed grain boundaries. These would be the predominant nucleation sites of  $\alpha$  and, hence, accelerate the nucleation.

Deformation structures within  $\gamma$  grains have been known to act as the effective nucleation sites of  $\alpha$  and to play an important role in  $\alpha$  grain refinement. The deformation structures are generally known as deformation bands. These regions are characterized by a high density of cells consisting of tangled dislocations. Dislocations are  $\alpha$  nucleation sites through its stress field. Consequently,  $\alpha$  nucleation appears to occur frequently at the deformation structures.

### 2.5.2 Growth of $\alpha$ in deformed $\gamma$ (isothermal)

When  $\alpha$  grains grow into deformed  $\gamma$ , their growth rate would be accelerated by the following two factors: (1) the enhancement of diffusivity by dislocations and super-saturated vacancies; and (2) the additional driving force associated with stored energy. Since carbon, whose diffusivity controls the growth rate of  $\alpha$  in high-strength low alloy (HSLA) steels, is an interstitial element, the former effect is considered to be small.

The parabolic rate constant growth of  $\alpha$  is given as Equation (2.21). The free energy of deformed  $\gamma$  is higher than that of undeformed  $\gamma$  by a stored energy, which is a function of dislocation density. Hence,  $C_\alpha$  (deformed) and  $C_\gamma$  (deformed) are higher than those in undeformed specimens. A similar calculation is applied as described in Section 2.4. We can find that the  $\alpha$  growth rate is slightly enhanced by the deformation of  $\gamma$ . The acceleration of growth rate by deformation is much less than the enhancement of nucleation rate.

### 2.5.3 $\alpha$ grain size formed from deformed $\gamma$ (isothermal)

For simplicity we assume:

- (1) That  $\gamma$  grain boundary surfaces are the nucleation sites and the additional nucleation sites produced by deformation are the deformation bands and annealing twin boundaries.
- (2) That the nucleation rates per unit area of deformation bands and annealing twin boundaries are equal to that of the grain boundary surface (although deformation bands are not planes but the regions with high density of cells; here they will be treated as planar defects because they are very thin).
- (3) That the total area of deformation bands and annealing twin boundaries per unit volume of  $\gamma$  is quadratic with respect to the strain:

$$\varepsilon (= \ln(1 - p)), \text{ i.e.:}$$

$$S_d \cdot b(p) + S_t \cdot b(p) = A(-\ln(1 - p))^2 \quad (2.35)$$

where  $A$  is a constant.

- (4) That the ratio  $\sqrt{I_s(p)} : \alpha(p)$  can be expressed as a function of strain  $\varepsilon$  from the experiment shown in Figure 2.20 as:

$$\frac{\sqrt{I_s(p)}}{\alpha(p)} = \frac{\sqrt{I_0}}{\alpha_0} + B \frac{\sqrt{I_0}}{\alpha_0} \{-\ln(1-p)\}^{1.3} \quad (2.36)$$

where  $I_0$  and  $\alpha_0$  are the nucleation rate and parabolic rate constant of growth in the nondeformed specimen respectively and  $B$  is a constant.

As discussed above, the  $\alpha$  grain size formed from nondeformed  $\gamma$  in the case of grain surface nucleation can be expressed by Equation (2.9). The assumptions made for deformed specimen  $S_{g \cdot b}$  in Equation (2.9) should be replaced by the effective interfacial area  $S_v$  which is the sum of the areas of grain boundary surface, annealing twin boundary and deformation bands ( $S_v(p) = S_{g \cdot b}(p) + S_{d \cdot b}(p) + S_{t \cdot b}(p)$ ). Furthermore, if both the nucleation and the growth rates are a function of strain, the  $\alpha$  grain size in the deformed specimen can be expressed as:

$$D_\alpha = \left( \frac{S_v(p) \sqrt{I_s(p)}}{2\sqrt{2} \alpha(p)} \right)^{-\frac{1}{3}} \quad (2.37)$$

Thus, if  $\sqrt{I_0}/\alpha_0$  and the coefficients  $A$  and  $B$  are determined from an experiment, the  $\alpha$  grain size formed from deformed  $\gamma$  can be calculated. Figure 2.22 shows an example of

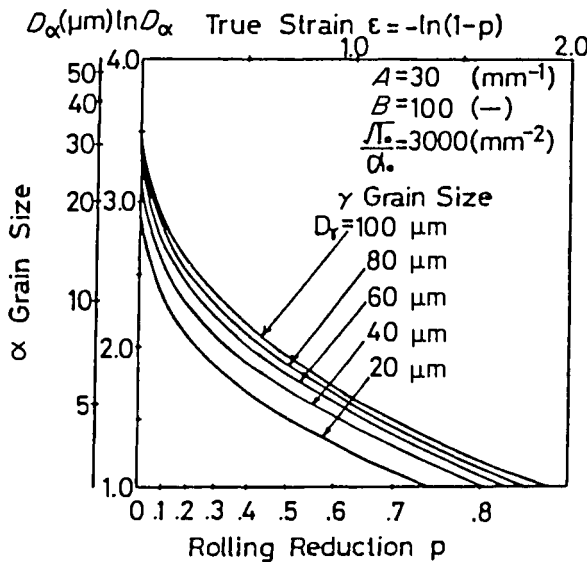


Figure 2.22 Calculated  $\alpha$  grain size formed from work-hardened  $\gamma$  as a function of rolling reduction for various  $\gamma$  grain sizes

such a calculation. Here, the calculated  $\alpha$  grain size using the commonly observed values of  $\sqrt{I_0}/\alpha_0$ ,  $A$  and  $B$ , is plotted as a function of the effective  $\gamma$  interfacial area for various  $\gamma$  grain sizes. From Figure 2.22 it is seen that the  $\alpha$  grain size formed from work-hardened  $\gamma$  decreases drastically with the increase in a rolling reduction for a small rolling reduction and decreases gradually for a large rolling reduction. Equations

(2.35)–(2.37) also show that the  $\alpha$  grain refinement by  $\gamma$  deformation is introduced mostly by the increase in the effective  $\gamma$  interfacial area when an initial  $\gamma$  grain is large and is introduced mostly by the enhancement of the  $\alpha$  nucleation rate on the grain boundaries, annealing twin boundaries and deformation bands when an initial  $\gamma$  grain size is small.

## 2.6 $\alpha$ grain refinement by accelerated cooling

Accelerated cooling after hot-rolling is currently being realized as a further advanced thermomechanical treatment in the hot-rolling process.<sup>24,25</sup> This cooling process is characterized by accelerated cooling in a  $\gamma \rightarrow \alpha$  transformation range just after controlled-rolling. It has been shown that the accelerated cooling refines the  $\alpha$  grain size and thus further improves both the strength and toughness.

The effect of accelerated cooling on  $\alpha$  grain refinement can be seen in a nondeformed specimen. Figure 2.23 shows the effect of cooling rate on  $\alpha$  grain size in an Fe–0.15 C

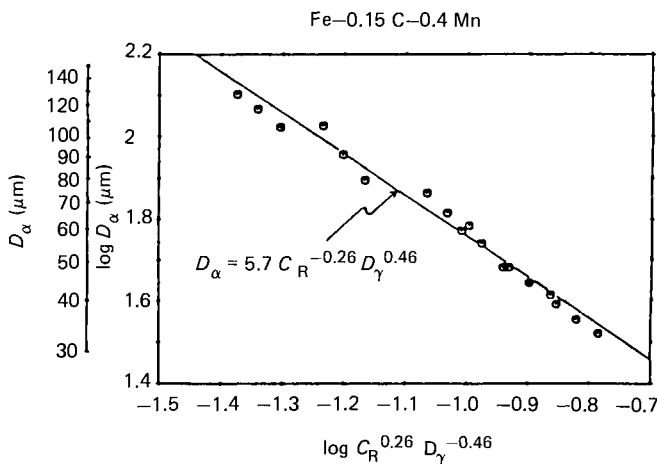


Figure 2.23  $\alpha$  grain size as a function of  $C_R^{-0.26} D_\gamma^{0.46}$

steel.<sup>51</sup> The measured  $\alpha$  grain sizes were plotted as a function of  $D_\gamma^{-0.46} C_R^{0.26}$ . All the data lie well on a straight line, indicating that  $D_\alpha$  can be expressed as functions of cooling rate  $C_R$  and the  $\gamma$  grain size  $D_\gamma$  as:

$$D_\alpha = 5.7 C_R^{-0.26} D_\gamma^{0.46} \quad (2.38)$$

(also shown in the experimental plots in Figure 2.9). This dependence of  $\alpha$  grain size on cooling rate means that when a cooling rate becomes 10 times faster,  $\alpha$  grain diameter becomes 0.55.

The principle of grain size refinement by accelerated cooling can be understood by considering the effect of transformation temperature on  $\alpha$  grain size in an isothermal transformation. As mentioned in Section 2.3, the grain size of isothermally formed  $\alpha$  depends on the ratio of the square root of nucleation rate to the parabolic rate constant

for various types of nucleation sites. Thus, when the ratio  $\sqrt{I}/\alpha$  increases with the decrease in the transformation temperature, the size of an isothermally formed  $\alpha$  grain decreases with the decrease in the transformation temperature.

The continuous cooling transformation can be considered as the sum of short-time isothermal holdings at successive temperatures, as described in Section 2.3 and Equations (2.19) and (2.20) which show  $N_\alpha$  and  $D_\alpha$  respectively.

In the accelerated cooling of work-hardened  $\gamma$  after hot-rolling,  $\alpha$  grain refinement may depend on rolling conditions. As discussed above,  $D_\alpha$  is a function of nucleation rate  $I$ , and  $I$  is a function of the transformation temperature. The effect of transformation temperature on the nucleation rate would be different for grain boundary nucleation and for nucleation on dislocations. Thus,  $D_\alpha$  would be a complex function of rolling conditions when accelerated cooling is applied after hot-rolling.

## 2.7 Summary

The current understanding on the  $\alpha$  grain refinement by hot-rolling and accelerated cooling have been described on the basis of transformation kinetics. It has been shown that  $\alpha$  grain size depends on the nucleation site density, nucleation frequency at a given site, and growth rate. For grain boundary surface nucleation,  $D_\alpha$  is proportional to  $D_\gamma^{\frac{1}{2}}$  and is inversely proportional to  $(\sqrt{I_s}/\alpha)^{\frac{1}{2}}$ . To obtain a fine  $\alpha$  grain,  $D_\gamma$  should be small and the value of  $\sqrt{I_s}/\alpha$  large.  $\gamma$  grain refinement by recrystallization is effective to obtain a fine  $\alpha$  grain. However, as long as the  $\gamma$  grain boundaries are the predominant nucleation sites of  $\alpha$ , the grain refinement obtained in  $\gamma$  turns out to be less effective in  $\alpha$  grain refinement than the deformation (work-hardening) of  $\gamma$ .  $\gamma$  deformation in an unrecrystallized temperature range accelerates substantially the  $\alpha$  nucleation at  $\gamma$  grain boundaries and within grains. The deformed  $\gamma$  grain boundaries may have a large number of ledges at which  $\alpha$  can nucleate with a smaller activation energy than that on the planar boundaries. Deformed annealing twin boundaries also act as the preferential nucleation sites of  $\alpha$ . This may be because the deformed annealing twin boundaries have similar structures to that of deformed grain boundaries. Within deformed  $\gamma$  grains, generally called 'deformation bands', are the regions with high densities of dislocations.  $\alpha$  nucleation appears to occur frequently at such regions. The growth rate of  $\alpha$  in deformed  $\gamma$  would be accelerated, but a thermodynamical calculation indicates that the increase in the parabolic rate constant by deformation is less than 10%. As a whole,  $\gamma$  deformation results in a large increase in the ratio of the nucleation rate to the parabolic rate constant and leads to  $\alpha$  grain refinement. The accelerated cooling refines a  $\alpha$  grain size. A phenomenological equation for  $D_\alpha$  as functions of cooling rate and  $D_\gamma$  has been presented. The principle of grain size refinement by accelerated cooling has been discussed and theoretical equations for  $D_\alpha$  introduced.

## References

1. MAKI, T., TSUZAKI, K. and TAMURA, I. *Trans Iron and Steel Inst. Japan*, **20**, 207 (1980)
2. HONEYCOMBE, R.W.K. *Met. Trans.*, **7A**, 915 (1976); CAMPBELL, K. and HONEYCOMBE, R.W.K. *Met. Sci.*, **8**, 197 (1974)
3. UMEMOTO, M., KOMATSUBARA, N. and TAMURA, I. *J. Heat Treating*, **1**, 3, 57 (1980)

4. CAHN, J.W. *Acta Met.*, **4**, 449 (1956)
5. SCHEIL, E. *Arch. Eisenhüttenw.*, **12**, 565 (1935)
6. UMEMOTO, M., NISHIOKA, N. and TAMURA, I. *J. Heat Treating*, **2**, 130 (1981); UMEMOTO, M., NISHIOKA, N. and TAMURA, I. *Trans. Iron and Steel Inst. Japan*, **22**, 629 (1982)
7. UMEMOTO, M., KOMATSUBARA, N. and TAMURA, I. *Solid-solid phase transformation*, p.1111 (1980)
8. KOZASU, I., SHIMIZU, T. and KUBOTA, H. *Trans Iron and Steel Inst. Japan*, **11**, 367-75 (1971)
9. TANAKA, T., TABATA, N., HATOMURA, T. and SHIGA, C. *Microalloying 75*, Union Carbide Corp., pp.88-89, (1977)
10. PRIESTNER, R., EARLY C.C. and RENDALL, J.H. *J. Iron and Steel Inst.*, **206**, 1252-62 (1968)
11. SEKINE, H. and MARUYAMA, T. *Strength of metals and alloys*, Iron and Steel Institute, p.85 (1973)
12. TOWLE, D.J. and GLADMAN, T., *Metal Sci.*, **13**, 246-56 (1979)
13. SELLARS, C.M. and WHITEMAN, J.A., *Metal Sci.*, **13**, 187-94 (1979)
14. CUDDY, L.J. *Met. Trans*, **12A**, 1313-20 (1981)
15. MACHIDA, M., KATSUMATA, M. and KAJI, H., *Steel-rolling*, Iron and Steel Institute of Japan, pp.1249-60 (1980)
16. CUDDY, L.J. *Met. Trans*, **15A**, 87-98 (1984)
17. BARRACLOUGH, D.R. and SELLARS, C.M. *Metal Sci.*, **13**, 257-67 (1979)
18. WEISS, H., GITTINGS, A., BROWN, G.C. and TEGUAT, W.J.McG. *J. Iron and Steel Institute*, **211**, 703-709 (1973)
19. KOZASU, I., OUCHI, C., SANPEI, T. and OKITA, T. *Microalloying 75*, Union Carbide Corp., pp.100-114 (1977)
20. SEKINE, H. and MARUYAMA, T. *Trans Iron and Steel Inst. Japan*, **16**, 427-36 (1976)
21. SEKINE, H. and MARUYAMA, T. *Microstructure and design of alloys*, Metals Society, pp.85-88 (1974)
22. OUCHI, C., SANPEI, T., OKITA, T. and KOZASU, I. *The hot-deformation of austenite*, American Institute Metallurgical Engineers, pp.316-40 (1976)
23. PRIESTNER, R. and DE LOS RIOS, E. *Metals Tech.*, **7**, 309-16 (1980)
24. OUCHI, C., TANAKA, J., KOZASU, I. and TSUKADA, K. *Optimization of processing properties and service performance through microstructural control*, pp.105-25, ASTM, STP672 (1979)
25. SEKINE, H., MARUYAMA, T., KAGEYAMA, H. and KAWASHIMA, Y. *Thermomechanical processing of micro-alloyed austenite*, pp.141-61 (1981)
26. UMEMOTO, M., OHTSUKA, H. and TAMURA, I. *Structure and properties of HSLA steels*, p.96 (1984)
27. GULLIVER, G.H. *J. Inst. Metals*, **19**, 145-49 (1981)
28. BRADLEY, J.R., RIGSBEE, J.M. and AARONSON, H.I. *Met. Trans*, **8A**, 323-33 (1977)
29. YOSHIMURA, H. and ISHII, M. *Tetsu-to-Hagané*, **69**, 1440-47 (1983) (in Japanese)
30. OUCHI, C., and OKITA, T. *Trans Iron and Steel Inst. Japan*, **24**, 726-33 (1984)
31. UMEMOTO, M., GUO, Z.H. and TAMURA, I. *High-strength low-alloy steels* 85, (1985)
32. ZENER, C. *J. Appl. Phys.*, **20**, 950-53 (1949)
33. HILLERT, M. and STAFFANSON, L.I. *Acta Chem. Scand.*, **24**, 3618-26 (1970)
34. AARONSON, H.I. and DOMIAN, H.A. *Am. Inst. Metall. Engrs*, **236**, 781-96 (1966)
35. WELLS, C., BATZ, W. and MEHL, R.F. *Trans Am. Inst. Metall. Engrs*, **188**, 553-60 (1950)
36. KAUFMAN, L., RADCLIFFE, S.V. and COHEN, M. *Decomposition of austenite by diffusional process*, V.F. ZACKAY and H.I. AARONSON, (eds), pp.313-52 (1962)
37. WAGNER, C. *Trans Am. Inst. Mech. Engrs*, **194**, 91-96 (1952)
38. LANGE, W.F. and AARONSON, H.I.: *Met. Trans*, (in press)
39. HILLERT, M. *Lecture on the theory of phase transformation*, H. I. AARONSON, (ed.) American Institute Mechanical Engineers, pp.1-50 (1975)
40. DUBE, C.A. Ph.D thesis, Carnegie Institute of Technology (1948)
41. MAKI, T., OKAGUCHI, S and TAMURA, I. *6th International conference on strength of metals and alloys*, p.529 (1982)
42. BECK, P.A. and SPERRY, P.R. *J. Appl. Phys.*, **21**, 150 (1950)
43. WEG, M.Y., SAKUMA, T. and NISHIZAWA, T. *Trans. JIM*, **22**, 733 (1981)
44. ZENER, C. *J. Appl. Phys.*, **20**, 950 (1949)
45. INAGAKI, H., KURIHARA, K. and KOZASU, I., *Trans. Iron and Steel Inst. Japan*, **17**, 75 (1977); INAGAKI, H. *Trans. Iron and Steel Inst. Japan*, **17**, 166 (1977)
46. TANAKA, T. and TABATA, N. *J. Iron and Steel Inst. of Japan* **69**, 1353 (1978) (in Japanese)
47. UMEMOTO, M., OHTSUKA, H., KATO, H. and TAMURA, I. *Structure and properties of HSLA steels*, p.107 (1984)
48. UMEMOTO, M., OHTSUKA, H. and TAMURA, I. *Trans Iron and Steel Inst. Japan* **23**, 775-84 (1983)
49. SANDBERG, A. and ROBERTS, W. *Thermomechanical processing of microalloyed austenite*, 405-31 (1981)
50. AMIN, R.K. and PICKERING, F.B. *Thermomechanical processing of microalloyed austenite*, pp.377-402
51. UMEMOTO, M., GUO, Z.H. and TAMURA, I. *Materials Science and Technology*, **3**, 249 (1987)

## Deformation of austenite in the recrystallization region

When hot-rolling is carried out in plate-mills in the conventional rolling temperature range, the austenite ( $\gamma$ ) grains of slabs, coarsened at the reheating, are considered generally to complete recrystallization during the time intervals between the reductions, and to be refined successively after every reduction,<sup>1-3</sup> as shown in Figures 3.1<sup>2</sup> and 3.2. Although conventional rolling operations are finished at 1050–900° C (according to the plate thickness) this process continues after a reduction at 850–800° C in carbon–manganese or silicon–manganese steels,<sup>2,3,4</sup> but stops after a reduction at

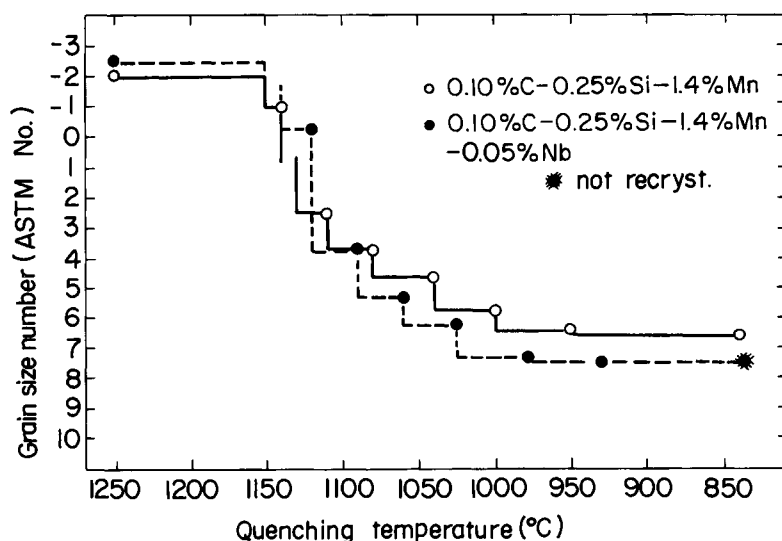
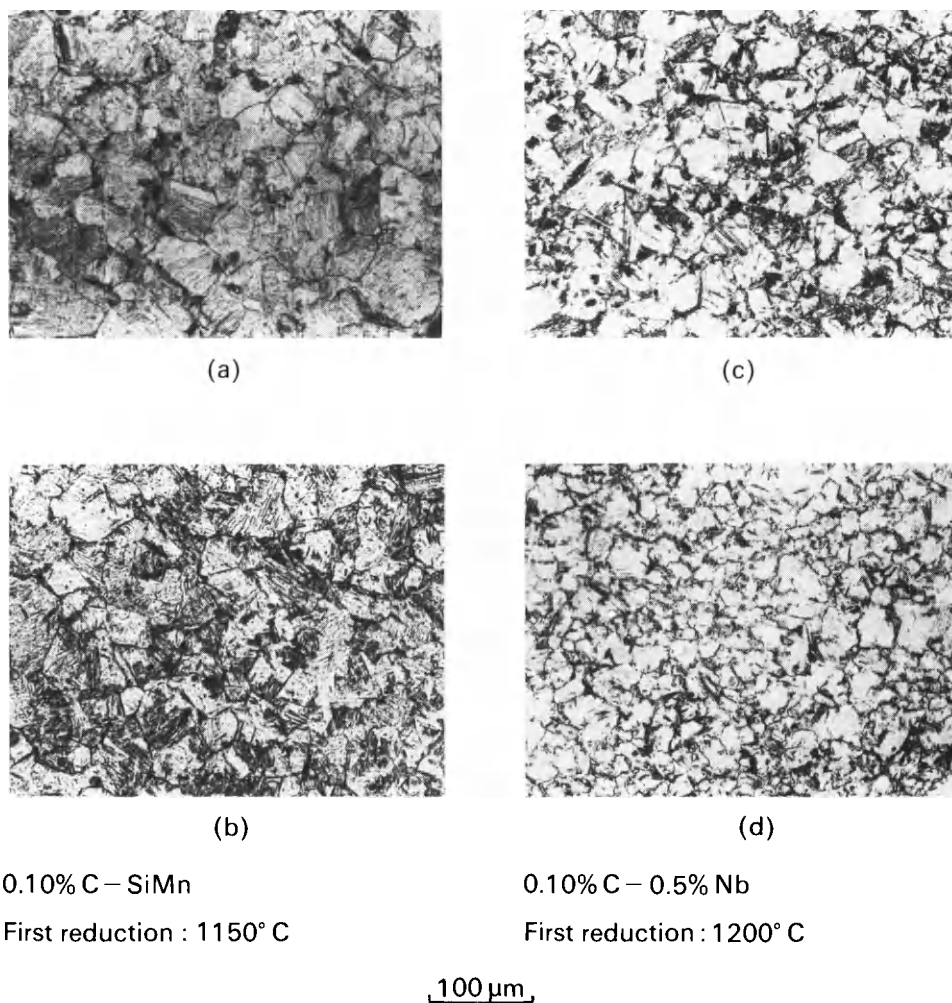


Figure 3.1 Change in  $\gamma$  grain size during successive reductions:

0.10% C–0.25% Si–1.4% Mn–0.005% N

0.10% C–0.26% Si–1.4% Mn–0.05% Nb–0.006% N

First reduction was applied at 1150° C after reheating at 1250° C, and quenching or next reduction was carried out 7 s after respective reduction. (After Sekine and Maruyama<sup>2</sup>)



*Figure 3.2* Refinement of recrystallized  $\gamma$  grains by successive hot-reductions: (a) after 7th reduction at 980° C; (b) after 8th reduction at 955° C of successive reductions from 1150° C (10 C•SiMn or 0.10 C–SiMn); (c) after 7th reduction at 1050° C; (d) after 8th reduction at 980° C of successive reductions from 1200° C (10 C•5 Nb or 0.10% C–0.05% Nb).

950–900° C in niobium-containing steels – which is about 100° C higher than in niobium-free steels (Table 3.1).<sup>2,3</sup> Convergence of grain refinement at the final stage of successive reductions is found both when the percentage reductions are held constant<sup>1</sup> and when increased in the scale of reductions as shown in Table 3.1 and Figure 3.1.

When reductions are applied at temperatures below those critical for recrystallization ( $T_C$ ), the  $\gamma$  grains are elongated in the rolling direction,<sup>5,6</sup> and annealing twins formed at reheating and during interpass times become distinctly visible, with deformation bands forming in the unrecrystallized grains<sup>5,6,7</sup> (Figure 3.3).  $T_C$  is also called the pancaking temperature ( $T_p$ ).<sup>8</sup>



TABLE 3.1 Rolling schedule and structures of 7s after respective reductions. (After Sekine and Maruyama<sup>2</sup>)

| Pass number              |                     | 1  | 2  | 3  | 4  | 5  | 6  | 7  | 8  |
|--------------------------|---------------------|----|----|----|----|----|----|----|----|
| Slab thickness (mm)      |                     | 75 | 68 | 60 | 50 | 40 | 30 | 20 | 12 |
| Percentage reduction (%) |                     | 9  | 12 | 17 | 20 | 25 | 33 | 40 | 42 |
| Steel                    | Rolling temperature |    |    |    |    |    |    |    |    |
| 10C · Si-Mn              | 1200–965° C         | R  | R  | R  | R  | R  | R  | R  | R  |
|                          | 1150–955° C         | R  | R  | R  | R  | R  | R  | R  | R  |
|                          | 1000–840° C         | P  | P  | P  | P  | P  | R  | R  | R  |
| 10C · 5Nb                | 1200–980° C         | R  | R  | R  | R  | R  | R  | R  | R  |
|                          | 1150–900° C         | R  | R  | R  | R  | R  | R  | R  | N  |
|                          | 1000–860° C         | N  | N  | N  | N  | N  | N  | N  | N  |

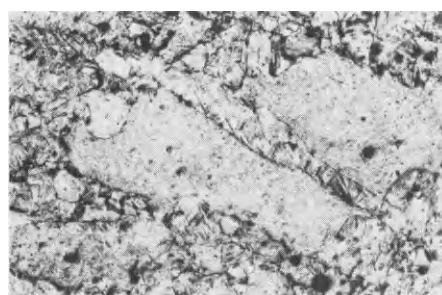
\* Steel is the same as that of Figure 3.1

Slab reheating temperature: 1250° C

R: 100% recrystallized

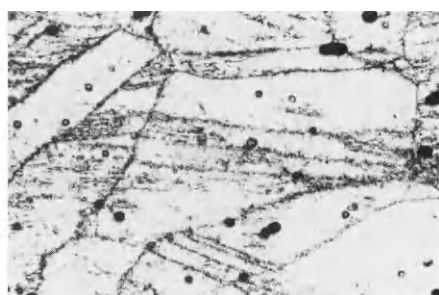
P: Partially recrystallized

N: Not recrystallized



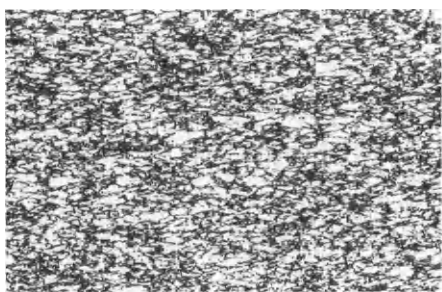
(a)

10C · SiMn (or 0.10% – SiMn)



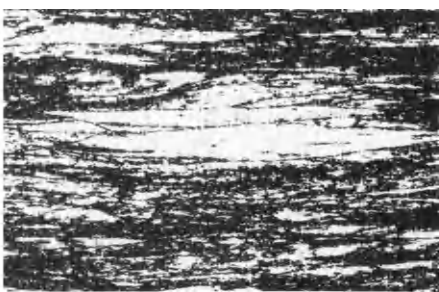
(b)

10C · 5Nb (or 0.10% C – 0.05% Nb)



(c)

10C · 5Nb (or 0.10% C – 0.05% Nb)



(d)

10C · 5Nb (or 0.10% C – 0.05% Nb)

200 μm

Figure 3.3 Partially recrystallized  $\gamma$  grains and elongated unrecrystallized  $\gamma$  grains in successive hot-reductions: (a) after 5th reduction at 965° C of successive reductions from 1000° C; (b) after 5th reduction at 960° C of successive reductions from 1000° C; (c) after 8th reduction at 900° C of successive reductions from 1150° C; (d) after 8th reduction at 860° C of successive reductions from 1000° C. Specimens are those for Table 3.1. (After Sekine and Maruyama<sup>2</sup>)



### 3.1 Metallurgical changes during and after constant-rate hot-deformation

As shown in Chapter 2,  $\gamma$  undergoes work-hardening, dynamic recovery and dynamic recrystallization corresponding to the amount of the deformation ( $\epsilon$ ) and the Zener–Hollomon parameter ( $Z$ ) during hot-deformation with a constant strain rate. The microstructures produced by these processes are unstable. Furthermore, structural changes take place during holding at temperature, aircooling from temperature and sometimes even during quenching after deformation. These static restoration processes after deformation are: (1) static recovery; (2) abnormal grain growth by strain-induced grain boundary migration; (3) classical static recrystallization; and (4) meta-dynamic or postdynamic recrystallization. When recrystallization is complete, further grain growth takes place to reduce the grain boundary area per unit volume. The work-hardened and dynamically recovered  $\gamma$  is softened by static recovery and static recrystallization with time at rates which depend on the prior deformation conditions and the holding temperature or the cooling rate after deformation. Static recrystallization can start when strain exceeds the critical value  $\epsilon_{CS}$  determined by the prior deformation conditions and the prior grain size. It has the incubation time for nucleation, during which only static recovery goes on. According to Sellars,<sup>9</sup> who examined various reported data, the recrystallization time decreases with increasing strain and deformation temperature,<sup>10,11</sup> (Figure 3.4) and the recrystallized grain size is refined with increasing strain<sup>12,13</sup> (Figure 3.5), in the lower strain region.

The observations by Djaic and Jonas<sup>11</sup> shown in Figure 3.4 indicate that abrupt changes in recrystallization time from strain-dependence to independence take place at the strains a little smaller than  $\epsilon_P$  ( $\epsilon_P$  is the peak strain shown in Figure 2.10(b), page 32). The similar critical strains over which recrystallized grain sizes become independent to applied strain, are also observed<sup>13</sup> in Figure 3.5. Although these critical strains are, of course, smaller than the critical strains for the steady dynamic recrystallization  $\epsilon_S$ , the recrystallization time and the recrystallized grain size are the same as those after straining over  $\epsilon_S$ . These abrupt changes correspond to the occurrence of metadynamic recrystallization without an incubation time and the critical strain may be related to the strain expected for the start of dynamic recrystallization  $\epsilon_C$ .<sup>9,11</sup> It arises because pre-existing recrystallization nuclei are present in the deformed structure by the onset of dynamic recrystallization,<sup>11</sup> as well as just after the straining over  $\epsilon_S$ .<sup>11</sup>  $\epsilon_C$  is of around  $0.7\epsilon_P$  as shown in Chapter 2, and Sellars says that the critical strains in recrystallization time in Figure 3.4 are around  $0.8\epsilon_P$  and those in recrystallized grain size in Figure 3.5 are a little greater than  $0.8\epsilon_P$ .<sup>9</sup> He named the strain of the intersection in Figure 3.5 over which the size of statically recrystallized grains becomes independent to applied strain  $\epsilon^*$ . Therefore, classical static recrystallization starts from a work-hardened and statically recovered structure after straining to the range from  $\epsilon_{CS}$  to  $\epsilon_C$ , and metadynamic recrystallization occurs starting from the partly or steadily recrystallized structure by dynamic recrystallization after straining over  $\epsilon_C$  or  $\epsilon^*$ . If there is a significant difference between  $\epsilon_C$  and  $\epsilon^*$ , classical static recrystallization and metadynamic recrystallization occur side-by-side after straining to the range from  $\epsilon_C$  to  $\epsilon^*$ .<sup>11</sup> There is another interpretation, namely that these two types of static recrystallization occur respectively in the work-hardened part and in the dynamically recrystallized part after straining to the

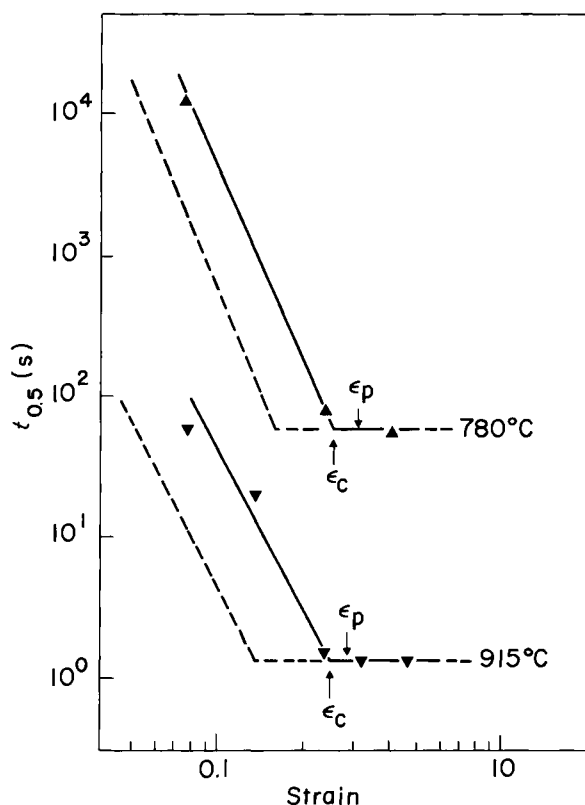


Figure 3.4 Dependence of time for 50% restoration by recrystallization on strain. (After Djaic and Jonas<sup>11</sup>)

range (II) from  $\epsilon_c$  to  $\epsilon_s$  in Figure 2.10(b).<sup>11</sup> The more consistent observations on these recrystallization behaviours using the same materials are necessary to give a satisfactory explanation on the transition in the recrystallization behaviours from strain-dependence to independence, though it may be a gradual transition.<sup>9</sup>

The rate of metadynamic recrystallization is fast and sometimes it completes during quenching after deformation.<sup>14,15</sup> It is a kind of static recrystallization, although it starts from a dynamically recrystallized structure. The grain structure is equiaxed and fairly uniform, has straight grain boundaries, and contains annealing twins, similar to the structure statically recrystallized by the nucleation and growth mechanism but different from the dynamically recrystallized structure. The grain size is determined only by  $Z$ ,<sup>9,16,17,18</sup> similar to the size of dynamically recrystallized grains, but increased compared with it.<sup>14,15</sup>

Sellars further proposed tentatively the following relations for the dependence of the critical strain for metadynamic recrystallization  $\epsilon^*$ , the recrystallization time  $t_{0.5}$  and the recrystallized grain size  $d$  on the deformation conditions and initial grain size  $d_0$ , after the examination of available reported data mainly by constant-rate deformation.<sup>9</sup>

$$\epsilon^* = A d_0^{0.67} Z^{0.15} \quad (3.1)$$

$$Z = \dot{\epsilon} \exp (Q_{\text{def}}/RT) \quad (3.2)$$

where  $Q_{\text{def}}$  is the activation energy for hot-deformation and of around 312 kJ/mol for carbon–manganese steels.

$$t_{0.5} = B d_0^2 \epsilon^{-4} \exp (Q_{\text{rex}}/RT) \quad (\epsilon_{\text{CS}} \leq \epsilon \leq \epsilon^*) \quad (3.3)$$

$$t_{0.5} = 4.24 \times 10^{13} B Z^{-0.6} \exp (Q_{\text{rex}}/RT) \quad (\epsilon \geq \epsilon^*) \quad (3.4)$$

where  $Q_{\text{rex}}$  is the activation energy for recrystallization and of around 300 kJ/mol for carbon–manganese steels.

$$d = C d_0^{0.67} \epsilon^{-1} \quad (\epsilon_{\text{CS}} \leq \epsilon \leq \epsilon^*) \quad (3.5)$$

$$d = 3.6 \times 10^3 C Z^{-0.15} \quad (\epsilon \geq \epsilon^*) \quad (3.6a)$$

It is noteworthy that the strain rate does not influence the recrystallization rate<sup>10</sup> and also that the deformation temperature does not have a significant effect on the size of recrystallized grains in static recrystallization.<sup>12,13</sup> There has been no investigation on the strain-rate dependence of statically recrystallized grain size at the strains below  $\epsilon^*$ ,

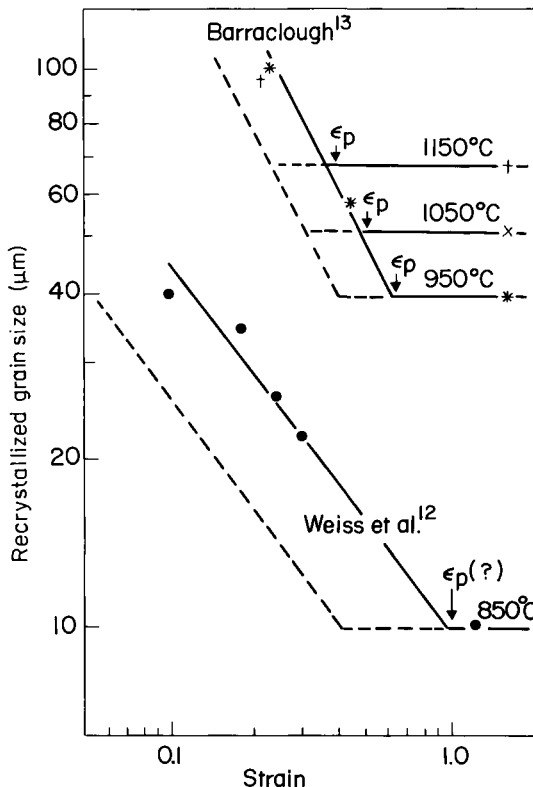


Figure 3.5 Dependence of statically recrystallized grain size on strain. (After Sellars<sup>9</sup>)

although Sellars proposed Equation (3.5) in which  $Z$  has no effect on the statically recrystallized grain size according to the strain rate independence of recrystallization time.<sup>10</sup> The critical strain for static recrystallization ( $\epsilon_{CS}$ ), i.e. the lower limit of strain to which Equations (3.3) and (3.5) are applicable, also has not been studied systematically by constant-rate deformation.

The following relation similar to Equation (3.6a) has been reported on the size of metadynamically recrystallized grains of copper<sup>16,17</sup> nickel and zone-refined  $\alpha$  iron<sup>17</sup> where  $\sigma_s$  is the steady-state flow stress (Figure 3.6):

$$d^{-1} \propto \sigma_s \propto \log Z \quad (\epsilon \geq \epsilon_s) \quad (3.6b)$$

It is considered that there is another critical deformation condition for abnormal grain growth by strain-induced grain-boundary migration at strains below  $\epsilon_{CS}$ , whose completion is prolonged even in higher temperatures.<sup>12</sup> Very little has been reported on this subject.

Once recrystallization is complete, grain growth takes place at a rate which is a function of time, temperature and, probably, starting grain size and steel chemistry. A few reported data appear to show that there is a following relation in grain growth after static recrystallization:

$$d^l = d_{\text{rex}}^l + D d_{\text{rex}}^m t^n \exp(-Q_{gg}/RT) \quad (3.7)$$

Sellars proposes that  $l=10$ ,  $m=0$ ,  $n=1$  and  $Q_{gg}=400$  kJ/mol for short times in higher temperatures,<sup>19</sup> but emphasizes that the evaluated growth rate is considered to be too

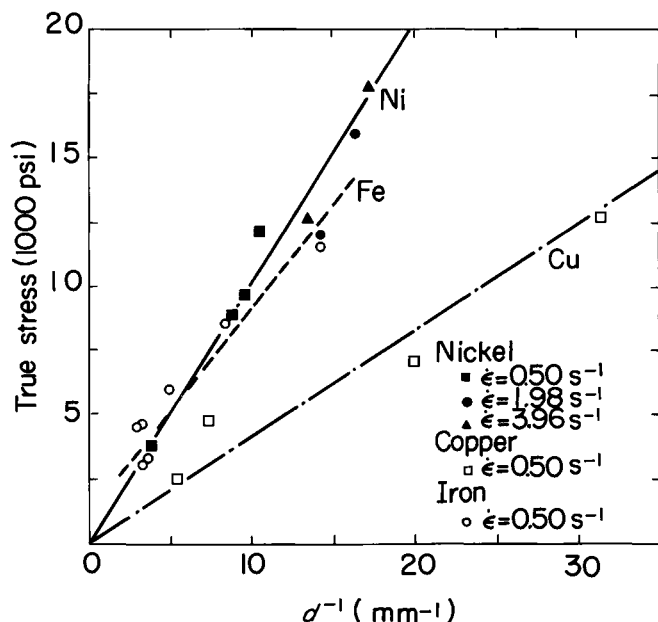


Figure 3.6 Relation between high-temperature strength and recrystallized grain size. (After Tegart<sup>17</sup>)

high at the final stage of rolling<sup>9,19</sup> where starting grain sizes  $d_{\text{rex}}$  are small and temperatures low. The data available at present do not allow such a relationship to be derived with any certainty, and considerable further work is required on this subject.<sup>9</sup>

### 3.2 Dynamic and metadynamic recrystallization by rolling hot-deformations

In rolling deformation, the strain rate is not constant during the period of a hot reduction but usually decreases with the progress of deformation in the commercial rolling by large-diameter rolls as shown in Figure 3.7, which might make the occurrence of dynamic recrystallization easy. The equivalent strain  $\varepsilon$  and strain rate  $\dot{\varepsilon}$  ( $\text{s}^{-1}$ ) during the period of a reduction, and the equivalent mean strain rate throughout a reduction ( $\bar{\varepsilon}$   $\text{s}^{-1}$ ) can be evaluated as follows:<sup>19,20</sup>

$$\varepsilon = \frac{2}{\sqrt{3}} \ln \frac{H}{h + 2R(1 - \cos \theta)} \quad (3.8)$$

$$\dot{\varepsilon} = \frac{2}{\sqrt{3}} \cdot \frac{\pi}{30} \cdot N \cdot \frac{2R \sin \theta}{h + 2R(1 - \cos \theta)} \quad (3.9)$$

$$\bar{\varepsilon} = \frac{2}{\sqrt{3}} \cdot \frac{\pi}{30} \cdot N \sqrt{\frac{R}{H}} \cdot \frac{1}{\sqrt{r}} \ln \frac{1}{1-r} \quad (3.10)$$

$$r = \frac{H-h}{H} \quad (r < 1) \quad (3.11)$$

where  $N$  and  $R$  are the rotating speeds in revolutions per minute and the radius of rolls  $H$  and  $h$  are the slab thicknesses before and after the reduction,  $r$  is the draught of the reduction and  $\theta$  is the angle from the end point of the reduction.

The effect of a varying strain rate during a deformation test on recrystallization behaviour has been reported for a ferritic stainless steel by Sah and Sellars.<sup>21</sup> Three specimens were hot-deformed under conditions of: (1) a constant; (2) an increasing; and (3) a decreasing, strain rate respectively, but at the same mean strain rate during the tests to the same strain over  $\varepsilon_p$  for the constant-rate deformation.  $\varepsilon_p$  was not observed under the condition of the increasing strain rate. In the case of the decreasing rate, it was observed at the strain greater than  $\varepsilon_p$  for the constant rate where the strain rate was still higher than the constant or the mean strain rate, the peak stress  $\sigma_p$  was higher in the decreasing rate deformation. The average size of statically recrystallized grains obtained during holding at the deformation temperature showed that systematic differences were maintained through the whole time lapse from small fractions recrystallized to complete recrystallization. The grain size for the increasing strain rate was finest and that for constant strain rate was coarsest, i.e. it showed a good correlation with the peak stress attained during the deformation. Conversely, the recrystallization rate and the growth rate were largest for the increasing strain rate and smallest for the decreasing rate, with the constant rate giving an intermediate value

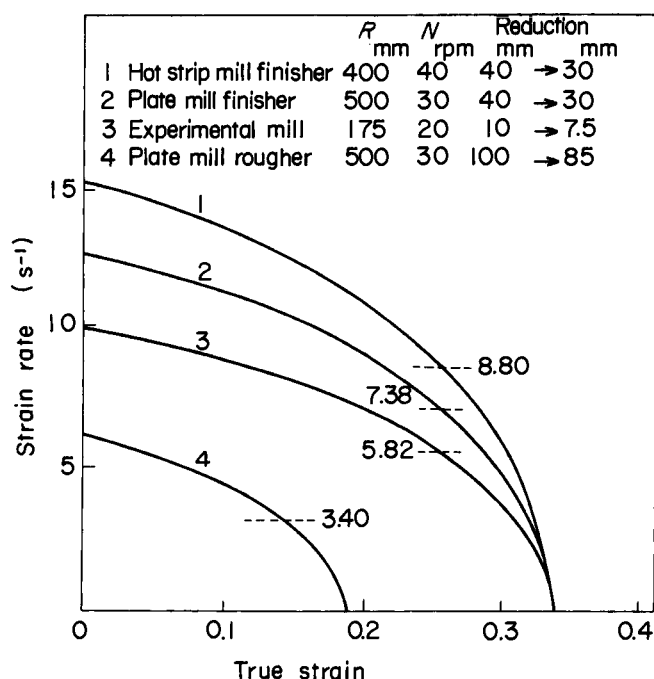


Figure 3.7 Change in strain rate during period of a rolling reduction in various rolling conditions (mean strain rate)

which showed a correlation with the strain rate prevailing in the last few per cent of the deformation.

It is considered that  $\varepsilon_p$  and  $\sigma_p$  in the decreasing strain rate deformation might be smaller and the recrystallized grain size might be coarser than those in the constant rate deformation, when the experiments had been carried out in conditions having a much higher value of  $Z$ . Even in this case, the order of the rate of recrystallization and growth might not be changed. This research result is considered to show the risk in the estimation of the recrystallization behaviours in rolling deformation by using  $\bar{\varepsilon}$  from those in constant-rate deformation.

The recrystallization behaviours of  $\gamma$  of steels in Table 3.1 were observed on the small slabs having large cooling rates, ice-brine quenched 7 s after the successive reductions with the constant time intervals of 7 s.<sup>2</sup> The representative change in the recrystallized grain size by successive reductions is shown in Figure 3.1. These rolling experiments were carried out with successive reductions of considerably higher amounts and considerably lower mean strain rates by using a small experimental mill.<sup>2</sup> Such rolling conditions are considered to be favourable to cause dynamic recrystallization. The grain sizes of the specimens in Table 3.1 were offered to examine the possibility of dynamic recrystallization in rolling reduction by using Equation (3.6b).

Figure 3.8 shows that almost all the grain sizes of niobium and silicon-manganese steels after the successive reductions can be expressed by simple functions of only  $\bar{Z}$  values for the respective last reductions, e.g. Equation (3.6b), independent of the grain size before the reduction or the history of the preceding reductions, where  $\bar{Z}$  has been evaluated by using 270 kJ/mol of the activation energy of self-diffusion of  $\gamma$  iron<sup>22</sup> and

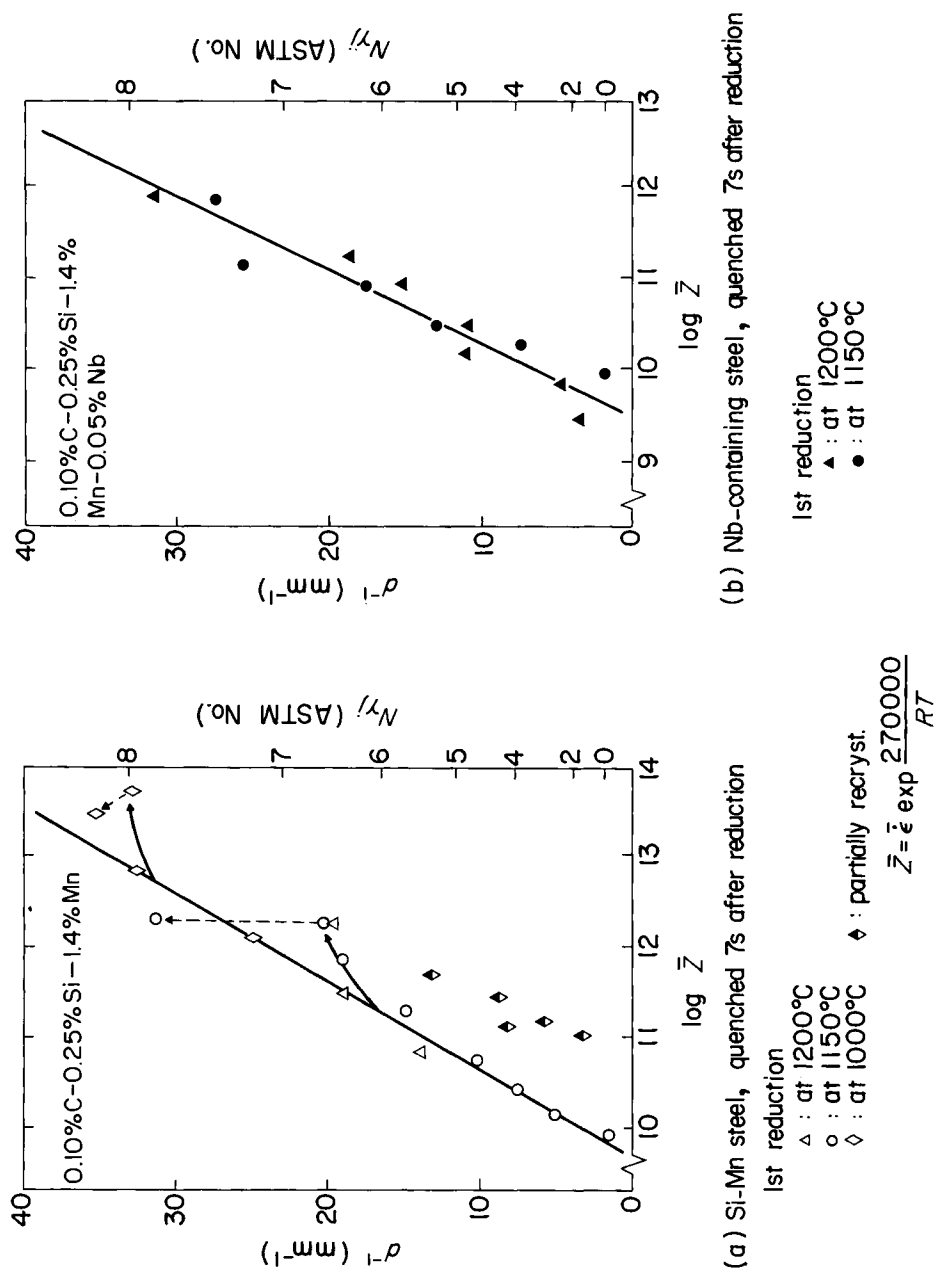


Figure 3.8 Relation between  $\bar{Z}$  and recrystallized  $\gamma$  grain size. (After Sekine and Maruyama<sup>2</sup>) Original data are taken from results for Table 3.1

Equation (3.10) for  $\bar{\epsilon}$ . Three grain sizes of the silicon–manganese steel after the final reductions are coarser than those expected from their reduction conditions and the linear relationship, which is shown by solid arrows in Figure 3.8(a). Such deviations from the straight line are not clear in Figure 3.8(b) for the niobium-containing steel by the scattering of data,\* but also found in the successive reductions of another nitrogen-reduced niobium-containing steel having a decreased pancaking temperature.<sup>23</sup> By decreasing the rolling speed of only the final reductions for the silicon–manganese steel to one-half, the obtained grain sizes approached a straight line, as shown by dotted arrows.<sup>2</sup> The results are well explained by the strain-rate dependence of the critical strains for dynamic and metadynamic recrystallization shown in Chapter 2 and Equation (3.1).

The one-pass reductions having high values of  $\bar{Z}$  similar to those in the final stage of successive reductions on the coarse-grained specimens, gave unrecrystallized structures or recrystallized grains coarser than the values expected from the linear relationship in Figure 3.8(a).<sup>23</sup> The results are also well interpreted in terms of the starting grain size dependence of the critical strains for dynamic and metadynamic recrystallization as shown in Equation (3.1). The attainment of the successive refinement of recrystallized grains by the preceding reductions<sup>24</sup> is considered to be also necessary to make possible the further refinement by the recrystallization mechanism giving the linear relation in Figure 3.8.

Supplementary experiments in which the specimens reduced in the same reduction history were quenched 1 s after, 7 s after and from the temperature just above  $A_{r3}$ , showed no distinct grain growth during cooling at least from 1 s after the reduction over the experimental error.<sup>2</sup>

On these experimental results, the recrystallization behaviour in which the reciprocal recrystallized grain size is defined only by a simple linear function of  $\log \bar{Z}$ , can be considered to be metadynamic recrystallization starting from structures partly or steadily restored by dynamic recrystallization during the reductions. Hereafter, this recrystallization behaviour is referred to as ‘dynamic’, and another mechanism which gives recrystallized grains coarser than those expressed by the straight line in Figure 3.8 is referred to as ‘static’. The recrystallized grain size  $d^{-1}$  ( $\text{mm}^{-1}$ ) of the silicon–manganese steel given by the straight line in Figure 3.8(a) is expressed as:

$$1/d = -94 + 9.7 \log \bar{Z} \quad (r \geq r_{\text{cd}}) \quad (3.12)$$

where  $Q_{\text{def}}$  is 270 kJ/mol.

### 3.3 Temperature–reduction–recrystallization

On the critical strain for static recrystallization  $\epsilon_{\text{CS}}$ , the refinement of  $\gamma$  grains by static recrystallization and the transition from static to dynamic recrystallization, the investigations have been more thoroughly by hot-rolling than by hot-tension or compression.

Figure 3.9 shows the recrystallization behaviours of  $\gamma$  grains coarsened by reheating to 1250°C in the silicon–manganese steel of Figures 3.1 and 3.8<sup>4,23</sup> and a niobium-

\* The larger scattering of data in the niobium-containing steel may be attributed to the difference in the precipitation behaviours of niobium carbonitrides<sup>14</sup> during successive reductions among the different series of experiments.



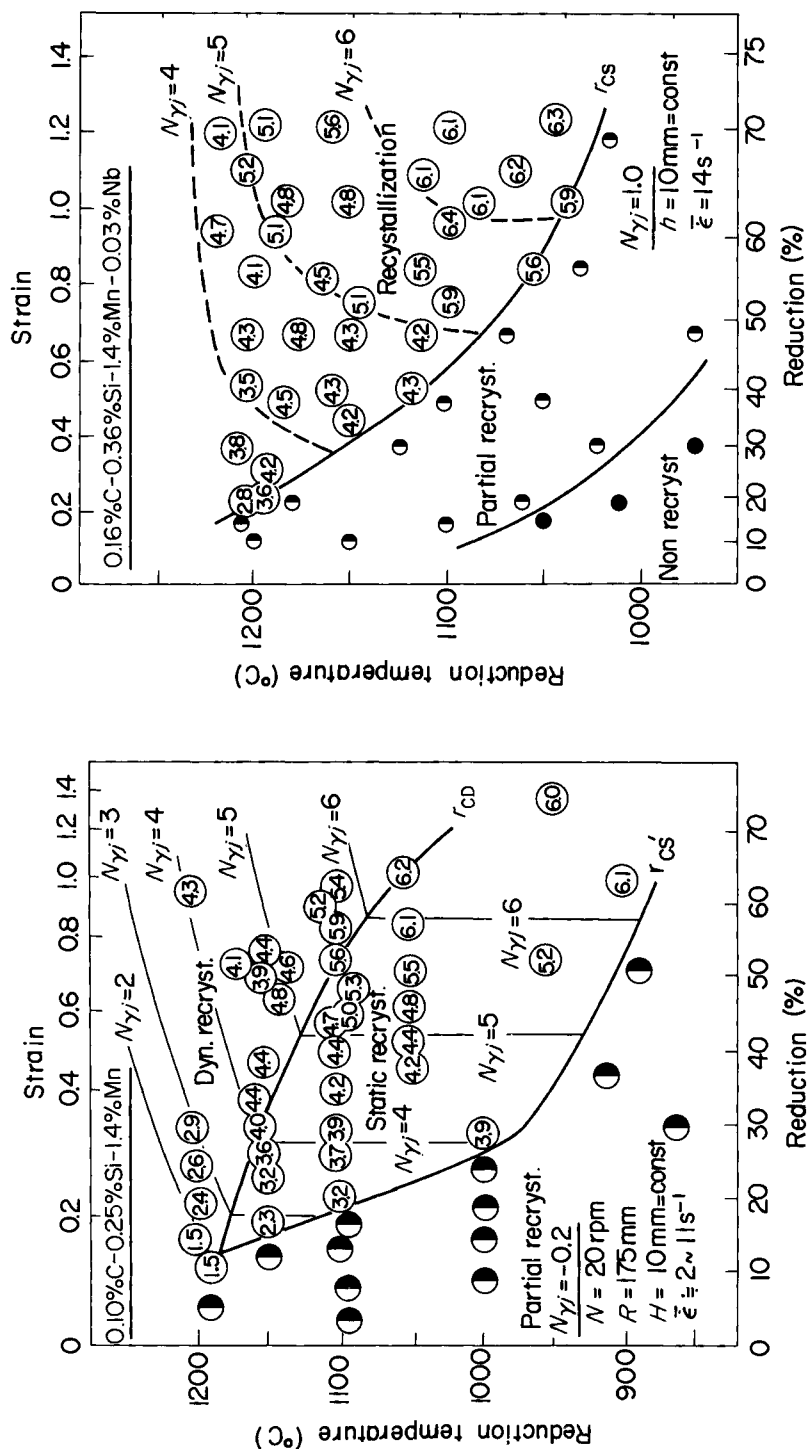


Figure 3.9 Temperature-recrystallization diagram of hot-rolled  $\gamma$  grains, where slab reheating temperature is 1250° C;  $N_{\gamma}$  is  $\gamma$  grain size before reduction;  $N_{\gamma}$  is recrystallized  $\gamma$  grain size. Figures in circles: observed  $N_{\gamma}$ ; (a) silicon-manganese steel quenched 1 s after reduction<sup>4</sup>; (b) niobium-containing steel, quenched 3 s after reduction<sup>25</sup> (After Sekine *et al.*<sup>4</sup> and Kozasu *et al.*<sup>25</sup>)

containing steel<sup>25</sup> respectively 1 s or 3 s after one-pass rolling. In these experiments, grain sizes before the reduction,  $N_{yi}$ , the thicknesses of slabs before<sup>4,23</sup> or after<sup>25</sup> the reduction,  $H$  or  $h$ , and the rotating speeds of rolls,  $N$ , are held constant. The mean strain rates increase with the increasing amount of hot-deformation. The figures in circles are ASTM grain size numbers of recrystallized grains,  $N_{yj}$ .

The temperature and the amount of a reduction strongly influence recrystallization behaviour. The whole specimen can be recrystallized 1 s or 3 s after a hot-deformation when the percentage reduction,  $r$ , is over the critical amount at a given temperature. The critical reduction for recrystallization  $r_{CS}$  increases with a decrease in the reduction temperature. Though the initial grain size is finer, which facilitates recrystallization,<sup>24</sup> the time interval from the hot-deformation to quenching is larger; the thicknesses of specimens after reductions are generally larger in niobium-containing steels (Figure 3.9(b)) than those in silicon–manganese steels (Figure 3.9(a)).  $r_{CS}$  is always larger in the niobium-containing steel. It means that niobium addition retards recrystallization.

Figure 3.9 clearly shows that there are two types of recrystallization behaviours in both steels. Equi- $N_{yj}$ -contours change their gradients at their half points. In the lower reduction and lower temperature region, the recrystallized grain size becomes finer with increasing the amount of a reduction and almost independent to the reduction temperature, like primary recrystallization after cold reduction. In the higher reduction and higher temperature region, it is insensitive to the amount of a reduction, primarily determined by the reduction temperature and refined with decreasing the temperature.

The grain sizes in the latter region of the silicon–manganese steel (Figure 3.9(a)), can be well described by the  $\bar{Z}$  values evaluated from their reduction conditions and Equation (3.12) giving the linear relation in Figure 3.9(a), i.e. the equi- $N_{yj}$ -curves in this region correspond to the equi- $\bar{Z}$ -contours. It is considered that, in this region where the recrystallized grain size can be determined only by  $\bar{Z}$ , the recrystallization nuclei have been prepared dynamically during the reduction, and fast static recrystallization or metadynamic recrystallization completes during aircooling of 1 s after reduction and quenching. The region is assigned to the region of dynamic recrystallization in Figure 3.9(a). The critical reduction for the transition of recrystallization behaviours is given as  $r_{CD}$  in Figure 3.9(a), which also increases with decreasing the reduction temperature, similar to  $\varepsilon^*$  shown in Equation (3.1).  $r_{CD}$  may correspond to  $\varepsilon^*$  in constant rate deformation over which the time for static recrystallization and the recrystallized grain size cease their dependence on strain<sup>9</sup> as shown in Figures 3.4 and 3.5.  $r_{CD}$  is thought to be independent to the time to quenching and the cooling rate down to quenching or the specimen thickness.

In the lower reduction and lower temperature region, the size of recrystallized grains cannot be determined by a function of only  $\bar{Z}$ , but can be refined by increasing the reduction and being independent of the reduction temperature similar to Equation (3.5) for constant-rate deformation. The main feature of recrystallization in this region is classical static recrystallization and nucleation and growth processes may succeed in deformed  $\gamma$  during the short time interval to quenching. When the thicknesses of specimens are larger or the time interval to quenching is longer, the range must be spread to the lower temperature and lower reduction side. Therefore, the critical reduction for

recrystallization is a function of slab thickness and time interval between the reduction and the quenching, so it is shown as  $r_{CS}$  by the dashed line in Figure 3.9.

The primary nucleation sites of recrystallized grains are the  $\gamma$  grain boundaries. Figure 3.10 shows the effect of the grain size before the reduction,  $N_{\gamma i}$ , on the recrystallization behaviours of the silicon-manganese steel.<sup>4,23</sup> By reducing the starting grain size,  $r_{CS}$  and  $r_{CD}$  are both reduced, i.e. static<sup>24</sup> and dynamic recrystallization can occur more easily, which is the same as in constant rate deformation as shown in Equations (3.1) and (3.3). The similar starting grain size dependence of  $r_{CS}$  has been reported for niobium-containing steels<sup>12,25,26</sup> as shown in Figure 3.11.<sup>25</sup> The critical reduction temperature for recrystallization  $T_C$  or the pancaking temperature  $T_P$  is not only influenced by steel chemistry, the amount of the reduction and the thickness of the slab, but by the draught schedule from the slab reheating to the reduction just prior to the relevant reduction, which determines the size of recrystallized grains just before the reduction. It is also to be written as  $T_{CS}$ .

Figure 3.10 further shows that the equi- $N_{\gamma j}$ -contours are common for all the starting grain size in their regions of dynamic recrystallization. Although dynamic recrystallization can occur at a smaller reduction by decreasing the starting grain size, the size of metadynamically recrystallized grains is determined only by the temperature and the

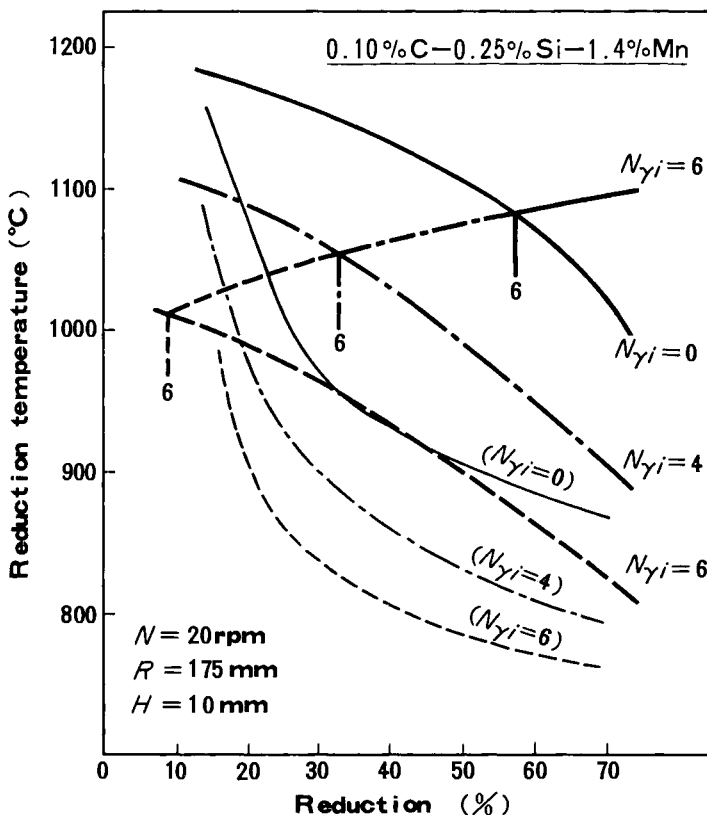


Figure 3.10 Effects of starting grain size on critical reductions for static and metadynamic recrystallization of  $\gamma$  in silicon-manganese steel. Starting grain size was changed by rolling at higher temperatures after reheating at 1250°C. (After Sekine *et al.*<sup>4</sup>)

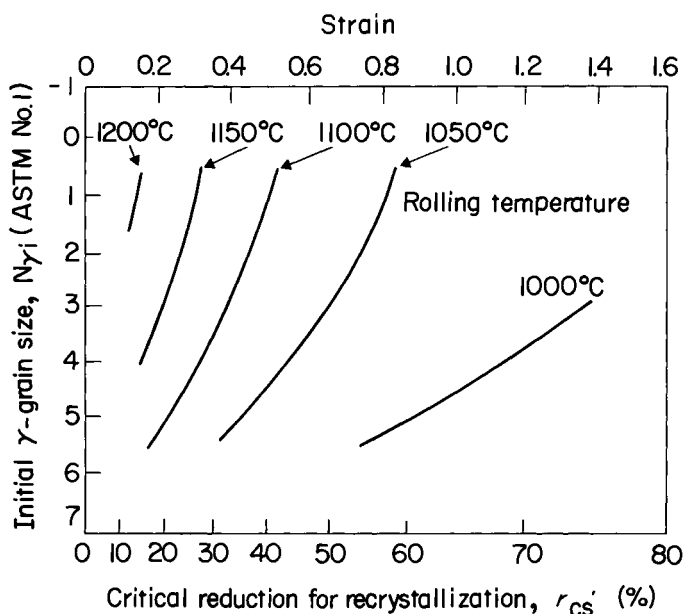


Figure 3.11 Effect of starting grain size on critical reduction for static recrystallization of  $\gamma$  in niobium-containing steel. Starting grain size was changed by rolling at higher temperatures after reheating at 1250°C. (After Kozasu *et al.*<sup>26</sup>)

mean strain rate of the reduction, independent of the starting grain size and almost to the amount of the reduction. The tendency is also about the same to that which Equation (3.6) shows for constant rate deformation. An increase in the amount of the rolling reduction slightly refines metadynamically recrystallized grains only through the increase in the mean strain rate of the reduction, as given by Equation (3.10).

Conversely the size of statically recrystallized grains is almost independent of the reduction temperature and is refined by decreasing the starting grain size and increasing the draught,<sup>1,24-27</sup> similar to Equation (3.5) for constant rate deformation.

A little but significant difference between Equation (3.1) and Figure 3.9 or 3.10 is in the temperature dependence of  $\varepsilon^*$  and  $r_{CD}$ . Equation (3.1) ought to give concave  $r_{CD}$  curves to Figures 3.9 and 3.10, where the  $r_{CD}$  curves follow Figure 3.14. The quantitative comparison containing the discussion on the above difference between Figures 3.9 and 3.10 and the above-mentioned relations by Sellars is made later.

The transition of recrystallization behaviour from static to dynamic is shown in another way in Figure 3.12<sup>4,23</sup> which has been obtained by using some of original data for Figure 3.10. By increasing the amount of a reduction holding the starting grain sizes and the reduction temperatures constant at the respective levels, the inverse diameter of statically recrystallized grains increases respectively corresponding to their experimental conditions. Further increase in the draught over their respective  $r_{CD}$  values changes the direction of the increase in values of  $1/d$ , and the size of recrystallized grains becomes finer along the single common straight line for metadynamic recrystallization through the increase in mean strain rate. Although only three cases are shown in Figure 3.12, numerous different lines showing the changes in sizes of the statically recrystallized grains can be drawn, e.g. by similar experiments under the

other combinations of starting grain sizes and reduction temperatures, or by changing the rotating speed of rolls holding other experimental conditions constant. When the various reductions having a same  $\bar{Z}$  value are applied, metadynamic recrystallization gives the finest grains among them.

Figure 3.5, which shows the dependence of the recrystallized grain size on strain and deformation temperature in constant rate deformation, corresponds to Figures 3.9 and 3.10 for rolling reduction. The broken lines in Figures 3.4 and 3.5, added by the authors according to Equations (3.3)–(3.6), correspond to the relations for the starting grain sizes finer than those of the solid lines.

Sellers has given provisionally the constants in the above-mentioned relations for carbon–manganese steels by rearranging the reported results as follows:<sup>9</sup>

$$A \text{ in Equation (3.1)} = 9.8 \times 10^{-4} (\mu\text{m}^{-0.67} \text{ s}^{-0.15})$$

$$B \text{ in Equations (3.5) and (3.6)} = 0.5 (\mu\text{m}^{0.33})$$

The quantitative comparisons of recrystallization behaviours between those reported

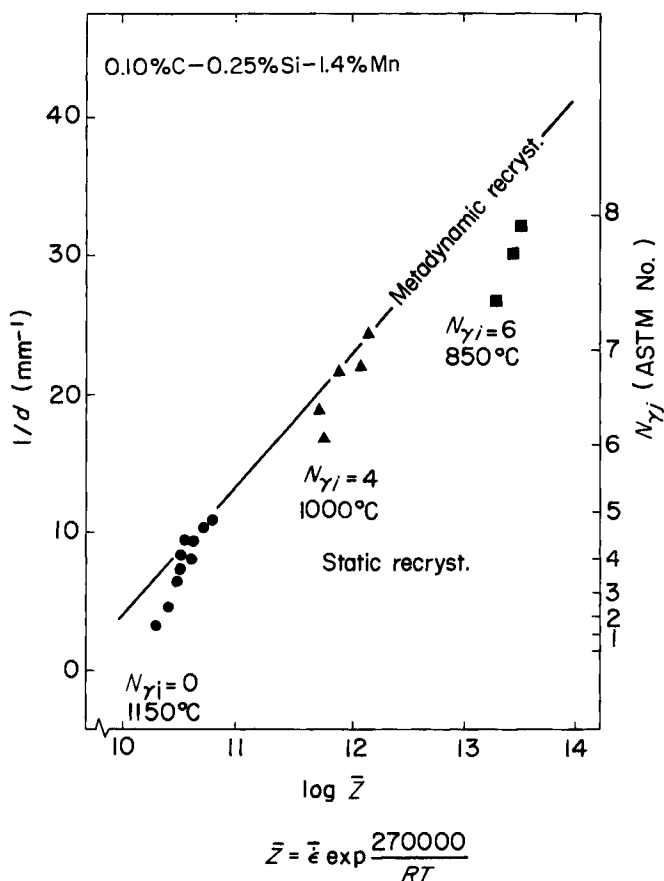


Figure 3.12 Transition of recrystallization behaviours from static to metadynamic by increasing a draught in silicon–manganese steel. (After Sekine *et al.*<sup>4</sup>)

for constant-rate deformation and for rolling reduction, are illustrated in Figures 3.13 and 3.14. Metadynamically recrystallized grain sizes are compared in Figure 3.13, where the line for constant rate deformation given by Equation (3.6) and all the ob-

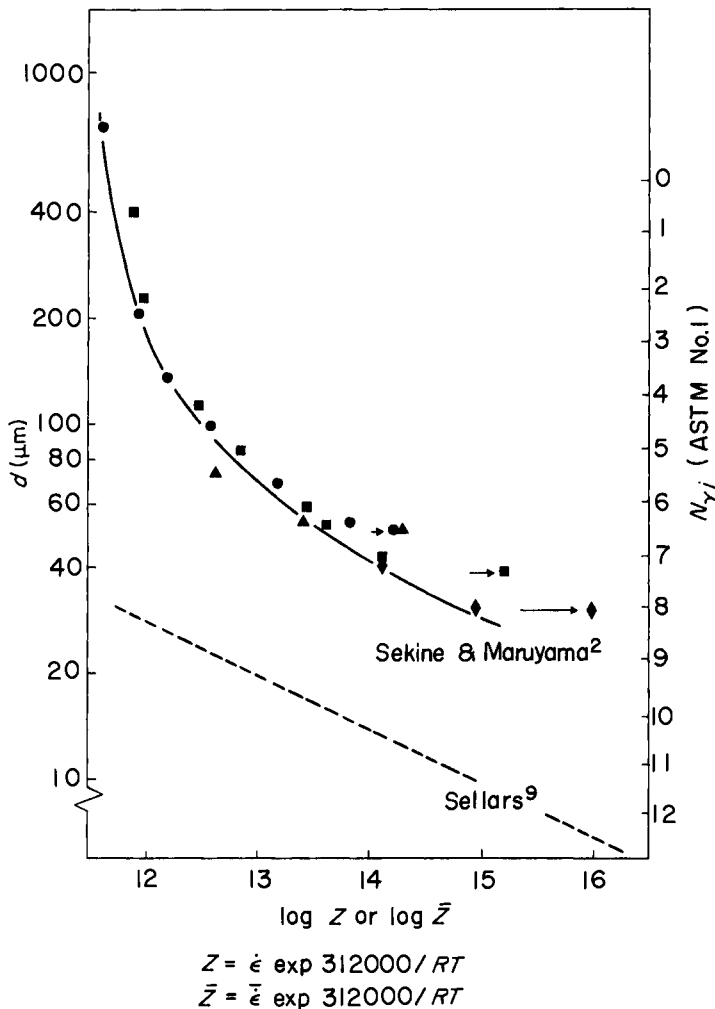


Figure 3.13 Comparison of  $\bar{Z}$ - or  $Z$ -dependence of metadynamically recrystallized grain sizes between rolling deformation (solid curve) – after Sekine and Maruyama,<sup>2</sup> and constant-rate deformation (broken line) – after Sellars<sup>9</sup>

served grain sizes given by open marks in Figure 3.8(a) by the rolling experiments are shown as a function of  $Z$  or  $\bar{Z}$  evaluated by using the same 312 kJ/mol for  $Q_{def}$  and the respective reduction conditions. Figure 3.14 illustrates the comparison of temperature–reduction–recrystallization diagrams for  $N_{yt}=4.0$  between that evaluated by using the above Sellars' relations for constant rate deformation and Figure 3.10 by rolling reduction. In Figure 3.14,  $\epsilon^*$  is converted to  $r_{CD}$  by using the

$$\text{relation } \epsilon^* = \frac{2}{\sqrt{3}} \ln \frac{1}{1 - r_{CD}}.$$

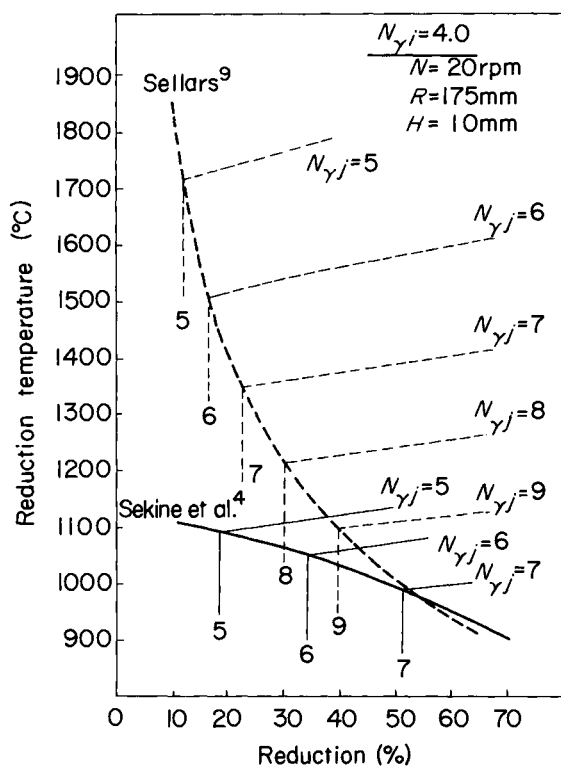


Figure 3.14 Comparison of temperature–reduction–recrystallization diagrams between rolling deformation (solid curves) – after Sekine *et al.*<sup>4</sup> and constant rate deformation (broken curves) – after Sellars<sup>9</sup>

The recrystallized grain sizes obtained by the rolling experiments are clearly coarser than those given by Sellars' relations and the difference becomes larger in the dynamic and the fine-grained static regions. However, the two relations for metadynamically recrystallized grain sizes – Equation (3.6) for constant rate deformation and the results by rolling deformation – are parallel in the greater  $Z$  region of fine grains in Figure 3.13. The already-mentioned difference in the curvatures of  $r_{CD}$  curves between them can be observed in Figure 3.14. It further shows that  $r_{CD}$  values obtained by the rolling experiments are much smaller than those given by  $\varepsilon^*$ , especially in the lower temperature and lower strain rate range.

The grain size difference in the fine-grained region may be explained partly by rapid grain growth down to quenching after the completion of recrystallization in the rolling experiments, as Sellars has evaluated.<sup>9</sup> Simple evaluation of grain growth by using Equation (3.7) and the numerical values given by Sellars,<sup>19</sup> show that the delayed quenching shifts equi- $N_{\gamma J}$ -contours in the dynamic region to the lower-temperature side and thereby apparent  $r_{CD}$  curves to the lower-reduction side especially in the higher-temperature range where the growth is the more accelerated. The smaller  $r_{CD}$  values and the coarser dynamically recrystallized grains in the rolling experiments in the higher-temperature region might be caused partly by the delayed quenching time and partly by assuming Equation (3.6b) is a criterion for the occurrence of metady-

dynamic recrystallization in the analysis of the results. These differences seem also to be contradictory to the results on the effects of strain-rate history on static recrystallization of a ferritic stainless steel,<sup>21</sup> described in Section 3.2. The ratio of the effective strain rate determining recrystallization behaviours to the mean strain rate in the rolling reduction, however, may be a function of deformation temperature, mean strain rate and further rolling shape factor,  $m$ , given by the following relation, which determines the strain rate history in a draught:

$$m = \frac{2\sqrt{R(H-h)}}{H+h} = \frac{\sqrt{R \cdot r}}{H} \left(1 - \frac{1}{2}r\right)^{-1} \quad (3.13)$$

The ratio might become smaller than one in the deformation of  $\gamma$  having a higher value of  $\bar{Z}$ . The rolling shape factor further determines the shear strain distribution in the through-thickness direction. Further detailed experimental approaches are required on the  $Z$ -dependence of the metadynamically recrystallized grain size and the effects of strain rate history and shear strain in a rolling deformation on recrystallization behaviour of  $\gamma$ .

Sellars and Whiteman<sup>19</sup> have proposed another  $Z$ -dependent relation (Equation (3.14)) different from Equation (3.5) for statically recrystallized grain size ( $\mu\text{m}$ ):

$$d = 25 \left( \frac{1}{6.7 \times 10^{-2}} \ln \frac{Z}{8.5 \times 10^9} \right)^{-\frac{1}{3}} \varepsilon^{-1} d_0^{\frac{1}{3}} (\varepsilon \leq \varepsilon_c) \quad (3.14)$$

Equation (3.14) gives equi- $N_{\gamma\gamma}$ -contours almost parallel to the temperature axis in the low temperature and low reduction region, and grain sizes finer than those evaluated by Equation (3.5) at the lower temperature range. However, the evaluated grain sizes in the higher temperature and higher reduction region become larger than those by Equation (3.5), sensitive to the reduction temperature and insensitive to the amount of the reduction, i.e. very similar to the dynamically recrystallized one. The equi- $N_{\gamma\gamma}$ -contours at the higher temperature side become parallel to those given by Equation (3.6a) and those of dynamically recrystallized grains in Figure 3.9 are between them.

Some studies by rolling experiments have reported that there are reduction-temperature-dependence<sup>27,28</sup> and strain-rate-dependence<sup>27</sup> in the statically recrystallized grain size. It seems, however, that a number of metadynamically recrystallized structures have been included in their analyses.

Towle and Gladman<sup>28</sup> have given the following relation to the recrystallized grain size of a type-304 austenitic stainless steel, where:

$$d = 2.24 \varepsilon^{-0.5} d_0 \bar{Z}^{-0.6} \quad (3.15)$$

if  $Q_{\text{def}}$  is 410 kJ/mol. They adjust the mean strain rates to be almost constant, and obtained the above  $\bar{Z}$ -dependence only from its temperature-dependence. When 312 kJ/mol given by Sellars for carbon–manganese steels<sup>9</sup> is adopted for  $Q_{\text{def}}$  and equi- $N_{\gamma\gamma}$ -contours for  $N_{\gamma\gamma} = 4$  are calculated by using Equation (3.15), it gives grain sizes comparable to those in Figure 3.10 in the neighbourhood of the  $r_{\text{CD}}$  curve, but finer in the static recrystallization region and coarser in the dynamic region. Further, it seems to



give a starting grain-size-dependence larger than that shown in Figure 3.10. Towle and Gladman also give a figure showing the relation of the time to 50% recrystallization and equivalent strain – similar to that of Figure 3.4 – which shows that the applied strains in their experiments seem to be confined only around  $r_{CD}$ .

Machida, Katsumata and Kaji<sup>27</sup> have given the following relation for calculating the recrystallized  $\gamma$  grain size of a niobium-containing steel obtained by quenching within 0.6 s after the reduction, and have shown that it is hardly affected by alloying elements. Equation (3.16) gives equi- $N_{\gamma j}$ -contours very similar to equi- $\bar{Z}$ -contours even in the lower temperature and lower reduction range, and the recrystallized grain size is intermediate between dynamically recrystallized grain sizes evaluated by using Equations (3.6) and (3.12) for various values of  $N_{\gamma i}$ :

$$N_{\gamma j} = -8.3\bar{\epsilon}^{-0.5} + \frac{1}{3}N_{\gamma i} - \frac{T}{100} + 23.5 \quad (3.16)$$

When Equation (3.16) is applied to the lower temperature and lower reduction range of static recrystallization in Figure 3.14, it gives grain sizes finer than those evaluated by using Equation (3.5). It seems that Equation (3.16) has been obtained mainly on meta-dynamically recrystallized specimens.

The above survey may mean that it is wise to assume that there has been no direct investigation on the strain-rate dependence of the grain size obtained by strictly static recrystallization, either by rolling or by constant-rate deformation, although the strain rate might have only a slight effect on the statically recrystallized grain size and its increase might not coarsen the recrystallized grains.

### 3.4 Controlled-rolling for refinement of recrystallized $\gamma$ grains

Figures 3.9 and 3.10 show that, when some one-pass reductions are applied at various temperatures, static recrystallization occurring after reductions at lower temperatures can give the grain size which is the finest and most stable to cope with the change in hot-deformation temperature. A deformation applied to the refined grain structure at some higher temperatures easily causes dynamic recrystallization, which tends to hinder further grain refinement. In such cases, decreasing the reduction temperature is advisable, because the metadynamically recrystallized grains are more refined by a reduction in the deformation temperature, and further grain refinement can be expected by rapid static recrystallization after the reduction at further-reduced temperatures. The main mechanism available for the positive refinement of recrystallized  $\gamma$  grains (recrystallization controlled rolling (RCR)<sup>4,23</sup>) should be static recrystallization.\*

Figure 3.15 (extracted from Figure 3.10) shows the reduction conditions to obtain the recrystallized grains finer than 5.0 in ASTM number starting from the grains of 4.0 in the silicon-manganese steels by using the experimental rolling-mill.<sup>4</sup> The conditions are in the region of higher reductions and lower temperatures than the equi- $N_{\gamma j}$ -contour of 5.0, which can be simplified to be in the hatched range in Figure 3.15, and

\* If  $r_{CD}$  in rolling reduction is as large as  $\epsilon^*$  in constant-rate deformation as shown in Figure 3.14, dynamic recrystallization may never take place, at least in plate-rolling, and only static recrystallization can be available for RCR.<sup>9,19</sup>

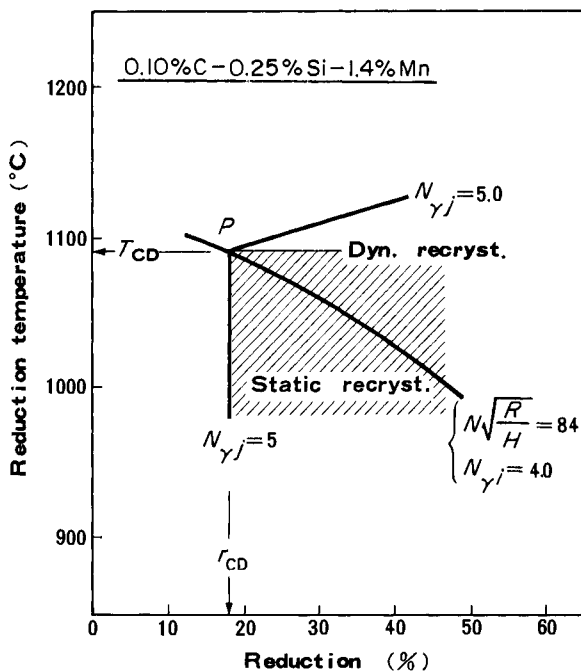


Figure 3.15 Lower critical reduction and upper critical reduction temperature to refine  $\gamma$  grains by recrystallization. (After Sekine *et al.*<sup>4</sup>)

generalized as follows. In order to obtain recrystallized grains finer than the required value  $N_{\gamma j}$  by a reduction starting from the structure of a given grain size  $N_{\gamma i}$ , the reduction must be applied in a higher draught at a lower temperature than  $r_{CD}$  and  $T_{CD}$  of the point P in Figure 3.15, which is the intersection of the  $r_{CD}$  curve for  $N_{\gamma i}$  with the equi- $\bar{Z}$ -contour corresponding  $N_{\gamma j}$ .

The critical reduction for the metadynamic recrystallization  $r_{CD}$  ought to depend not only on the starting grain size  $N_{\gamma i}$  and the reduction temperature  $T$ , but on the strain rate of the reduction  $\dot{\epsilon}$  as  $\dot{\epsilon}^*$  in constant-rate deformation.<sup>9</sup> The values of  $r_{CD}$  and  $T_{CD}$  obtained by using the experimental rolling-mill have to be translated to those in the rolling by commercial rolling-mills having different values of  $N\sqrt{R/H}$  in Equation (3.10), which are related to the mill capacities and determine strain rates. The dependence of  $r_{CD}$  on the strain rate or  $N\sqrt{R/H}$  has not been obtained by rolling experiments, although its  $N_{\gamma i}$  and  $T$  dependences are given in Figures 3.9(a) and 3.10. The relation of  $Z$ -dependence such as is shown in Equation (3.1) cannot be available, for it shows  $T$ -dependences different from those obtained by rolling experiments as shown in Figure 3.14. However, there are the following generally noticed relations (Equations (3.17) and (3.18)) between the critical strains for metadynamic and dynamic recrystallization in constant-rate deformation:<sup>9,15</sup>

$$\dot{\epsilon}^* \propto \dot{\epsilon}_p \propto \dot{\epsilon}_s \quad (3.17)$$

$$\dot{\epsilon}_p \text{ or } \dot{\epsilon}_s \propto \dot{\epsilon}^n \quad (3.18)$$

The dependence of  $\varepsilon_p$  or  $\varepsilon_s$  on  $\dot{\varepsilon}$  experimentally obtained in constant-rate deformations may be considered to be provisionally available for evaluation of the relation between  $r_{CD}$  and  $\bar{\varepsilon}$  when  $N_{\gamma i}$  and  $T$  are respectively held constant. In the reported stress-strain curves for different carbon-manganese steels by hot-torsion tests, the critical deformation for dynamic recrystallization,  $\varepsilon_p^{29}$  or  $\varepsilon_s^{30}$  shows the following strain-rate dependence, where  $n$  is almost constant-independent to  $T$  (and so  $N_{\gamma i}$ ) and the chemical composition of the steel.<sup>4</sup>  $n$  varies from 0.17 to 0.22,<sup>4</sup> which is slightly higher than 0.15 in Equation (3.1).

Using the linear relation between  $\bar{Z}$  and  $1/d$ , (Equation (3.12)), the numerical values of  $r_{CD}$  and  $T_{CD}$  in Figures 3.9(a) and 3.10, and the mean value of  $n$ , 0.195, the sets of  $r_{CD}$  and  $T_{CD}$  were evaluated graphically as functions of  $N\sqrt{R/H}$  for various combinations of the starting and the aimed-for grain sizes for the silicon-manganese steels.<sup>4</sup> An example is shown by the solid curves in Figure 3.16, which gives the critical rolling

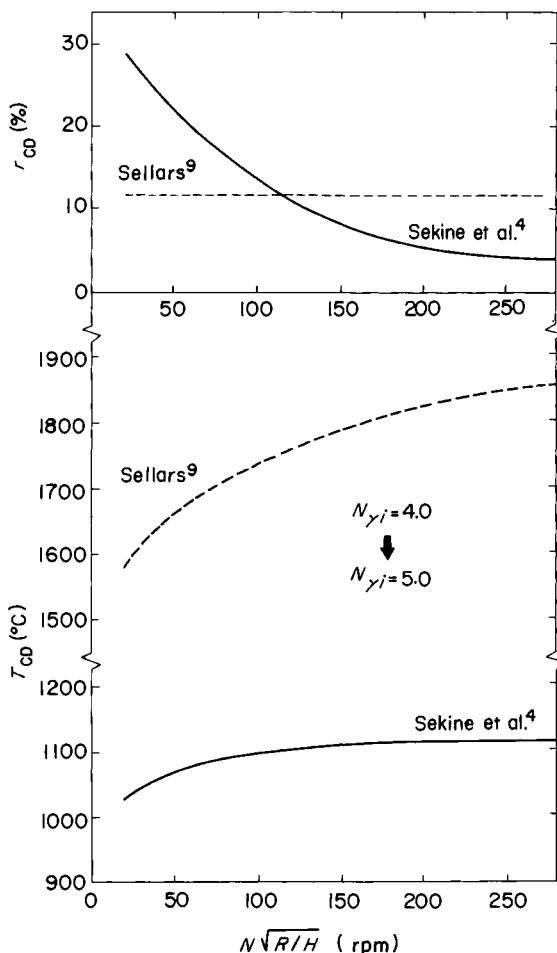


Figure 3.16 Comparison of  $N\sqrt{R/H}$ -dependence of critical rolling conditions for refinement of recrystallized  $\gamma$  grains of silicon-manganese steel between rolling deformation (solid curves) – after Sekine *et al.*<sup>4</sup> and constant rate deformation (broken curves) – after Sellars<sup>9</sup>

conditions to obtain  $N_{\gamma j} = 5.0$  starting from  $N_{\gamma i} = 4.0$ . When  $N_{\gamma i}$  is coarser than 4.0 these two curves shift to the higher-reduction side and to the higher-temperature side respectively, and when  $N_{\gamma j}$  is finer than 5.0 toward the higher-reduction side and the lower-temperature side. A reduction higher than  $r_{CD}$  at  $T_{CD}$  or a reduction of  $r_{CD}$  at temperatures higher than  $T_{CD}$  causes metadynamic recrystallization, and the former gives the recrystallized grains finer than the aimed size and the latter, coarser grains.

The solid curves in Figure 3.16 show that the increase in  $N\sqrt{R/H}$  reduces the value of  $r_{CD}$  and raises the value of  $T_{CD}$ , i.e. the increase in rolling speed holding the amount and the temperature of the reduction constant refines the statically recrystallized grains, which is the situation shown in Equations (3.14)–(3.16).

The results of the similar evaluation carried out by using Equations (3.5) and (3.6) by Sellars<sup>9</sup> are also shown in Figure 3.16 by the broken curves. The increase in  $N\sqrt{R/H}$  raises  $T_{CD}$  but does not change  $r_{CD}$ . The increase in rolling speed can refine the metadynamically recrystallized grains by increasing  $Z$  up to the switchover to the statically recrystallized grains, after which no grain refinement can occur as Equation (3.5) shows. The broken  $T_{CD}$  curve is significantly higher than the solid curve and conventional rolling temperatures, which leads to the view that dynamic recrystallization of  $\gamma$  cannot take place and the refinement of recrystallized grains proceeds by static recrystallization in conventional plate-rolling.<sup>9,19</sup>

The difference in the  $N\sqrt{R/H}$  dependence of two  $r_{CD}$  curves in Figures 3.16 is mainly caused by the difference in the temperature-dependence of  $r_{CD}$  (or  $\varepsilon^*$ ) shown in Figure 3.14. The  $r_{CD}$  curve, given up to the change in reduction temperatures, always gives the  $r_{CD}$  values decreasing with the increase in  $N\sqrt{R/H}$  as the solid curve in Figure 3.16.  $\varepsilon^*$  in Equation (3.1) gives the concave  $r_{CD}$  curve as shown in Figure 3.14 and originally has been obtained at the intersection of Equations (3.5) and (3.6), the former not having the fundamentally  $Z$ -dependence.<sup>9</sup> The solid curves in Figure 3.16 also have been obtained by assuming the mean strain-rate dependence of  $r_{CD}$  similar to that of  $\varepsilon_p$  or  $\varepsilon_s$  in constant-rate deformation. The strain rate in rolling deformation continues to decrease during a reduction, and even the mean strain-rate changes not only by the rotating speed of rolls, but by the ratio of  $R$  to  $H$ . There is no certification for the equivalent treatment of  $N$  and  $\sqrt{R/H}$  in expressing the strain-rate dependence of  $r_{CD}$  and for the adoption of the same value of  $n$  derived from the constant-rate experiments for the evaluation of the  $N\sqrt{R/H}$  dependence. Whether the discrepancy in Figure 3.16 is intrinsic to their respective forms of deformation or not is important for the application of research results to rolling practice; nevertheless, it is still unresolved because of the lack of direct research into the dependences of  $r_{CD}$  and statically recrystallized grain size on the rotating speed of rolls and  $R/H$  and on the strain-rate dependence of the statically recrystallized grain size after constant-rate deformation.

The successive change in the recrystallized grain size of silicon–manganese steel after each sequential pass can be estimated by using a series of figures such as Figure 3.16 or Equations (3.1)–(3.7),<sup>9</sup> when the initial grain size at reheating and the draught schedule are well defined. It must be stressed, however, that recrystallization after hot-deformation does not occur under all conditions, but it is necessary to apply a deformation larger than  $r_{CS}$  as shown in Figure 3.9 in order to cause static recrystallization. The evaluations on the silicon–manganese steel by using conventional draught schedules in real production mills and the solid curves of figures such as Figure 3.16,

have shown that the first reductions are usually smaller than the lower critical reduction  $r_{CD}$  for any grain refinement  $N_{\gamma j} \geq N_{\gamma i}$  when the  $\gamma$  grains are coarsened by reheating, e.g. to 1250° C, as Tanaka *et al.*<sup>31</sup> have pointed out on a niobium-containing steel. The grain sizes recrystallized at first cannot be estimated. These rolling conditions may correspond to those in the region for the partial recrystallization or the nonrecrystallization regions in Figure 3.9.<sup>31</sup>

Tanaka *et al.*<sup>31,32</sup> have shown that, when the first reduction less than  $r_{CS}$  is applied in the nonrecrystallized region in Figure 3.9, very coarse grains are locally produced due to strain-induced grain boundary migration, and they are not recrystallized after the successive reductions and transform into the coarse bainitic structure detrimental to impact properties. However, when the reductions per pass are less than  $r_{CS}$  but are of amounts sufficient to cause partial recrystallization during reduction time-intervals, are given from the first reduction repeatedly, the recrystallized fraction increases with the number of reductions and the complete and uniform recrystallized structure can be obtained after several reductions. The interpretation on the cause of the mixed grain structure by Jones and Rothwell<sup>33</sup> and Irani, Burton and Lathum<sup>34</sup> that successive reductions applied to the partially recrystallized structure would recrystallize again only already recrystallized fine grains, has been revised experimentally. New recrystallized fine grains are formed after the subsequent reductions in the unrecrystallized portion where the strain by the preceding reduction is not fully released during the time interval to the next reduction.<sup>32,35</sup> Once complete recrystallization takes place, static recrystallization after the next hot-deformation proceeds more easily because of the refinement of the starting grain size and the increase in the percentage reduction being possible by the decrease in slab thickness.

Similar recrystallization behaviour also can be found in a recrystallization sequence of the silicon-manganese steel in Table 3.1, the first reduction of which started at 1000° C. Such a process seems to take place generally when thicker slabs are reheated to high temperatures.

Once the overall static recrystallization takes place, the grain size decreases progressively by successive reductions until a limiting value is reached,<sup>1,2</sup> as shown in Figure 3.1. Priestner, Earley and Randall<sup>1</sup> found that the limiting grain size did not depend on the starting grain size but only on the percentage reduction and the finishing temperature and that, further, when the starting grain size was finer than the limit determined by the given conditions, the volume of the grains remained unchanged after the successive reductions. It suggests the occurrence of dynamic recrystallization, and may be explained by it.<sup>25</sup>

The analysis of successive structural changes in conventional draught schedules by assuming a wholly recrystallized and fairly refined starting grain structure and by using the solid curves in Figure 3.16 and the like, shows that a certain extent of grain refinement by static recrystallization proceeds in the first several hot-deformations, but that the temperature of the slab becomes higher than  $T_{CD}$  for the given reduction and the given grain size before the reduction at the intermediate stage of the reductions, i.e. dynamic recrystallization takes place. When the slab thickness is still large, dynamic recrystallization occurs by the following hot-deformations and further effective grain refinement becomes impossible, for the recrystallized grain size already has come to be determined only by the slab temperature falling slowly and by the strain rate being determined by the geometry of the reduction. This may be observed as the convergence

of grain refinement reported by Priestner, Earley and Randall.<sup>1</sup> The more effective refinement has been achieved in the early stages of hot-deformation, the earlier this situation is reached. It is necessary to achieve the further grain refinement, stop the rolling operation, wait for the temperature of the slab to fall and reopen the rolling at lower temperatures sufficient to cause static recrystallization or dynamic recrystallization giving finer grains.

The similar convergence can be also found in the statically recrystallized structures of thinner plate after the effective grain refinement by successive dynamic recrystallization, as shown in Figures 3.1 and 3.8(a). When a hot-deformation has been applied at a temperature around its  $T_{CD}$  and achieved the effective grain refinement by dynamic or static recrystallization, the next reduction, applied even at a reduced temperature sufficient to cause static recrystallization, hardly brings the further effective refinement. This is because the statically recrystallized grain size is the same as that of dynamically recrystallized grains by the hot-deformation of the same amount at the  $T_{CD}$ , which is higher than the relevant reduction and not so reduced from the preceding reduction temperature. In these cases, a further decrease in reduction temperature cannot bring finer recrystallized grains and cannot cause recrystallization; only an increase in the amount of the hot-deformation can be effective in further grain refinement.

Even when only static recrystallization occurs after the reductions in the final stage of rolling, the efficiency of grain refinement by a constant percentage reduction decreases with each reduction but more slowly than in the case of the convergence. The reason is that the power of the starting grain size dependence in statically recrystallized grain size is smaller than 1, as shown in Equations (3.5), (3.14) and (3.16).

Figure 3.12 shows that recrystallized grains cannot be refined over the size of the grains metadynamically recrystallized by the reduction having the same value of  $\bar{Z}$ . When the reheating temperature of the slab is low and the starting grain size is finer than the size of metadynamically recrystallized grains determined by the  $\bar{Z}$  values of the successive reductions, the grains are hot-deformed but their volume may not be recrystallized. When a constant-rate deformation in a reduced  $Z$  is applied to a higher strain, the material is not fractured by the occurrence of dynamic recrystallization and the grains are coarsened at the range of steady-state deformation after the several peaks in the stress-strain curve.<sup>15,29</sup> However, a rolling deformation usually cannot be possible at such a higher strain, and grain coarsening by dynamic recrystallization has not been reported in rolling deformation. There has been no study on metadynamic recrystallization starting from hot-deformation in the range of multiple peaks in constant-rate deformation.

There are two sets of curves in Figure 3.16, but similar propositions are possible for controlled-rolling aiming for the refinement of recrystallized  $\gamma$  grains, (with the exception of an increase in rolling speeds in the temperature range of static recrystallization). They are: (1) the decrease in reduction temperatures; and (2) increase in rolling speeds in the temperature range of dynamic recrystallization, which may also cause static recrystallization. Even if  $r_{CD}$  values are large enough to suppress dynamic recrystallization in rolling deformation (as shown by the broken line in Figure 3.16) the decrease in reduction temperature is effective to suppress the grain growth after static recrystallization. In the temperature range of static recrystallization, increase in draught of each pass reduction becomes effective, and the increase in rolling speeds also might be recommended although detailed experimental confirmation is required on the effect.

Another possibility is that the decrease in the slab reheating temperature reduces the grain size before the first hot-deformation and also decreases the temperature range of successive hot-deformations.

The improvement in notch ductility: (1) by transferring a finite number of reductions in the final stage of rolling to lower temperatures in the rolling of ships' plates in European plate-mills;<sup>36</sup> (2) by prescribing in a few the lowest amounts of their reductions per pass;<sup>36</sup> and (3) specifying the start of hot-rolling at temperatures lower than 1200° C in as-rolled IN-steels,<sup>37</sup> can be explained by  $\gamma$  grain refinement by recrystallization controlled-rolling. Some European plate-mills only specified the total amount of reduction at lower temperatures for rolling ships' plates<sup>36</sup> where the  $\alpha$  grain refinement might be caused by controlled-rolling below the recrystallization stop temperature ( $T_{CS}$  or  $T_P$ ), to be explained in Chapter 4.

In the early stages of controlled-rolling for niobium-containing steels, the roughing or the reductions at higher temperatures has not been regulated and has terminated at temperatures considerably higher than their  $T_{CS}$ . The application of recrystallization controlled-rolling to niobium-containing steels becomes roughing controlled-rolling.<sup>4,23</sup> The decrease in the temperatures of several reductions in the final stage of roughing, as shown in Table 1.1, has refined  $\alpha$  grains and raised notch ductility.<sup>4,23,38</sup> It can be explained in terms of the refinement of the recrystallized grains before the finishing or the hot-deformations in the nonrecrystallization temperatures. The discovery by Jones and Rothwell<sup>33</sup> and Irani, Burton and Latham<sup>34</sup> that reductions of fairly higher draughts while control-rolling thicker niobium-containing steel plates in fairly equally spaced intervals over the whole temperature range improves notch ductility, can be also explained by the mechanism of recrystallization controlled-rolling. Jones and Rothwell<sup>33</sup> and Irani, Burton and Latham<sup>34</sup> further confirmed that the decrease in the starting temperature of rolling, the concentration of the roughing draught to the several final reductions (by decreasing the number of passes and the increase in the rolling speed) could also improve notch toughness or alleviate the load of the finishing in the work-hardened temperature range. The low-temperature slab-reheating of niobium- or vanadium-containing steels<sup>25,33,34,37,39-41</sup> has spread rapidly, for it makes possible the simultaneous improvement of notch ductility with the decrease in the holding period between roughing and finishing. It was adopted widely in hot-rolling conventional steels after the oil crisis, improving yield strength and toughness.

The decrease in reduction temperatures and the increase in draughts and rolling speeds, effective to  $\gamma$  grain refinement, also raise the repulsive force and the torque of rolling. A powerful rolling-mill favours not only controlled-rolling below  $T_{CS}$ , but above  $T_{CS}$ . Recrystallization controlled-rolling also becomes difficult when the width and the thickness of products become larger.<sup>36</sup>

## 3.5 Effects of alloying elements on recrystallization behaviour

### 3.5.1 Recrystallization kinetics

Effects of microalloying elements such as niobium on recrystallization kinetics of de-



formed  $\gamma$  have been studied from the start of the study on controlled-rolling for high-strength low-alloy (HSLA) steels. The strong effects of retarding recrystallization are mainly caused by the reduction-strain-induced precipitation of their nitrides and/or carbides which have been in solution at least at reheating.<sup>6</sup> Niobium, titanium and vanadium are strong nitride and carbide formers even in  $\gamma$  phase, and their nitrides and carbides have the same crystal structures of fcc. The order of their retardation strengths is in the order of their affinities to nitrogen and carbon, and so their strengths depend on the nitrogen and carbon contents. The details will be discussed in Chapter 5.

Other more soluble substitutional alloying elements also have some weak effects on recrystallization kinetics. Silicon and manganese retard recrystallization in proportion to their addition amounts up to 1%, but thereafter the effects are saturated.<sup>42</sup> Molybdenum<sup>42,43</sup> and copper<sup>42</sup> in solid solution are reported to have the fairly large retarding effects over that of vanadium in 0.1% C–Mn steels, but their effects are smaller than those of niobium and titanium in solid solution in sufficiently denitrized and decarburized steels.<sup>43</sup> Manganese, nickel, chromium and vanadium have weak retarding effects, but the order of their strengths is in dispute.<sup>32,43</sup>

No studies have been done on the effects of interstitial atoms on recrystallization kinetics, except by Sakai and Ohashi,<sup>44</sup> who have shown that the increase in carbon decreases the activation energy of hot-deformation ( $Q_{\text{def}}$ ) and facilitates the occurrence of dynamic recrystallization.

### 3.5.2 Recrystallized grain size

There have been only a few reports on the effects of alloying elements on recrystallized grain size.<sup>9,27</sup>

Figures 3.5, 3.9 and 3.12 show that the size of metadynamically recrystallized grains is in line with that of statically recrystallized grains at  $\varepsilon^*$  or  $r_{\text{CD}}$  and is always the smallest in those recrystallized by the reductions having the same value of  $\bar{Z}$  in a given steel. The addition of an element effective for refining metadynamically recrystallized grains is also effective for refining statically recrystallized grains.

An early study on controlled-rolling of niobium-containing steels by Rossard<sup>14</sup> has shown, by hot-torsion tests, that an addition of 0.04% Nb increases  $\sigma_p$ , refines dynamically and metadynamically recrystallized grains at least at deformation temperatures below 1000° C and retards metadynamic recrystallization and grain growth after the completion of metadynamic recrystallization. The mean grain size increases during metadynamic recrystallization, starting from a completely dynamically recrystallized structure, and takes about 0.6 and 3.0 s at 1000° C in the steels with and without niobium respectively. The grain growth after its completion continues in the silicon–manganese steel but can be almost ignored in the niobium-containing steel at 1000° C holding. The retardation of the grain growth is caused by strain-induced precipitation of fine niobium carbide or niobium nitride.<sup>45</sup> Kozasu *et al.*<sup>25</sup> have also studied the change in grain size after recrystallization by rolling and holding experiments and reported that grain growth, at least from 3 s after rolling, does not occur in a 0.03% Nb steel at 1050° C, although some, or a considerable amount of coarsening, takes place in the niobium steel at 1200° C or in the niobium-free steel even at 1050° C respectively. These results suggest that at least the straight line in Figure 3.8(b) for the

niobium-containing steel may correspond to the relation between  $\bar{Z}$  and the size of metadynamically recrystallized grains. The difference in grain sizes of two steels with and without niobium shown in Figure 3.1 can be explained by the effects of added niobium on both recrystallized grain size and grain growth.

Sellars<sup>9</sup> has presented a relationship similar to Equation (3.5) giving statically recrystallized grain size for niobium-containing steels in which the available results by various authors are considered and which has smaller strain dependence and gives finer grains than those for carbon–manganese steels.

It seems appropriate to find out the base composition favourable to recrystallization controlled-rolling in order to study the effects of addition elements on the position of the straight line for metadynamically recrystallized grain size in the  $\log \bar{Z} - 1/d$  diagram. The value of  $Q_{\text{def}}$  is a function of the steel chemistry, but the size of metadynamically recrystallized grains is almost determined by the reduction temperature and insensitive to the value of  $Q_{\text{def}}$ . By assuming the same value of  $Q_{\text{def}}$  for various steels studied, the value of  $\log \bar{Z}$  becomes independent of the steady-state flow stress but is to be regarded as a common parameter of rolling actions mainly determined by the reduction temperature.

Such a study by rolling experiments starting from the 0.10% C–0.25% Si–1.4% Mn–0.005% Ni steel<sup>4</sup> has shown, that the size of metadynamically recrystallized grains is not substantially affected by alloy addition in a low  $\bar{Z}$  range, but the following effects appear only when the reduction is applied at temperatures lower than 1050°C. The increase of silicon to 0.8%, the substitution of 1.4% Mn by chromium, nickel or copper in the same quantities, and the addition of vanadium up to 0.03%, hardly change the position of the straight line in Figure 3.8(a). The increase in carbon to 0.20% causes little change in the position, but the reduction to 0.05% decreases the gradient of the straight line and coarsens the recrystallized grains at higher values of  $\bar{Z}$ . The increase in manganese to 2% slightly refines the recrystallized grains at higher  $\bar{Z}$ . These results mean that conventional silicon–manganese steels are of very favourable steel chemistries as the base compositions of controlled-rolled steels, giving the rolled products the properties stable to the compositional fluctuation. However, only the substitution of 0.5% Mn for the same amount of molybdenum significantly shifts the straight line to the finer side, although the addition of molybdenum raises the critical strain for static,<sup>42,43</sup> and dynamic<sup>8,46</sup> recrystallization.

Figure 3.17<sup>4</sup> shows that these effects of molybdenum appear even in the 0.1% addition and that the  $\gamma$  grains of molybdenum-containing steels become finer than those of the silicon–manganese steel after the successive reductions by the same schedule so long as static or dynamic recrystallization can occur by the reductions. The detailed study on the temperature–reduction–recrystallization figures of a 0.1%C–0.25% Si–1.4% Mn–0.2% Mo steel has given the following results. Although the  $r_{\text{CS}}$ ,  $r_{\text{CD}}$  and  $T_{\text{CD}}$  values for the coarse grain structure, as in the early stage of rolling, are respectively higher than those in silicon–manganese steel, the  $r_{\text{CD}}$  value decreases to the level of silicon–manganese steel, but the  $T_{\text{CD}}$  value remains higher than that of silicon–manganese steel when the grains before the reduction become finer. It means that the recrystallized grains can be refined in molybdenum-containing steels without the intentional decrease in the reduction temperatures at the final stage of rolling.

Such effects of molybdenum are considered to be caused by molybdenum atoms in solution,<sup>46</sup> for molybdenum does not precipitate in  $\gamma$  under the additional elements.

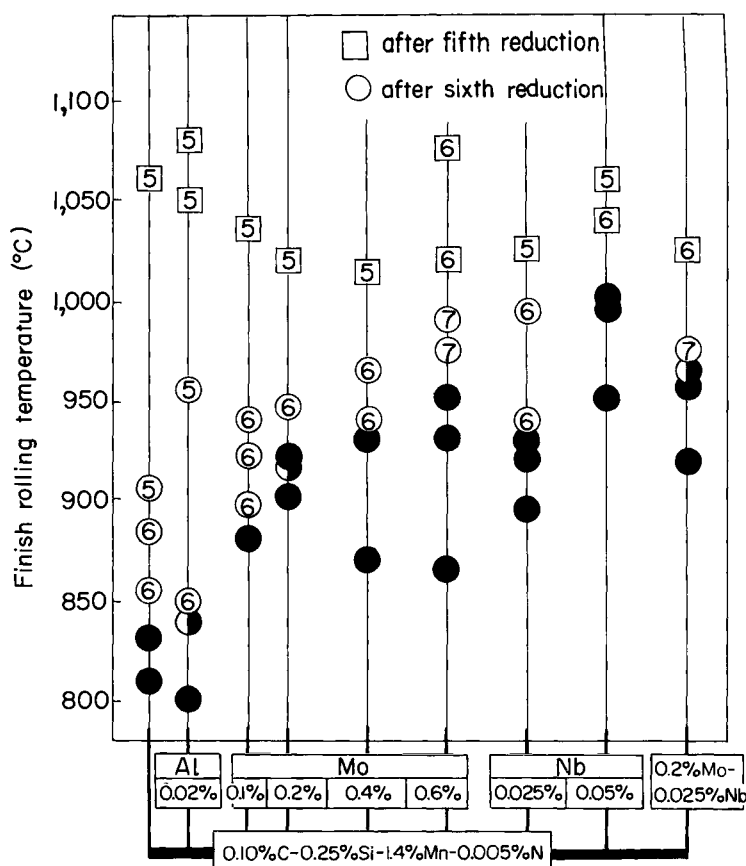


Figure 3.17 Effects of molybdenum addition on  $\gamma$  recrystallization behaviours. After reheating at 1250°C, five fixed reductions and a sixth constant reduction at various temperatures were applied and specimens quenched 1 s after the fifth or sixth reductions. Figures in squares or circles: observed  $N_{\gamma}$  (After Sekine *et al.*<sup>4</sup>)

They are available even after the low-temperature reheating of slabs different from the effect of niobium. Molybdenum is a favourite addition element for controlled-rolling.

The effects of alloying elements in Equation (3.16) for grain size 0.6 s after the reduction have been reported by Machida, Katsumata and Kaji.<sup>27</sup> Recrystallized grain sizes after the reductions in temperatures over the range 1050–1000°C can be evaluated by Equation (3.16) and are hardly affected by the alloying elements such as carbon from 0.03 to 0.31%, manganese from 1.40 to 2.25%, niobium to 0.059%, vanadium to 0.062%, molybdenum to 0.30% and titanium to 0.54%.

In the studies of rolling experiments it becomes difficult strictly to separate the effects of an alloying element on recrystallization kinetics and growth kinetics. It is necessary to study them by using deformation apparatus able to quench the structure immediately after the deformation. Although the strain-induced precipitates from supersaturated  $\gamma$  retard recrystallization and grain growth, the presence of the precipitates before reduction may also change the recrystallized grain size through the change in deformation structure. This is an important factor in titanium-containing steels, low-

temperature-reheated niobium-containing steels and extra-low-temperature-reheated aluminium-killed steels. Such an effect by alloying elements on recrystallization behaviours may be superimposed on the starting grain-size dependence in these steels. These important considerations have not yet received systematic study.

## References

1. PRIESTNER, R., EARLEY, C.C. and RANDALL, J.H. *J. Iron and Steel Inst.*, **206**, 12 (1968)
2. SEKINE, H. and MARUYAMA, T. *The microstructure and design of alloys*, The Metals Society, Vol. I, p.85 (1973)
3. DILAMORE, I.L., DEWSNAP, R.F. and FROST, M.G. *Metals Tech.* 294 (1975)
4. SEKINE, H., MARUYAMA, T., KAGEYAMA, H. and KAWASHIMA, Y. *Thermomechanical processing of microalloyed austenite*, A.J. DE ARDO *et al.* (eds), The Metallurgical Society of the American Institute of Metallurgical Engineers, p.141 (1982)
5. KOZASU, I. and SHIMIZU, T. *Trans Iron and Steel Inst. Japan*, **11**, 359 (1971)
6. SEKINE, H. and MARUYAMA, T. *Tetsu-to-Hagané*, **58**, 1424 (1972); *Trans Iron and Steel Inst. Japan*, **16**, 427 (1976)
7. INAGAKI, H. *Trans Iron and Steel Inst. Japan*, **23**, 1059 (1983)
8. JONAS, J.J. and AKBEN, M. *Metals Forum*, **4**, 92 (1981)
9. SELLARS, C.M. *Hot-working and forming processes*, C.M. SELLARS and G.J. DAVIES, (eds), The Metals Society, p.3 (1979)
10. MORRISON, W.B. *J. Iron and Steel Inst.*, **210**, 618 (1972)
11. DJAIC, R.A.P. and JONAS, J.J. *Metallurg. Trans*, **4**, 621 (1973)
12. WEISS, H. GITTANS, A., BROWN, G.G. and TEGART, W.J. MCG. *J. Iron and Steel Inst.*, **211**, 703 (1973)
13. BARRACLOUGH, D.R. Ph.D. thesis, University of Sheffield (1974)
14. ROSSARD, C. *The microstructure and design of alloys*, The Metals Society, Vol. II, p.175 (1973)
15. SAKUI, S., SAKAI, T. and TAKEISHI, K. *Tetsu-to-Hagané*, **62**, 856, (1976); *Trans Iron and Steel Inst. Japan*, **17**, 718 (1977)
16. MCQUEEN, H.J., and BERGERSON, S. *Metal Sci. J.*, **6**, 25 (1979)
17. TEGART, W.J. MCG. *Ductility*, American Society of Metals, p.133 (1968)
18. LUTTON, M.J. and SELLARS, C.M. *Acta Metallurg.*, **17**, 1033 (1969)
19. SELLARS, C.M. and WHITEMAN, J.A. *Metal Sci.*, **13**, 187 (1979)
20. SIMS, R.B. *Proc. Inst. Mech. Eng.*, **168**, 191 (1954)
21. SAH, J.P. and SELLARS, C.M. *Hot-working and forming processes*, C.M. SELLARS and G.J. DAVIES, (eds), The Metals Society, p.62 (1979)
22. BUFFINGTON, F.S., HIRANO, K. and COHEN, M. *Acta Metallurg*, **9**, 434 (1961)
23. SEKINE, H. and MARUYAMA, T. *Seitetsu Kenkyu*, 289, 43 (1976)
24. GRANGE, R.A. *Fundamentals of deformation processing*, W.A. BACKOFEN, (ed.) Syracuse University Press, p.299 (1964)
25. KOZASU, I., OUCHI, S., SAMPEI, T. and SHIGA, C. *Microalloying 75*, Union Carbide Corp, p.107 (1977)
26. TANAKA, T. TABATA, N., HATOMURA, T. and SHIGA, C. *Microalloying 75*, Union Carbide Corp., p.120 (1977)
27. MACHIDA, M., KATSUMATA, M. and KAJI, H. *Steel rolling*, Vol. II, Iron and Steel Institute of Japan, p.1249 (1981)
28. TOWLE, D.J. and GLADMAN, T. *Met. Sci.*, **13**, 246 (1979)
29. ROSSARD, C. and BLAIN, P. *Rev. Met.*, **6**, 573 (1958)
30. MOROZUMI, F. *Tetsu-to-Hagané*, **52**, 895 (1966)
31. TANAKA, T., FUNAKOSHI, T., UEDA, M., TSUIBOI, J., YASUDA, T. and UTAHASHI, C. *Microalloying 75*, Union Carbide Corp., p.399 (1977)
32. TANAKA, T., ENAMI, T., KIMURA, M. SAITO, Y. and HATOMURA, T. *The metallurgy of hot-working of steels*, Iron and Steel Institute of Japan, p.145 (1982)
33. JONES, J.D. and ROTHWELL, A.B. *International Steel Institute Special Report No. 108*, p.78 (1968); *Deformation under hot-working conditions*, The Iron and Steel Institute, p.78 (1968)
34. IRANI, J.J., BURTON, D. and LATHUM, D.J. *British Iron and Steel Research Association Open Report No. MG/C/31/68* (1968)
35. PHILLIPO, B.L. and CRANE, F.A.A. *J. Iron and Steel Inst.*, **211**, 653 (1973)
36. VANDERBRECK, R.W. *Weld. J.*, **37**, 114-S (1958)
37. NAKAMURA, H. Japanese Patent Sho-41-9183 (1966)

38. KUBOTA, H., KOZASU, I., SHIMIZU, T., MURAI, S. and KANEKO, Y. *Nippon Kokan Technical Report No. 46*, p.625 (1969); *Nippon Kokan Technical Report Overseas*, p.23 (1971)
39. DE KAZINCZY, F., AXNÄS, A. and PACHLEITNER, P. *Jernkont Ann.*, **147**, 408 (1963)
40. GONDOH, H., GOHDA, S. and KIMURA, I. *International Institute of Welding Document No. IX*, pp.416–64 (1964); *Tetsu-to-Hagané*, **53**, 629 (1967)
41. CIVALLERO, M. and PARRINI, C. *Scientific technology of iron and steel*, Vol. II, Iron and Steel Institute, Japan, p.758 (1971)
42. MAEBARA, Y., KUNITAKE, T. and FUJINO, N. *Tetsu-to-Hagané*, **67**, 362 (1981)
43. YAMAMOTO, S., OUCHI, C. and OSUKA, T. *Thermomechanical processing of microalloyed austenite*, A.J. DE ARDO *et al.* (eds), The Metallurgical Society of the American Institute of Mechanical Engineers, p.613 (1982)
44. SAKAI, T. and OHASHI, M. *Tetsu-to-Hagané*, **67**, 2000 (1981)
45. LEBON, A., ROFES-VERNIS, J. and ROSSARD, C. *Mem. Sci. Rev. Met.*, **70**, 577 (1973)
46. BACROIX, B., AKBEN, M.G. and JONAS, J.J. *Thermomechanical processing of microalloyed austenite*, A.J. DE ARDO *et al.* (eds), The Metallurgical Society of the American Institute of Mechanical Engineers, p.293 (1982)

## Deformation of austenite in the nonrecrystallization region

### 4.1 Retardation of recrystallization of $\gamma$

Because of the relation between austenite ( $\gamma$ ) and ferrite ( $\alpha$ ) grain sizes, the refinement of  $\alpha$  grain structure is achieved mainly through that of  $\gamma$  grain structure. Though  $\alpha$  grain size decreases with the decrease in  $\gamma$  grain size, the former reaches a limiting value of  $\sim 10 \mu\text{m}$  and cannot attain further decrease when an  $\gamma$  grain size becomes about  $10 \mu\text{m}$ , as shown in Figure 4.1,<sup>1</sup> i.e. there is a limit in attaining  $\alpha$ -grain refinement through  $\gamma \rightarrow \alpha$  transformation when  $\alpha$  is produced from recrystallized, strain-free  $\gamma$ . However, a limiting  $\alpha$  grain size can be broken by the transformation from deformed  $\gamma$  to  $\alpha$ .<sup>2,3,4</sup> The controlled-rolling makes full use of the beneficial effect of deformed  $\gamma$  on  $\alpha$  grain refinement. The controlled-rolling has been shown to consist of three stages: (1) deformation in the  $\gamma$ -recrystallization region; (2) deformation in the nonrecrystallization region; and (3) deformation in the  $(\gamma + \alpha)$  two-phase region.<sup>5,6</sup>

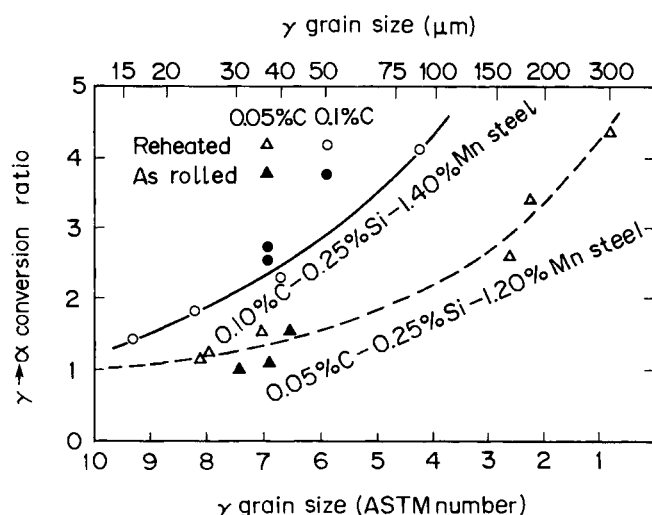


Figure 4.1 Relation between  $\gamma : \alpha$  conversion ratio (ratio of  $\gamma$  grain size to  $\alpha$  grain size) and  $\gamma$ -grain size immediately before transformation in as-hot-rolled, and reheated plain carbon steels. (After Sekine and Maruyama<sup>1</sup>)

Figure 4.2<sup>6</sup> illustrates schematically the three stages of the controlled-rolling process, and the microstructural change caused by deformation in each stage. Stage 1: coarse  $\gamma$  grains (a) are refined by repeated deformation and recrystallization (b), but still transforms to relatively coarse  $\alpha$  grain structure (b'). Stage 2: deformation bands are formed in elongated, unrecrystallized  $\gamma$  grains (c), and  $\alpha$  nucleates on the deformation bands as well as  $\gamma$  grain boundaries, giving fine  $\alpha$  grain structure (c'). Stage 3: deformation in the  $(\gamma + \alpha)$  two-phase region continues stage 2 and also deforms  $\alpha$ , producing a substructure (d). During cooling after deformation, unrecrystallized  $\gamma$  transforms to equiaxed  $\alpha$  grains, while deformed  $\alpha$  changes into subgrains (d').

Grain refinement through repeated recrystallization does not proceed indefinitely but reaches a certain limiting value (b) and thereby results in relatively coarse  $\alpha$  grains (b'). A means of breaking the limiting value is to divide the  $\gamma$  grain. Since a recrystallized  $\gamma$  grain (b) is divided by deformation bands (c), the final  $\alpha$  grain structure is much finer for (c') than for (b'). The deformation in the two-phase region causes not only further grain refinement but a mixed structure consisting of equiaxed grains and subgrains. Additional strengthening is obtained by subgrain hardening.

The fundamental difference between conventional hot-rolling and controlled-rolling is that, in the former,  $\alpha$  grains nucleate exclusively at  $\gamma$  grain boundaries, whereas in the

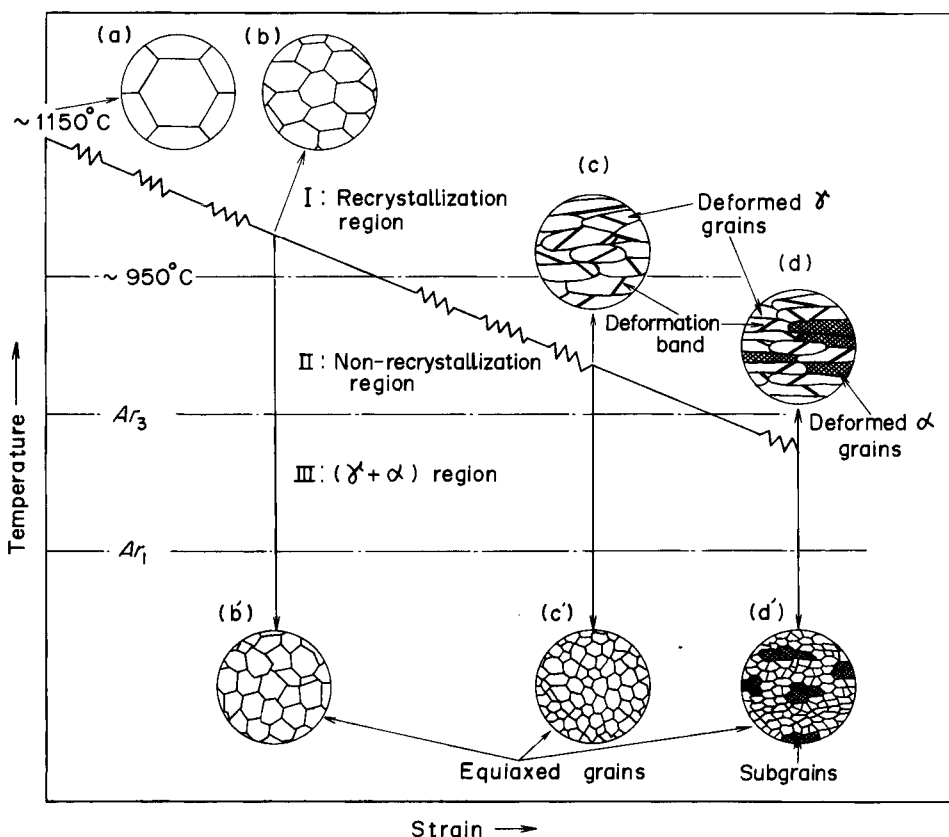


Figure 4.2 Schematic illustration of three stages of controlled-rolling process and change in microstructure with deformation in each stage. (After Tanaka<sup>6</sup>)



latter, nucleation occurs at grain interiors as well as grain boundaries, which leads to a large difference in the final  $\alpha$  grain structure between the two. The fact that the deformation band is equivalent to the  $\gamma$  grain boundary with regard to  $\alpha$ -nucleating potentiality, means that a  $\gamma$  grain is divided into several blocks by deformation bands.

Since unrecrystallized  $\gamma$  grains containing deformation bands promotes the  $\gamma \rightarrow \alpha$  transformation, controlled-rolling can be defined from a different viewpoint, as a process for accelerating transformation and thereby producing fine-grained  $\alpha$  in steel with medium hardenability which, without being control-rolled, will transform to a bainitic structure, giving poor toughness.

As mentioned above, transformation from deformed  $\gamma$  to  $\alpha$  produces much finer  $\alpha$  grain size than that from recrystallized, strain-free  $\gamma$  to  $\alpha$ . Therefore, it is very important to produce the as-deformed  $\gamma$  state, which is realized by the suppression and/or retardation of recrystallization after deformation. There are two factors which delay recovery and recrystallization: (1) temperature; and (2) alloying elements.

Yamamoto, Ouchi and Osuka<sup>7</sup> have investigated the effect of alloy elements on the recovery and recrystallization behaviour of deformed  $\gamma$ . Figure 4.3<sup>7</sup> depicts the softening behaviour of interstitial-free manganese steels with different niobium contents which were strained to 69% in compression with strain rate of  $10 \text{ s}^{-1}$  at  $900^\circ \text{C}$ , where softening ratios of 20 and 50% correspond to the onset of recrystallization and 30% recrystallization respectively. As niobium content increases, the onset of recrystallization (20% softening) is prolonged markedly. As almost all niobium atoms remain dissolved in 0.002% C steel, the retardation of recovery and recrystallization is caused by solute niobium atoms. Temperature also plays a very important role in determining softening kinetics, as shown in Figure 4.4.<sup>7</sup> In niobium-free steel, softening proceeds very rapidly and there is a little influence from temperature on the start of recrystallization while, in niobium steel, the onset of recrystallization is greatly retarded by the decrease in temperature. It is to be noted that though solute niobium atoms and lowering of temperature retard the onset recrystallization, they do not retard the progress of recrystallization. Though the incubation time for the onset of recrystallization (20%

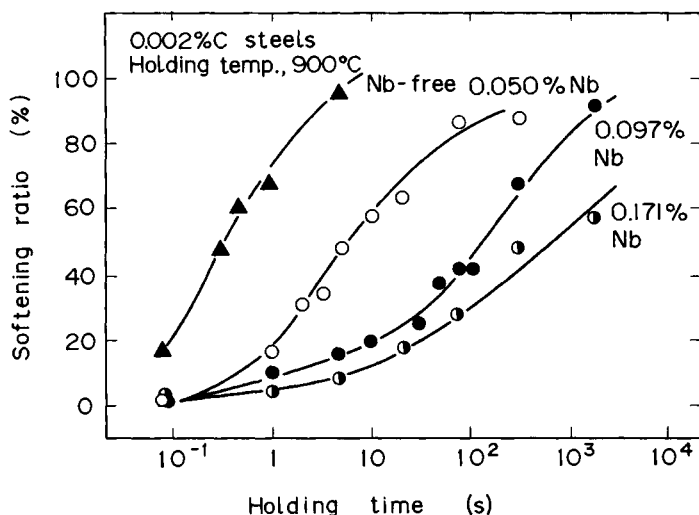


Figure 4.3 Effect of niobium on softening behaviour in 0.002% C–1.54% Mn steels with different niobium content. (After Yamamoto, Ouchi and Osuka<sup>7</sup>)

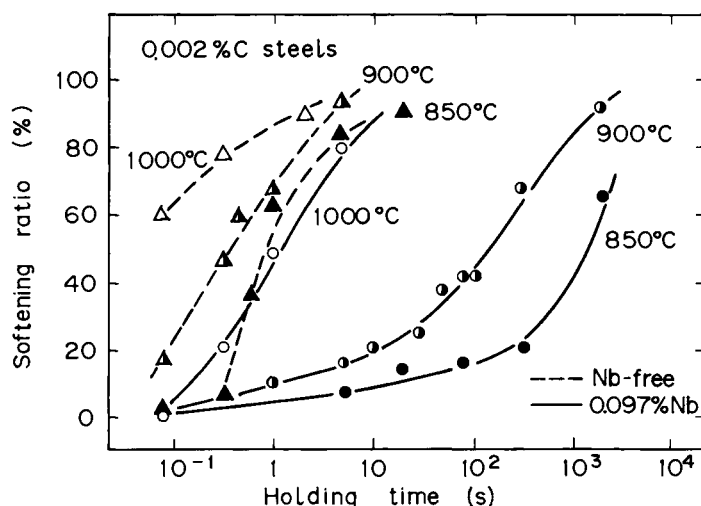


Figure 4.4 Dependence of softening behaviour on temperature in 0.002% C–1.56% Mn steel with or without niobium. (After Yamamoto, Ouchi and Osuka<sup>7</sup>)

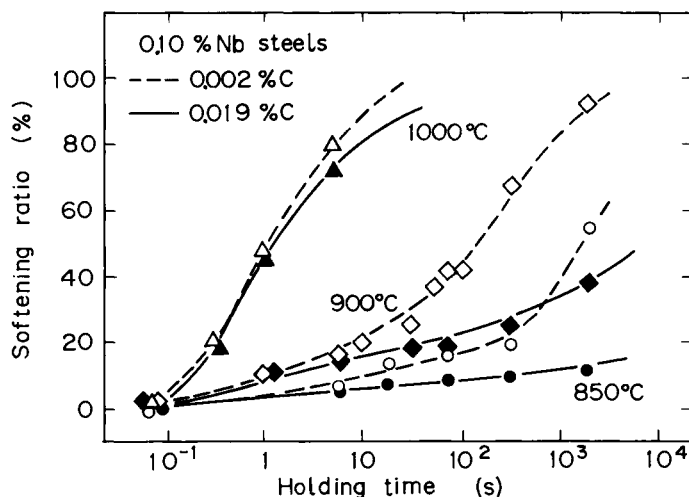


Figure 4.5 Effects of temperature and carbon content on the softening behaviour in 0.097% Nb steels. (After Yamamoto, Ouchi and Osuka<sup>7</sup>)

softening) is different depending on niobium content and/or temperature, once started, recrystallization behaviour follows substantially the same curve.

Figure 4.5<sup>7</sup> depicts the softening behaviours of interstitial-free 0.097% Nb and 0.019% C–0.095% Nb steels at 850, 900 and 1000°C. While the two steels exhibit almost the same softening behaviour at 1000°C, high-carbon steel gives much slower softening behaviour at 900 and 850°C than interstitial-free steel. Figure 4.6<sup>7</sup> shows the progress of precipitation of niobium carbonitrides with holding time at 900°C in three niobium steels with different carbon contents, where precipitates were measured by chemical analysis. No precipitation is observed to occur for the whole range of holding time in 0.002% C steel. While, in 0.006% and 0.019% C steels, strain-induced precipitation of niobium carbonitrides occurs rather quickly after a certain incubation time.

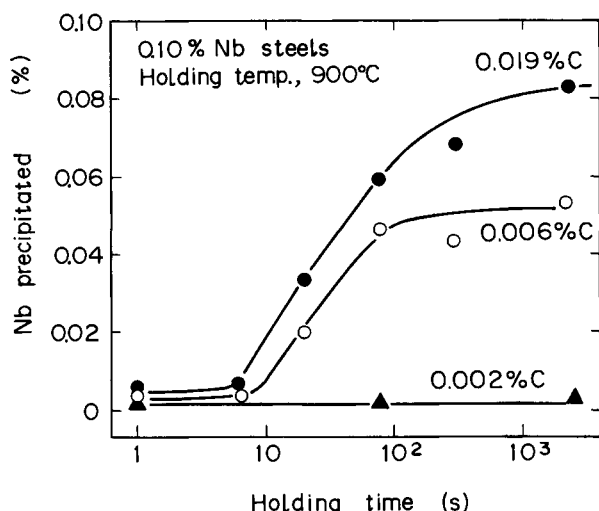


Figure 4.6 Progress of strain-induced precipitation of niobium carbonitrides in 0.002% C-0.097% Nb, 0.006% C-0.097% Nb, and 0.019% C-0.095% Nb steels at 900°C. (After Yamamoto, Ouchi and Osuka<sup>7</sup>)

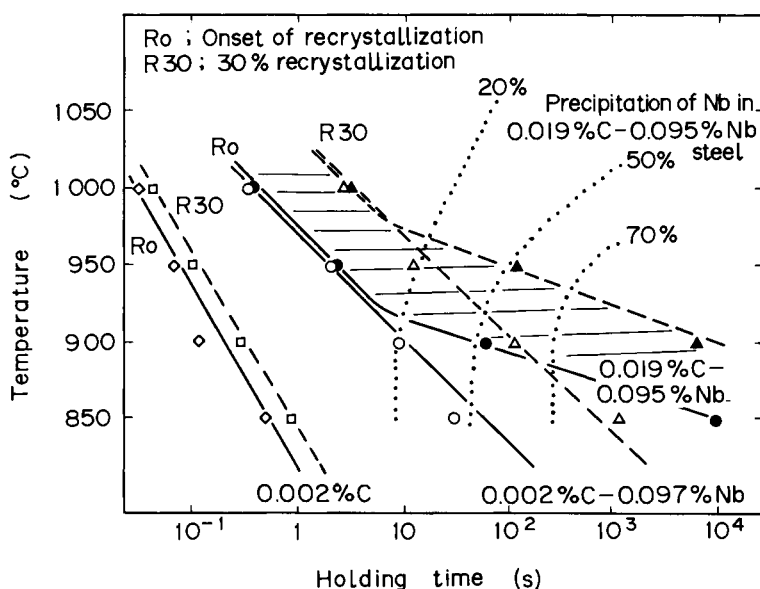


Figure 4.7 Recrystallization-temperature-time diagrams are superimposed with precipitation-temperature-time diagram for 0.002% C, 0.002% C-0.097% Nb, and 0.019% C-0.095% Nb steels. (After Yamamoto, Ouchi and Osuka<sup>7</sup>)

Comparing Figures 4.5 and 4.6, it is evident that when strain-induced precipitation precedes the onset of recrystallization (20% softening), recrystallization is retarded markedly. It is noteworthy that strain-induced precipitates retard not only the onset but the progress of recrystallization.

The recrystallization-temperature-time diagram and the precipitation-temper-

ature–time diagram are superimposed for carbon–manganese and carbon–manganese–niobium steels, as shown in Figure 4.7.<sup>7</sup> The onset of recrystallization increases in a linear manner with decreasing temperature in 0.002% C steels. The addition of 0.097% Nb to 0.002% C steel retards the onset of recrystallization by the order of 1 to 2. In 0.019% C–0.095% Nb steel, the onset of recrystallization and 30% recrystallization are the same with those of 0.002% C–0.097% Nb steel in the region where the amount of niobium carbonitrides is less than 20% of the total niobium. However, in the region where the amount of niobium carbonitrides is more than 30%, both the onset of recrystallization and 30% recrystallization are greatly retarded.

The recrystallization–precipitation–time diagram shown in Figure 4.7 indicates that the onset of recrystallization is delayed by the recovery-retarding effect of solute niobium, and that under conditions where recrystallization is impeded due to solute drag effect, the operation of the recrystallization process is prevented or retarded until precipitation is complete or nearly complete if strain-induced precipitation of niobium carbonitrides occurs. In other words, solute niobium atoms retard recovery and recrystallization till the occurrence of strain-induced precipitation, while strain-induced precipitates retard the onset and progress of recrystallization.

Jonas and Akben,<sup>8</sup> and Jonas and Weiss<sup>9</sup> have also presented the same idea on the effect of niobium on recrystallization behaviour, shown in Figure 4.8.<sup>9</sup> When the time

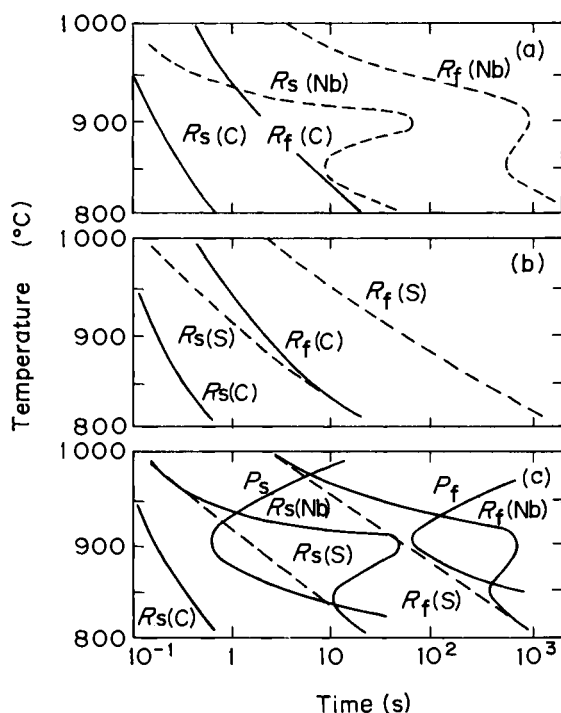


Figure 4.8 (a) Comparison of recrystallization kinetics of plain carbon and niobium-modified steel reported by le Bon; (b) derived effect of niobium as solute (S) on recrystallization kinetics of niobium-modified steel of (a); (c) superimposition of precipitation–temperature–time diagram for dynamic precipitation and derived recrystallization–temperature–time diagram of (b) for rate of solute-modified recrystallization;  $R_s$  and  $R_f$ , and  $P_s$  and  $P_f$  represent start and finish for recrystallization and precipitation respectively. (After Jonas and Weiss<sup>9</sup>)

for the start of precipitation  $P_s$  is longer than the recrystallization start time  $R_s$ , the recrystallization–precipitation–time curve has the normal dependence on temperature affected by a solute drag. When  $P_s$  is less than  $R_s$ , the nucleation and growth of recrystallization is severely impeded. When the retarding effect by solute atoms is weak, as in vanadium steel, recrystallization is complete before the occurrence of strain-induced precipitation and significant retarding effects cannot be expected.

So far, the effect of niobium on recrystallization behaviour has been explained. Though vanadium is a strong carbide-forming element, it has a slight recovery-retarding effect, whereas titanium exerts a very strong recrystallization-retarding effect. Besides those carbide-forming elements, other substitutional elements have some effect on the recrystallization behaviour. Yamamoto, Ouchi and Osuka<sup>7</sup> have shown that the effects of alloy elements on recrystallization retardation is well associated with the change in lattice constant caused by the addition of alloy elements exhibited in Figure 4.9.

## 4.2 Formation and role of deformation bands

Figure 4.10(a) shows a pancaked  $\gamma$  grain structure produced by deformation of  $\gamma$  in the nonrecrystallization region.<sup>6</sup> A number of bands in pancaked grains can be seen, many of which run from grain boundary to grain boundary in two roughly parallel lines. These bands are usually called deformation bands. Figure 4.10(b) shows a partly transformed grain structure; after deformation in the nonrecrystallization region, material is held below  $A_{r3}$  temperature for a short time and subsequently quenched.<sup>6</sup>  $\alpha$  grains

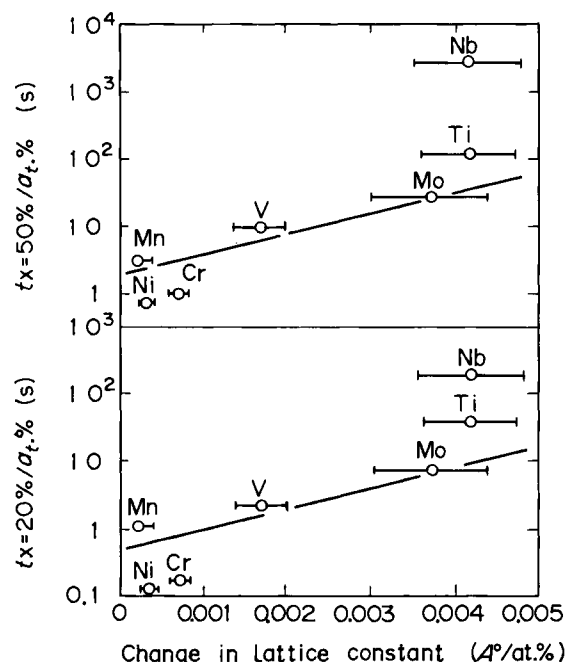


Figure 4.9 Relation between softening of 20% and 50% and the change in lattice constant caused by substitutional solute addition. (After Yamamoto, Ouchi and Osuka<sup>7</sup>)

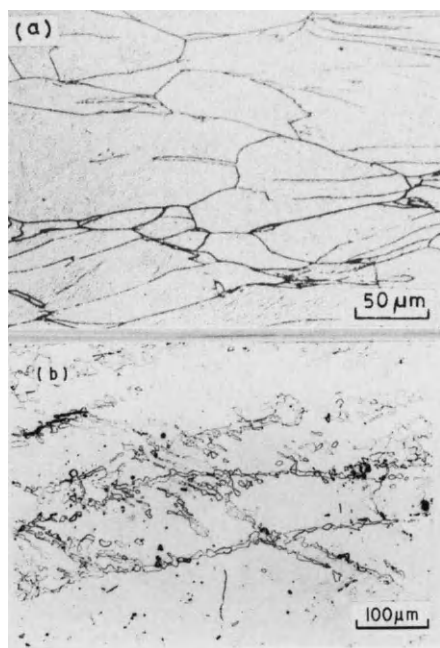


Figure 4.10 (a) Elongated  $\gamma$  grains with deformation bands produced by deformation in the nonrecrystallization region; (b) proeutectoid  $\alpha$  formation in a partially transformed grain structure. (After Tanaka<sup>6</sup>)

are nucleated at deformation bands as well as  $\gamma$  grain boundaries, individual  $\alpha$  grains being formed frequently inside  $\gamma$  grains. That is, when deformed  $\gamma$  transforms to  $\alpha$ , the deformation band as well as the  $\gamma$  grain boundary provide nucleation sites for  $\alpha$  grains. Whereas, when strain-free  $\gamma$  (recrystallized  $\gamma$ ) transforms to  $\alpha$ ,  $\gamma$  grain boundaries alone provide for nucleation sites for  $\alpha$  grains. This difference in transformation behaviour between deformed  $\gamma$  and strain-free  $\gamma$  brings about differences in final  $\alpha$  grain structure. The studies on deformation bands are not numerous.<sup>1,4,10-12</sup> As shown in Figure 4.11, deformation band density increases slightly in the strain range of less than 30%, beyond which it increases rapidly with increasing reduction.<sup>4</sup> The deformation band density is barely affected by deformation temperature in the nonrecrystallization region, but it decreases rapidly when the temperature exceeds 1000°C<sup>4</sup> while, according to Sekine and Maruyama,<sup>1</sup> the apparent  $\gamma$  grain boundary area ( $\gamma$  grain boundary plus deformation bands) increases with an increasing amount of reduction, reaching a steady level above ~30% reduction. With an increasing amount of reduction, the  $\gamma$  grain boundary area increases gradually, while deformation band density increases rapidly, indicating that  $\alpha$  grain refinement resulting from deformation in the nonrecrystallization region is due mainly to an increase in the deformation band. The grain boundary area is increased only by a factor of about 2 when total deformation in the nonrecrystallization region is 70–80%.<sup>13</sup> It is also important to note that even when the deformation band is saturated in number, about 10% of  $\gamma$  grains contain very few deformation bands,<sup>1</sup> and that not all deformation bands have the same  $\alpha$ -nucleation potential;<sup>4</sup> some bands have only very thin and straight bands of  $\alpha$ , implying poor nucleation capacity. Even the introduction of deformation bands cannot bring about uniform and homogeneous  $\gamma$  grain structure and thereby homogeneous  $\alpha$  grain structure. Inhomogeneity in grain structure is the fate of as-hot-rolled material which

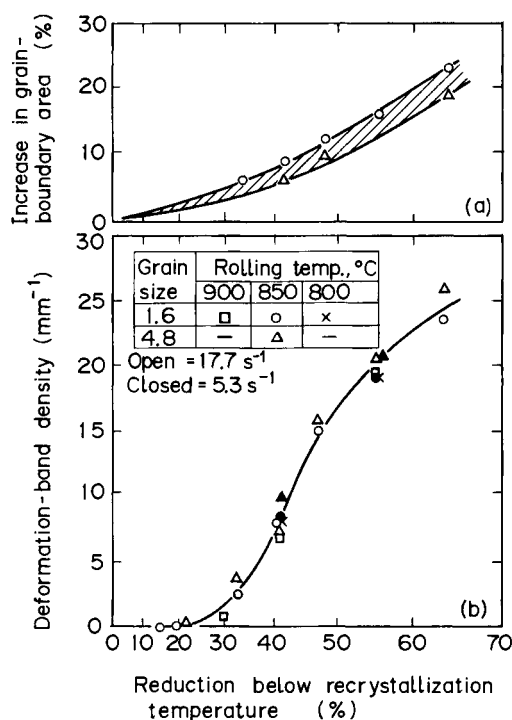


Figure 4.11 Dependence of  $\gamma$  grain-boundary area and deformation band density on the reduction in nonrecrystallization region; in this 0.03% Nb steel, initial grain size was varied by rolling in two passes at higher temperatures after reheating to  $1250^\circ\text{C}$ . (After Kozasu *et al.*<sup>4</sup>)

can, however, be reduced with a decrease in recrystallized  $\gamma$  grain size before deformation in the nonrecrystallization region.

The  $\alpha$  grain size correlates with effective  $\gamma$  interfacial area  $S_v$  (grain boundary area plus deformation bands) shown in Figure 4.12.<sup>4</sup> Although an increase in  $S_v$  causes  $\alpha$  grain refinement, for a fixed  $S_v$  value, deformation in the nonrecrystallization region refines  $\alpha$  grains more effectively than that in the recrystallization region. According to Ouchi *et al.*,<sup>14</sup> in the early stage of transformation the transformation rate is given by  $N_s \times S_v$ , where  $N_s$  is the nucleation rate per unit boundary area. While  $\gamma$  grain refinement through recrystallization increases only the  $S_v$  value, deformation in the nonrecrystallization region increases both  $N_s$  and  $S_v$ . As grain-boundary area in deformed  $\gamma$  possesses higher energy than that in recrystallized  $\gamma$ ,  $\alpha$  nucleation rate is higher for the former than for the latter. In a sense, general diffusional transformation controlled by the interface nucleation growth mechanism is accelerated by the deformation in the nonrecrystallization region.<sup>14</sup>

The ratio of  $\gamma$  grain size to  $\alpha$  grain size accompanying transformation reduces with decreasing  $\gamma$  grain size, reaching a limiting value of  $\sim 1$  in both hot-rolled and normalized steels.<sup>1</sup> However, when rolled heavily in the nonrecrystallization region, the ratio is 2.3–2.5, where the  $\alpha$  grain size is determined by the linear intercept method in the through-thickness (Z) direction,<sup>1</sup> showing the superior effect on grain refinement of deformation in the nonrecrystallization region. In practice, when finely recrystallized  $\gamma$



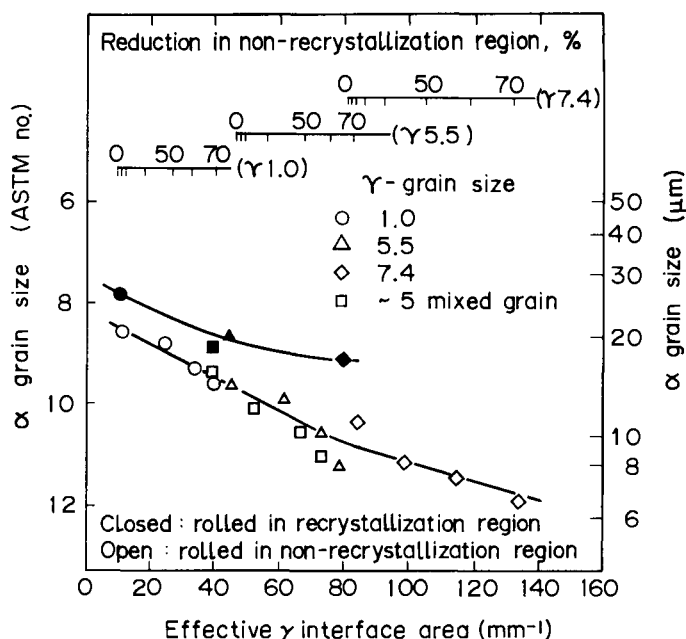


Figure 4.12 Dependence of  $\alpha$  grain size on effective  $\gamma$  interface area in niobium steels hot-rolled in the recrystallization region and in the nonrecrystallization region respectively. (After Kozasu *et al.*<sup>4</sup>)

is given 70–80% reduction in the nonrecrystallization region,  $\alpha$  grain size is  $\sim 12$  in ASTM number, whereas normalization produces at most grain size number  $\sim 10$ .<sup>1</sup>

It has been stressed that, during  $\gamma \rightarrow \alpha$  transformation, the deformation band plays the same role with the  $\gamma$  grain boundary, providing nucleation sites for  $\alpha$  grains. This means that  $\gamma$  grains are divided into several blocks (grains) by deformation bands. A comparison between conventional hot-rolling and controlled-rolling is similar to that between normalizing and quenching. Figure 4.13<sup>15</sup> illustrates transformation behaviour and resultant grain structure in hot-rolled and heat-treated materials. In both conventionally hot-rolled and normalized materials, proeutectoid  $\alpha$  grains form exclusively at  $\gamma$  grain boundaries. As the result, there is a limit in achieving fine  $\alpha$  grain size. On the other hand, in controlled-rolled and quenched materials,  $\gamma$  grains are divided into several blocks, thereby causing very fine  $\alpha$  grain structure. Clearly, the mechanism of grain division is different between controlled-rolling and quenching. The former is due to the introduction of deformation bands, and the latter to martensite transformation. It is noteworthy that, besides quenching, it is only controlled-rolling that can divide  $\gamma$  grains.

So far, it has been stressed that the essence of controlled-rolling is to deform  $\gamma$  at the nonrecrystallization region, that deformation of  $\gamma$  at the nonrecrystallization region is to introduce deformation bands within  $\gamma$  grains, and that the introduction of deformation bands is to divide  $\gamma$  grains into several blocks and thereby increase nucleation sites for  $\alpha$  grains and achieve finer  $\alpha$  grain structure. In a sense, the deformation band

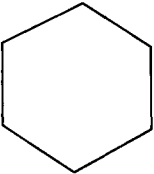

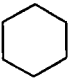
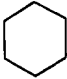
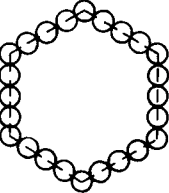
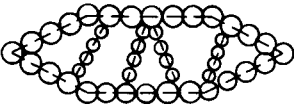
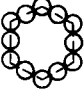

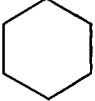
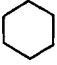
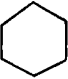

|                              | Conventional hot-rolling  | Controlled rolling  | Normalizing   | Quenching  |
|------------------------------|---|---|---|--|
| $\gamma$ grain structure     |  | <br>Deformation band |  |                              |
| Nucleation of $\alpha$ grain |  |                      |  | <br>Lath                     |
| $\alpha$ grain structure     |  |                      |  | <br>Cementite<br>(Tempering) |

Figure 4.13 Nucleation sites for  $\alpha$  grains and resulting  $\alpha$  grain structures in hot-rolled and heat-treated steels. (After Tanaka<sup>15</sup>)

plays the most essential role in controlled-rolling. However, the nature of the deformation band which is produced during rolling at the nonrecrystallization region is not yet accurately known.

If the banded structure shown in Figure 4.10(a) is the deformation band in a true sense of the word, the deformation band is sure to be able to divide  $\gamma$  grains. Since there is large disorientation between the two neighbouring regions across the deformation band, it becomes a kind of large-angle grain boundary.<sup>16-18</sup> That these deformation bands are frequent sites for the nucleation of recrystallization is also well established.<sup>17,19,20</sup>

Inagaki<sup>21</sup> and Umemoto, Tamura and Otsuka<sup>22</sup> were the first to shed light on the nature of the deformation band. Inagaki<sup>21</sup> has arrived at the conclusion that the banded structure hitherto described as the 'deformation band' is not the deformation band in the true sense of the term, but is an annealing twin, a view derived from the discovery that the so-called 'deformation band' consists of two parallel straight lines with very sharp contrast as seen in Figure 4.10(a) and that the 'deformation band' is very similar to 'annealing twins' observed in fcc metals in every respect. He also observed that in reheated and subsequently quenched specimens, several types of annealing twins are formed which correspond quite well with the classification of annealing twins formed in fcc metals, indicating that they are exactly annealing twins formed in the  $\gamma$  phase. Although annealing twins are not necessarily clearly visible due to their coherency with the matrix, they become more distinct when deformed, because the coherency is destroyed by deformation and the original twin boundary is surrounded by the region with high strain. Inagaki does not always deny the existence of true deformation bands. Although he insists that those broad and straight bands are an-

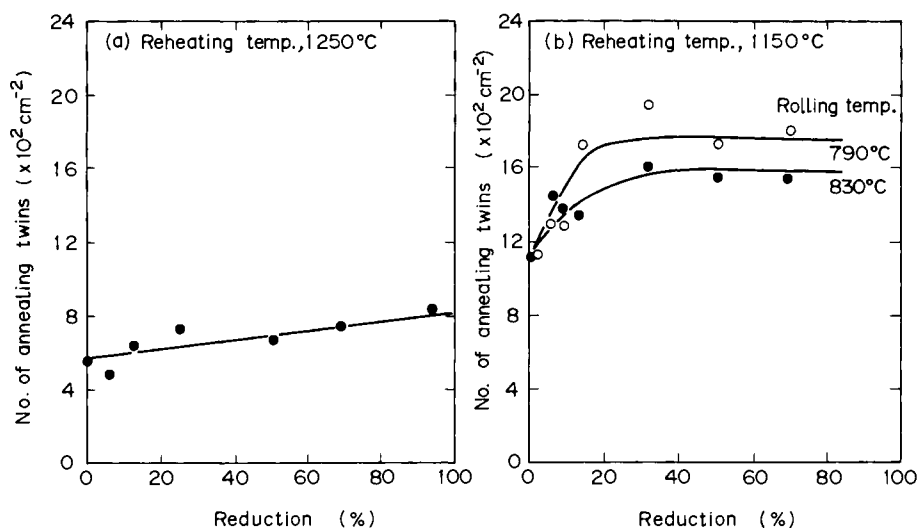


Figure 4.14 Effect of reheating temperature and the amount of reduction on the density of annealing twins; reheating temperatures are: (a) 1250°C, and (b) 1150°C. (After Inagaki<sup>21</sup>)

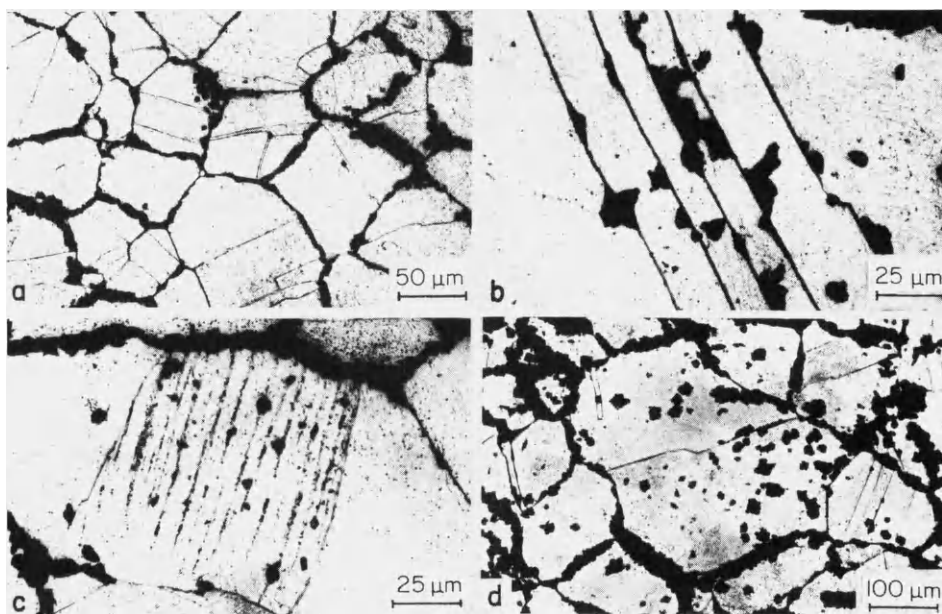


Figure 4.15 Optical micrographs showing various types of nucleation sites for pearlite observed in deformed tool steel: (a) nucleation at grain boundaries; (b) nucleation at annealing twins; (c) nucleation at deformation bands; and (d) nucleation in the interiors of grains. (After Umemoto, Tamura and Otsuka<sup>22</sup>)

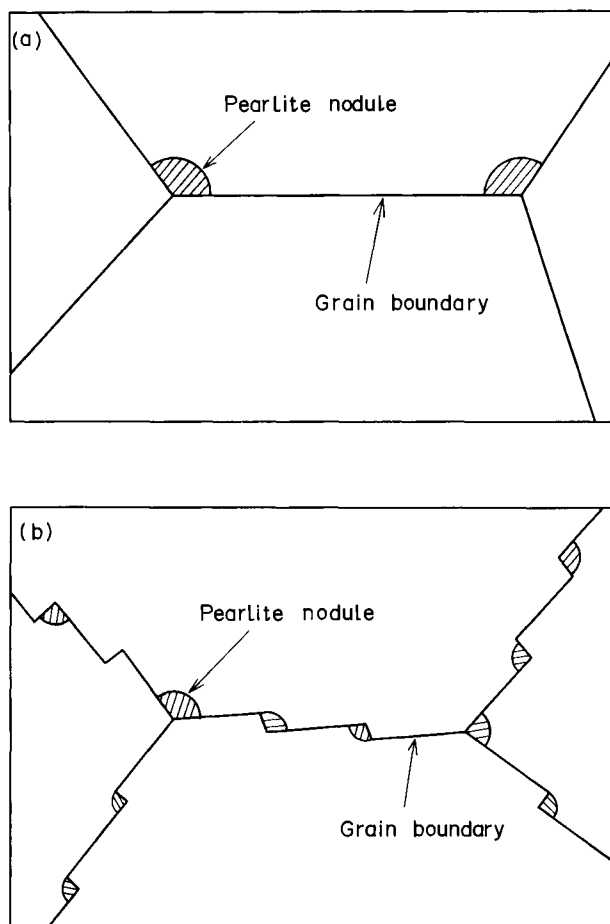


Figure 4.16 Schematic illustration of nucleation sites for pearlite nodules: (a) triple junctions of grain boundaries in strain-free  $\gamma$ ; and (b) grain boundaries as well as triple junctions in deformed  $\gamma$ . (After Umemoto, Tamura and Otsuka<sup>22</sup>)

nealing twins, he also admits that deformation bands exist as wavy, narrow, ribbonlike structures.

In controlled-rolling, in which successive rolling passes are given in the temperature range of slab-reheating to just above  $A_{r3}$ , annealing twins formed during reheating will disappear in the process of recrystallization, and annealing twins which provide for nucleation sites for  $\alpha$  grains, will be newly formed during the recrystallization process.<sup>21</sup> Figure 4.14 depicts the influences of reheating temperature and the amount of deformation on the density of annealing twins.<sup>21</sup> The density is much higher at 1150°C than 1250°C. The density increases at lower reductions and becomes saturated above a 20% reduction in material reheated to 1150°C. When hot-rolled, the twin boundary loses the coherency with the matrix and is severely distorted. Furthermore, to accommodate the strain compatibility across the twin boundary, the region in the vicinity of twin boundary is highly strained and thereby becomes a preferred site for  $\alpha$  nucleation. Regions in the vicinity of  $\gamma$  grain boundaries are also severely distorted to ac-

commodate strain compatibility across other grain boundaries. Thus, Inagaki<sup>21</sup> has proposed that the introduction of highly strained regions near grain boundaries and annealing twins is more essential to the enhancement of  $\alpha$  nucleation, and thereby to the grain refinement, than the formation of true deformation bands.

For the purpose of confirming nucleation sites for transformation, Umemoto, Tamura and Otsuka<sup>22</sup> have investigated the pearlite transformation from deformed  $\gamma$  in tool steel. Figure 4.15 shows various nucleation sites for pearlite transformation in tool steel which was rolled 30% in the nonrecrystallization region: (1) in the initial stage of transformation, pearlite nucleation occurs preferentially at grain boundaries; (2) with the progress of transformation, pearlite nucleation occurs at annealing twin boundaries as well as at  $\gamma$  grain boundaries; (3) pearlite forms at deformation bands; and (4) pearlite nucleation occurs in the interior of grains.<sup>22</sup>

In strain-free  $\gamma$ , the preferred nucleation sites for pearlite nodules are triple junctions of grain boundaries, while in deformed  $\gamma$  the preferred nucleation sites are on grain boundaries as well as at triple junctions, shown schematically in Figure 4.16.<sup>22</sup> This indicates that enhancement of transformation in deformed  $\gamma$  is mainly due to the increase in nucleation sites at grain boundaries. The relative importance of nucleation sites for transformation is considered to be dependent on the amount of deformation. When the amount of deformation is not large,  $\gamma$  grain boundaries are the most preferential and important sites, while with the increasing amount of deformation, annealing twin boundaries and deformation bands become more and more important.

### 4.3 Strain-induced and/or strain-enhanced transformation

Deformation in the nonrecrystallization region produces as-deformed  $\gamma$ , i.e. accumulation of strain in terms of dislocations, cell structure and deformation bands, occurs. The accumulation of strain causes increases in the number of nucleation sites and increased nucleation rate during transformation which, in turn, brings about several features such as a rise in the  $\gamma \rightarrow \alpha$  transformation temperature, increase in the transformation rate, the lowering of hardenability of steel, a separate transformation to  $\alpha$  and martensite dual-phase,<sup>23-25</sup> and so forth. Each feature will be described in more detail in the following.

The measurement of strain-induced  $A_{r3}$  temperature has been performed by a variety of techniques: (1) thermal analysis,<sup>4,26</sup> (2) dilatometric methods with a compression device,<sup>27,28</sup> and (3) microstructural change.<sup>29</sup> However, these measurements were not always carried out with precision, or under the conditions where real controlled-rolling was simulated, because of the limitations imposed by instruments and/or the difficulty in simulating controlled-rolling. Tanaka and Tabata<sup>30</sup> have shown that the strain-induced  $A_{r3}$  temperature can be determined correctly by measuring texture intensity, which can be applied to any controlled-rolling condition. Their result is shown in Figure 4.17 where the  $A_{r3}$  temperature rises with the increasing amount of reduction in the nonrecrystallization region. However, the rise in the  $A_{r3}$  temperature is much more remarkable for coarse-grained, than for fine-grained, material. This is because strain induces  $\alpha$  formation in coarse-grained material which, in strain-free conditions, will transform to upper bainite.

Smith and Siebert<sup>28</sup> have investigated the effect of deformation on the continuous-

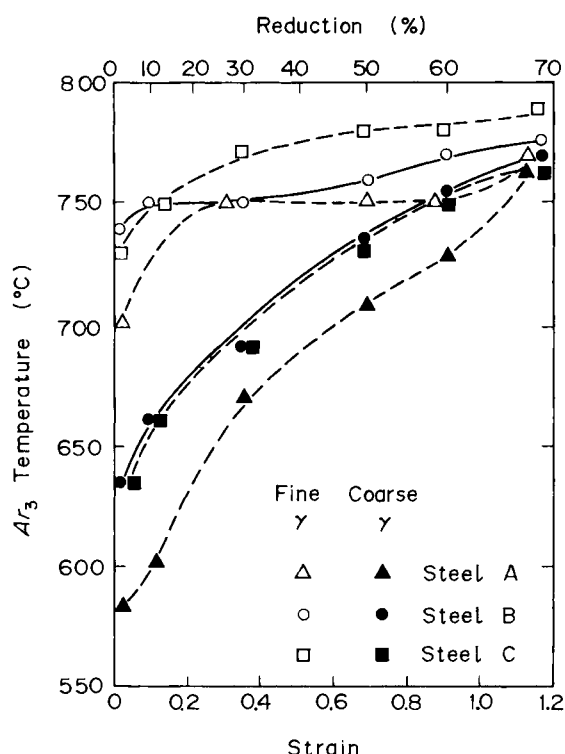


Figure 4.17 Effects of amount of deformation in nonrecrystallization region and initial grain size on  $\gamma \rightarrow \alpha$   $A_{r3}$  temperature measured by texture development in niobium steel. (After Tanaka and Tabata<sup>30</sup>)

cooling–transformation diagram in 0.1% C–0.39% Mo–B steel, shown in Figure 4.18. In a specimen that was not deformed at all,  $\gamma$  and pearlite noses are located at longer times. While in a specimen deformed 50%,  $\alpha$  nose is shifted markedly to shorter time, exhibiting remarkable acceleration of  $\alpha$  formation due to the deformation in the nonrecrystallization region. On the other hand, bainite formation does not seem to be influenced by deformation. The effect of deformation on the start of polygonal  $\alpha$  formation is expressed in terms of the amount of deformation and chemical composition, shown in Figure 4.19,<sup>28</sup> where the ordinate represents the limiting cooling rate for the avoidance of polygonal  $\alpha$  formation. In each steel, the limiting cooling rate increases in a linear manner with strain, reflecting the large effect of strain on accelerated transformation to polygonal  $\alpha$ .

In tool steel, pearlite nucleation occurs much earlier for deformed, than for strain-free,  $\gamma$ .<sup>22</sup> In the early stage of transformation, pearlite nucleation occurs preferentially at prior  $\gamma$  grain boundaries, the number of pearlite nodules being much larger for deformed, than for strain-free,  $\gamma$ . In strain-free  $\gamma$ , pearlite nucleation occurs exclusively at prior  $\gamma$  grain boundaries, while in deformed  $\gamma$ , pearlite nodules nucleate not only at grain boundaries, but at annealing twin boundaries, deformation bands and in the interiors of grains, as shown in Figure 4.15. It is to be remembered here that the density of annealing twins is the same between strain-free and deformed  $\gamma$  and that annealing twins become nucleation sites for pearlite nodules only in deformed  $\gamma$ .

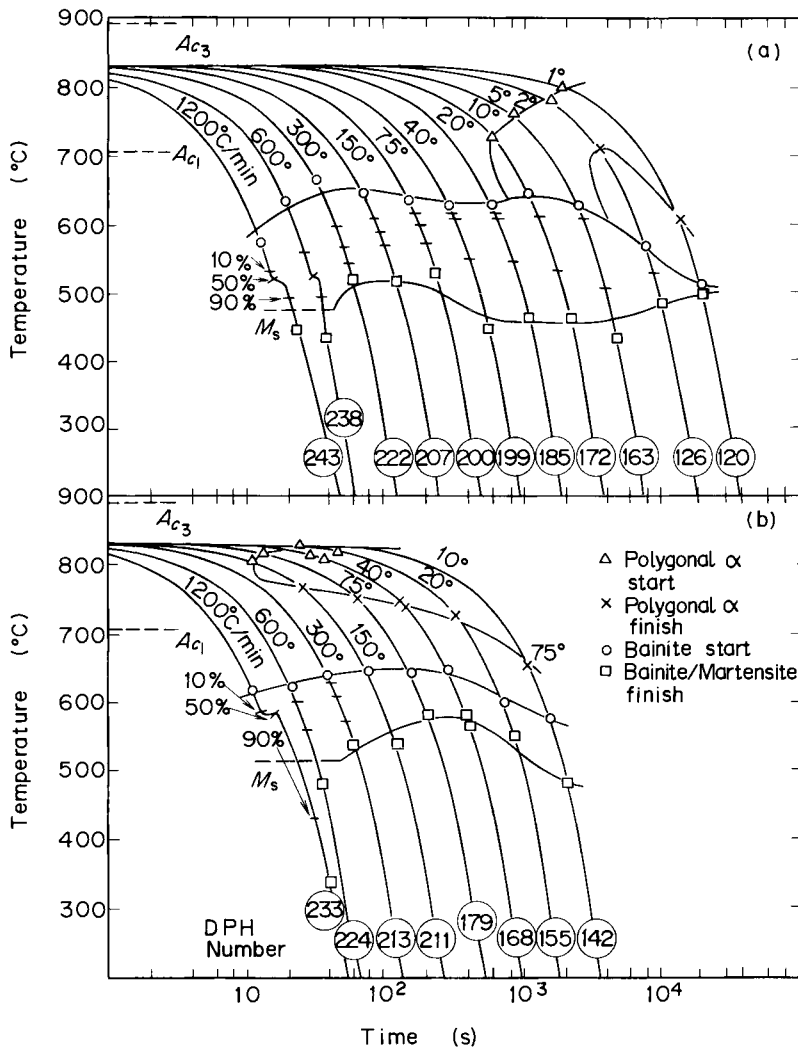


Figure 4.18 Continuous-cooling transformation diagram of 0.1% C-0.39% Mo-B steel in: (a) the undeformed condition; and (b) thermomechanically worked to 50% reduction. (After Smith and Siebert<sup>28</sup>)

According to Umemoto, Tamura and Otsuka,<sup>22</sup> there are three factors which enhance pearlite formation in deformed  $\gamma$ : (1) the increase in  $\gamma$  grain boundary area due to grain elongation; (2) the increase in nucleation sites inside grains; and (3) the increase in nucleation rate at grain boundaries. Among these three factors, the increase in nucleation rate at grain boundaries is the most important factor, followed by the increase in nucleation sites inside grains, with the increase in  $\gamma$  grain boundary area having the least effect. The pearlite nucleation rate at the grain boundary has been observed to be 8 times larger in material rolled 30% than in material not rolled. This is because the densities of the highly strained regions at  $\gamma$  grain boundaries are remarkably increased by deformation, thereby enhancing nucleation rates, as shown in Figure 4.16. Inagaki<sup>21</sup> also demonstrated that the introduction of highly strained regions near



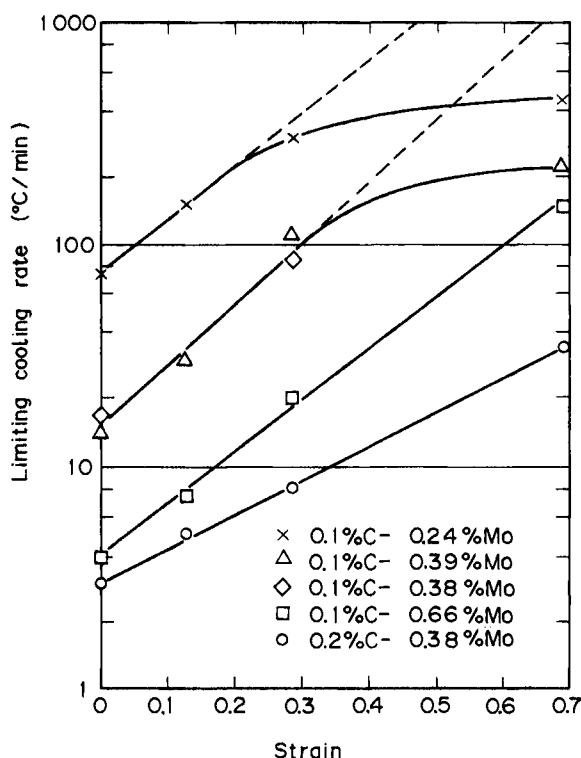


Figure 4.19 Effect of  $\gamma$  deformation on the limiting cooling rate for the avoidance of polygonal  $\alpha$  formation during continuous cooling of low-carbon, molybdenum-boron structural steels. (After Smith and Siebert<sup>28</sup>)

grain boundaries or near the boundaries of annealing twins seems to be essential to the enhancement of  $\alpha$  nucleation and, therefore, to the grain refinement.

Roberts, Lidefelt and Sandberg<sup>31</sup> also emphasized the importance of grain boundary  $\alpha$  nucleation in deformed  $\gamma$ . Deformation in the nonrecrystallization region quite frequently produces bulges at  $\gamma$  grain boundaries, where the activation energy for  $\alpha$  formation is lowered, resulting in the enhancement of  $\alpha$  formation.

It is to be noted that the most frequent nucleation sites differ depending on the amount of deformation; when the amount of deformation is small, the  $\gamma$  grain boundary is the most important while, with an increasing amount of deformation, the annealing twin boundary and deformation band become more and more important sites for transformation.

So far it has been shown that deformation in the nonrecrystallization region causes strain-enhanced transformation. This enhancement and, in particular, enhancement in  $\alpha$  transformation, has wide applications. In the following, three applications will be described briefly.

- (1) In as-hot-rolled and normalized conditions, niobium-bearing steel very often exhibits a mixed structure consisting of coarse  $\alpha$  and upper bainite, thereby deteriorating the notch toughness. This is because niobium in solution retards transformation, and thereby suppresses the formation of  $\alpha$  and pearlite. When deformed

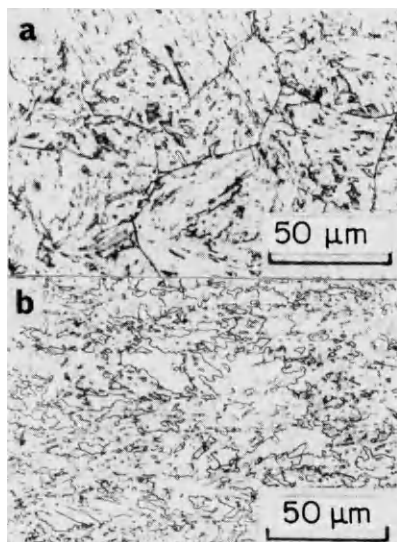


Figure 4.20 (a) Upper bainite structure; and (b) acicular  $\alpha$  structure produced by conventional hot-rolling and controlled-rolling respectively in 0.06% C–0.2% Si–1.96% Mn–0.42% Mo–0.06% Nb steel. (After Tanaka<sup>6</sup>)

in the nonrecrystallization region, however, niobium-bearing steel gives a fine  $\alpha$  grain structure dispersed with pearlite, thereby improving the notch toughness remarkably, as can be inferred from the continuous-cooling-transformation curves shown in Figure 4.18. In other words, deformation in the nonrecrystallization region changes hardenable steel into less hardenable steel through the enhancement of  $\alpha$  transformation.

- (2) The second application is the acicular  $\alpha$ . The acicular  $\alpha$  steel is obtained by the controlled-rolling of low carbon–manganese–molybdenum–niobium steel and its microstructure consists of fine nonequiaxed  $\alpha$  grains dispersed with small cementite and martensite islands, as seen in Figure 4.20(b)<sup>6</sup>. When the same steel is conventionally hot-rolled or normalized, it shows a typical upper bainitic structure, exhibited in Figure 4.20(a).<sup>6</sup>

The acicular  $\alpha$  is defined as a highly substructured, nonequiaxed phase that forms on continuous cooling by a mixed diffusion and shear mode of transformation at a temperature slightly higher than the upper bainite transformation range.<sup>32</sup> With the progress of transformation, the temperature of material decreases whereby the transformation mode becomes shear-dominated.

There is no distinction between acicular  $\alpha$  transformation and bainite transformation. Acicular  $\alpha$  is different from bainitic  $\alpha$  with respect to the prior  $\gamma$  grain boundary network and cementite and martensite morphologies. In the bainitic structure, the prior  $\gamma$  grain boundary network is retained and platelike cementites are formed at coarse lath boundaries as well as the prior grain boundaries; in the acicular  $\alpha$  structure the prior  $\gamma$  grain boundary network is completely eliminated having a fine-grained structure, and small cementite and martensite islands are scattered throughout the matrix (Figure 4.20).

In diffusionless transformation products, notch toughness generally deteriorates and transition temperature increases with the increase in transformation temperature, i.e. the transition temperature is the lowest in martensite, with lower bainite

and upper bainite being the next lowest. Though the starting temperature of transformation is higher for acicular  $\alpha$  than for upper bainite, the transition temperature is much lower for the former than for the latter. Because of the before-mentioned difference in microstructure between bainite and acicular  $\alpha$ , there is a distinct difference in brittle fracture facet unit which, in turn, causes a large difference in transition temperature between the two. In the bainitic structure, a facet unit is nearly equal to the prior  $\gamma$  grain size, whereas in acicular  $\alpha$  a facet unit is much smaller than the prior  $\gamma$  grain size, giving lower transition temperature.

- (3) The third application is the dual-phase steel which has microstructure consisting of  $\alpha$  grains dispersed with fine martensite islands. It is characterized by continuous yielding, followed by rapid work-hardening, which results in low yield but high tensile strength and large elongation, thereby bestowing superior formability.<sup>33-37</sup>

Dual-phase steel can be produced in as-hot-rolled condition by the suitable combination of chemical composition and rolling condition.<sup>23,25,38-41</sup> When hardenable steel is control-rolled, thereby accelerating  $\gamma \rightarrow \alpha$  transformation, microstructure becomes a mixture consisting of polygonal  $\alpha$  and untransformed  $\gamma$ . With the progress of  $\gamma \rightarrow \alpha$  transformation, interstitial carbon and nitrogen atoms diffuse from  $\alpha$  to  $\gamma$  and thereby scavenge the  $\alpha$  matrix on the one hand and stabilize untransformed  $\gamma$  through enrichment of carbon and nitrogen on the other. On cooling, stabilized  $\gamma$  transforms to martensite at low temperatures and/or remains untransformed. In order to obtain the dual-phase structure in the as-hot-rolled condition, it is desirable to contain both strong-forming elements like silicon and transformation-delaying elements such as manganese, chromium and/or molybdenum.<sup>25</sup> The coexistence of the two types of elements with the opposite character causes separation of  $\gamma$  into  $(\gamma + \alpha)$  two-phases, which is to a high degree enhanced by the deformation in the nonrecrystallization region.<sup>25</sup>

Figure 4.21<sup>25</sup> illustrates the effect of deformation in the nonrecrystallization region on continuous-cooling-transformation behaviour in 0.05% C–1.0% Si–1.5% Mn–1.0% Cr steel. In strain-free  $\gamma$  the  $\alpha$ -forming region is narrow, followed by a wide region of bainite formation. The transformation behaviour of deformed  $\gamma$  has two characteristics: (1) enhancement of  $\alpha$  formation; and (2) suppression of bainite formation, leading to martensite formation from untransformed  $\gamma$ . The  $\alpha$ -forming temperature is raised and  $\alpha$ -starting time is shortened, which is more remarkable with the increasing amount of deformation. With the increase in the amount of deformation whereby the  $\alpha$ -forming region is enlarged, the bainite-forming region is shifted to a shorter time, which makes it easy to cause a  $\alpha$ -martensite dual-phase structure. It is also to be noted that pearlite formation is less retarded in deformed  $\gamma$ . Thus, in heavily deformed  $\gamma$  there is a wide region where  $\alpha$  and untransformed  $\gamma$  coexist, which is very convenient for the production of dual-phase steel in as-hot-rolled coil. The optimum processing for obtaining dual-phase steel strip is shown in Figure 4.22;<sup>25</sup> controlled-rolled strip is supercooled appropriately and held at that temperature for  $\alpha$  formation, and then rapidly cooled to coiling temperature. In the coiled state, the enrichment of the  $\gamma$  phase with carbon and nitrogen occurs, thereby scavenging the  $\alpha$  matrix on the one hand and stabilizing untransformed  $\gamma$  on the other. During the gradual cooling of hot coil,  $\gamma$  transforms to martensite.

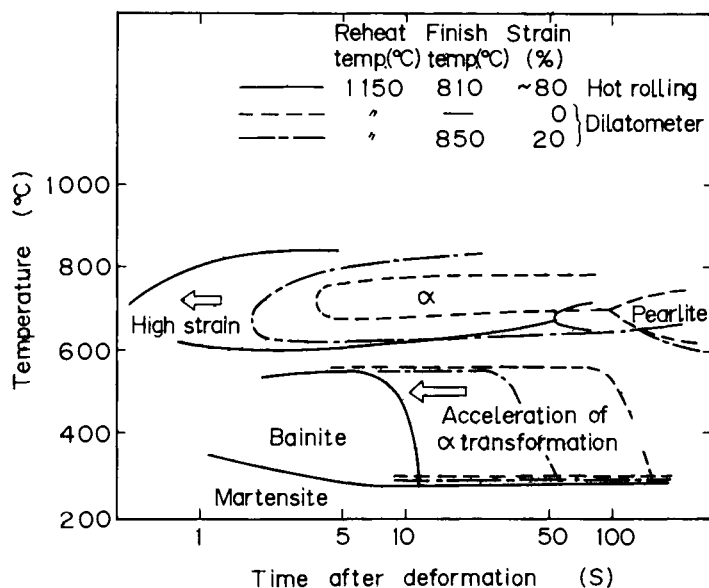


Figure 4.21 Effect of the amount of deformation in the nonrecrystallization region on the transformation kinetics in 0.05% C-1.0% Si-1.5% Mn-1.0% Cr steel; 0% and 20%, and 80% deformations were given by dilatometer with compression device, and hot-strip mill respectively. (After Mano *et al.*<sup>25</sup>)

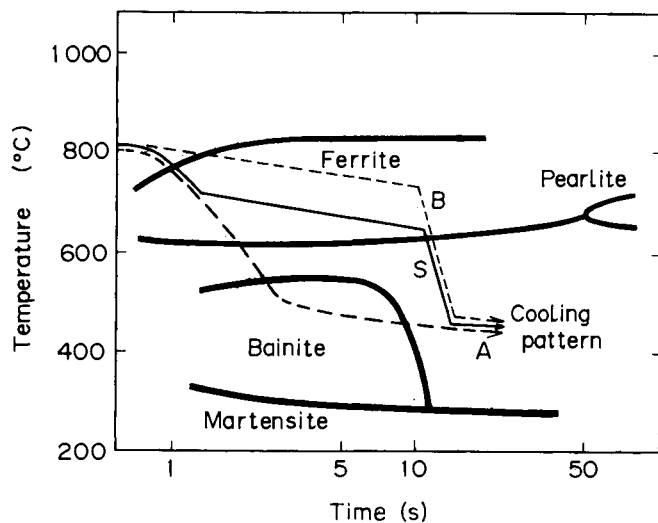


Figure 4.22 Various cooling patterns are superimposed on a continuous-cooling diagram of 0.05% C-1.0% Si-1.5% Mn-1.0% Cr steel deformed in the low-temperature  $\gamma$  region. In pattern S, deformed  $\gamma$  is supercooled to a certain temperature to accelerate  $\alpha$  formation, followed by rapid cooling to coiling temperature. Patterns A and B are not effective in producing dual-phase structure. (After Mano *et al.*<sup>25</sup>)

## References

1. SEKINE, H. and MARUYAMA, T. *Seitetsu Kenkyu*, 289, 11920 (1976)
2. KOZASU, I., SHIMIZU, T. and KUBOTA, H. *Trans Iron and Steel Inst. Japan*, **11**, 367 (1971)
3. FUKUDA, M., HASHIMOTO, T. and KUNISHIGE, K. *Microalloying 75*, Union Carbide Corp., p.136 (1977)
4. KOZASU, I., OUCHI, C., SANPEI, T. and OKITA, T. *Microalloying 75*, Union Carbide Corp., p.120 (1977)
5. TANAKA, T., TABATA, N., HATOMURA, T. and SHIGA, C. *Microalloying 75*, Union Carbide Corp., p.107 (1977)
6. TANAKA, T. *Intl. Metals Rev.*, **4**, 185 (1981)
7. YAMAMOTO, S., OUCHI, C. and OSUKA, T. *Thermomechanical processing of microalloyed austenite*, American Institute of Mining, Metallurgical, and Petroleum Engineers, p.613 (1982)
8. JONAS, J.J. and AKBEN, M.G. *Metal Forum*, **4**, 92 (1981)
9. JONAS, J.J. and WEISS, I. *Met. Sci.*, **13**, 238 (1979)
10. OUCHI, C., OKITA, T., SANPEI, T. and KOZASU, I. *Tetsu-to-Hagané*, **63**, A53 (1977)
11. KAJI, H., KATSUMATA, M., MACHIDA, M. and KINOSHITA, S. *Tetsu-to-Hagané*, **60**, S295 (1974)
12. SEKINE, H., MARUYAMA, T. and KAWASHIMA, Y. *Tetsu-to-Hagané*, **60**, S557 (1974)
13. MORRISON, W.B. and CHAPMAN, J.A. *Philos. Trans Roy. Soc.*, **282A**, 289 (1976)
14. OUCHI, C., SANPEI, T., OKITA, T. and KOZASU, I. *The hot-deformation of austenite*, American Institute of Mining, Metallurgical, and Petroleum Engineers, p.316 (1977)
15. TANAKA, T. *J. Soc. Materials Sci. Japan*, **30**, 611 (1980)
16. BARRETT, C.S. *Structure of metals* (2nd edn), pp.372 and 453, McGraw-Hill (1952)
17. DILLAMORE, I.L., MORRIS, P.L., SMITH, C.J.E. and HUTCHINSON, W.B. *Proc. Roy. Soc.*, **329A**, 405 (1972)
18. KREISLER, A. and DOHERTY, R.D. *Metal Sc.*, **12**, 551 (1978)
19. HU, H. *Recovery and recrystallization of metals*, Gordon and Breach, p.311 (1963)
20. INOKUTI, Y. and DOHERTY, R.D. *Acta Met.*, **26**, 61 (1978)
21. INAGAKI, H. *Trans. Iron and Steel Inst. Japan*, **23**, 1059 (1983)
22. UMEMOTO, M., TAMURA, I. and OTSUKA, H. *Tetsu-to-Hagané*, **68**, S1384 (1982)
23. COLDREN, A.P. and TITHER, G. *J. Metals*, **30**, 4, 6 (1978)
24. HASHIMOTO, T., SAWAMURA, T. and OHTANI, H. *Tetsu-to-Hagané*, **65**, 1589 (1979)
25. MANO, J., NISHIDA, M., TANAKA, T., KATO, T., AOYAGI, N. and YAMADA, N. *Tetsu-to-Hagané*, **68**, 1297 (1982)
26. MACKENZIE, C.R. and YOUNG, R.W. *J. Iron and Steel Inst.*, **209**, 918 (1971)
27. SAITO, Y., and TANAKA, T. *Tetsu-to-Hagané*, **61**, S211 (1975)
28. SMITH, Y.E. and SIEBERT, C.A. *Metall. Trans*, **2**, 1711 (1971)
29. FUKUDA, M., HASHIMOTO, T. and KUNISHIGE, K. *Tetsu-to-Hagané*, **58**, 1832 (1972)
30. TANAKA, T. and TABATA, N. *Tetsu-to-Hagané*, **64**, 1353 (1978)
31. ROBERTS, W., LIDEFELT, H. and SANDBERG, A. *Hot-working and forming processes*, The Metals Society, p.38 (1980)
32. SMITH, Y.E., COLDREN, A.P. and CRYDERMAN, R.L. *Toward improved ductility and toughness*, Climax Molybdenum Company (Japan), p.119 (1952)
33. HAYAMI, S. and FURUKAWA, T. *Microalloying 75*, Union Carbide Corp., p.311 (1975)
34. RASHID, M.S. SAE Paper No. 760206 (1976); No. 770211 (1977) Society of Automotive Engineers, Inc.
35. DAVIES, R.G. *Metall. Trans*, **9A**, 41 (1978)
36. DAVIES, R.G. and MAGEE, G.L. *Structure and properties of dual-phase steels*, Vol. I, American Institute of Mining, Metallurgical and Petroleum Engineers, p.1 (1979)
37. TANAKA, T., NISHIDA, M., HASHIGUCHI, K. and KATO, T. *Structure and properties of dual-phase steels*, Vol. I, American Institute of Mining, Metallurgical and Petroleum Engineers, p.221 (1979)
38. SUDO, M. and IWAI, T. *Tetsu-to-Hagané*, **68**, 1185 (1982)
39. SUGISAWA, S., HAMAMATSU, S., KIKUCHI, K. and KUNISHIGE, K. *Tetsu-to-Hagané*, **68**, 1256 (1982)
40. OKITA, T., HOSOYA, Y. and NAKAOKA, K. *Tetsu-to-Hagané*, **68**, 1313 (1982)
41. FURUKAWA, T., TANINO, M., MORIKAWA, H. and ENDO, M. *Tetsu-to-Hagané*, **68**, 1323 (1982)

---

## Deformation in the (austenite plus ferrite) two-phase region

---

### 5.1 Deformation behaviour of the ( $\gamma + \alpha$ ) two-phase region

A limiting  $\gamma$  grain size achieved by deformation in the recrystallization region is broken by deformation in the nonrecrystallization region. Grain refinement due to deformation in the nonrecrystallization region reaches a limiting value at 60–70% reduction. This limit can be broken only by deformation in the ( $\gamma + \alpha$ ) two-phase region. Besides grain refinement, deformation in the two-phase region has a substantially different effect on microstructure and mechanical properties. Microstructural change caused by deformation in the two-phase region has already been shown schematically in Figure 4.2 (page 81).

In order to know the effect of deformation in the two-phase region, two factors must be known: (1) the variation in properties with a fraction of deformed  $\alpha$  at a constant amount of deformation; and (2) the amount of deformation at a constant fraction of deformed  $\alpha$ . Figure 5.1(a) and (b)<sup>1</sup> shows the changes in yield and tensile strengths, and toughness properties with deformation in the two-phase region in plain carbon steel and niobium steel respectively, where the amount of deformation was varied at a constant volume fraction of  $\alpha$ . With increasing amounts of deformation, yield and tensile strengths increase, while 50% shear fracture appearance transition temperature (FATT) and the impact energy decrease in both steels. There is a rapid increase in strength in the initial stage of deformation followed by gradual increase. Increases in yield and tensile strengths are larger for niobium steel than for plain carbon steel. This is because niobium carbonitrides in the former retard recrystallization more effectively and thereby cause a larger controlled-rolling effect.

Microstructural change caused by deformation in the two-phase region is shown in Figure 5.2.<sup>1</sup> Deformation in the  $\gamma$  region alone produces a microstructure consisting of equiaxed  $\alpha$  grains with low dislocation density (Figure 5.2(a) and (b)). Deformation in the two-phase region produces a mixed grain structure, which consists of equiaxed  $\alpha$  grains and ‘cold-worked’ grains in terms of an optical microscopic scale or of polygonal grains and subgrains in terms of an electron microscopic scale (Figure 5.2(c) and (d)). The deformed  $\gamma$  transforms to polygonal  $\alpha$  grains, while the deformed  $\alpha$  changes into cells and/or subgrains depending on the degree of recovery. In deformed  $\alpha$ , recrystallization is very sluggish, producing cells and/or subgrains. This is because of the stabilization of the sub-boundary network due to strain-induced precipitation of

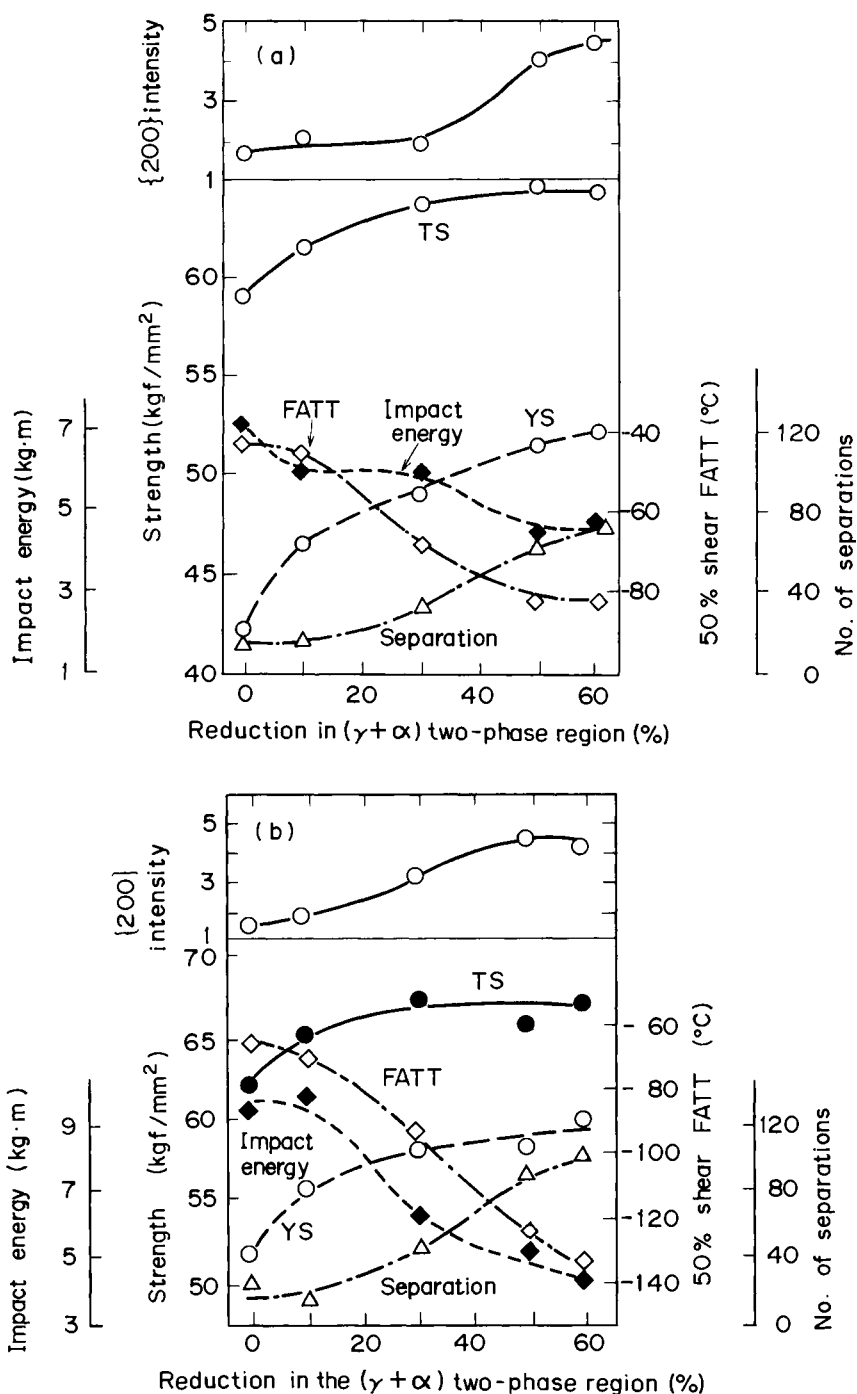


Figure 5.1 Intensity of {200} reflection, tensile properties, and the Charpy impact properties plotted against amount of reduction in the  $(\gamma + \alpha)$  region in: (a) plain carbon steel; and (b) niobium steel; reductions of 62.5% at 1020°C and 50% at 850°C, and various amounts of hot-deformation at 710°C were given successively. (After Tanaka *et al.*<sup>1</sup>)



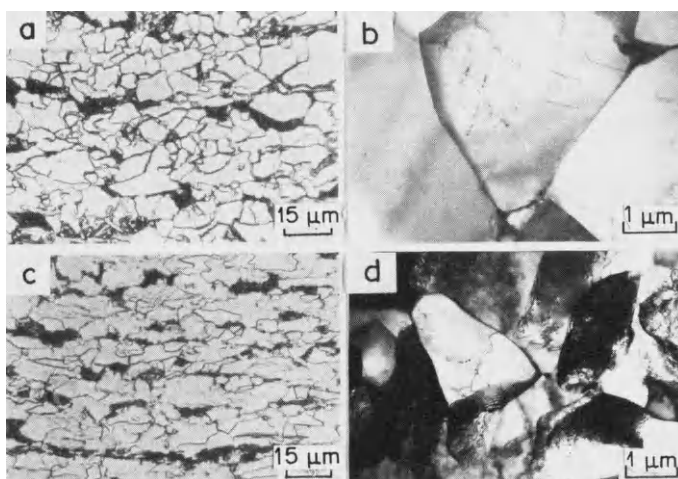


Figure 5.2 Change in microstructure with amount of reduction in the  $(\gamma + \alpha)$  region in niobium steel. Reductions are 0% and 30% for (a) and (b), and (c) and (d) respectively. (After Tanaka *et al.*<sup>1)</sup>)

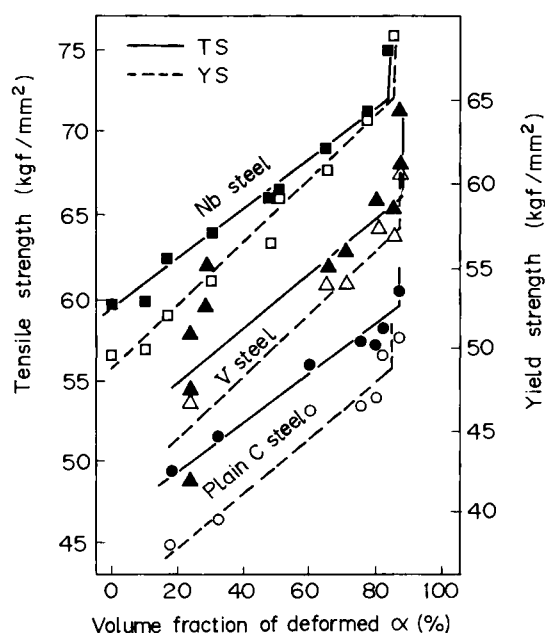


Figure 5.3 Relation between volume fraction of deformed  $\alpha$  and tensile properties of steels 50% rolled in the  $\gamma$ - $\alpha$  region in plain carbon, vanadium and niobium steels. (After Hashimoto, Sawamura and Ohtani<sup>7)</sup>)

niobium carbonitrides and/or vanadium carbonitrides.<sup>2-5</sup> It is postulated that during rolling,  $\gamma \rightarrow \alpha$  transformation can occur on the unrecovered dislocation substructure.<sup>6</sup> Thus, newly formed  $\alpha$  grains soon impinge on existing  $\alpha$  grains and cannot grow further. This kind of mutual interaction between deformed  $\gamma$  and  $\alpha$  produces a further decrease in  $\alpha$  grain size.

Figure 5.3 depicts a relation between the volume fraction of deformed  $\alpha$  and tensile properties in plain carbon, vanadium, and niobium steels, where the volume fraction of deformed  $\alpha$  was varied at constant amounts of deformation of 50%.<sup>7</sup> In each steel, yield and tensile strengths increase linearly with volume fraction of deformed  $\alpha$ , though the slope is smaller for plain carbon steel than for vanadium and niobium steels. In Figure 5.3, an increase in volume fraction is achieved by lowering the deformation temperature in the two-phase region, which increases the ease of recovery of deformed  $\alpha$ . In this respect, the change in the volume fraction of deformed  $\alpha$  causes the change in substructure of deformed  $\alpha$  which, in turn, has some effect upon mechanical properties.

In Figure 5.1, strengths increase gradually with increasing amount of deformation at high deformations, indicating that recovery is easier to proceed with increasing amounts of deformation. Coldren, Eldis and Tither<sup>8</sup> showed that the decrease in yield strength occurred due to partial or complete recrystallization of deformed  $\alpha$  in molybdenum–niobium steel when deformation exceeded a critical amount. Anyway, there is an optimum fraction of deformed  $\alpha$  and an optimum reduction to be applied below  $A_{r3}$ –30% and 20% in molybdenum–niobium steel for molybdenum and niobium respectively.<sup>8</sup>

The effects of volume fraction of deformed  $\alpha$  and amount of reduction upon mechanical properties seem to be different between Figures 5.1 and 5.3. This is because of the difference in the degree of precipitation hardening due to vanadium and/or niobium carbonitrides and in the degree of recovery and recrystallization. Substructure of deformed  $\alpha$  changes substantially, depending on such variables as deformation temperature, amount of deformation, reduction per pass, degree of precipitation, etc. Table 5.1 shows various restoration processes which are possibly operative during and after deformation of  $\alpha$ . With increasing amounts of deformation, dislocation density increases and the cell structure develops. When hot-deformation is performed near and beyond the peak stress in a stress–strain curve, the dynamic recovery occurs and thereby causes subgrain structure. After deformation, if material is held at high temperatures or slowly cooled, static recovery and/or recrystallization take place, thereby producing subgrain and/or polygonal grain structure. When deformation is performed below the peak stress and rapidly cools recovery progresses insufficiently, thereby producing cell structure. In plain carbon steel recovery occurs fairly rapidly, while in niobium steels, it is retarded by the stabilization of cell and subgrain boundaries due to the solute niobium drag effect and strain-induced precipitation of niobium carbonitrides. Strengthening due to deformed  $\alpha$  is larger in steels containing niobium

TABLE 5.1 Restoration processes during and after hot-deformation of  $\alpha$  and accompanied phenomena

| <i>Factor</i>       | <i>During hot-deformation</i>               | <i>After hot-deformation</i>  |
|---------------------|---|---|
| Restoration process | Dynamic recovery                            | Static recovery<br>Recrystallization  |
| Grain Structure     | Cell structure<br>Subgrain                  | Cell structure<br>Subgrain<br>Polygonal grain   |
| Precipitation       | Dynamic precipitation<br>at low strain rate | Strain-induced precipitation<br>of niobium carbonitrides<br>and/or vanadium carbonitrides |

and/or vanadium than in plain carbon steel, which results from the combined effect of retardation of recovery and precipitation hardening due to niobium carbonitrides, and vanadium carbonitrides.

Hot-deformation of  $\alpha$  is generally governed by dynamic recovery, though some investigators<sup>9,10</sup> reported the dynamic recrystallization. Figure 5.4 depicts stress-strain curves of plain carbon steel in the temperature range of 650–900°C.<sup>11</sup> In the  $(\gamma + \alpha)$  two-phase region from 650 to 750°C, flow stress increases very rapidly in the initial stage of straining, followed by gradual increase, finally arriving at the steady state. That there is no peak stress in stress-strain curves implies the operation of dynamic recovery instead of dynamic recrystallization in the steady-state region. Cell structure is formed in the work-hardening region, while subgrain structure is produced in the steady-state region, corresponding to the occurrence of dynamic recovery. In niobium steel, recovery is much more difficult, since solute niobium atoms have a strong retarding effect upon recovery.<sup>12,13</sup> In vanadium steel, however, recovery behaviour is similar to that of plain carbon steel, since solute vanadium atoms do not have a strong effect on recovery.<sup>12</sup>

In practice, multipass rolling is performed, where reduction per pass is much smaller than that for the commencement of dynamic recovery as shown in Figure 5.4. However, since strain continues to accumulate with the progress of multipass rolling, the total strain accumulated reaches the steady state, and thereby causes dynamic recovery. Therefore, there is no essential difference in the recovery behaviour between one-pass, and multipass, rolling.

So far, it has been shown that strengthening due to deformed  $\alpha$  results mainly from cell and/or subgrain hardening. When deformation temperature is high, and dynamic recovery and subsequent static recovery and recrystallization proceed, strengthening is mainly due to  $\alpha$  grain refinement, whereas when deformation temperature is low, and recovery and recrystallization are retarded, strengthening is mainly due to cell and/or subgrain structure, as shown in Table 5.1. Therefore, strengthening by the deformation in the two-phase region is dependent on the degree of recovery and recrystallization which is, in turn, dependent on deformation temperature, amount of deformation, cooling rate after deformation, and the addition of microalloying elements.

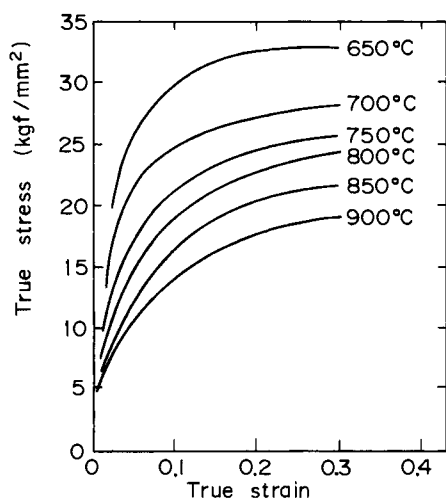


Figure 5.4 Effect of deformation temperature on stress-strain curves in 0.16% C-0.3% Si-1.9% Mn steel deformed at strain rate of  $7 \text{ s}^{-1}$ . (After Yamamoto, Okita and Ouchi<sup>11</sup>)

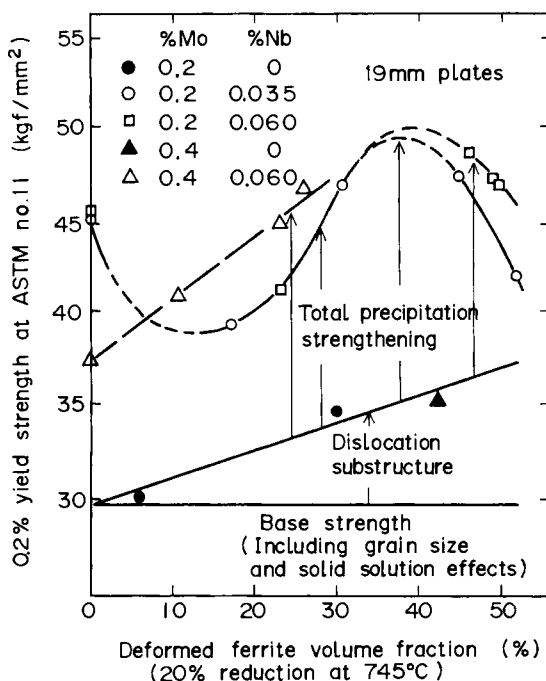


Figure 5.5 Variation of yield strength with increasing amounts of deformed  $\alpha$  with 20% deformation at 745°C. (After Coldren, Eldis and Tither<sup>8</sup>)

Besides the above-mentioned substructure hardening, there is heavy precipitation hardening due to strain-induced precipitation of niobium and vanadium carbonitrides. Figure 5.5 shows the influence of an increasing volume fraction of deformed  $\alpha$  on substructure hardening plus precipitation strengthening when the final reduction was held constant at 20%.<sup>8</sup> In molybdenum steel, yield strength increases in a linear manner with increasing volume fraction of deformed  $\alpha$ . The total precipitation strengthening, including strain-induced precipitation in the  $\alpha$  matrix after transformation, is quite different, depending on alloy content and the volume fraction of deformed  $\alpha$ . In 0.2% Mo-Nb steels, there is an optimum volume fraction where the maximum strength is obtained. Further increase in volume fraction results in a fall-off in strength. The fall-off is caused by a decrease in the contribution from niobium carbonitride precipitation strengthening resulting from excessive precipitation in the  $\gamma$  caused by the extra deformation employed to achieve the maximum amount of deformed  $\alpha$ .

## 5.2 Anisotropy and texture

When compared in terms of the same carbon equivalent, a controlled-rolled steel has greater strength than a conventionally hot-rolled one, and it exhibits a lower transition temperature than normalized, or quenched and tempered, steel. However, controlled-rolled steel has its own disadvantages, the most serious being the anisotropy in mechanical properties due to the texture development.

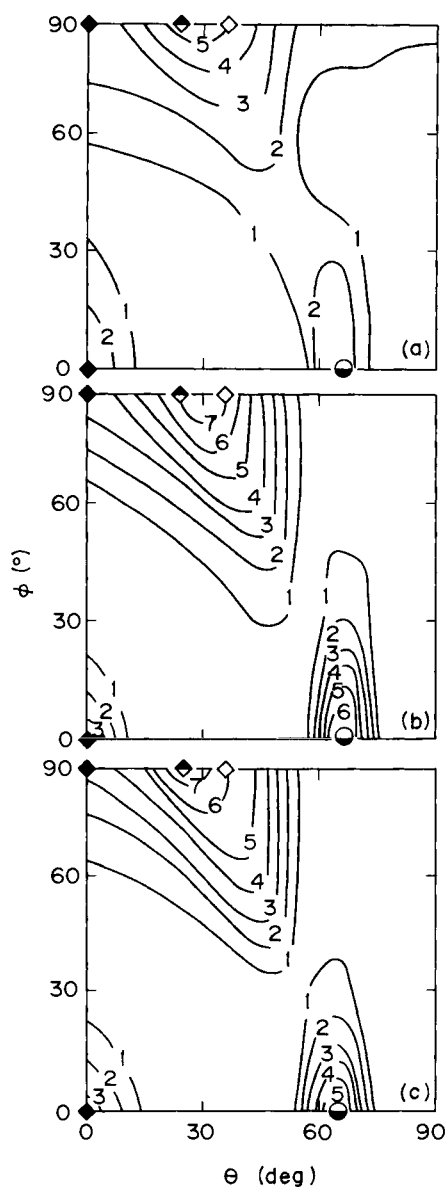


Figure 5.6 Sections at  $\phi = 45^\circ$  of crystallite orientation distributions, showing transformation textures of controlled-rolled steels with: (a) polygonal  $\alpha$ -pearlite; (b) acicular  $\alpha$ ; and (c) martensite:  $\blacklozenge$ :  $\{001\}\langle 110 \rangle$ ,  $\diamond$ :  $\{113\}\langle 1\bar{1}0 \rangle$ ,  $\circ$ :  $\{112\}\langle 1\bar{1}0 \rangle$ ,  $\bullet$ :  $\{332\}\langle 11\bar{3} \rangle$ . (After Yutori and Ogawa<sup>22</sup>)

In controlled-rolled steel a crystallographic texture develops,<sup>14-24</sup> whose magnitude depends on whether deformation is carried out in the nonrecrystallization region or in the two-phase region, or whether the microstructure consists of  $\alpha$  or bainite. Yutori and Ogawa<sup>22</sup> reported that, even when deformation in the nonrecrystallization region is given under the same rolling conditions, the intensity in texture differs, depending on transformed microstructure (Figure 5.6).<sup>22</sup> All three structures exhibit a similar texture, consisting of  $\langle 110 \rangle // \text{RD}$  (rolling direction) orientations with the strongest component of and  $\{332\} \langle 11\bar{3} \rangle$ . However, there is a remarkable difference in intensity between  $\{113\} \langle 1\bar{1}0 \rangle$  polygonal  $\alpha$ -pearlite and acicular  $\alpha$  or martensite. When steel

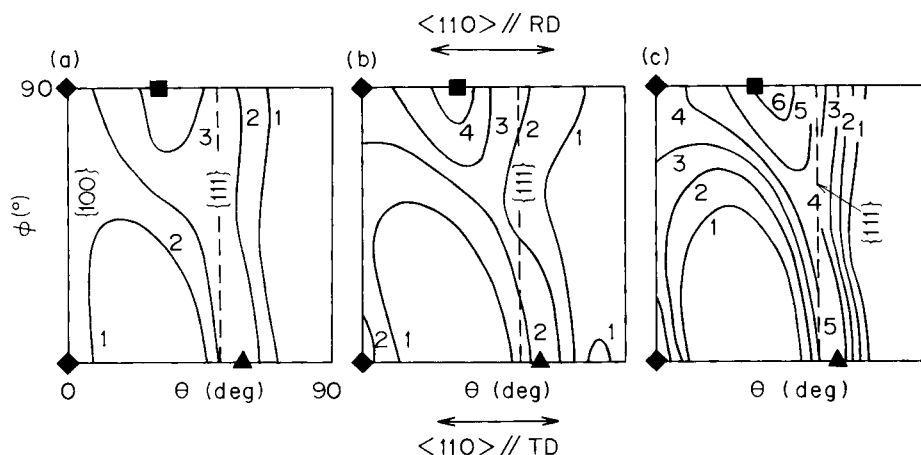


Figure 5.7  $\phi = 45^\circ$  of crystallite orientation distribution function for steel deformed in the nonrecrystallization region and subsequently in the  $(\gamma + \alpha)$  region; deformations in the  $(\gamma + \alpha)$  region were: (a) 0%; (b) 10%; and (c) 60%;  $\blacklozenge$ :  $\{001\} \langle 110 \rangle$ ,  $\blacksquare$ :  $\{112\} \langle 110 \rangle$ , and  $\blacktriangle$ :  $\{554\} \langle 225 \rangle$ . (After Tanaka<sup>15</sup>)

has a low manganese and/or nickel content, producing an  $\alpha$  structure, it shows a weak texture intensity. However, with an increasing manganese and/or nickel content the microstructure becomes bainitic, developing a texture with  $\{332\} \langle 11\bar{3} \rangle$  and  $\{311\} \langle 01\bar{1} \rangle$  orientations.<sup>22</sup>

As shown in Figure 5.2,  $\alpha$  phase deformed in the two-phase region remains mainly in the recovered condition in niobium steel. This means that the texture developed by deformation in the two-phase region is the 'cold-rolled' texture. One example of texture developed by deformation in the two-phase region is shown in Figure 5.7.<sup>15</sup> Exhibiting a  $\alpha$ -pearlite structure, the three have basically the same texture, the intensity being raised with an increasing reduction in the two-phase region. A weak texture with  $\{112\} \langle 110 \rangle$  and  $\{554\} \langle 225 \rangle$  components develops as a result of heavy deform-

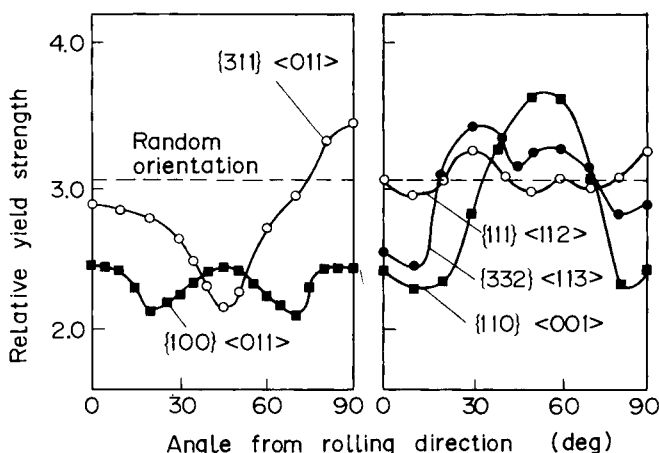


Figure 5.8 Anisotropies of relative yield strength calculated for  $\langle 110 \rangle // \text{RD}$  ideal orientation. (After Inagaki, Kurihara and Kozasu<sup>23</sup>)

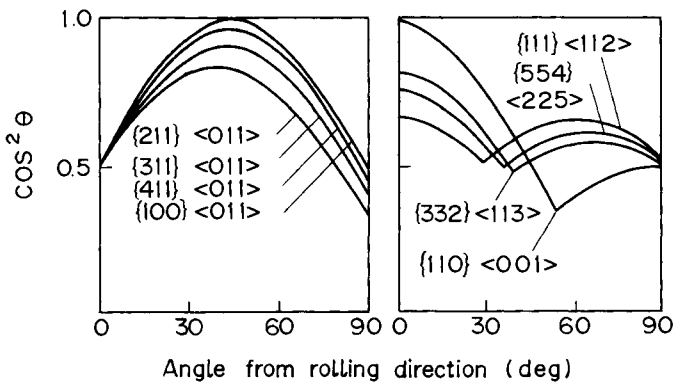


Figure 5.9 Anisotropies of orientation factor for brittle fracture,  $\cos^2\theta$ , calculated for various ideal orientations.  $\theta$  is the angle between the test direction and normal to plane. (After Inagaki, Kurihara and Kozasu<sup>23</sup>)

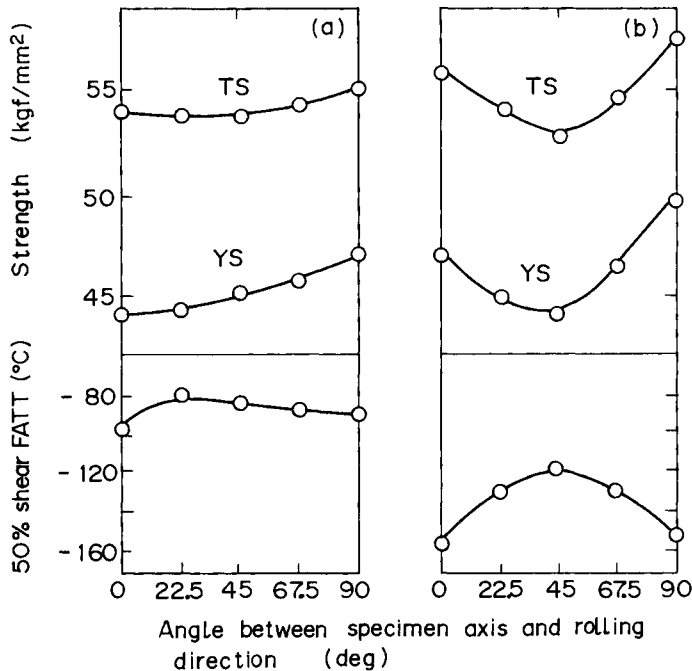


Figure 5.10 Anisotropies of strength and 50% shear FATT: finish-rolled in (a) nonrecrystallization region; and (b)  $(\gamma + \alpha)$  region. (After Tanaka<sup>15</sup>)

ation in the  $\gamma$  region alone. Deformation in the two-phase region produces textures consisting of: (1)  $\langle 110 \rangle // \text{RD}$  partial fibre texture; (2)  $\langle 100 \rangle // \text{ND}$  (normal direction, where the  $\langle 100 \rangle$  axis is perpendicular to the plate surface) texture; and (3) texture with a strong  $\{554\} \langle 225 \rangle$  component. Texture (3) does not have a detrimental effect on mechanical properties, but (1) causes plane anisotropy and (2) causes embrittlement in the through-thickness (Z) direction. The plane anisotropy in mechanical properties caused by the  $\langle 110 \rangle // \text{RD}$  texture was examined theoretically and experimentally by



Inagaki, Kurihara and Kozasu<sup>23</sup> and Inagaki.<sup>24</sup> In Figure 5.8, yield strength is plotted against the angle made between the text direction and the rolling direction calculated for various ideal orientations, where yield strength is expressed in terms of relative strength.<sup>23</sup> Though yield strength differs much more depending on orientation and angle,  $\{311\} \langle 01\bar{1} \rangle$  orientation (which develops most strongly by deformation in the  $\gamma$  region alone or in the two-phase region) shows the largest angle-dependence. Figure 5.9 depicts a relation between the toughness parameter and the angle calculated for various ideal orientations, where toughness is represented in terms of normal stress acting on the cleavage surface, i.e. the  $\{100\}$  plane.<sup>23</sup> The diagonal ( $45^\circ$ ) direction has low strength but high susceptibility to cleavage fracture (high transition temperature). The longitudinal (L) ( $0^\circ$ ) and transverse (T) ( $90^\circ$ ) directions exhibit high strength and low susceptibility to cleavage fracture (low transition temperature). Figure 5.10 shows plane anisotropy developed in steels finished-rolled in the nonrecrystallization region or in the two-phase region.<sup>15</sup> The former develops a weak texture, showing indistinct anisotropy, while the latter develops strong plane anisotropy due to an intensive texture, which is in good agreement with the theoretical predictions shown in Figures 5.8 and 5.9.

### 5.3 Separation

Embrittlement in the Z direction resulting mainly from the formation of texture is more serious than plane anisotropy in controlled-rolled steel. Figure 5.11 shows

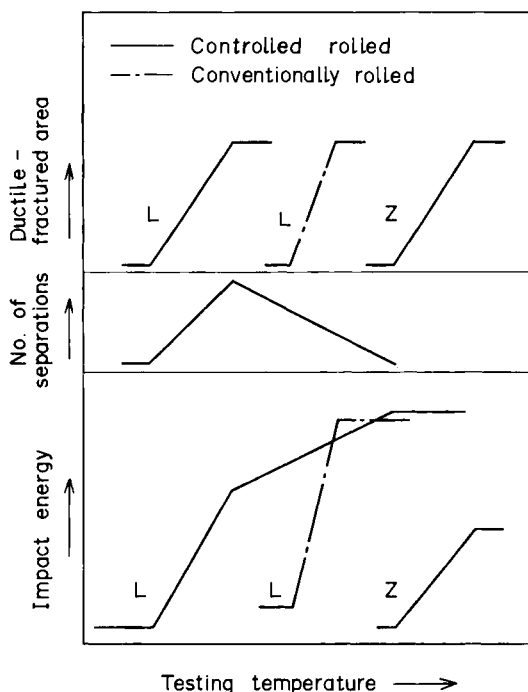


Figure 5.11 Schematic representation of the Charpy transition curves in longitudinal (L) and through-thickness (Z) directions of controlled-rolled steel. (After Kozasu<sup>25</sup>)

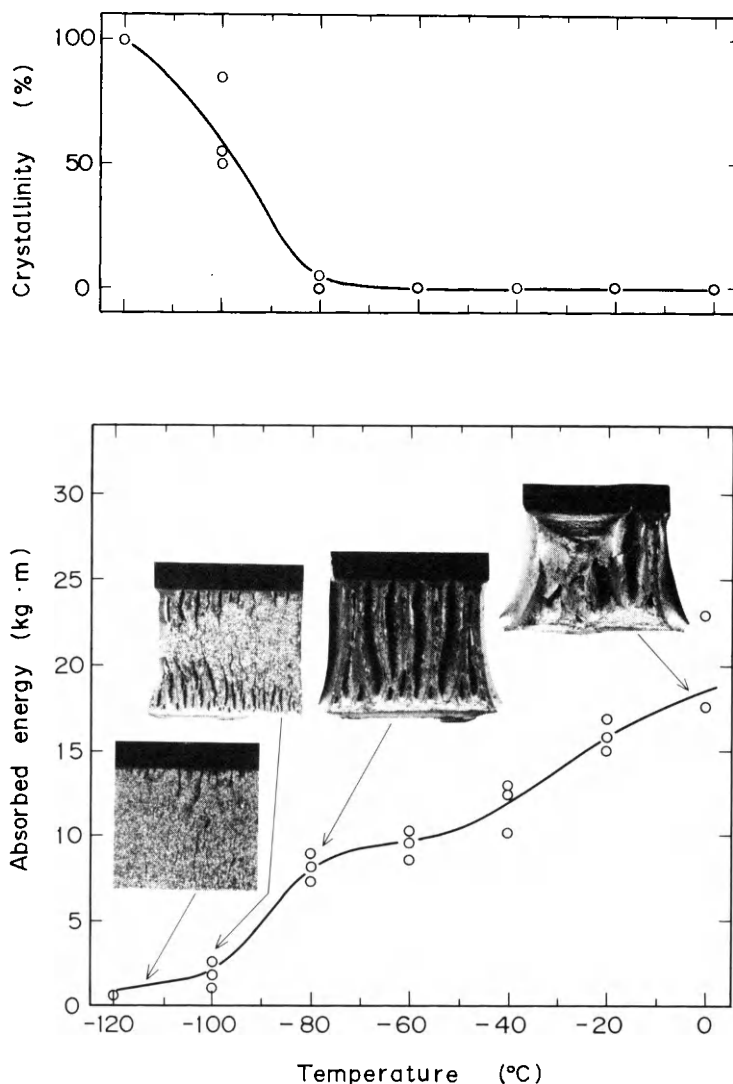


Figure 5.12 The Charpy transition curves and occurrence of separations in steels deformed in the  $(\gamma + \alpha)$  region

schematically the Charpy transition curves and number of separations in the L and Z directions, where curves of the T direction are located near those of the L direction.<sup>25</sup> The difference in transition temperature between the L and Z directions is more than 100° K. The low transition temperature in the L direction is due to separations (very often called delamination or splitting) which occur in a brittle manner in a fractured Charpy specimen parallel to the plate surface.<sup>16,21,26-29</sup> As shown in Figure 5.12, the number of separations is the greatest near the temperature where the ductile-fractured area becomes just 100%, being nil in the brittle range or at high temperatures.<sup>14</sup> In contrast to conventionally hot-rolled steel, the Charpy impact energy of controlled-rolled steel increases with increasing temperature even in the ductile-fracture region,

while the number of separations decreases. Impact energy reaches the shelf energy and separations disappear when temperature reaches the transition temperature in the Z direction.

The occurrence of separations, accompanied by the lowering of transition temperature, has been explained in terms of the critical stress criterion.<sup>30,31</sup> When the Charpy specimen is given a bending force, the maximum stresses are induced at the plastic-elastic interface just beneath a notch under the plane-strain condition, as shown in Figure 5.13.<sup>32</sup> Induced stress is the greatest in the L direction, followed by the Z and T directions, when a longitudinal specimen is considered. The condition for the occurrence of separation is given by:

$$\sigma_f^L > \sigma_{yy} \quad (5.1)$$

$$\sigma_f^Z = \sigma_{zz} \quad (5.2)$$

where  $\sigma_f^L$  and  $\sigma_f^Z$  are the cleavage fracture strengths in the L and Z directions, and  $\sigma_{yy}$  and  $\sigma_{zz}$  are the stresses acting in the L and Z directions, respectively.

As is clear from Equations (5.1) and (5.2), separation occurs only when there is anisotropy in the fracture strength, i.e. only when fracture strength is lower for the Z direction than for the L direction. As the occurrence of separation changes the stress state from plane strain to plane stress, it becomes more difficult for brittle fracture to occur. Embury *et al.*<sup>33</sup> and Miyoshi *et al.*<sup>27</sup> have reported that separated material

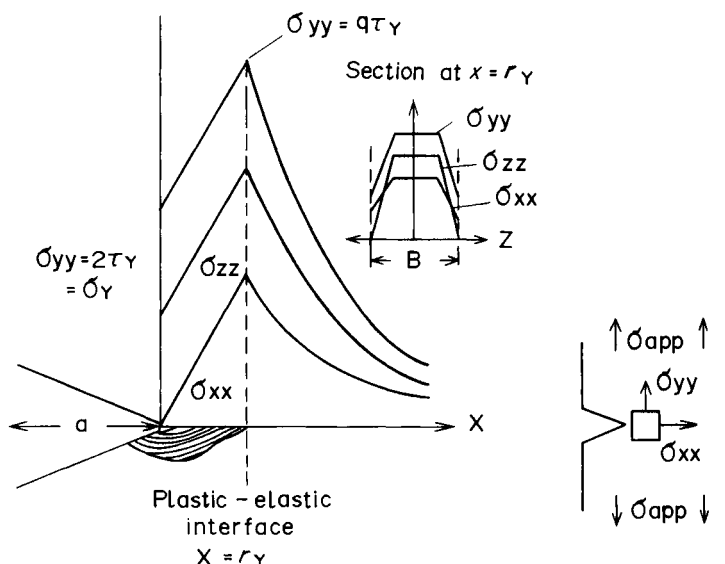


Figure 5.13 Distribution of principal stresses in the Charpy specimen in plane strain condition where the maximum stress is induced at plastic-elastic interface. (After Kott<sup>32</sup>)

behaves in a similar manner to that of laminated plate.

Through-thickness embrittlement has been studied by many investigators,<sup>21,27-41</sup> and the following causes have been suggested:

- (1) A crack starts at a manganese sulphur inclusion which has been flattened by low-temperature finish-rolling, and develops along grains with  $\{100\}$  orientation and/or a banded structure.<sup>34,38,39</sup>
- (2) The clusters of crystal grains with  $\{100\}$  orientation are the main sources of separation cracks,<sup>27,28,36</sup> (since separations occur even in steel with an extremely low sulphur content).<sup>42</sup> This is strongly supported by the observation that separation increases with increasing intensity in the  $\{100\}$  texture.
- (3) Intergranular failure along prior  $\gamma$  boundaries, probably embrittled by the segregation of impurities, increases the occurrence of separations.
- (4) Temper embrittlement caused by the segregation of phosphorus from matrix to  $\alpha$  grain boundaries in the rich layer during slow cooling after coiling reduces boundary toughness in hot-rolled strip.<sup>39</sup>
- (5) Dimensional anisotropy of the microstructure produced by controlled-rolling –  $\gamma$  grain in the case of the intergranular fracture, and  $\alpha$  grain in the case of transgranular fracture – is the main cause of through-thickness embrittlement.<sup>31,35,37</sup>
- (6) Pearlite and/or a bainite banded structure.<sup>41</sup>
- (7) A combination of effects (1)–(6).<sup>35,36</sup>

Matsuda *et al.*<sup>29</sup> have proposed a quite different and unique interpretation for the formation mechanism of the separation. Colonies of crystal grains with  $\{110\}$  orientation and  $\{111\}$  orientation develop in parallel to the rolling plane in steel deformed in the two-phase region (Figure 5.14). The colony size increases with increasing intensity of the texture, arriving at  $100\mu\text{m}$  in severely deformed material. When the Charpy specimen is given a bending force, plastic deformation occurs just beneath a notch preceding the formation of the main crack. As the  $\{100\}$  colony and the  $\{111\}$  colony

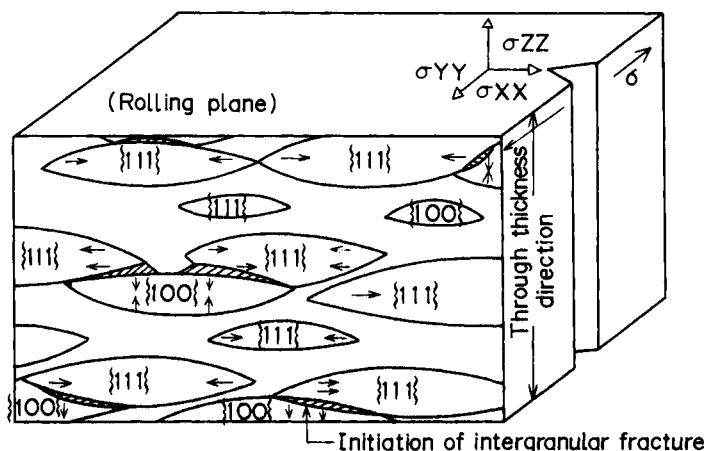


Figure 5.14 Schematic illustration of the formation mechanism of separation. Cracks initiate at boundaries between  $\{100\}$  and  $\{111\}$  colonies due to strain anisotropy. Arrows indicate direction of maximum shear strain. (After Matsuda *et al.*<sup>29</sup>)

have strain anisotropy, the grain boundary between the  $\{100\}$  colony and the  $\{101\}$  colony becomes difficult to maintain under the increasing degree of deformation, thereby initiating crack nuclei there. That is, the  $111\{100\}$  colony is easily contracted in the Z direction, whereas it is very difficult for the  $\{111\}$  colony to be contracted in the Z direction, though it is easy for it to be contracted in the T direction; with increasing bending the deformation crack has a propensity to initiate at colony boundaries. Once initiated, the crack develops along colony boundaries in material with a strong texture, or along the  $\{100\}$  plane in a brittle manner in material with a weak texture. To support this interpretation, Matsuda *et al.* showed that the depth of separation was nearly equal to plastic zone size, and that though brittle fracture strength in the Z direction decreases with the development of texture, the ratio of brittle fracture strength in the Z direction to that in the L direction was  $\sim 0.8$  even in specimens severely deformed in the two-phase region, which makes it difficult to satisfy the condition of Equations (5.1) and (5.2).

The mechanism initiating separation may depend on chemical composition, micro-structure and hot-rolling condition. When stress is induced in the Z direction, a crack initiates at the place where the fracture strength is the lowest, and develops along the second-weakest location. When flattened manganese sulphide exists in steel, it triggers the initiation of a crack, which develops along grains with  $\{100\}$  orientation and/or bainite and/or the pearlite band, depending on the situation. If manganese sulphide exists very rarely in steel with an extremely low sulphur content, separation will be initiated at the second-weakest location.

Separation has a marked effect on transition temperature and absorbed energy. The latter is influenced most markedly near the temperature where shear area becomes just 100%, i.e. exhibiting the greatest number of separations.<sup>25,27</sup> As shown in Figure 5.15, both absorbed energy and 50% shear FATT decrease with the increasing number of separations.<sup>1</sup> As is clear from the above explanation, the low-temperature toughness in the L and T directions is improved by the sacrifice of that in the Z direction.

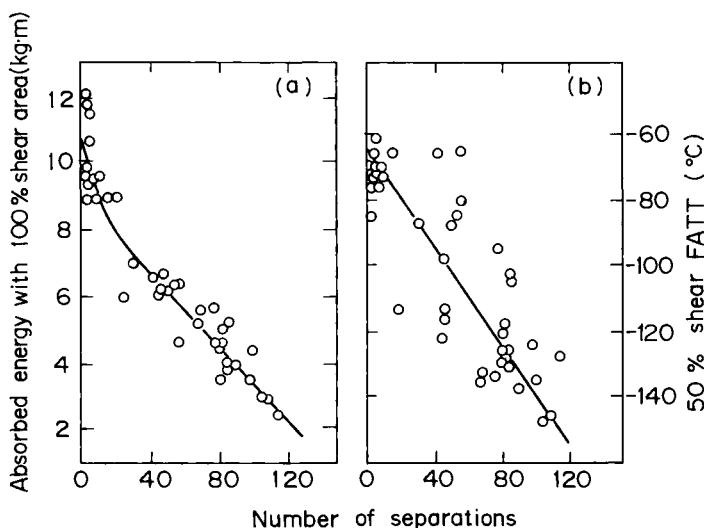


Figure 5.15 Influence of number of separations on: (a) absorbed energy with 100% shear area; and (b) 50% shear FATT in controlled-rolled steels. (After Tanaka *et al.*<sup>1</sup>)

## 5.4 Elimination of separation

Various methods have been proposed to prevent the occurrence of separations.<sup>1,41,43,44</sup> In order to eliminate flattened manganese sulphide which triggers the initiation of separations, inclusion-shape control has been employed, which converts elongated sulphide to a globular inclusion by the addition of rare earth metals<sup>43,45</sup> and/or calcium.<sup>44,46</sup> Advancing the sulphide-shape control technique, a new desulphurization method has been developed, which can reduce sulphur content to an extremely low level. Finish-rolling in the  $\gamma$  region results in the formation of a weak  $\{100\}$  texture, suppressing markedly the occurrence of separation. A decrease in phosphorus content is desirable, since it causes temper embrittlement during slow cooling after coiling in hot-rolled strip.<sup>39</sup> Once initiated, separation has a propensity to propagate along the banded structure.<sup>41</sup> Mori *et al.*<sup>41</sup> have reported that the occurrence of separation is determined by the combined effect of band density and  $\{100\}$  intensity, and that the addition of chromium disperses a banded structure, thereby suppressing the occurrence of separations.

## References

1. TANAKA, T., TABATA, N., HATOMURA, T., and CHIGA, C. *Microalloying 75*, Union Carbide Corp., p.107 (1977)
2. LE BON, A., ROFES-VERNIS, J. and ROSSARD, C. *Mém. Sci. Rev. Metall.*, **70**, 577 (1973)
3. SEKINE, H. and MARUYAMA, T. *Trans Iron and Steel Inst. Japan*, **16**, 427 (1976)
4. DAVENPORT, A.T., MINER, R.E. and KOT, R.A. *The hot-deformation of austenite*, American Institute of Mining, Metallurgical and Petroleum Engineers, p.186 (1977)
5. BROWN, E.L., DE ARDO, A.J. and BUCHER, J.H. *The hot-deformation of austenite*, American Institute of Mining, Metallurgical and Petroleum Engineers, p.250 (1977)
6. PRIESTNER, R. and DE LOS RIOS, E. *Heat treatment 76*, The Metals Society, p.129 (1976)
7. HASHIMOTO, T., SAWAMURA, T. and OHTANI, H. *Tetsu-to-Hagané*, **65**, 1425 (1979)
8. COLDREN, A.P., ELDIS, G.T. and TITHER, G. *Micon 78: optimization of processing properties and service performance through microstructural control*, American Society for Testing and Materials, p.126 (1979)
9. GLOVER, G. and SELLARS, C.M. *Metall. Trans*, **3**, 2271 (1972)
10. GLOVER, G. and SELLARS, C.M. *Metall. Trans*, **4**, 765 (1973)
11. YAMAMOTO, S., OKITA, T. and OUCHI, C. *Tetsu-to-Hagané*, **64**, A223 (1978)
12. YAMAMOTO, S., OUCHI, C. and OSUKA T. *Thermomechanical processing of microalloyed austenite*, American Institute of Mining, Metallurgical and Petroleum Engineers, p.613 (1982)
13. JONAS, J.J. and AKBEN, M.G. *Metal Forum*, **4**, 92 (1981)
14. KOZASU, I. and INAGAKI, H. *Nippon Kinzoku Gakkai Kaiho*, **15**, 261 (1976)
15. TANAKA, T., *Intl Metals Rev.*, **4**, 185 (1981)
16. COLEMAN, T., DULIEU, D. and GOUCH, A. *The microstructure and design of alloys*, Vol. I, The Metals Society, p.70 (1974)
17. KOZASU, I. *Trans Iron and Steel Inst. Japan*, **12**, 241 (1972)
18. TERAZAWA, T., HIGASHIYAMA, H. and SEKINO, S. *Toward improved ductility and toughness*, Climax Molybdenum Company (Japan), p.101 (1972)
19. JONES, A. and WALKER, B. *British Steel Corporation Open Report No. SM/612/A* (1974)
20. BRAMFITT, B.L. and MARDER, A.R. *Processing and properties of low-carbon steel*, American Institute of Mining, Metallurgical and Petroleum Engineers, p.191 (1973)
21. SPEICH, G.R. and DABKOWSKI, D.S. *The hot-deformation of austenite*, American Institute of Mining, Metallurgical and Petroleum Engineers, p.557 (1977)
22. YUTORI, T. and OGAWA, R. *Tetsu-to-Hagané*, **65**, 1747 (1979)
23. INAGAKI, H., KURIHARA, K. and KOZASU, I. *Tetsu-to-Hagané*, **61**, 991 (1975)
24. INAGAKI, H. *Trans Iron and Steel Inst. Japan*, **17**, 166 (1977)
25. KOZASU, I. *36th and 37th Nishiyama Memorial Lecture*, The Iron and Steel Institute of Japan, p.65 (1975)

26. MORRISON, W.B. *Met. Technol.*, **2**, 33 (1975)
27. MIYOSHI, E., FUKUDA, M., IWANAGA, H. and OKAZAWA, T. *Crack propagation in pipelines*, Institute of Gas Engineers, Paper No. 4 (1974)
28. MIYOSHI, E., FUKUDA, M., IWANAGA, H. and OKAZAWA, T. *Tetsu-to-Hagané*, **62**, 688 (1976)
29. MATSUDA, S., KAWASHIMA, Y., SEKIGUCHI, S. and OKAMOTO, M. *Tetsu-to-Hagané* **68**, 435 (1982)
30. KAZINCZY, F.D. and BACKOFEN, W.A. *Trans Am. Soc. Metall.*, **53**, 55 (1961)
31. BALDI, G. and BUZZICHELLI, G. *Met. Sci.*, **12**, 459 (1978)
32. KNOTT, J.F. *Effect of second-phase particles on the mechanical properties of steel*, The Iron and Steel Institute, p.44 (1971)
33. EMBURY, J.D., PETCH, N.J., WRAITH, A.E. and WRIGHT, E.S. *Trans Am. Inst. Mech. Engrs*, **239**, 114 (1967)
34. KOZASU, I. and KUBOTA, H. *Trans Iron and Steel Inst. Japan*, **11**, 321 (1971)
35. SCHOFIELD, R., ROWNTREE, G., SARMA, N.V. and WEINER, R.T. *Met. Technol.*, **1**, 325 (1974)
36. EMBURY, J.D. and COOPER, K. *Can. Metall. Q.* **14**, 69 (1975)
37. HORNBOGEN, E. and BECKMANN, K.D. *Arch. Eisenhüttenwes.*, **47**, 553 (1976)
38. IINO, M., MIMURA, H. and NOMURA, N. *Trans Iron and Steel Inst. Japan*, **17**, 450 (1977); *Trans Iron and Steel Inst. Japan*, **18**, 33 (1978)
39. FUKUDA, M., KUNISHIGE, K. and SUGIZAWA, S. *Tetsu-to-Hagané*, **64**, 740 (1978)
40. ALMOND, E.A. *Metall. Trans*, **1**, 2038 (1970)
41. MORI, T., ENAMI, T., FUNAKOSHI, T. and OKABE, R. *Tetsu-to-Hagané*, **63**, S796 (1977)
42. MIYOSHI, E., FUKUDA, M., HASHIMOTO, T. and ASAI, Y. *Tetsu-to-Hagané*, **60**, S220 (1974)
43. LUYCKX, L., BELL, J.R., MCLEAN, A. and KORCHYNSKY, M. *Metall. Trans*, **1**, 3341 (1970)
44. PIRCHER, H. and KLAPDAR, W. *Microalloying 75*, Union Carbide Corp. p.232 (1977)
45. BROWNRIGG, A. and CHAMBERS, F.M. *J. Iron and Steel Inst.*, **208**, 1078 (1970)
46. HAIDA, O., EMI, T., SANBONGI, K., SHIRAISHI, T. and FUJIWARA, A. *Tetsu-to-Hagané*, **64**, 1538 (1978)



## Deformation resistance at elevated temperatures

### 6.1 Strain hardening and restoration

Hot-deformation resistance of metals is one of the fundamental material properties at high temperature and the data gained are used primarily for two purposes: (1) designing the mechanical and electrical capacities of hot-working facilities; and (2) operating hot-rolling mills, with particular reference to the use of computers. The various parameters influencing deformation resistance and the interrelationships between these parameters are given in Figure 6.1. The effects of hot-deformation variables and the alloying elements on the hot-strength of austenite ( $\gamma$ ) in high-strength low-alloy (HSLA) steels are described in this chapter, and Chapter 7 deals with the microstructural effect which is of importance in controlled-rolling of HSLA steels.

Hot-strength of steel can be determined experimentally by using methods such as high-temperature tension, compression and torsion testing (or thermomechanical simulation).<sup>1-4</sup> The true stress-strain curves obtained in these tests are controlled by concurrent processes of strain-hardening and restoration; thermomechanical simulation brings about a situation in which hot-strength is largely dependent on temperature

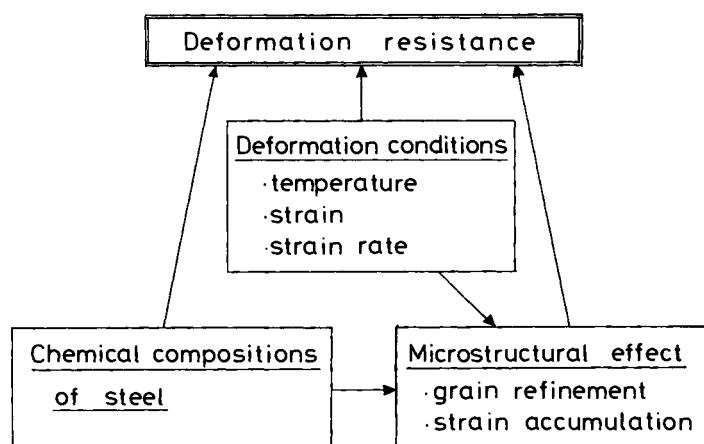


Figure 6.1 Interrelationship of various parameters influencing deformation resistance

(a) Dynamic recovery (b) Dynamic recrystallization

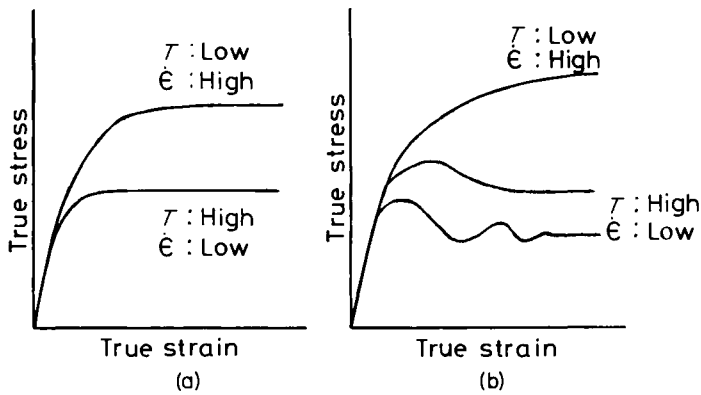


Figure 6.2 Schematic representation of stress–strain curves in dynamic restoration processes: (a) dynamic recovery; (b) dynamic recrystallization

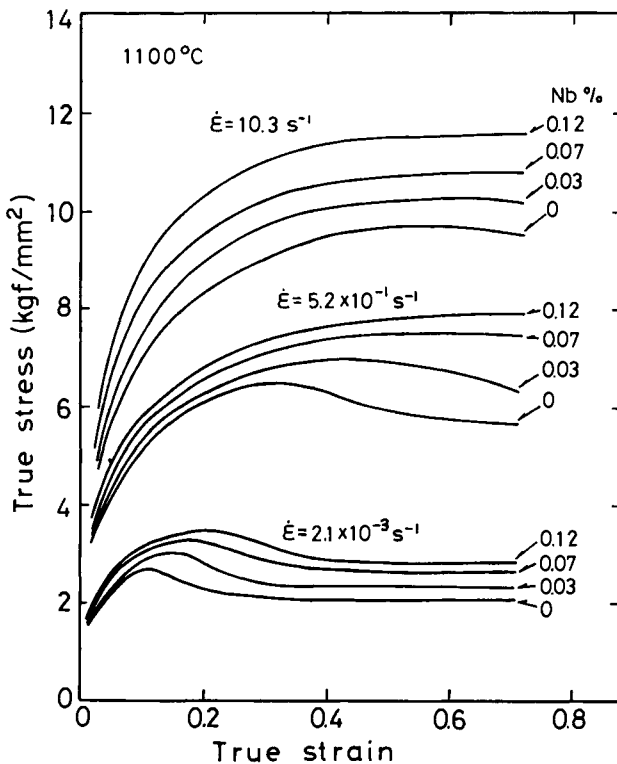


Figure 6.3 Effect of niobium content on stress–strain curves in steels with 0.08% C–1.54% Mn

and strain rate. Dynamic restoration in various metals and alloys is classified into two types – dynamic recovery and dynamic recrystallization – which give rise to different behaviour of the true stress–strain curve as shown schematically in Figure 6.2. The difference in both processes becomes clear on the stress–strain curve obtained by de-

formation at the lower strain rate. The stress-strain curve in dynamic recovery is characterized by work hardening in the smaller strain, followed by steady-state flow stress in the higher strain; that of dynamic recrystallization exhibits the peak stress before the start of steady-state flow stress or the oscillatory type of flow stress behaviour. For most commercial steels, dynamic recovery behaviour is observed in iron and carbon steel deformed in the ferritic region, or in ferritic alloy steels such as silicon iron. Dynamic recrystallization takes place in the hot-deformation of  $\gamma$  including HSLA steels and austenitic alloy steels.

Examples of the true stress-strain curve in niobium-bearing HSLA steels are shown in Figure 6.3. The compression testing was conducted at 1100°C with various strain rates. High strain-rate deformation results in a continuous work-hardening with straining, and the dynamic recrystallization type of stress-strain curve occurs in the slower strain-rate deformation. The increase of niobium content in steel increases flow stress, and also the strain at peak stress. The variations of the peak stress and the strain at the peak stress with niobium content, temperature and strain rate are summarized in Figure 6.4. The decrease of temperature and the increase of strain rate rapidly increase both values, similar to the effect of the increase in niobium content. Dynamic recryst-

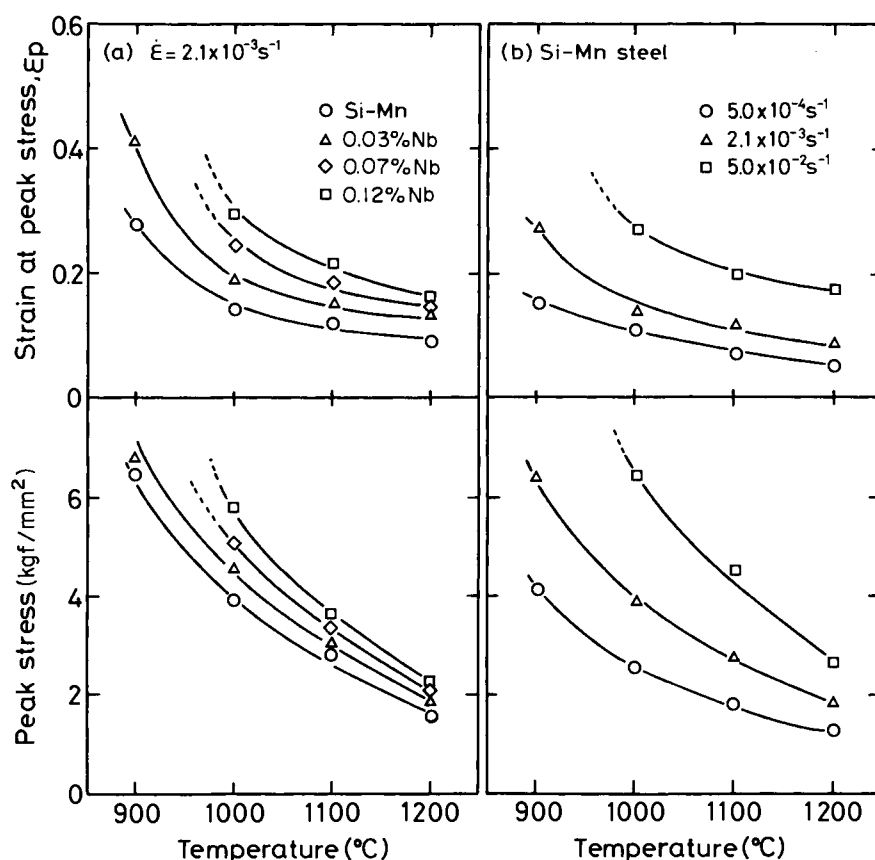


Figure 6.4 Effect of deformation temperature, strain rate and niobium content on peak stress ( $\sigma_p$ ) and strain at peak stress ( $\epsilon_p$ ): (a)  $\dot{\epsilon} = 2.1 \times 10^{-3}$ ; (b) silicon-manganese steel

tallization starts approximately at a strain of peak stress<sup>5</sup> and, thus, it can be noted that the increase of niobium content in steel retards dynamic recrystallization of  $\gamma$ .

The remarkable dependence of the flow stress on the temperature and strain rate suggests that the hot-deformation process is controlled by a thermally activated process. The general relationship between strain rate  $\dot{\epsilon}$ , temperature  $T$  and flow stress  $\sigma$  is expressed by Equation (6.1):

$$\dot{\epsilon} = A \{ \sinh(\alpha\sigma) \}^n \exp(-Q/RT) \quad (6.1)$$

where  $A$ ,  $\alpha$  and  $n$  are constants, and  $Q$  is an activation energy associated with the rate-controlled softening process.

At relatively lower stress or higher stress, Equation (6.1) is approximated by the power relation or exponential relation respectively as follows:

$$\dot{\epsilon} = B\sigma^m \exp(-Q/RT) \quad (6.2)$$

$$\dot{\epsilon} = C \exp(\beta\sigma) \exp(-Q/RT) \quad (6.3)$$

where  $B$ ,  $C$ ,  $m$  and  $\beta$  are constant values.

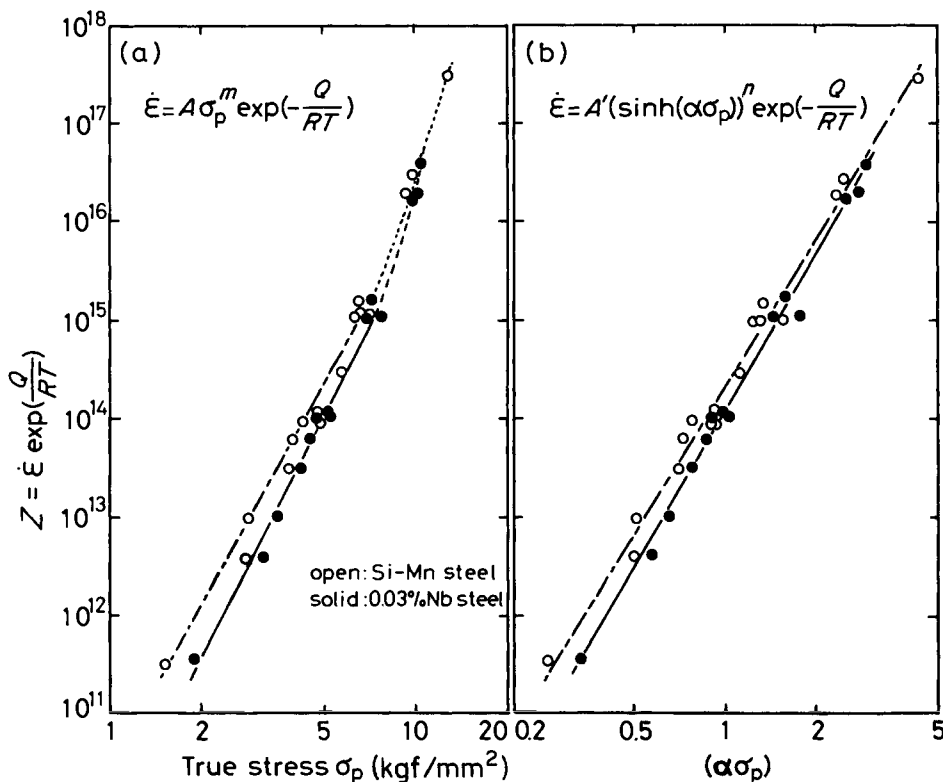


Figure 6.5 Relation of  $Z$  parameter and peak stress in 0.10% C-1.45% Mn and 0.03% Nb steels

TABLE 6.1 The range of rolling variables in various mills

| <i>Rolling-mill</i> * <sup>1</sup> | <i>Speed</i><br>(m/s) | <i>Strain rate</i><br>(s <sup>-1</sup> ) | <i>Pass reduction</i><br>(%) | <i>True strain</i> | <i>Finishing rolling temperature</i><br>(°C)† |
|------------------------------------|-----------------------|--|------------------------------|--------------------|---|
| Plate-mill                         | 2–6                   | 1–40                                     | 5–30                         | 0.05–0.35          | 700   |
| Strip-mill                         | 3–16                  | 15–200                                   | 10–45                        | 0.10–0.55          | 750   |
| Shape-mill                         | 2–5                   | 5–40                                     | 5–40                         | 0.05–0.50          | 800   |
| Bar-mill                           | 5–18                  | 30–200                                   | 15–30                        | 0.15–0.40          | 800   |

Notes:

\*<sup>1</sup> Finishing mill

† For controlled-rolling

Equations (6.1–6.3) can be expressed by the Zener–Hollomon parameter  $Z$  which is the strain rate compensated by the temperature:

$$Z = \dot{\epsilon} \exp (Q/RT) \quad (6.4)$$

The validity of the above equations has been confirmed on various metals and alloys and in a wider range of deformation conditions covering creep and hot-working. Figure 6.5 shows the relation of  $Z$  value to the peak stress in silicon–manganese steel and 0.03% niobium-bearing steel analysed by Equations (6.1) and (6.2). The experimental data agree well with Equation (6.1) in a wider range of the peak stress, while agreement with Equation (6.2) is limited to the range of lower peak stress. The values of  $m$ ,  $n$  and  $Q$  obtained from these analyses have been reported on many metals and alloys and are summarized by McQueen *et al.*<sup>6</sup>

It is important to note that hot-strength of  $\gamma$  should be evaluated under the heading of deformation conditions adopted in the relevant hot-rolling processes. The ranges of strain rate and rolling pass strain in the various types of hot-rolling mills are listed in Table 6.1, together with the finishing rolling temperature in controlled-rolling. It is seen that the strain of a respective rolling pass in the plate mill or strip mill is limited to below 0.35 and 0.55 respectively, and that strain rate in any rolling mill process is always around 5 s<sup>-1</sup> and above. Hot-deformation of  $\gamma$  under these rolling variables causes continuous work-hardening without reaching peak stress on the stress–strain curve. Exceptional hot-working processes which can afford extremely large pass strains over 80% are those of hot extrusion and the plate-mill; in these processes, dynamic recrystallization may occur depending on deformation temperature.

## 6.2 Metallurgical factors affecting hot-strength

The metallurgical factors affecting hot-strength of steels involve alloying elements, grain size and phase structures such as  $\gamma$  and ferrite ( $\alpha$ ) or a mixture of both phases. The strengthening of  $\gamma$  due to alloying elements used in HSLA steels is mainly described here. Most strength data shown in this section were obtained by hot-compression testing with strain rates of from 10 s<sup>-1</sup> to 21 s<sup>-1</sup>.

Carbon and nitrogen can exist as interstitial atoms, or precipitates of carbides or

nitrides in  $\gamma$ . The strengthening effect due to carbon dissolved interstitially in  $\gamma$  has not yet been made clear, despite the extensive data available from past studies. The main reason for this appears to be that there are different hot-deformation conditions as well as different ranges of carbon content in each investigation.<sup>7,8</sup>

The general consensus is that carbon content has a negligible effect on the hot-strength of  $\gamma$  in either deformation with a lower strain rate or at higher temperatures, and that a high strain-rate deformation yields an increase of hot-strength with increasing carbon content, particularly in the range of carbon content below 0.40%. Figure 6.6 shows such an example, namely where carbon content was varied from 0.008% to 0.25% in steels with 0.25% Si–1.10% Mn. It is notable that the strengthening due to carbon becomes apparent at temperatures below 900°C. Conversely, a variation of nitrogen content in HSLA steels is, in general, too small to cause a significant change of hot-strength, yet nitrogen may influence it through austenitic grain refinement due to the formation of nitrides such as aluminium nitride or titanium nitride.

Elements used in substitutional alloys may strengthen  $\gamma$  through solid solution hardening, precipitation hardening and grain refinement, in a manner similar to the way steel is strengthened at ambient temperature. Figure 6.7 gives the solid solution hardening effects in the various alloying elements in the 0.10% C–0.25% Si–1.10% Mn steel. Molybdenum and then silicon markedly increase hot-strength, whereas copper, nickel and manganese exert insignificant influences. Chromium has only an intermediate effect. These alloying effects on hot-strength are consistent with other results investigated in the steels with the different basic compositions.<sup>7</sup> The effects of the microalloying elements such as niobium, titanium and vanadium are summarized in Figure 6.8. Despite a small addition of less than 0.10%, niobium and titanium increase the hot-strength substantially. Vanadium has the least effect among these three microalloying elements. The thermomechanical cycle adopted in compression testing for this investigation was as follows: (1) reheating at 1250°C; (2) first-stage deformation at 1050°C for the  $\gamma$  grain refinement; and (3) second-stage deformation at 900°C. Because the dynamic precipitation of niobium carbonitrides is suppressed under the high strain-rate deformation,<sup>9</sup> the increase of hot-strength with niobium content observed in Figure 6.8 appears to be due to niobium dissolved in  $\gamma$  rather than to precipitates.

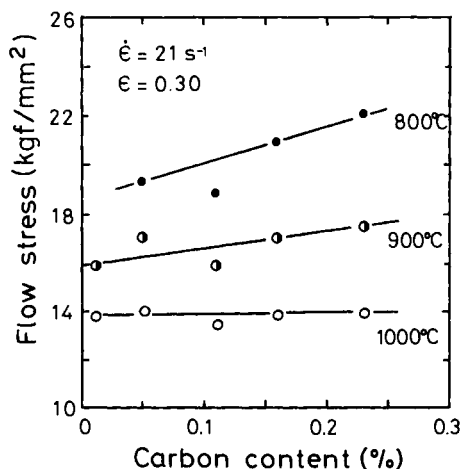


Figure 6.6 Effect of carbon content of hot-strength in 1.10% Mn steels

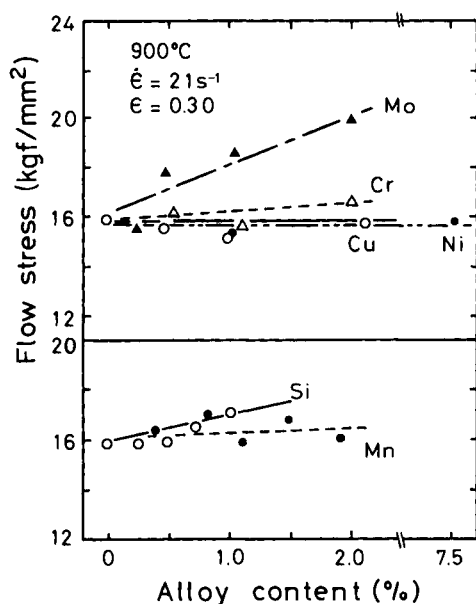


Figure 6.7 Effect of alloying elements on hot-strength in 0.10% C-1.10% Mn steel

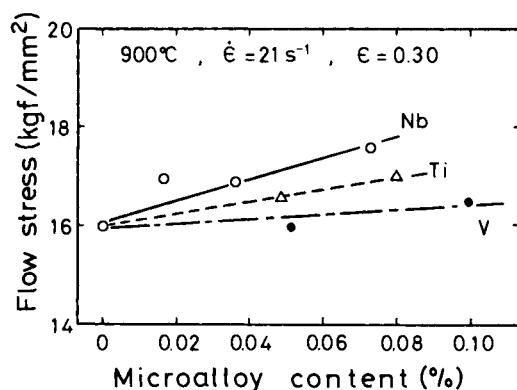


Figure 6.8 Effect of microalloying elements on hot-strength

The undissolved or strain-induced precipitates of niobium carbonitrides may affect hot-strength differently from solute niobium, but the quantitative relationship of the size and volume fraction of precipitates and hot-strength of  $\gamma$  has not been made clear enough for us to form a firm opinion on this point.

The solid solution hardening can be correlated with atomic diameter difference between a solute element and iron. Table 6.2 presents this correlation for the various solute elements, together with the results analysed by Tegart and Gittins.<sup>7</sup> Alloying elements with a large size difference tend to increase hot-strength. Niobium causes the largest increment of hot-strength, although its misfit is smaller than molybdenum. As already noted, the flow stress in hot-deformation is controlled by the concurrent processes of strain-hardening and dynamic restoration (the latter process is not negligible even in the high strain-rate deformation). From this point of view, it appears that the extremely large increase in hot-strength when niobium is used may arise from the

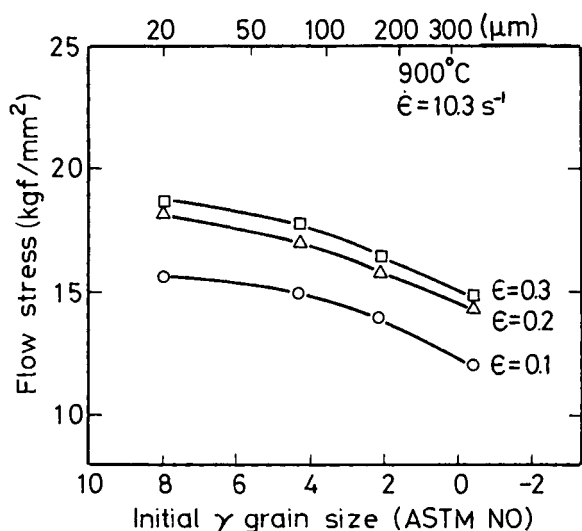


TABLE 6-2 Relation between misfit factor and stress increment

|            | Misfit<br>factor <sup>1</sup><br>(%) | $\Delta\sigma_{0.3}$ at 900° C<br>(kg/mm <sup>2</sup> at %) | $\Delta\sigma_{0.3}/\sigma_{0.3}$<br>(%/at %) | $\Delta\sigma/\sigma$ at 1000° C†<br>(%/ at %) |
|------------|--------------------------------------|---|---|--|
| Silicon    | -10.0                                | 0.60  | 3.8   | 8.3  |
| Manganese  | + 5.9                                | 0.33  | 2.1   | 5.3  |
| Copper     | -0.88                                | 0   | 0   |  |
| Nickel     | - 3.4                                | 0   | 0   | -0.1   |
| Chromium   | - 3.1                                | 0.29  | 1.8   | 2.1  |
| Molybdenum | - 5.7                                | 3.4   | 21  | 13   |
| Niobium    | +11.0                                | 33  | 210   |  |
| Vanadium   | + 1.7                                | 4.6   | 29  |  |
| Titanium   | +12.3                                | 10  | 63  |  |

Notes:

\*Metal data book

†Tegart<sup>7</sup>Figure 6.9 Effect of initial  $\gamma$  grain size on hot-strength in 0.08% C-1.45% Mn steel

suppression of dynamic recovery due to solute niobium in  $\gamma$ .

The  $\gamma$  grain size influences the hot-strength of  $\gamma$  to a much smaller degree than the strengthening of  $\alpha$  due to grain refinement at ambient temperature. This is seen in Figure 6.9, where the  $\gamma$  grain size in 0.08% C-1.45% Mn steel was varied by changing the reheating temperatures from 900 to 1250° C. The flow stress at a given strain increases by about 1.2 times with a refinement in the grain size from 0 to 8 in the ASTM grain-size number.

Hot-strengths of the representative commercial steels are presented in Figure 6.10. The chemical compositions of these steels are listed in Table 6.3. The  $\gamma$  of HSLA steels is 20–30% stronger than that of mild steel, and the change of strength between the mild steel and 18–8 stainless steel is a factor of 1.5, or 1.6 times at the most. On the other

TABLE 6.3 Chemical composition of steels used

| Steel                        | C    | Si   | Mn   | P     | S     | Ni   | Cr   | Mo   | Nb    | V     |
|------------------------------|------|------|------|-------|-------|------|------|------|-------|-------|
| Mild steel                   | 0.05 | 0.01 | 0.17 | 0.009 | 0.021 | —    | —    | —    | —     | —     |
| Silicon manganese            | 0.08 | 0.22 | 1.45 | 0.014 | 0.010 | —    | —    | —    | —     | —     |
| Silicon manganese<br>niobium | 0.08 | 0.22 | 1.54 | 0.016 | 0.010 | —    | —    | —    | 0.034 | —     |
| HT80                         | 0.12 | 0.19 | 0.98 | 0.007 | 0.005 | 0.71 | 0.50 | 0.22 | —     | 0.034 |
| X-80                         | 0.06 | 0.27 | 1.99 | 0.019 | 0.003 | 0.26 | —    | 0.40 | 0.052 | —     |
| 18-8 stainless steel         | 0.08 | 0.75 | 1.56 | 0.010 | 0.008 | 9.07 | 18.7 | 0.22 | —     | —     |

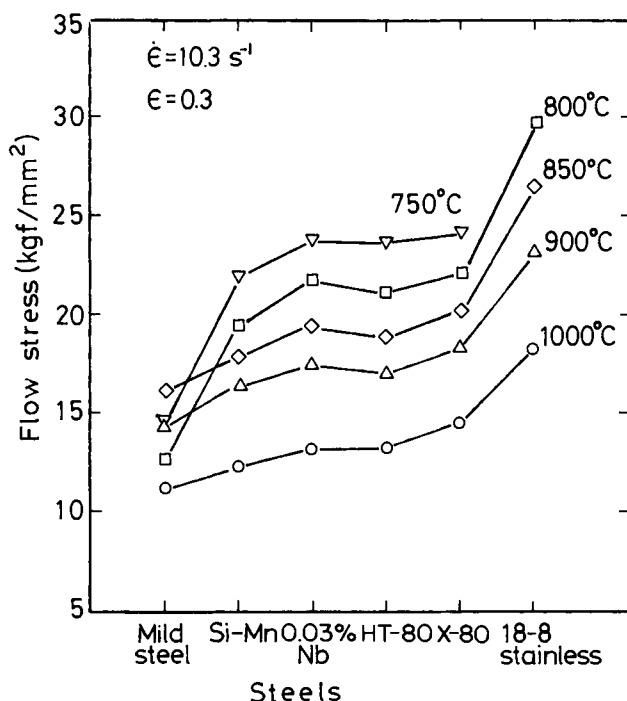


Figure 6.10 Hot-strength of commercial steels at various hot-deformation temperatures

hand, the reduction of the hot-deformation temperature from 1000 to 800°C in a given steel gives rise to twice-higher strength. Thus, it can be concluded that a variation of chemistry among the various HSLA steels results in a much smaller change of hot-strength in  $\gamma$ , compared with the effect of the hot-deformation conditions.

It is also seen in Figure 6.10 that the strength of mild steel at 800 or 750°C is lower than the strength at 850°C. This is explained by the  $\gamma \rightarrow \alpha$  transformation below 850°C in this steel. As  $\alpha$  is weaker than  $\gamma$ , the plain carbon steel often exhibits this transition of strength at the transformation temperature. Hot-strength in the intercritical region depends on both the volume fraction and the strength of  $\gamma$  and  $\alpha$ . The  $\gamma \rightarrow \alpha$  transformation kinetics in HSLA steels is not so rapid as that of plain carbon steel because of the relatively high manganese content in HSLA steels. As a result, the change of hot-strength accompanying the transformation in HSLA steels is not so remarkable as observed in plain carbon steel.

### 6.3 Hot-deformation resistance formulae

For the purpose of prediction of mill load and then optimization of rolling schedule, it is convenient to formulate hot-deformation resistance as a function of rolling parameters and chemistry of steels. While several equations of deformation resistance have been established experimentally, each rolling-mill section of steelworks has been using its own formula to fit its situation. In the following, two equations of deformation resistance established by Shida<sup>10</sup> and Misaka and Yoshimoto<sup>11</sup> are described, both equations being well known and widely used in Japan.

The general-function form of the variables in these equations takes the dependence of the flow stress or deformation resistance on temperature, strain and strain rate as  $e^{A/T}$ ,  $\varepsilon^n$  and  $\dot{\varepsilon}^m$  respectively. That is, the average deformation resistance  $K_{fm}$  at strain  $\varepsilon$  is expressed as follows:

$$K_{fm} = \frac{1}{\varepsilon} \int_0^\varepsilon K_f \cdot d\varepsilon = C e^{A/T} \cdot \varepsilon^n \cdot \dot{\varepsilon}^m \quad (6.5)$$

where  $K_f$  is the flow stress expressed as a function of strain. The constant values of  $C$ ,  $A$ ,  $n$  and  $m$  are determined experimentally.

Shida's equation was formulated from the data obtained by using a cam plastometer. The stress-strain curves for the eight carbon steels in the range of carbon content from 0.01 to 0.80% were determined over the ranges of strain rate from 0.2 to 30 s<sup>-1</sup>, strain up to 0.6 and temperature from 650 to 1200°C. Therefore, Equation (6.6) involves the effects of carbon content  $C$  and both the ranges of  $\gamma$  and  $\alpha$  phases, as shown in the following:

$$K_f = K \{1.3(\varepsilon/0.2)^n - 0.3(\varepsilon/0.2)\} (\dot{\varepsilon}/10)^m \quad (6.6)$$

where  $K = 0.28 \exp \{5/t - 0.01/(C + 0.05)\} \quad (t \geq t_d)$ ,

$$K = 0.28 \cdot g \cdot \exp \{5/t_d - 0.01/(C + 0.05)\} \quad (t \leq t_d),$$

$$g = 30 (C + 0.9) [t - 0.95 (C + 0.49)/(C + 0.42)]^2 + (C + 0.06)/(C + 0.09)$$

$$m = (-0.019C + 0.126)t + (0.075C - 0.050) \quad (t \geq t_d)$$

$$m = (0.081C - 0.154)t + (-0.019C + 0.207) + 0.027/(C + 0.32) \quad (t \leq t_d)$$

$$n = 0.41 - 0.07C \quad t = T(^{\circ}\text{K})/1000$$

$$t_d = 0.95 (C + 0.41)/(C + 0.32)$$

On the other hand, Misaka made a mathematical model for a hot-strip mill and established the deformation resistance equation using drop-hammer-type high-speed compression equipment. Steels investigated covered the carbon content from 0.06 to 1.16%. Strain was varied up to 0.30 and strain rate was around 80 s<sup>-1</sup>.

$$K_{fm} = \exp \left( 0.126 - 1.75 C + 0.594 C^2 + \frac{2851 + 2968 C - 1120 C^2}{T} \right) \cdot \dot{\epsilon}^{0.21} \cdot \dot{\epsilon}^{0.13} \quad (6.7)$$

To this equation, thereafter, were added the terms for correction of the transformation temperature and alloying elements besides carbon.<sup>1,2</sup>

## References

1. CORDES, J.N. and HOOK, R.E. *Met. Trans*, **1**, 111 (1970)
2. DJAIC, R.A. and JONAS, J.J. *J. Iron and Steel Inst.*, **210**, 256 (1972)
3. OUCHI, C. and OKITA, T. *Trans Iron and Steel Inst. Japan*, **22**, 543 (1982)
4. BLAIN, P. and ROSSARD, C. *IRSID External Report No. 46* (1968)
5. PAWELSKI, O., RUDIGER, U. and KASPAR, R. *Stahl u. Eisen*, **98**, 181 (1978)
6. MCQUEEN, H.J., PETKOVIC, R., WEISS, H. and HINTON, L.G.M. *Proceedings, International conference on the hot-deformation of austenite*, American Institute of Mining, Metallurgical and Petroleum Engineers, p.113 (1977)
7. TEGART, W.J. MCG. and GITTINS, A. *Proceedings, International conference on the hot-deformation of austenite*, American Institute of Mining, Metallurgical and Petroleum Engineers, p.1 (1977)
8. STEWART, M.J. *Proceedings International conference on the hot-deformation of austenite*, American Institute of Mining, Metallurgical and Petroleum Engineers, p.47 (1977)
9. WEISS, I. and JONAS, J.J. *Met. Trans*, **10A**, 831 (1979)
10. SHIDA, S. *J. Japan Soc. Tec. Plasticity*, **10**, 610 (1969)
11. MISAKA, Y. and YOSHIMOTO, T. *J. Japan Soc. Tec. Plasticity*, **8**, 414 (1967)
12. MISAKA, Y., YOKOI, T., TAKAHASHI, R. and NAGAI, H. *J. Iron and Steel Inst. Japan* (in Japanese), **67**, A53 (1981)

## Softening behaviour immediately after rolling and strain accumulation

### 7.1 Softening behaviour immediately after hot-rolling

The softening behaviour of hot-deformed metals immediately after rolling is controlled by the kinetics in the static restoration process (which consists of static recovery and recrystallization). It has been considered in the past that complete restoration would always occur during the interpass time between subsequent rolling passes; as a result, the effect of the microstructural changes based on static restoration on the hot-strength of steel have been ignored. On the other hand, controlled-rolling practice, particularly in microalloyed steels, aims to develop the nonrecrystallized austenitic structure by rolling at the temperatures below the recrystallization temperature of austenite ( $\gamma$ ), which can bring about the very refined transformed microstructure. This means that the strain given in each previous rolling pass is not completely restored and accumulates successively during multipass rolling in the plate- or strip-mill. As the  $\gamma$  deformed at a high strain rate causes strain-hardening, this strain accumulation virtually increases deformation resistance. The noticeable increase in the mill load experien-

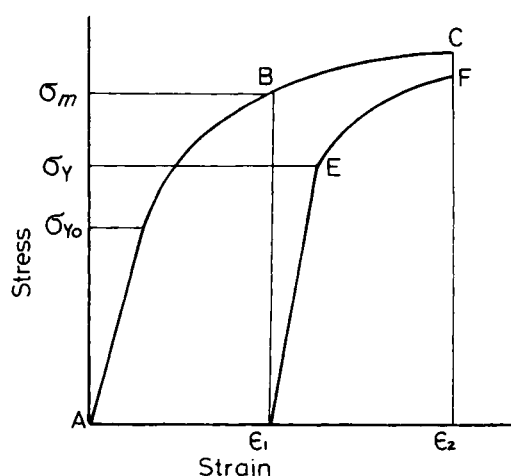


Figure 7.1 Schematic representation of stress-strain curves in intermittent multistage pass deformation

ced commonly in controlled-rolling practice is mainly due to this strain accumulation effect, besides the simple effect of rolling in the lower temperature range of  $\gamma$ .<sup>1-3</sup>

The degree of softening taking place during the interpass time in hot-working can be evaluated by the intermittent multistage hot-deformation experiments using hot-compression or torsion-testing equipment. The true stress-strain curve for the first- and second-stage deformation in multistage hot-deformation is presented in Figure 7.1. The flow stress in the second stage deformation can be varied primarily by the interstage time and strain in the first stage. The metallurgical factors that affect the static recovery and recrystallization kinetics also influence the softening. The softening ratio ( $X_s$ ) is defined by the following equation:

$$X_s = (\sigma_m - \sigma_y) / (\sigma_m - \sigma_{y_0}) \quad (7.1)$$

where  $\sigma_{y_0}$  and  $\sigma_y$  are the yield stresses in the first and second deformation respectively, which are mostly taken as 0.25% offset flow stress, and  $\sigma_m$  is the flow stress corresponding to strain in the first stage in this figure.

The case of no softening, like cold-working, gives  $X_s = 0$ , since  $\sigma_y = \sigma_m$ , and after full recrystallization  $\sigma_y$  is nearly equal to  $\sigma_{y_0}$ , so that  $X_s \approx 1.0$ . The small difference in  $\sigma_y$  and  $\sigma_{y_0}$  in this case is due to the variation in grain size after recrystallization. For evaluation of the softening ratio, it is necessary to select strain rate and interstage time corresponding to the operation conditions in the various hot-working processes. For instance, the interpass time between rolling passes in a plate-mill becomes around 10 s, and that of a finishing stand in a strip-mill less than 1 s.

Figure 7.2 exhibits the example of the stress-strain curves obtained by an intermittent two-stage press deformation with a strain rate of  $10.3 \text{ s}^{-1}$ . The 0.03% Nb-bearing

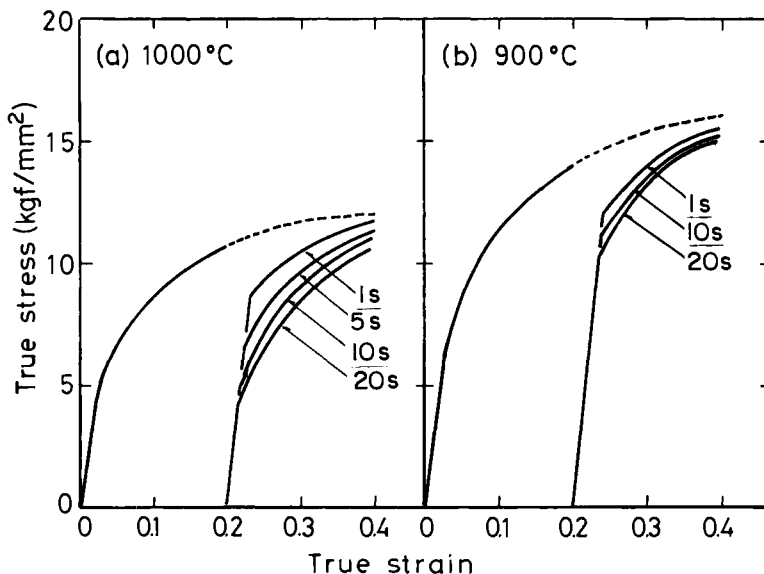


Figure 7.2 Stress-strain curves in multistage pass deformation tests: 0.03% Nb steel. Interpass time is noted: (a) 1000°C; (b) 900°C

steel was deformed at 900 and 1000° C, the interstage time being varied from 1 to 20 s. It is seen that the yield stress in the second-press stage decreases rapidly to that of the first stage during a short interpass time at 1000° C. On the other hand, the reduction in the yield stress in the second pass during holding times up to 20 s becomes much smaller at 900° C. The softening ratio obtained from these data reflects the progress of static recovery and recrystallization.

## 7.2 Factors affecting softening

The metallurgical variables associated with the static restoration kinetics affect softening in addition to the temperature and the interstage time. These include the chemistry of steel, particularly microalloying elements such as niobium, the initial grain size, and strain of the preceding passes. The softening behaviour investigated by means of multistage hot-compression testing is described below, focusing on the effect of the metallurgical variables. Figures 7.3 and 7.4 give the relation of the interpass time and softening ratio in 0.08% C–0.25% Si–1.50% Mn steel and 0.03% Nb-bearing steel respectively. The initial  $\gamma$  grain size was controlled at 53  $\mu\text{m}$  in the first-stage pass at 1100° C, and the values of the softening ratio were obtained from the stress–strain curves in the second- and third-stage pass with a respective strain of 0.20. The increases of the interpass time and the temperature result in the higher softening values. The transition from recovery to recrystallization takes place at the point where the gradients of the straight lines change in both figures. The softening value corresponding to each of these transition points may vary depending on strain or the initial grain size. Under an interpass time of around 10 s, static recrystallization in niobium-free and niobium-bearing steels starts at temperatures above 800 and 900° C respectively. The

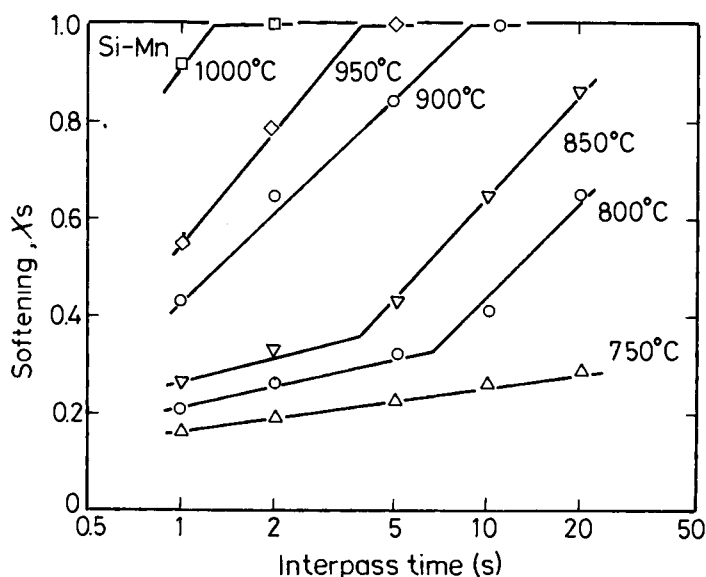


Figure 7.3 Effect of interpass time and deformation temperature on the softening ratio: silicon–manganese steel, prestrain 0.2



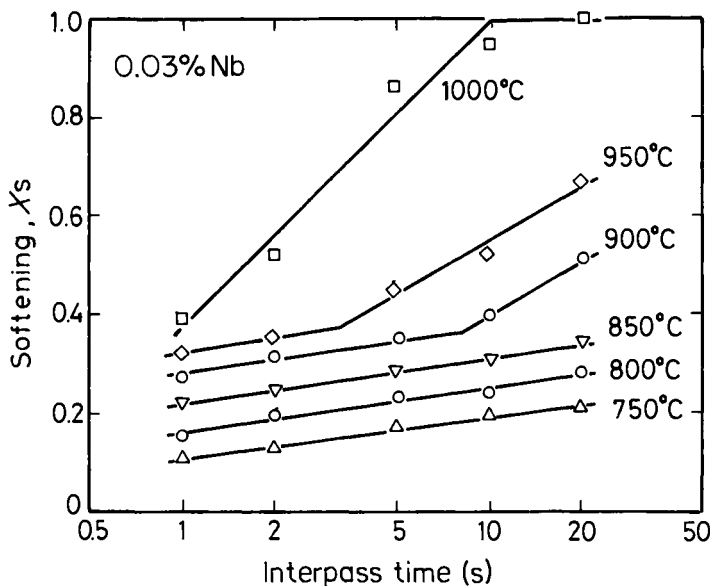


Figure 7.4 Effect of interpass time and deformation temperature on the softening ratio; 0.03% Nb steel, prestrain 0.2

softening values in the range controlled only by static recovery decrease with a reduction of temperatures as seen in Figure 7.4. The softening of the first and second pass kinetics is also influenced by the initial grain size. Figure 7.5 shows this effect in silicon-manganese steel. The initial grain size was varied by changing the reheating temperature from 900 to 1250°C, and three-step deformation was conducted at 900°C, a respective strain being 0.10. The softening ratio obtained from the first and second pass is influenced very little by variations of the initial grain size due to relatively small strain. However, the softening ratio obtained from the second and third pass remarkably increases with refinement of the initial grain size; correspondingly, the increase in strain through strain accumulation and grain refinement promotes static recrystallization. In practical controlled-rolling in plate-mill or strip-mill, the  $\gamma$  grain size is successively refined through repeated recrystallization during rougher rolling, approaching up to grain size numbers around 7 or 8.<sup>4</sup> Under these refined grain sizes, a niobium-free steel gives a high softening ratio even in rolling below 900°C. This is confirmed from Figure 7.5. The effect of prestrain (which is the amount of strain in the first press) is shown in Figure 7.6, which compares the niobium-free and 0.03% niobium-bearing steels, with a relatively fine initial grain size around 40  $\mu\text{m}$ . The difference in the softening ratio in both steels is clear, and the niobium-bearing steel maintains a very low softening ratio even in high prestrain deformation. Other microalloying elements, such as titanium, which retard the static recrystallization of  $\gamma$  appear to have the same effect as niobium.

The substitutional alloying elements such as manganese or silicon affect the softening behaviour very little compared with the micro-alloying elements. However, where a rolling condition such as the interpass time is shorter than 1 s, various solute elements give rise to a variation of softening behaviour. This example is presented in Figure 7.7,

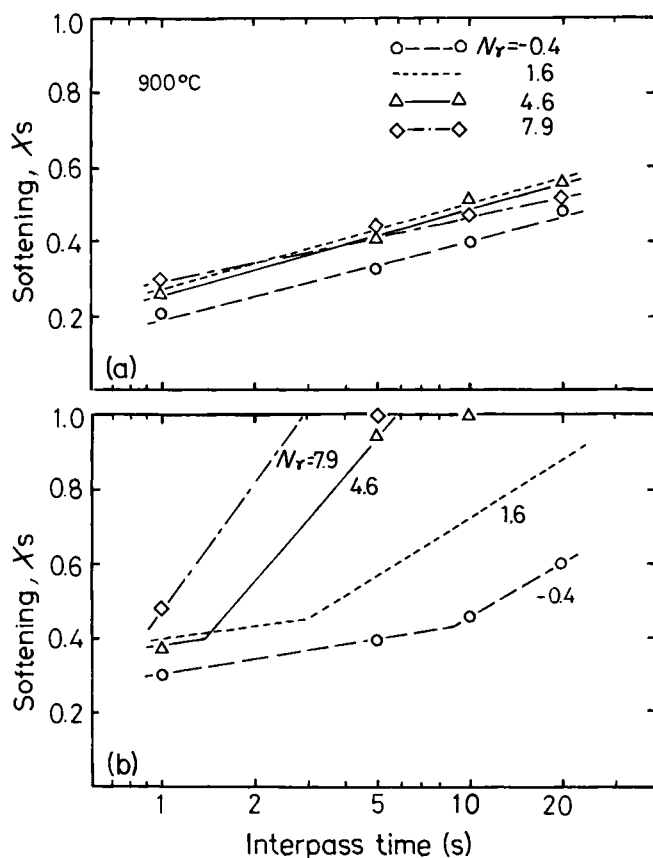


Figure 7.5 Effect of initial  $\gamma$  grain size on the softening ratio: silicon-manganese steel, three-step compression testing, each pass step-strain 0.1: (a) pass 1  $\rightarrow$  2; (b) pass 2  $\rightarrow$  3

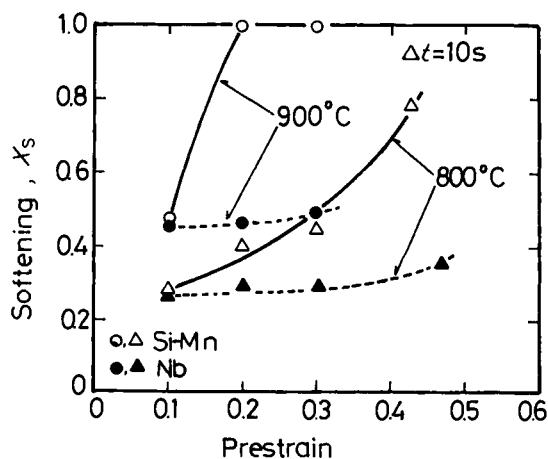


Figure 7.6 Effect of prestrain on the softening ratio; silicon-manganese and 0.03% Nb steel

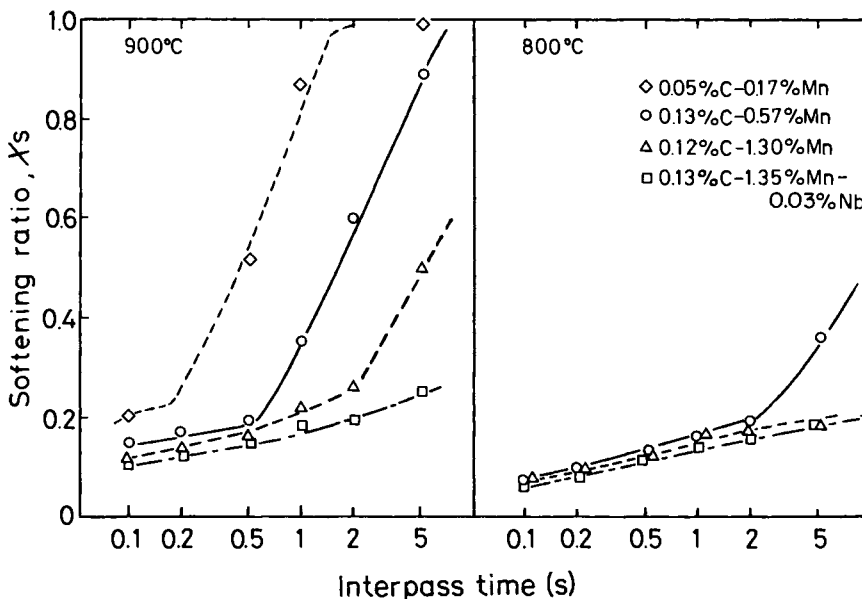


Figure 7.7 Effects of the interpass time and steel chemistry on softening ratio of four steels, prestrain 0.25: (a) 900°C; (b) 800°C

where the softening of the several steels containing different amounts of carbon and manganese is investigated under the interpass time between 0.1 and 5 s. The increase of the manganese and carbon contents in steel evidently reduces the softening ratio at 900°C, and a plain carbon-manganese steel causes some variations of the softening arising only from static recovery at 800°C. These results suggest that the increased content of the substitutional alloying elements in high-strength low-alloy (HSLA) steels reduces the softening ratio depending on the interpass time of rolling, and that during multipass rolling at the finishing stands of strip-mill or bar-mill, strain accumulation can take place even in the steel without any microalloying element.

### 7.3 Introduction of strain accumulation into deformation resistance formulae

The deformation resistance formulae described in Chapter 6 do not take account of strain accumulation because both the effect arising from the microstructural changes is not yet fully understood, and the strain evaluated in the formulae is an individual pass reduction of rolling. In studies conducted during the last decade, several procedures for the introduction of a strain accumulation effect into a deformation resistance equation have been proposed.<sup>1-3</sup> The simplest method is to assume the extreme case of complete or no restoration,<sup>1</sup> i.e. where a respective strain during multipass rolling becomes either completely nonadditive or completely additive respectively. Here, a more general method to deal with the strain accumulation effect is described. This is based on an evaluation of residual strain from the softening data. The strain of  $\epsilon$  in the deformation resistance equation expressed as  $K=f(\epsilon)$  is taken as the sum of  $\alpha_i$  and  $\beta_i$ , where  $\alpha_i$  is the

strain corresponding to the reduction of the  $i$ th pass and  $\beta_i$  is the residual strain accumulated during the preceding rolling passes up to the  $i$ th pass. That is, the effective strain  $\varepsilon_i$  in the  $i$ th pass and the residual strain coefficient  $\lambda_i$  are expressed and defined in the following equations, respectively:

$$\varepsilon_i = \alpha_i + \beta_i \quad (7.2)$$

$$\lambda_i = \beta_i / \varepsilon_{i-1} = \beta_i / (\alpha_{i-1} + \beta_{i-1}) \quad (7.3)$$

$\lambda_i = 1$  is the state of no restoration, with  $\beta_i = \varepsilon_{i-1}$ , and  $\lambda_i = 0$  corresponds to the case of no residual strain with  $\beta_i = 0$ . The general expression for the effective strain in the  $i$ th pass is given as follows;

$$\begin{aligned} \varepsilon_i = & \alpha_i + \alpha_{i-1} \cdot (\lambda_i) + \alpha_{i-2} \cdot (\lambda_{i-1} \cdot \lambda_i) + \dots \\ & + \alpha_2 \cdot (\lambda_3 \cdot \lambda_4 \dots \lambda_i) + \alpha_1 \cdot (\lambda_2 \cdot \lambda_3 \dots \lambda_i) \end{aligned} \quad (7.4)$$

The value of  $\lambda$  is a function of the interpass time, temperature and metallurgical variables such as chemistry of steel, and can be evaluated quantitatively by analysing the data from the intermittent multistage hot-deformation experiments. In the following, the evaluation procedure of the  $\lambda$  values is described for the case of controlled-rolling in a plate-mill.

When the strains given in the three-step deformation are  $\alpha_1$ ,  $\alpha_2$  and  $\alpha_3$  and the corresponding flow stresses at these strains are  $\sigma_1$ ,  $\sigma_2$  and  $\sigma_3$  respectively as shown schematically in Figure 7.8, the residual strain coefficients  $\lambda_2$  and  $\lambda_3$  can be calculated based on the function  $\sigma = f(\varepsilon)$ , which is formulated from the true stress-strain curves in

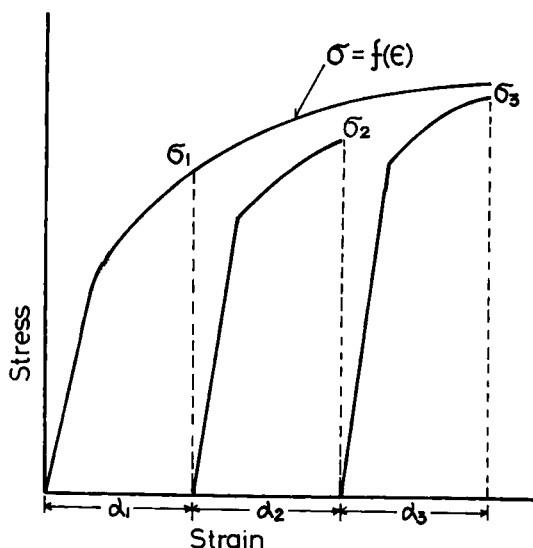


Figure 7.8 Schematic illustration of flow stress  $\sigma_i$  and strain  $\alpha_i$  for analysing the residual strain in three-step compression testing:  $\alpha_1 = \alpha_2 = \alpha_3 = 0.1$ ,  $\sigma = f(\varepsilon)$  was given in the one-pass stage testing

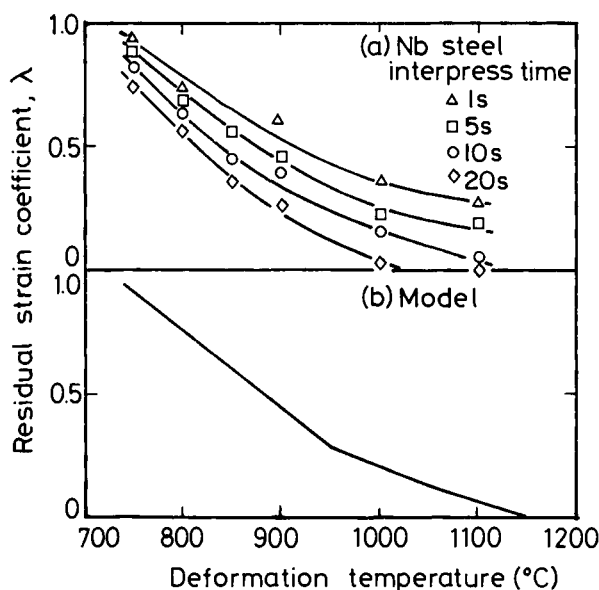


Figure 7.9 Residual strain coefficient as a function of deformation temperature and interpass time: (a) experimental interpass results for 0.03% Nb steel; (b) solid line – model used for the calculation of effective strain

one-pass experiments. That is, the residual strain of  $\beta_2$  is obtained by satisfying the relation  $f(\alpha_2 + \beta_2) = \sigma_2$ , and thus:

$$\lambda_2 = \beta_2 / \alpha_1 \quad (7.5)$$

Following the same procedure,  $\lambda_3$  can be obtained from the residual strain  $\beta_3$  up to the third-pass stage. Figure 7.9(a) gives a result of the residual strain coefficient in niobium-bearing steel obtained by the three-step deformation testing. The temperature was varied from 750 to 1100°C and the strains  $\alpha_1$ ,  $\alpha_2$  and  $\alpha_3$  were the same, being 0.10. The  $\lambda$  values shown in this figure were taken as an average value of  $\lambda_2$  and  $\lambda_3$  because of a small difference between them in the present case. It is noted that the decrease of the temperature and the interpass time increase the values of  $\lambda$ . These variations of residual strain coefficient are similar to the behaviour of the softening ratio, and in fact, the temperature-dependence of  $\lambda$  approximated for modelling described in the following section (Figure 7.9(b)) shows nearly the same tendency as that of  $1 - X_s$ . By using the values of  $\lambda$  obtained, the effective strain  $\varepsilon_i$  can be calculated from Equations (7.2) or (7.4) and it is introduced to the strain term in the deformation resistance equation.

## 7.4 Computer simulation for predicting mill load

Nowadays, mill operation by means of a process computer is widely conducted in plate- and strip-mills. One of the major benefits arising from computer operation is the optimization of rolling schedules achieved by utilizing the maximum applicable mill load or torque in rolling mills. While main rolling variables in controlled-rolling

practice, such as the reheating temperature or the finishing-rolling temperature, tend to be based on the conditions which satisfy requirements for the mechanical properties of steels, rolling-mills have different mill specifications and limitations on rolling. It is vital to establish a prediction model of the mill load in controlled-rolling. In general, rolling pass schedules in the lower temperature region in controlled-rolling practice are restricted by the maximum mill load rather than the maximum torque applicable to a specific rolling-mill. Thus, in Equation (7.6), mill load is described according to hot-rolling theory, and a comparison of the predicted and observed mill loads is presented as an example of controlled-rolling in a wide plate-mill.

The mill load  $P$  is expressed by:

$$P = KLBQ \quad (7.6)$$

where  $K$  is the hot-deformation strength,  $L$  is the arc length of contact between the work roll and the plate,  $B$  is the width of the plate and  $Q$  is a roll pressure function in which the peening effect and roll flattening are considered.<sup>5</sup> The strain rate and strain involved in the deformation resistance equation are given as follows:

$$\dot{\epsilon} = \frac{2\pi N}{60\sqrt{r}} \sqrt{\frac{R_0}{h_0}} \ln \frac{1}{1-r} \quad (7.7)$$

where  $r = \Delta h/h_0$

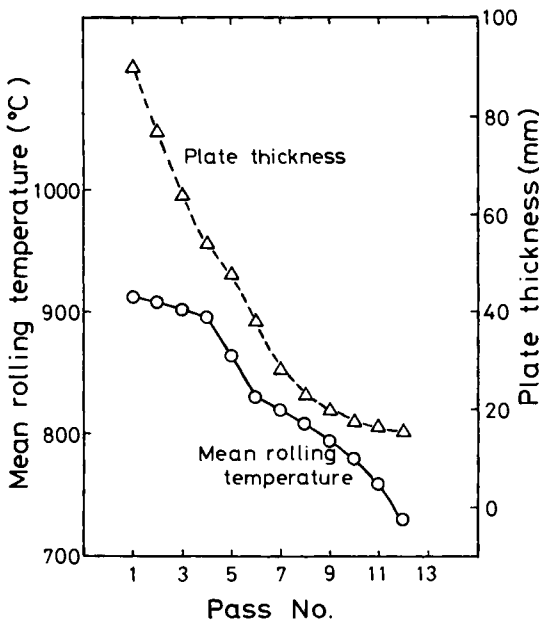


Figure 7.10 Changes in rolling temperature and plate thickness in a reversing wide plate-mill

$$\varepsilon = \ln \frac{h_0}{h_1} = \ln \frac{1}{1-r} \quad (7.8)$$

where  $N$  is the pace of the work roll, in revolutions per minute,  $R_0$  is the roll radius,  $h_0$  and  $h_1$  are the entry and delivery thicknesses of the plate respectively. The average rolling temperature  $T_m$  of the plate is calculated from the surface temperature  $T_s$ , assuming quasi steady-state aircooling as follows:

$$T_m - T_s = \varphi H \quad (7.9)$$

where  $H$  is the thickness of the plate and the constant of proportionality  $\varphi$  is expressed as follows:

$$\varphi = [\varepsilon \sigma \{ (T_s + 273)^4 - (T_a + 273)^4 \} + \alpha C (T_s - T_a)] / 6R \quad (7.10)$$

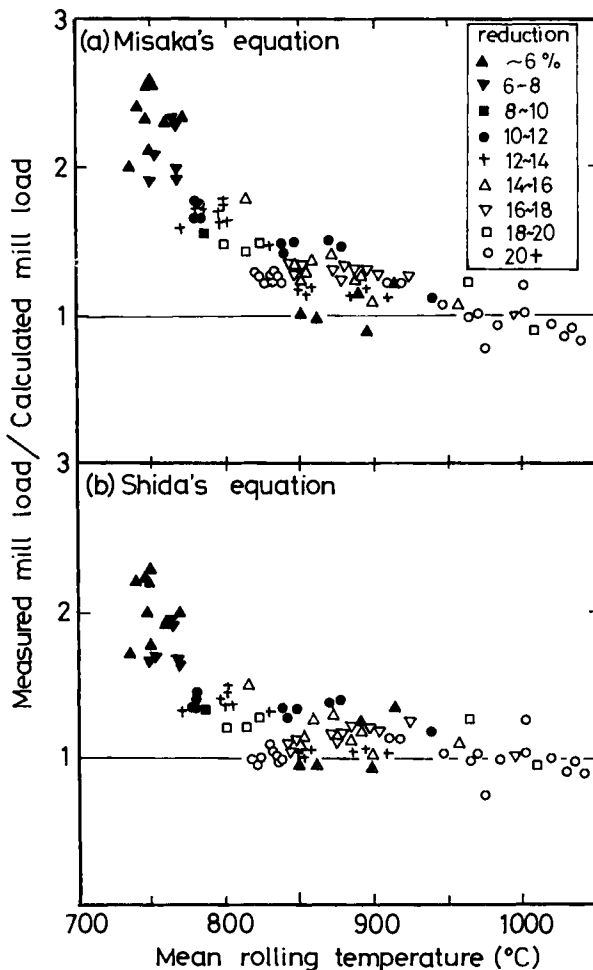


Figure 7.11 Comparison of measured and calculated mill loads; a respective pass strain is used for the hot-strength equations: (a) Misaka's equation<sup>6</sup>; (b) Shida's equation<sup>7</sup>



where  $\varepsilon$  is the emissivity,  $\sigma$  is Boltzmann's constant,  $\alpha C$  is the heat loss ratio by convection,  $T_a$  is the atmospheric temperature, and  $R$  is the thermal conductivity.

The mill load and the surface temperature of the plate during successive rolling passes were measured during controlled-rolling in a 4.572-m wide plate-mill, and were analysed by using Equations (7.9) and (7.10). The rolling-pass schedule in the finishing mill is shown in Figure 7.10, together with a variation of the average temperatures based on the surface temperatures. The plate had a thickness of 16 mm and was API X-65 grade, with 0.12% C–1.34% Mn–0.03% Nb–0.05% V. Deformation resistance equations developed by Misaka and Yoshimoto<sup>6</sup> and Shida<sup>7</sup> noted in Chapter 6 were used for the calculation of the mill load. In Figure 7.11, a ratio of the calculated and observed mill loads is plotted against the rolling temperature. In this case, the strain in both deformation resistance equations was taken as a rolling-pass reduction varying in the range from 6 up to 29%. The discrepancy between measured and calculated mill loads evidently increases with decreasing rolling temperatures, although better matching is observed above 900°C. This discrepancy in the lower-temperature region arises from ignorance of the residual strain affecting the hot-deformation strength, which is cumulatively increasing during multipass rolling in the nonrecrystallized austenitic region.

On the other hand, in a comparison of mill load shown in Figure 7.12, it is the case that the predicted mill load was calculated based on the hot-deformation strength, to which the effective strain was introduced. A pass strain was replaced by the effective strain, which was calculated using the residual strain coefficient. The temperature

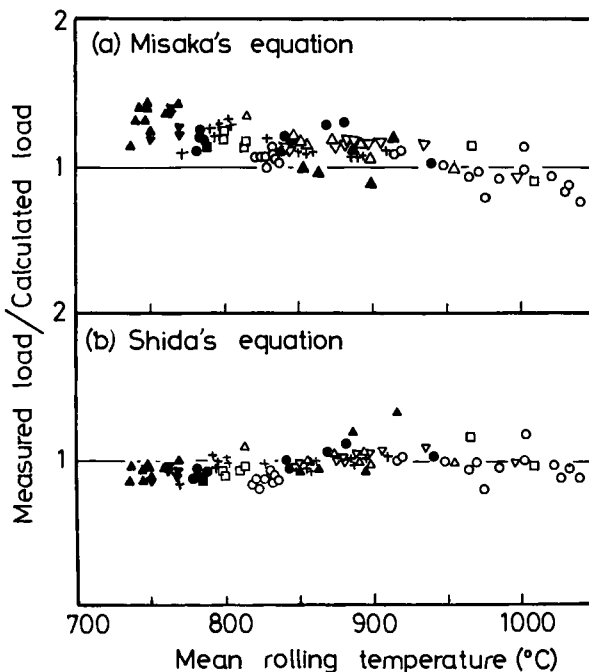


Figure 7.12 Comparison of measured and calculated mill load. Effective strain is used in place of the respective pass strains: (a) Misaka's equation<sup>6</sup>; (b) Shida's equation<sup>7</sup>

dependence of  $\lambda$  values was approximated as shown in the bottom of Figure 7.9, taking account of the interpass time of the reversing plate-mill. It is evident that much better coincidence between calculated and measured mill load is obtained over a wider range of rolling-temperatures, compared with the results in Figure 7.11. These analyses indicated that the effective strain in the final stage of controlled-rolling increased by up to 0.50 as a result of the accumulation of an individual pass strain of around 0.10.

The above procedure based on the effective strain was confirmed to be applicable for prediction of mill load in a hot-strip mill.<sup>8</sup> The several other methods are possible for evaluation of deformation resistance in controlled-rolling. In any case, it is important to take account of the effects on deformation resistance of the microstructural changes which take place during rolling, as well as an exact simulation of rolling-variables such as the strain rate or the interpass time.

## References

1. WHITTAKER, H.J., WALKER, B. and ADAMS, M.A. *Proceedings, International conference on the science and technology of iron and steel*, Iron and Steel Institute of Japan, p.662 (1971)
2. GITTINS, A., EVERETT, J.R. and TEGART, W.J. McG. *Metals Tech.*, **4**, 377 (1977)
3. OUCHI, C., OKITA, T., ICHIHARA, T., and UENO, Y. *Trans Iron and Steel Inst. Japan*, **20**, 833 (1980)
4. SEKINE, H. and MARUYAMA, T. *The strength of metals and alloys*, Vol. I, Iron and Steel Institute, p.85 (1973)
5. SAITO, Y., *J. Japan Soc. Tech. Plasticity*, **11**, 736 (1970)
6. MISAKA, Y. and YOSHIMOTO, T. *J. Japan Soc. Tech. Plasticity*, **8**, 414 (1967)
7. SHIDA, S. *J. Japan Soc. Tech. Plasticity*, **10**, 610 (1969)
8. OUCHI, C., OKITA, T., OKADO, M. and NOMA, Y. *Steel rolling*, Iron and Steel Institute of Japan, p.1272 (1980)

## Transformation behaviour of austenite after thermomechanical treatment

### 8.1 Transformation from recrystallized $\gamma$

The grain size just after transformation is generally finer than that of the phase before transformation especially in cooling transformation. Figure 8.1 shows the relationship between austenite ( $\gamma$ ) and ferrite ( $\alpha$ ) grain sizes before and after transformation in three aircooled silicon–manganese steels having the same plate thickness of 7 mm.<sup>1,2</sup> There is no difference in the relationship for the transformation from isotropic strain-free  $\gamma$  grains between the normalized and the as-rolled steels, when the composition and the

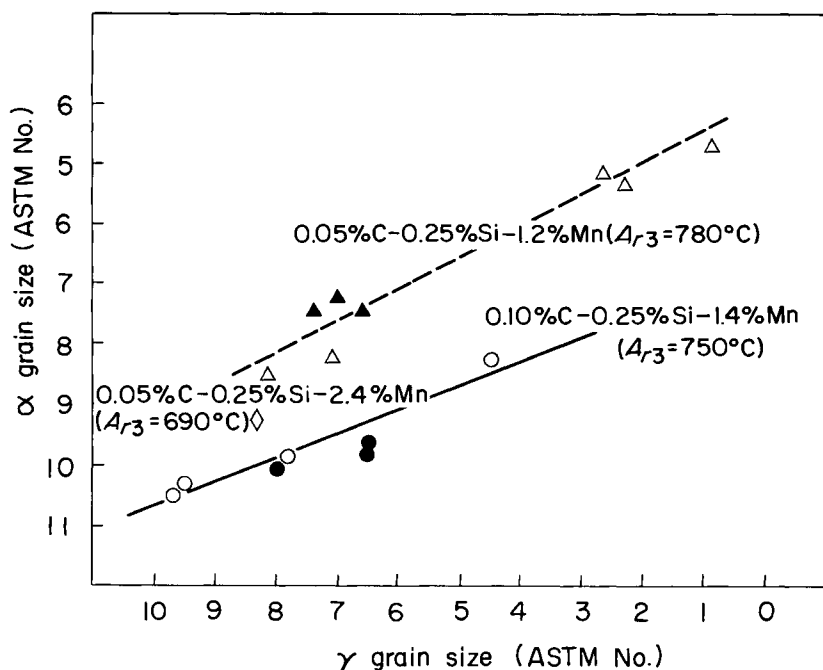


Figure 8.1  $\gamma$  grain size and  $\alpha$  grain size before and after transformation in silicon–manganese steels. Aircooled 7-mm thick plate – open: aircooled after reheating; solid: aircooled after hot reductions. (After Sekine and Maruyama<sup>1</sup> and Sekine *et al.*<sup>2</sup>)

plate thickness (or the cooling rate) are the same. Transformed  $\alpha$  grains are generally finer than  $\gamma$  grains and the finer  $\gamma$  grains transform to the finer  $\alpha$ -pearlite structure, for  $\alpha$  grains nucleate at  $\gamma$  grain boundaries.  $\alpha$  grains of normalized steels are generally finer than those of as-rolled steel, because  $\gamma$  grains at normalizing temperatures are finer than those recrystallized and grown down to the transformation after conventional hot-reductions. The grain refinement in controlled-rolled ships' plates carried out since the 1950s<sup>3</sup> has been mainly brought about by the refinement of recrystallized  $\gamma$  grains by low-temperature finish-rolling.

Refining the  $\gamma$  grains before transformation raises the  $A_{r3}$  temperature and increases the amount of proeutectoid  $\alpha$ , as shown by solid circles in Figure 8.2.<sup>4</sup> This figure clearly shows that the fraction of  $\alpha$  in a conventionally rolled and aircooled plate is

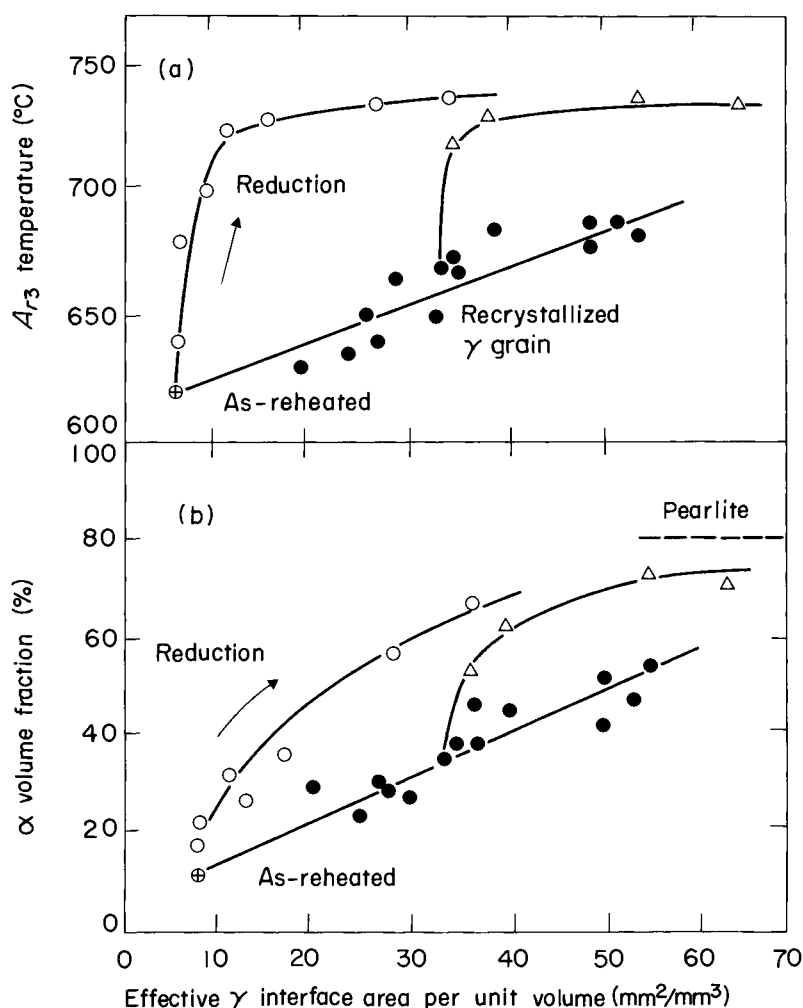
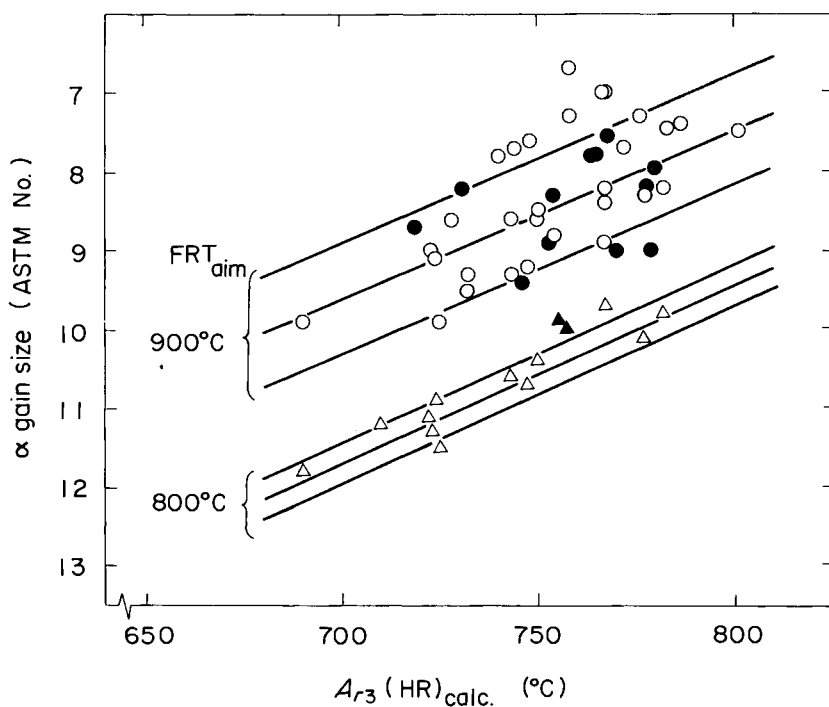


Figure 8.2 Change in transformation behaviour of niobium-containing steel with variations in effective  $\gamma$  interfacial area. 0.16% C-0.36% Si-1.4% Mn-0.03% Nb, aircooled 8 mm-thick plate – solid: transformation from recrystallized  $\gamma$ ; open: transformation from unrecrystallized  $\gamma$ . (After Kozasu *et al.*<sup>4</sup>)

smaller than the equivalent amount and approached to the value by the  $\gamma$  grain refinement. In the transformation from comparably coarse-grained  $\gamma$ , the  $\alpha$  fraction and the concentration of carbon in residual  $\gamma$  at the  $A_{r1}$  temperature cannot reach their equivalent amounts even in aircooling. It brings the apparent increase in pearlite fraction into the final structure, i.e. introduces degenerate pearlite or upper bainite. Lamellar structure in rolled plates – the traces of alloy segregation during solidification – becomes remarkable by normalizing, which can be explained by the concentration of cementite in pearlite lamellae accompanied by the decrease in pearlite fraction in transformation from fine-grained  $\gamma$  at normalizing temperature.

When the  $\gamma$  grain size is constant,  $\alpha$  grains are the more refined in steels having the lower  $A_{r3}$  temperatures, as shown in Figures 8.1 and 8.3.<sup>5</sup> It may be that the lower  $A_{r3}$  temperature retards the growth of  $\alpha$  grains into untransformed  $\gamma$  matrices and promotes the further nucleation of new  $\alpha$  grains. Figure 8.1 further suggests that finer  $\alpha$  grains may be obtained in steels containing more carbon than among steels having the same  $A_{r3}$  temperature. It can be explained by the observed result,<sup>2</sup> that the nucleation of  $\alpha$  grains and their growth into  $\gamma$  matrices are still continued after the appearance of pearlite even in conventional aircooling, i.e. the greater presence of pearlite the more suppressed the growth of already transformed  $\alpha$  grains and accelerated the further  $\alpha$



$$A_{r3}(\text{HR})_{\text{calc.}} = 868 - 396C + 24.6\text{Si} - 68.1\text{Mn} - 36.1\text{Ni} - 207\text{Cu} - 24.8\text{Cr} (\pm 13^\circ\text{C})$$

Figure 8.3 Change in  $\alpha$  grain size with  $A_{r3}$  temperature after hot-deformations. Rolled to 7 mm-thick plate and aircooled  $A_{r3}(\text{HR})_{\text{calc}}$  (result of regression analysis)  $\text{FRT}_{\text{aim}}$  (aimed finish-rolling temperature) open: silicon-manganese steels; solid: silicon-manganese steels containing chromium, nickel or copper. (After Sekine<sup>6</sup>)

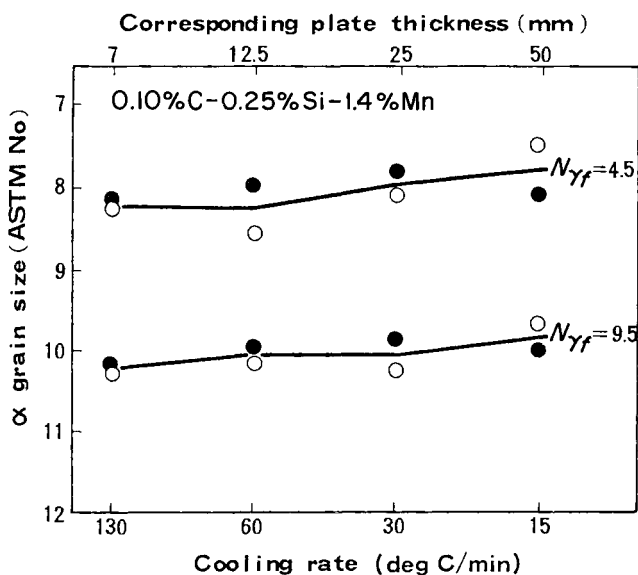


Figure 8.4 Plate-thickness dependence of  $\alpha$  grain refinement in aircooling transformation of silicon-manganese steel – open: aircooled down to room temperature; solid: quenched from  $A_1$  temperature.  $N_{\gamma_f}$   $\gamma$  grain size just before transformation. (After Sekine *et al.*<sup>2</sup>)

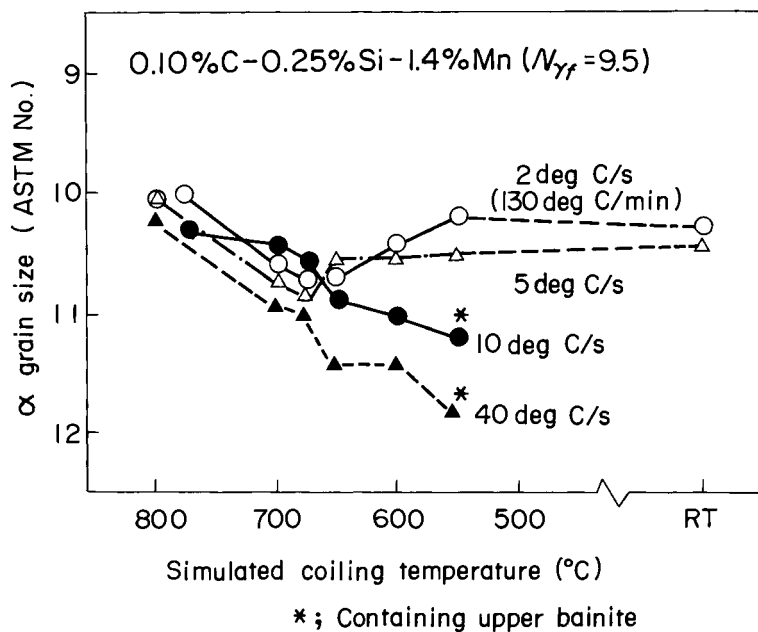


Figure 8.5 Change in  $\alpha$  grain size with cooling rate and coiling temperature in silicon-manganese steel. Simulated cooling rate after coiling: 42° C/h.  $N_{\gamma_f}$   $\gamma$  grain size just before transformation in ASTM number. (After Sekine *et al.*<sup>2</sup>)

nucleation.  $\alpha$  grains transformed from recrystallized  $\gamma$  matrices of the same size in niobium- or vanadium-nitrogen-microalloyed steels are more refined than those expected in alloy-free steels.<sup>1,6</sup> It may also be explained by the retardation of the growth of  $\alpha$  grains into untransformed  $\gamma$  matrices by the precipitated alloy carbonitrides rather than by the additional  $\alpha$  nucleation by these precipitates.

The ratio for  $\gamma \rightarrow \alpha$  transformation<sup>7</sup> – the ratio of the  $\gamma$  grain diameter to the  $\alpha$  grain diameter before and after the cooling transformation – is a function of the  $\gamma$  grain size when the cooling rate is constant, as shown in Figure 4.1, (page 80). The ratio is much larger than 1 when  $\gamma$  grains are comparably coarse, decreases with the refinement of  $\gamma$  grains, and approaches a limiting value of about 1 when  $\gamma$  grain size becomes about 11 in ASTM number. There is a limit to the  $\alpha$  grain refinement by the refinement of

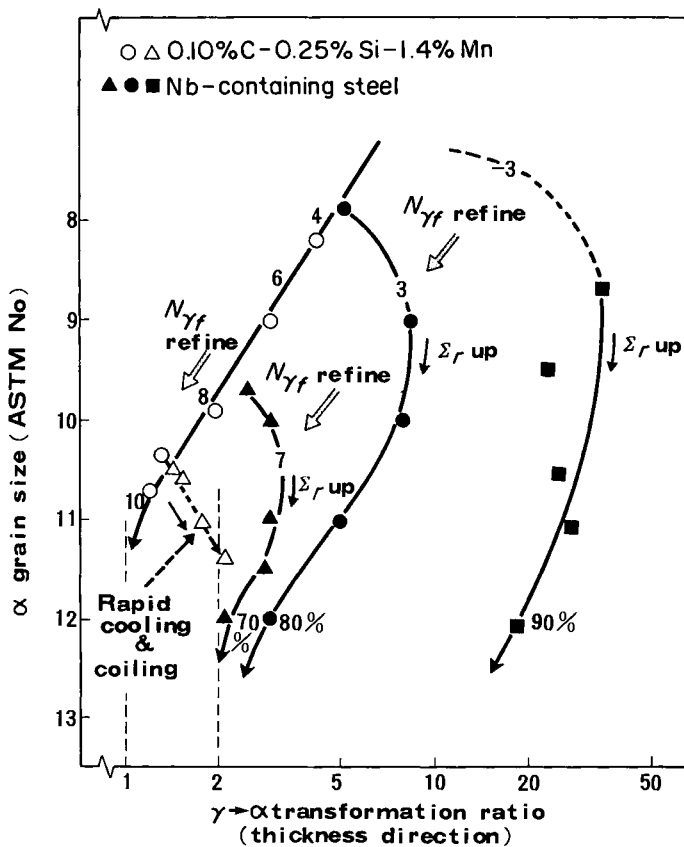


Figure 8.6 Changes in  $\alpha$  grain size and  $\gamma \rightarrow \alpha$  transformation ratio with  $\gamma$  grain size, cooling rate and total reduction at nonrecrystallization temperatures in silicon-manganese and niobium-containing steel. (After Sekine *et al.*<sup>2</sup>)

Open: 0.10% C-0.25% Si-1.4% Mn-0.005% N

○; air-cooled 7-mm thick plate

△; accelerated-cooled and coiled at 600°C

Solid: 0.11% C-0.26% Si-1.36% Mn-0.05% Nb-0.04% V-0.004% N

Finish-rolled at temperatures below 800°C and aircooled 13-mm thick plate

$N_{\gamma f}$ ;  $\gamma$  grain size before transformation in silicon-manganese steel or  $\gamma$  grain size at start of reductions at nonrecrystallization temperatures in niobium-containing steel  $\Sigma_r$ ; total amount of reductions at nonrecrystallization temperatures

recrystallized  $\gamma$  grains in the aircooling transformation.<sup>7</sup> The means of raising the converging  $\gamma \rightarrow \alpha$  transformation ratio are: (1) the controlled-rolling in the non-recrystallization region; and (2) the accelerated cooling after rolling.

The plate-thickness dependence of  $\alpha$  grain refinement by transformation and of the grain growth after transformation in silicon–manganese steel is given in Figure 8.4.<sup>2</sup> It indicates that there is a slight cooling-rate dependence in the  $\gamma \rightarrow \alpha$  transformation ratio, and no coarsening of  $\alpha$  grains after transformation, at least in the cooling-rate range of aircooled heavy plates. It shows that the grain refinement and the improvement in yield strength and toughness in thinner as-rolled plates cannot be attributed to their larger cooling rate but to the  $\gamma$  grain refinement through their unintended low-temperature finish-rolling.

$A_{r3}$  temperatures are lowered and the growth of nucleated  $\alpha$  grains retarded by increasing the cooling rate. A sudden decrease in cooling rate during transformation by coiling hot-strip stimulates the nucleation of new  $\alpha$  grains, and the coiling at the temperatures about  $A_{r1}$  brings the sudden appearance of pearlite which also retards the growth of  $\alpha$  grains. Figure 8.5<sup>2</sup> shows the effects of accelerated cooling and coiling on the size of  $\alpha$  grains transformed from a fine-grained  $\gamma$  structure in the same silicon–manganese steel. The effect of accelerated cooling becomes remarkable at cooling rates over  $5^\circ\text{C/s}$ , which corresponds to that of 12.5-mm thick strips on run-out tables. When strips of the steel are cooled at  $2\text{--}5^\circ\text{C/s}$ , there may be the optimum coiling temperatures to give the finest  $\alpha$  grains just below the  $A_{r1}$  temperature. At higher cooling-rates, the larger the cooling rate and the lower the coiling temperature, the finer the grains to be obtained. Too-drastic lowering of coiling temperature brings about a coarse bainitic structure which lessens toughness. The optimum coiling temperature for toughness in  $\alpha$ –pearlite steels seems to be the  $A_{r1}$  temperature in the adopted cooling rate.

Open triangles and the dotted line in Figure 8.6<sup>2</sup> show the changes in the  $\gamma \rightarrow \alpha$  transformation ratio and the  $\alpha$  grain size by increasing cooling rate, which are obtained from the results coiled at  $600^\circ\text{C}$  in Figure 8.5. The  $\gamma \rightarrow \alpha$  transformation ratio increases and the limit of the ratio of 1 in aircooled fine-grained  $\gamma$  is removed by accelerated cooling.

## 8.2 Transformation from nonrecrystallized $\gamma$

The process of transformation from nonrecrystallized  $\gamma$  grains in thermomechanical processing has already been described in Chapter 4. In this section it is summarized in relation to the practice of controlled-rolling with some supplementary research results.

The deformation of  $\gamma$  grains below recrystallization temperature accelerates markedly the subsequent diffusional transformation more than the refinement of  $\gamma$  grains. It elevates the  $A_{r3}$  temperature (Figures 4.17 (page 94) and 8.2), increases the amount of proeutectoid  $\alpha$  (Figure 8.2) and refines the transformed  $\alpha$  grains (Figure 4.12) (page 89). It brings the increase in  $\gamma$  interfacial surfaces effective to  $\alpha$  nucleation, such as: (1) the increase in  $\gamma$  grain boundary areas by their elongation; (2) the activation of annealing twin boundaries in  $\gamma$  grains to the  $\alpha$  nucleation-sites;<sup>8</sup> and (3) the introduction of deformation bands<sup>1</sup> into deformed  $\gamma$  grains. The acceleration of transformation, how-



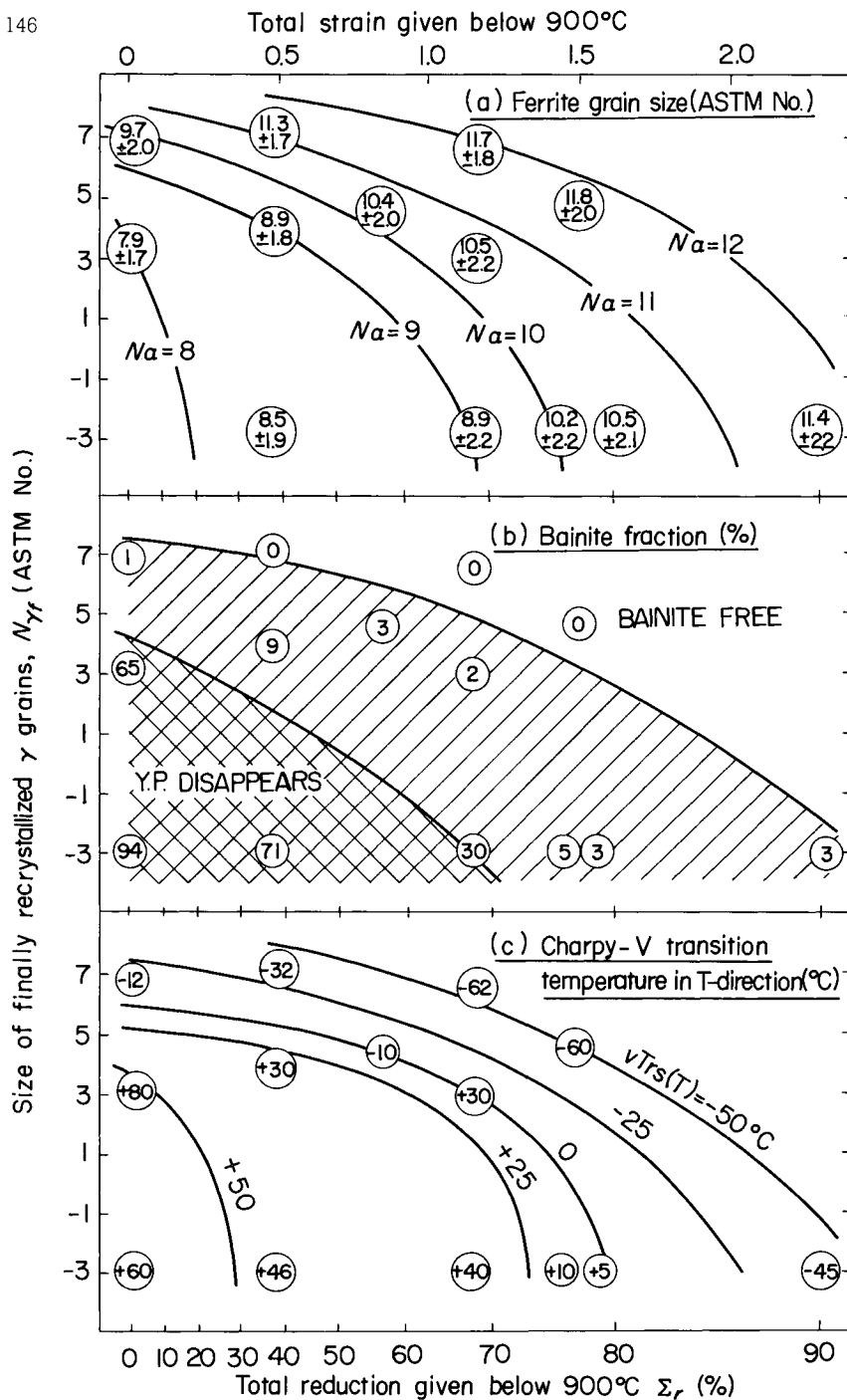


Figure 8.7 Effects of  $\gamma$  grain size at start and total amount of nonrecrystallization-temperature rolling on transformed structure and toughness of niobium-containing steel: (a)  $\alpha$  grain size (ASTM number); (b) bainite fraction (%); (c) Charpy V-notch transition temperature in T direction ( $^{\circ}\text{C}$ ). (After Sekine and Maruyama<sup>1</sup> and Sekine *et al.*<sup>2</sup>)  
 0.11% C-0.26% Si-1.36% Mn-0.05% Nb-0.04% V-0.004% N  
 Reheated at  $1250^{\circ}\text{C}$ , finish-rolled at temperatures below  $800^{\circ}\text{C}$  and aircooled 13-mm thick plate.  
 $N_{\gamma f}$  is finally recrystallized  $\gamma$  grain size obtained by metadynamic recrystallization after reductions at higher temperatures

ever, is due mainly to the increase in the  $\alpha$  nucleation frequency at unit  $\gamma$  grain boundary area<sup>9</sup> which, in turn, is due to the severely concentrated strain on, and in, the vicinity of the grain boundaries.<sup>8</sup> It could explain the common tendency, shown in Figures 4.12, 4.17 and 8.2, that the acceleration of transformation is pronounced even with a small amount of deformation in which the increases in the above-mentioned  $\gamma$  interfacial surfaces are still gradual.<sup>4</sup> With the increase in the amount of deformation, the boundaries of annealing twins lose the coherency with matrices<sup>8</sup> and become the additional nucleation sites of  $\alpha$  grains.  $\alpha$  grains also nucleate at deformation bands<sup>8</sup> but their contribution may become remarkable only at higher reductions, for their density is generally not so high except at high reduction<sup>8</sup> (compare Figures 4.11 and 4.14 (pages 88 and 91)). Thus, it becomes clear that it is possible to obtain a fine-grained  $\alpha$ -pearlite structure having good toughness by controlled-rolling and to refine the polygonal  $\gamma$  grains at the start of nonrecrystallization temperature reductions. Figure 8.7<sup>1,2</sup> shows clearly that the refinement of  $\gamma$  grains before deformation at temperatures below the pancaking temperature, and the increase in the amount of the deformation, are interchangeable or additive in the guarantee or the improvement of toughness.<sup>4</sup>

The recrystallization temperatures of simple silicon-manganese steels in successive reductions are about 800–850°C, which are considerably lower than conventional rolling temperatures and too close to their  $A_{r3}$  temperatures. The addition of niobium, titanium and molybdenum makes easy the controlled-rolling in the nonrecrystallization temperature region by elevating the pancaking temperatures of steels.

In precipitation-hardened controlled-rolled steels, the amount of carbon is usually reduced largely to improve toughness and weldability and to guarantee the amount of solute niobium at low-temperature reheating of slabs.<sup>10</sup> The amount of manganese is increased<sup>10</sup> to hold their  $A_{r3}$  temperatures low enough to: (1) maintain the total reduc-

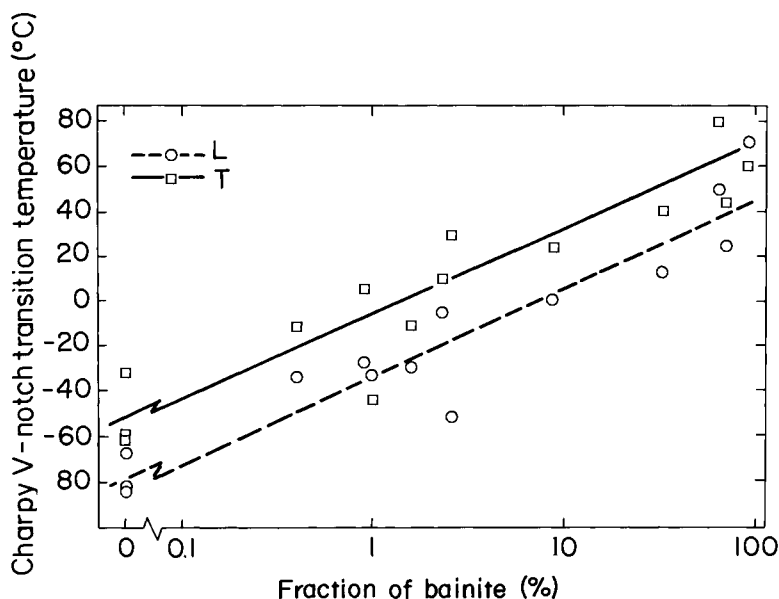


Figure 8.8 Deterioration of toughness by increase in upper bainite in niobium-containing steel. Test piece was the same as that of Figure 8.7. (After Sekine and Maruyama<sup>1</sup>)

tions between the pancaking temperatures and the  $A_{r3}$  temperature; (2) raise the effective  $\gamma \rightarrow \alpha$  transformation ratio; and (3) suppress the overageing of precipitated alloy carbonitrides.<sup>1</sup> Coarse acicular  $\alpha$  and upper bainite are apt to appear in the conventionally rolled state of high-manganese steels and niobium-containing steels,<sup>11</sup> and lessen their toughness<sup>11</sup> (Figure 8.8).<sup>1</sup> These low-temperature transformation products can be reduced effectively or eliminated by skilful controlled-rolling even in steels containing niobium and the higher amount of manganese (Figure 8.7(b)).<sup>1</sup> The process is facilitated by the rise in the nucleation rate of polygonal  $\alpha$  grains and in their site density due to nonrecrystallization-temperature rolling.

The total density of activated twin boundaries and deformation bands increases with increasing the total reduction but is insensitive to the reduction temperature and the rolling speed, as shown in Figure 4.11 (page 88). When the amount of reduction per pass is increased or the number of passes is reduced, holding the total reduction constant, the density also continues to increase up to 25 or 30% reduction per pass (Figure 8.9),<sup>1</sup> a draught hardly attained in the reductions of work-hardened  $\gamma$  grains by conventional finishing mills. Accordingly, the increase in activated twin boundaries and deformation bands is to be expected mainly because of the increase in the total amount of the reductions<sup>4</sup> with the possible largest reduction per pass.<sup>1</sup>

Not all of the  $\gamma$  grains contain annealing twins or deformation bands, neither twins nor bands being observed in about 10% of  $\gamma$  grains even after heavy deformation<sup>1</sup> (Figure 8.10).<sup>1</sup> Furthermore, not all twins or bands have the same  $\alpha$  nucleation potential.<sup>4</sup> These inhomogeneities cause the mixed grain structure or the admixture of coarse bainitic structure after transformation, lessening toughness. The comparison of structures and toughness of steels having the same mean  $\alpha$  grain size given in Figure 8.7 shows that the standard deviation in  $\alpha$  grain size and the fraction of upper bainite are more reduced, and the Charpy V-notch transition temperature is more improved, in

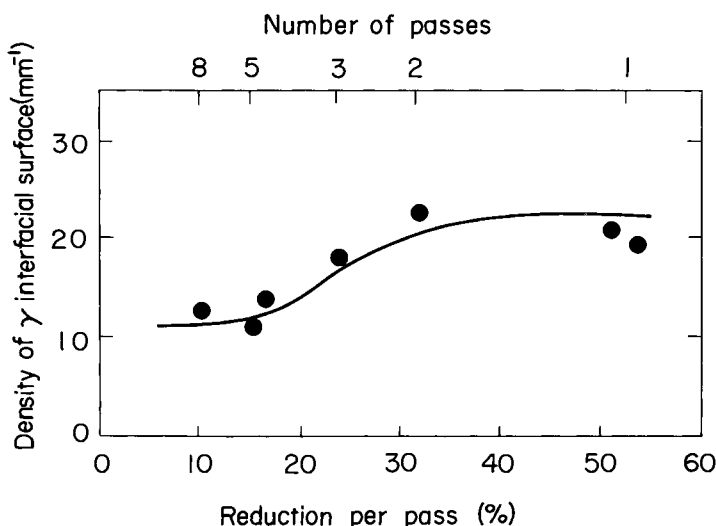


Figure 8.9 Change in density of  $\gamma$  interfacial surfaces through thickness direction with amount of reduction per pass holding total reduction constant. (After Sekine and Maruyama<sup>1</sup>)

0.10% C–0.26% Si–1.4% Mn–0.05% Nb–0.006% N

Rolled in 1 to 8 reductions at temperature from 1000 to 860°C after reheating at 1250°C

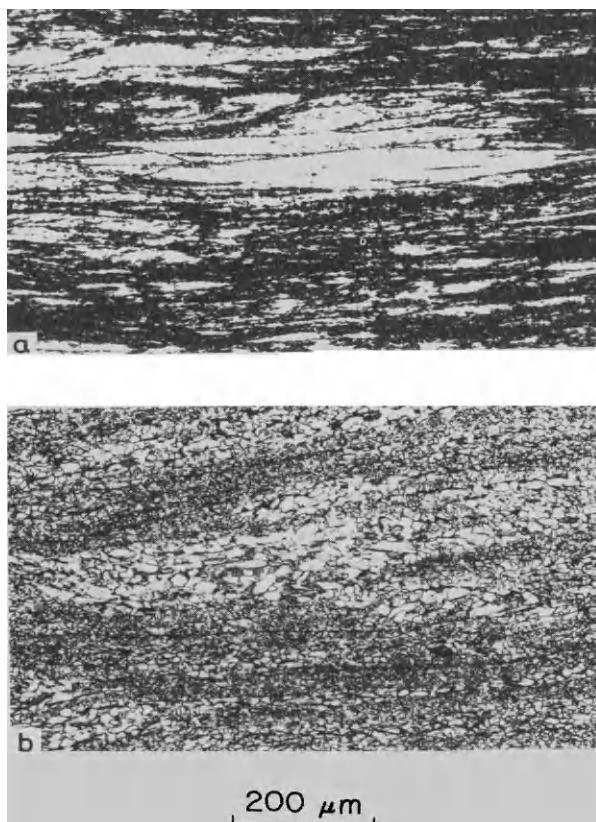


Figure 8.10 Structures before and after transformation of niobium-containing steel rolled only in nonrecrystallization region: (a) unrecrystallized  $\gamma$  grain containing neither annealing twin nor deformation band in steel quenched after final reduction; (b) coarse-grained  $\alpha$  structure in steel aircooled after reductions. (After Sekine and Maruyama<sup>1</sup>)  
 0.10% C–0.26 Si–1.4 Mn–0.05 Nb–0.006 N  
 75 mm (1250°C)  $\rightarrow$  8 reductions (1000/860°C)  $\rightarrow$  7 mm

steels which started the reductions at nonrecrystallization temperatures from the finer recrystallized  $\gamma$  grains. It is noteworthy that the Charpy V-notch absorption energy at the ductile region in the transverse direction, given in Figure 8.11, rapidly decreased when the total amount of the reduction became larger than 70%. Figure 8.12, obtained from Figures 8.7(c) and 8.11 and compared at the same transition temperature, shows that controlled-rolling started its reductions below the pancaking temperature at the more refined  $\gamma$  grains, giving the higher shelf energy in a transverse direction. The results in Figures 8.7–8.12 were obtained using the test pieces cut from the converter-melt direction-melt and broken-down slab containing a reduced amount of sulphur. Manganese sulphides are more elongated to the rolling direction in work-hardened  $\gamma$  grains than in recrystallized  $\gamma$  grains. Figure 8.12 is the consequence of the uniformity in  $\alpha$  grain structure and the deformation of inclusions.

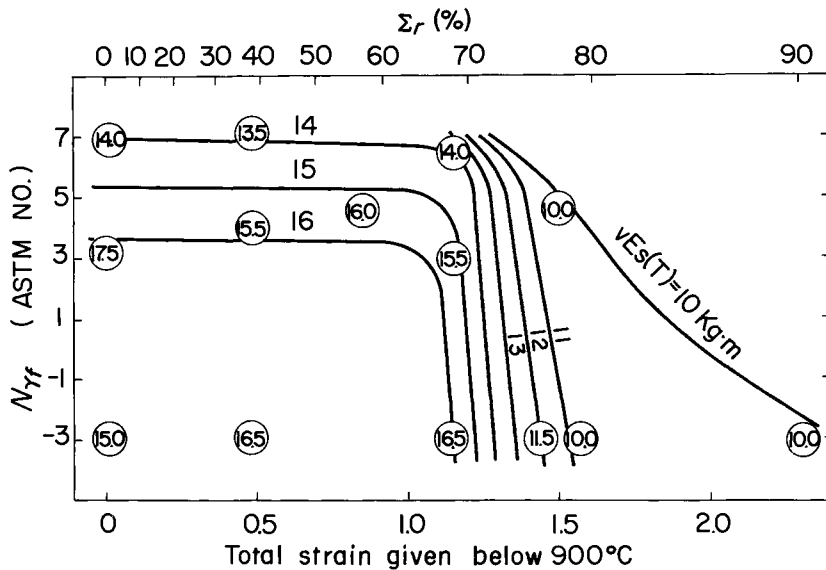


Figure 8.11 Effects of  $\gamma$  grain size and total amount of reductions at nonrecrystallization temperatures on Charpy V-notch shelf energy in the T direction. Test piece was the same to that of Figure 8.7. Figures in circles are observed shelf energies in kilogram metres. (After Sekine and Maruyama<sup>1</sup>)

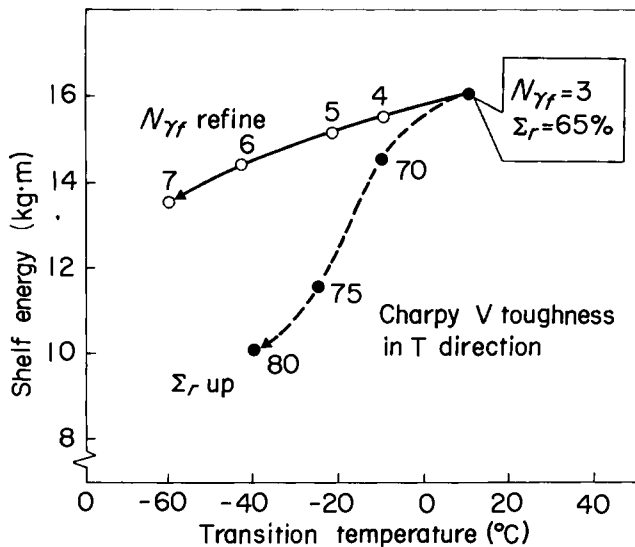


Figure 8.12 Comparison of toughness between two types of controlled-rolling in niobium-containing steel. Obtained from Figures 8.7(c) and 8.10. (After Sekine and Maruyama<sup>1</sup> and Sekine *et al.*<sup>2</sup>)

In the early mill trials on the controlled-rolling of niobium-containing steels carried out by the British Iron and Steel Research Association (BISRA), it was observed – in thicker plates – that the mixed grain structure was reduced and the toughness improved by: (1) giving reductions of higher draughts at fairly equally spaced intervals over the

whole temperature range; or (2) by setting the holding period at temperatures above 1100 or below 950° C (if possible after the reduced temperature reheating of slabs).<sup>1,2</sup> It can be explained as the effect of the refinement of recrystallized  $\gamma$  grains by the reductions in the recrystallization temperature range, which is extended to the temperatures lower than their expected range.

So far in this chapter, the nucleation of  $\alpha$  grains in deformed  $\gamma$  grains has been discussed. However, after site saturation, the distribution of  $\alpha$  nucleation sites and the differences in their potentials may affect the growth of nucleated  $\alpha$  grains during and after the transformation and the resultant structure. The increase in  $\gamma$  grain boundary area by hot-deformation is not so large as to overenhance the  $\alpha$  nucleation sites.<sup>9</sup> Nevertheless, an increase in the amount of deformation brings a decrease in the distance between apparent  $\gamma$  grain boundaries (including other interfacial surfaces through thickness direction and the decrease in their curvature), which can increase the chance of collision between growing  $\alpha$  grains having nucleated at the confronting interfaces.

Figure 8.13 shows that the shape of proeutectoid  $\alpha$  grains after the heavy deformation in the nonrecrystallization temperature range is not completely isotropic, but is like a pancake crushed in the thickness direction.<sup>1</sup> It probably means that there is collision of the growing  $\alpha$  grains nucleated at the different and confronting interfaces, but the possibility of their coalescence is smaller than that of neighbouring  $\alpha$  grains nucleated at the same interfaces.

The  $\gamma \rightarrow \alpha$  transformation ratio in the cooling from unrecrystallized  $\gamma$  grains can be defined as the ratio of the distance between the elongated  $\gamma$  grain boundaries (not including other  $\gamma$  interfacial surfaces) through thickness direction to the diameter of the transformed  $\alpha$  grains.<sup>2</sup> The change with the starting  $\gamma$  grain size and the amount of the deformation can be obtained using the results in Figure 8.7(a) and is also shown by solid symbols in Figure 8.6. By increasing the total number of reductions below the recrystallization temperature the  $\gamma \rightarrow \alpha$  transformation ratios are increased, starting from the respective values for the sizes of strain-free polygonal  $\gamma$  grains, reached at their maximum values and finally seeming to converge on to two. The more refined the finally recrystallized grains are, the smaller the maximum values and the more rapid the convergence to the value of two becomes. The role of annealing twin boundaries and deformation bands as the nucleation sites are decreased by refining the size of finally recrystallized grains,<sup>9</sup> shows the progress of site saturation at  $\gamma$  grain boundaries.<sup>9</sup> The fact that the  $\gamma \rightarrow \alpha$  transformation ratio has the maximum, shows the presence of site saturation at all the nucleation sites and the successive coalescence of nucleated  $\alpha$  grains during transformation. With consideration for the crushed shape of the transformed  $\alpha$  grains, the convergence of the  $\gamma \rightarrow \alpha$  transformation ratio on the value of two, strongly suggests that, in the transformation from the heavily deformed  $\gamma$ , statistically in the T (thickness) direction, two  $\alpha$  grains nucleated at both sides of an elongated  $\gamma$  grain boundary and/or only one  $\alpha$  grain nucleated across the  $\gamma$  boundary and one  $\alpha$  grain in those nucleated at another interface in a deformed  $\gamma$  grain can finally survive the coalescence. Deformed  $\gamma$  grain boundaries can be considered to be the most effective nucleation sites even after the heavy deformation in the nonrecrystallization region. The not-so-large aspect ratio in the crushed  $\alpha$  grains transformed after the heavy deformation strongly suggests that the coalescence of the neighbouring  $\alpha$  grains nucleated at the common flattened interface may not occur so easily.

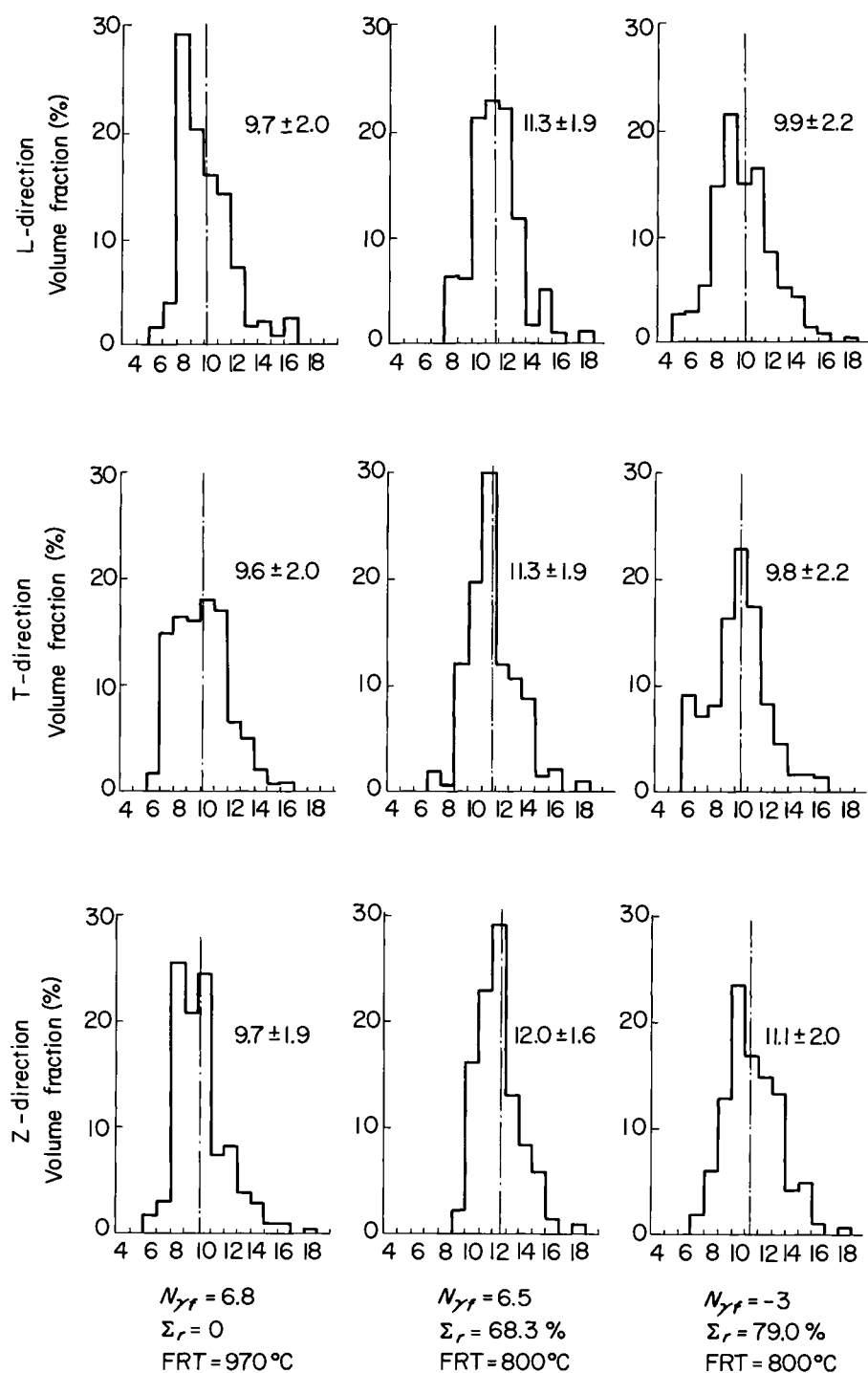


Figure 8.13 Shape of  $\alpha$  grains in controlled-rolled niobium-containing steel. Test piece was the same as that for Figure 8.7. (After Sekine and Maruyama<sup>1</sup>)

The experiments in Figures 8.7–8.9 and 8.11 have been carried out to obtain the optimum allotment of reductions to recrystallization and nonrecrystallization temperature regions, but the results show clearly that the slab reheating at temperatures below  $\gamma$  grain coarsening temperature, and the concentration of reductions to nonrecrystallization temperature range, are effective especially for the controlled-rolling of thicker plates.

## References

1. SEKINE, H. and MARUYAMA, T. *Seitetsu Kenkyu*, **289**, 43 (1976)
2. SEKINE, H., MARUYAMA, T., KAGAYAMA, H. and KAWASHIMA, Y. *The thermomechanical processing of microalloyed austenite*, A.J. De ARDO *et al.* (eds) The Metallurgical Society of the American Institute of Metallurgical and Petrochemical Engineers, p.141 (1982)
3. VANDERBECK, R.W. *Weld. J.*, **37**, 114S (1958)
4. KOZASU, I., OUCHI, C., SAMPEI, T. and OKITA, T. *Microalloying 75*, Union Carbide Corp., p.120 (1977)
5. SEKINE, H. *Progress in manufacturing processes and properties of heavy plates* (86/87th Nishiyama Anniversary Technical Lecture), Iron and Steel Institute of Japan, p.123 (1982)
6. SEKINE, H. and MARUYAMA, T., *Trans Iron and Steel Inst. Japan*, **16**, 427 (1976)
7. SEKINO, S., MORI, N. and TAMUKAI, S. *Tetsu-to-Hagané*, **58**, 1044 (1972)
8. INAGAKI, H. *Trans Iron and Steel Inst. Japan*, **23**, 1059 (1983)
9. UMEMOTO, M., OHTSUKA, H. and TAMURA, I. *Trans Iron and Steel Inst. Japan*, **23**, 775 (1983)
10. DUCKWORTH, W.E., PHILLIPS, R. and CHAPMAN, J.A. *J. Iron and Steel Inst.*, **203**, 1198 (1965)
11. DE KAZINCZY, F., AXNÄS, A. and PACHLEITNER, P. *Jernkont. Ann.*, **147**, 408 (1963)
12. IRANI, J.J., BURTON, D., JONES, J.D. and ROTHWELL, A.B. *Strong tough structural steels*, The Iron and Steel Institute, p.110 (1967)



---

## Alloying elements and impurities

---

### 9.1 Microalloying elements

The chemical compositions of high-strength low-alloy (HSLA) steels produced by thermomechanical processes are determined primarily by taking account of strength, toughness, ductility and weldability. The alloying elements commonly used in HSLA steels and impurity elements may be categorized into three groups from their different roles and influences on the mechanical properties of steels:

- (1) Microalloying elements – niobium, vanadium, titanium, aluminium and boron.
- (2) Substitutional elements – silicon, manganese, molybdenum, copper, nickel and chromium.
- (3) Impurities and sulphide shape-control additives – phosphorus, sulphur, calcium, rare earth metals (REM) and zirconium.

The alloying elements in the first two groups control mainly the strength and toughness as well as the transformed microstructure, and the elements in the third group primarily affect ductility of controlled-rolled plates. Carbon and nitrogen play a critical role on weldability of HSLA steels, and an optimum level of carbon content is determined by overall considerations of the base-metal properties and weldability or carbon equivalent.

Alloying additives which can exert a remarkable or specific influence on the properties and the microstructure under an addition of less than around 0.10% weight in steel are called microalloying elements. The effective and rational utilization of the microalloying elements such as niobium, vanadium or titanium provides a basis for improvement in both strength and toughness achieved by thermomechanical processing in HSLA steels, and therefore it is important to understand the fundamental behaviours of the microalloying elements such as solubility, precipitation of carbide or nitride and retardation of austenitic recrystallization. The differences in these behaviours among the microalloying elements are described in the first part of this chapter, and then the mechanical properties obtained by controlled-rolling in each microalloyed steel are presented.

#### 9.1.1 Solubility products

Niobium, vanadium and titanium have different affinities with carbon and nitrogen in

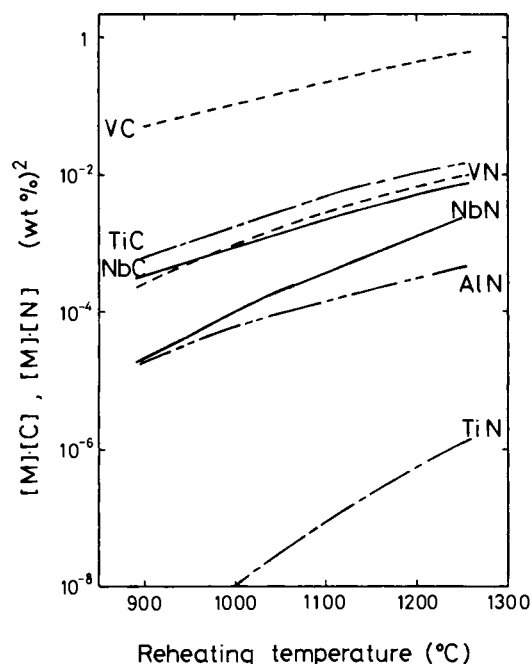


Figure 9.1 Solubility products of carbides and nitrides in  $\gamma$

austenite ( $\gamma$ ), and this causes the different solubility products of carbide and nitride in respective microalloying elements as shown in Figure 9.1.<sup>1</sup> In the temperature range 1100–1250° C commonly adopted as a slab-reheating temperature, titanium nitride is the most stable compound and vanadium carbide the most soluble into  $\gamma$ . Niobium carbide and titanium carbide lie between the two compounds, and the amount of niobium or titanium content dissolved in  $\gamma$  at the reheating temperature can be varied widely, depending on the temperature and carbon content. Excepting aluminium nitride with a hexagonal structure, these carbides and nitrides are isomorphous with cubic structures, and are soluble in each other. That is, carbide or nitride in steel contains some amounts of nitrogen or carbon respectively, and they are often called carbonitrides. Figure 9.1 shows that all the nitrides have lower solubilities in  $\gamma$  than the respective carbides, and this may be true in ferrite ( $\alpha$ ). In commercial microalloyed steels, vanadium and niobium are precipitated as carbonitrides. Vanadium nitride and niobium nitride are seldom formed in the commercial microalloyed steels except in the very low-carbon-high-nitrogen steel. On the other hand, in titanium-bearing steel, titanium nitride is first formed, and after all the nitrogen is combined as titanium nitride, titanium carbide may subsequently precipitate with increasing titanium content.

The undissolved carbides and nitrides at the reheating temperature contribute to refinement of the initial austenitic grain size. Figure 9.2 gives variations of grain size with the reheating temperature in various microalloyed steels. All the steels have the same basic compositions with 0.10% C–0.25% Si–1.50% Mn–0.03% Al–0.006% N, and are reheated at each temperature for 1 h. The grain size in silicon–manganese and niobium-bearing steels is controlled by dissolution behaviour of aluminium nitride and

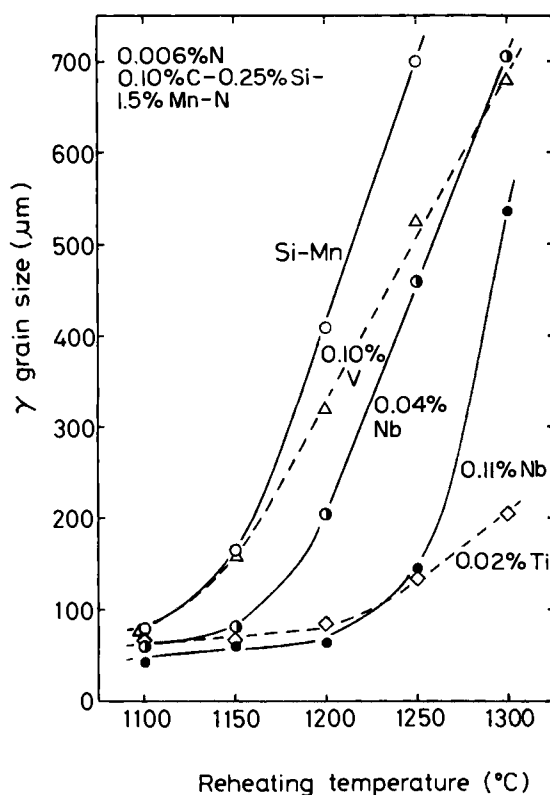


Figure 9.2 Variation of  $\gamma$  grain size with reheating temperature

niobium (carbide and nitride) respectively, and the increase of niobium content up to 0.11% substantially refines the grain size even at 1250° C. The grain-coarsening temperature in vanadium-bearing steel is almost the same with that of silicon-manganese steel due to the high solubility of vanadium (carbide and nitride) in  $\gamma$ . The increase of nitrogen content in this steel exerts a small influence on the grain-size behaviour. The titanium-bearing steel exhibits an extremely high grain-coarsening temperature above 1250° C. This is brought about by pinning the austenitic grain boundaries due to the very stable titanium nitride precipitates which are mostly formed during solidification of steel.<sup>2</sup>

The reduction of the slab-reheating temperature, often adopted in controlled-rolling, can decrease simultaneously the initial grain size and rolling temperatures during rougher rolling. Both factors enhance the refinement and homogeneity of the recrystallized grain size achieved in the final stage of rougher rolling, which can improve remarkably the low-temperature toughness in controlled-rolled plate, particularly with the heavier thickness. The reduction of the reheating temperature in niobium- or titanium-bearing steel is accompanied by the decreases of niobium or titanium content dissolved in  $\gamma$ , and these partly dissolved elements can cause the retardation effect of austenitic recrystallization and also precipitation hardening in the later stage of controlled-rolling.

### 9.1.2 Retardation of $\gamma$ recrystallization

The beneficial effect of controlled-rolling as a high-temperature thermomechanical treatment is brought about by retardation of austenitic recrystallization due to microalloying elements, and from this standpoint, the numerous basic studies on austenitic recrystallization have been conducted during the last 20 years. The fundamental knowledge obtained from these investigations has made possible a rational design for a microalloying system in HSLA steels. Two experimental methods that have been used for investigation of austenitic recrystallization are: (1) the direct observation of the austenitic structure in the specimens quenched after hot-working;<sup>3</sup> and (2) the high-temperature mechanical testing method,<sup>4</sup> in which softening ratio is evaluated from a variation of flow stress obtained by the interrupted multistage deformation described in Chapter 7. In Figures 9.3 and 9.4, the static recrystallization kinetics investigated in the latter method are compared among different microalloyed steels. The basic composition of steels is 0.10% C–0.25% Si–1.45% Mn, and the initial grain size is controlled to 150  $\mu\text{m}$  in all the steels. In these figures, the increase in the softening ratio from 0 to 20% and the following increase up to 100% are due to progress in static recovery and static recrystallization respectively. It is seen from the comparison of silicon–manganese steel and 0.04% Nb steel that the addition of niobium remarkably retards recrystallization kinetics below 900°C. The 0.08% Ti steel exhibits similar recrystallization behaviour to that of niobium steel, while a single addition of vanadium in the range of nitrogen content below 0.0150% has a weak retardation of recrystallization. Consequently, the microalloyed steel which can give rise to the very refined transformed microstructure through the transformation from the nonrecrystallized austenitic

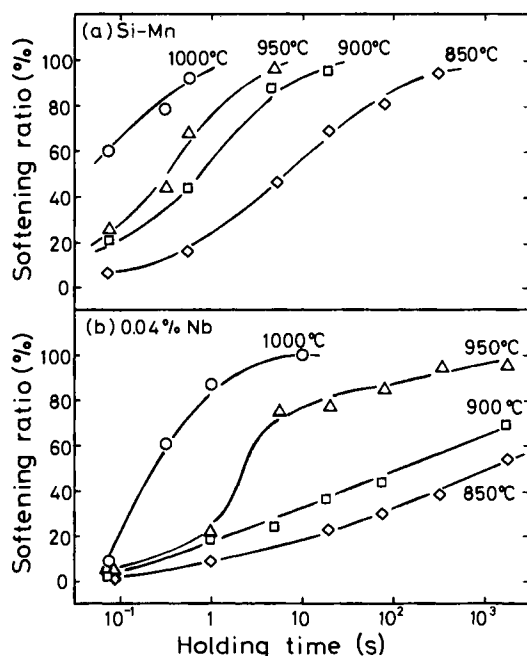


Figure 9.3 Static recrystallization kinetics in  $\gamma$ : (a) silicon–manganese steel; (b) 0.04% Nb steel. Prestrain is 0.50

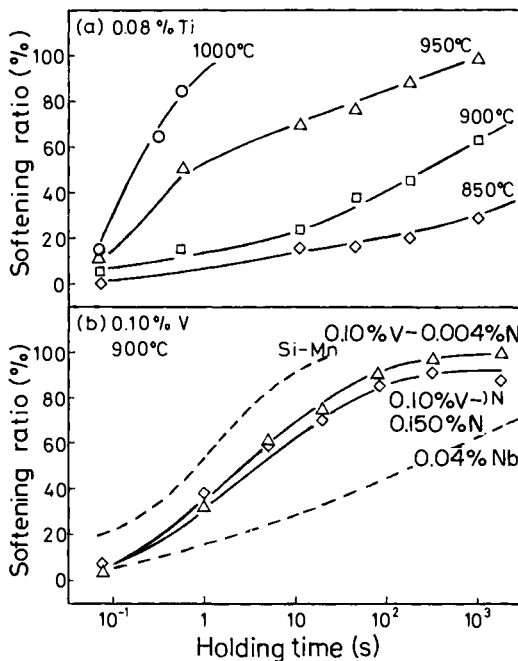


Figure 9.4 Static recrystallization kinetics in  $\gamma$ : (a) 0.08% Ti steel; (b) 0.10% V steel at 900°C. Prestrain is 0.50

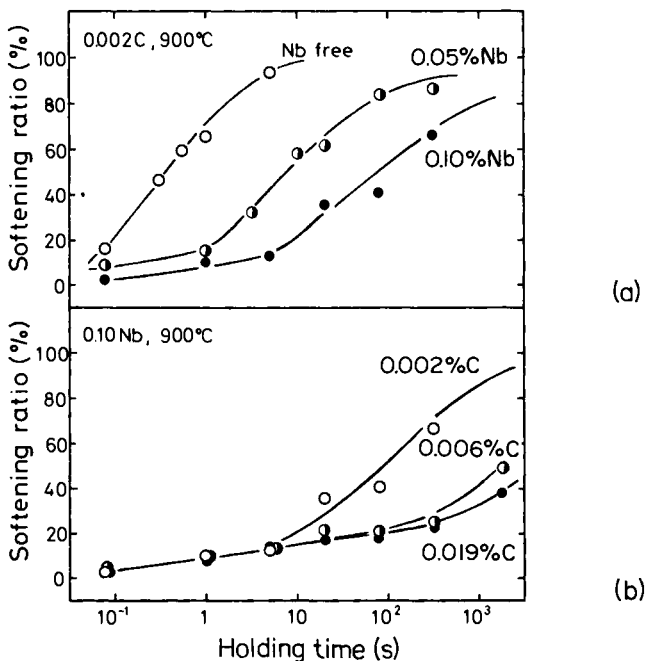


Figure 9.5 Static recrystallization kinetics in niobium-bearing steel. Niobium content is varied up to 0.20% in Fe-0.25% Si-2.0% Mn steel, and carbon content is varied from 0.002 to 0.012% in 0.10% Nb steel: (a) 0.002% C steel at 900°C; (b) 0.10% Nb steel at 900°C. Prestrain is 0.50

structure is either niobium- or titanium-bearing steel, and vanadium is usually added simultaneously in these steels in view of the additional strengthening due to precipitation hardening.

With regard to the retardation of austenitic recrystallization due to microalloying elements, two mechanisms based on solute drag and strain-induced precipitation have been proposed.<sup>5,6</sup> To clarify this point, the austenitic recrystallization was studied in the iron-manganese-niobium system containing extremely low carbon and nitrogen,<sup>7</sup> which facilitated the investigation of the solute niobium effect. Figure 9.5 arises from this study and demonstrates that solute niobium evidently retards the austenitic recrystallization. It is confirmed that this retardation effect by solute niobium is extremely large among various solute elements. However, the continuous increase of carbon content in 0.10% Nb-bearing steel results in much larger retardation of recrystallization kinetics. Consequently, strain-induced precipitation of carbides and nitrides of niobium taking place in deformed  $\gamma$  primarily causes the retardation of recrystallization, while solute niobium may contribute to the suppression of the progress of static recovery in the stage before the start of strain-induced precipitation. Although the strain-induced precipitation of titanium carbide similar to that of carbides and nitrides of niobium may occur in titanium-bearing steels, high solubility of vanadium carbide in vanadium-bearing steel tends to maintain vanadium in solution even in the low-temperature region of  $\gamma$ .

### 9.1.3 Grain refinement and precipitation hardening

The strength and toughness obtained by controlled-rolling in microalloyed steels largely depend on grain refinement and precipitation hardening, although these properties

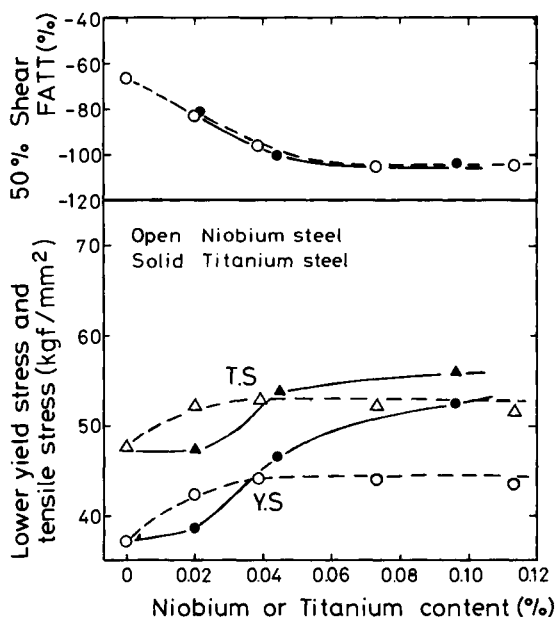


Figure 9.6 Changes of the strength and Charpy transition temperature with niobium and titanium

can be widely changed by variables of controlled-rolling and the basic compositions of steel. The typical variations of strength and the transition temperature in Charpy V-notch impact testing with the contents of niobium and titanium are presented in Figure 9.6. The basic composition in both steels is 0.10% C–0.25% Si–1.50% Mn, and the reheating temperature and the finishing rolling temperature are 1100 and 780° C respectively, with a total reduction below 900° C of 70%.

Contrasting with a plateau of strengthening observed in the content over 0.04% in niobium steel, titanium-bearing steels result in the larger and continuous increase of strength with increasing titanium content up to 0.10%. The improvement of low-temperature toughness tends to saturate in the content around 0.06% in both steels. The variations of these properties are attributable to grain refinement and precipitation hardening due to carbides and nitrides of niobium or titanium carbide, and the latter strengthening effect is associated with niobium or titanium content dissolved at the reheating temperature.

The simultaneous addition of niobium and vanadium is frequently adopted in a higher-strength level of steel or in a thicker plate. Although superior low-temperature toughness obtained in niobium- or titanium-bearing steel cannot be realized easily in a straight vanadium steel, niobium–vanadium steel can give rise to an excellent combination of strength and toughness. In Figure 9.7, vanadium content is varied up to 0.10% in 0.10% C–1.30% Mn–0.035% Nb and 0.15% Mo–0.035% Nb steels. It is evident that precipitation hardening due to vanadium carbide can get over the plateau of strengthening observed in a straight niobium steel, and that the strength increment of about 7 kg/mm<sup>2</sup> is obtained by the addition of 0.10% vanadium without a lessening of toughness.

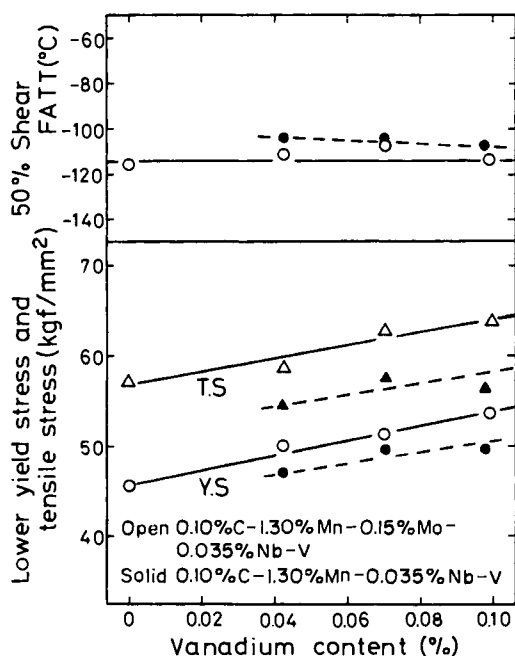


Figure 9.7 Changes of the strength and Charpy transition temperature with vanadium content in 0.035% Nb steel and 0.15% Mo–0.035% Nb steel

As for precipitation hardening of microalloying elements, it is important to note that these elements can enhance the hardenability of steel. Recent progress in thermo-mechanical processing tends to obtain higher strength and toughness by combining controlled-rolling and controlled-cooling or accelerated cooling.<sup>8,9</sup> The transformed microstructure obtained in these processes is modified from  $\alpha$ -pearlite to  $\alpha$ -bainite or acicular  $\alpha$ . The microalloying elements can assist to increase the bainite volume fraction under a specific accelerated cooling condition. The addition of boron in HSLA steel has the same effect,<sup>10</sup> and these strengthenings due to transformed microstructures are described in Section 9.2.

## 9.2 Substitutional alloying elements

The substitutional alloying elements such as manganese or molybdenum: (1) strengthen the steel through solid solution-hardening; (2) grain refinement due to depression of the  $\gamma \rightarrow \alpha$  transformation temperature; and (3) modification of the transformed microstructure. In general, effect (3) is more remarkable on strengthening compared with (1) and (2). The dominant microstructure in HSLA steels produced by controlled-rolling is the polygonal  $\alpha$ -pearlite, and the decrease of carbon content can yield a pearlite-reduced or pearlite-free steel. The increase in the manganese:carbon ratio under a reduced carbon content gives rise to an acicular  $\alpha$  or an ultra-low carbon-bainite structure. The quantitative strengthening effect in a respective element can vary with the transformed microstructure and the plate thickness or cooling rate.

Numerous studies have been conducted to evaluate the relationships between microstructural and compositional parameters and their mechanical properties. As an example of these relationships for the  $\alpha$ -pearlite structure, Table 9.1 presents the results of multiple-regression analysis for the relation of the ultimate tensile strength and chemistry of steels prepared by laboratory heats. The variables of controlled-rolling are a reheating temperature of 1200° C and the finishing rolling temperature of 800° C

TABLE 9.1 Effect of alloying elements on ultimate tensile strength (in kilograms per square millimetre percentage weight)

|       |                | C            | Mn           | Cu     | Ni     | Cr     | Mo     | V       |
|-------|----------------|--------------|--------------|--------|--------|--------|--------|---------|
| Case* | Thickness (mm) | 0.04<br>0.11 | 1.36<br>1.92 | < 0.44 | < 0.52 | < 0.52 | < 0.41 | < 0.117 |
| A     | 12             | 101.3        | 16.1         | 4.2    | 6.0    | 10.6   | 25.0   | 43.9    |
|       | 20             | 89.6         | 9.4          |        |        |        | 23.1   | 29.4    |
| B     | 12             | 164.9        | 26.9         | 11.0   | 10.5   | 23.4   | 46.9   | 88.7    |
|       | 20             | 125.9        | 25.5         |        | 10.9   | 18.5   | 36.6   | 86.6    |

\* Case A is a single addition of respective elements and case B is a simultaneous addition of two or three elements. Basic composition of steels is 0.22% Si–0.045% Nb–0.026% Al.

with a cumulative rolling reduction below 900° C of 70%. A single addition of copper, nickel, chromium and molybdenum and a simultaneous addition of two or three elements in a combination such as copper–nickel or copper–nickel–molybdenum are investigated in the steels with a basic composition of 0.25% Si–0.045% Nb–0.03% Al. Molybdenum causes the largest strengthening among the alloying elements in many



cases, and manganese and chromium are intermediate. Copper and nickel result in a weak strengthening on a single-addition basis. The simultaneous addition of two or three elements always yields the synergistic strengthening effect, which indicates that, for instance, the combined addition of copper and nickel in respective amounts of 0.15% can strengthen the steel to a larger extent, compared with a single addition of 0.30% copper or 0.30% nickel. The Charpy transition temperature does not depend strongly on respective elements, although manganese and nickel are favourable elements for improvement of low-temperature toughness.

The start temperature of the  $\gamma \rightarrow \alpha$  transformation ( $A_{r3}$  temperature) after controlled-rolling depends on the chemistry of steel as well as rolling variables and cooling rate or plate thickness. In general, deformation of  $\gamma$  accelerates the  $\gamma \rightarrow \alpha$  transformation, raising the  $A_{r3}$  temperature.<sup>11</sup> Under a controlled-rolling condition with a cumulative rolling reduction below 900° C over 30% in niobium-bearing steel, the  $A_{r3}$  temperature is determined by chemistry and the plate thickness as shown in Equation (9.1):<sup>12</sup>

$$A_{r3}(^{\circ}\text{C}) = 910 - 310\text{C} - 80\text{Mn} - 20\text{Cu} - 15\text{Cr} - 55\text{Ni} - 80\text{Mo} + 0.35(t - 8) \quad (9.1)$$

where  $t$  is plate thickness, in millimetres.

Manganese, molybdenum and nickel, which substantially depress the  $A_{r3}$  temperature, can enhance the  $\alpha$ -grain refinement and also modify the transformed microstructure. The  $\alpha$  stabilizing elements such as silicon or aluminium, which raise the  $A_{r3}$  temperature, are not extensively utilized as alloying elements in HSLA steel plates because of the deterioration of low-temperature toughness.

The increase of manganese content over 1.8% under a reduced carbon content less than 0.06% causes the microstructural transition from polygonal  $\alpha$ -pearlite to acicular  $\alpha$ , which consists of the mixed structure of  $\alpha$  and bainite. The strengthening in the acicular  $\alpha$  structure depends mainly on the volume fraction of bainite with high dislocation density, and this, in turn, is associated with a lowering of the  $\gamma \rightarrow \alpha$  transformation temperature of the steel. Therefore, the strength of acicular  $\alpha$  steel largely depends on carbon, manganese or molybdenum content, and the effects of copper, nickel and chromium are supplementary.

The addition of boron in high-manganese steels under a further reduction of carbon content below 0.04% can yield the ultra-low carbon-bainite structure.<sup>13,14</sup> This microstructure is different from acicular  $\alpha$  in respect of a single structure of bainite without  $\alpha$ , and the bainite is formed directly from the deformed austenitic grain boundaries stabilized by boron. Because of the extremely reduced carbon content, bainite in this type of steel has superior low-temperature toughness and ductility, and weldability such as cold cracking susceptibility is remarkably improved. In Figure 9.8, the strength and Charpy transition temperature in acicular  $\alpha$  steel and ultra-low carbon-bainite steel are compared in relation to carbon content. Under a given basic composition of 0.25% Si-2% Mn-0.05% Nb, boron-free steel forms the acicular  $\alpha$  and the addition of titanium gives rise to ultra-low carbon-bainite structure. In the latter steel, 0.02% titanium is simultaneously added to protect boron against boron nitride formation. The decrease of the strength with reducing carbon content in boron-free steel is due to the decrease of the volume fraction of bainite formed in the acicular  $\alpha$  products. Conversely, boron-added steel results in a relatively small dependence of the strength

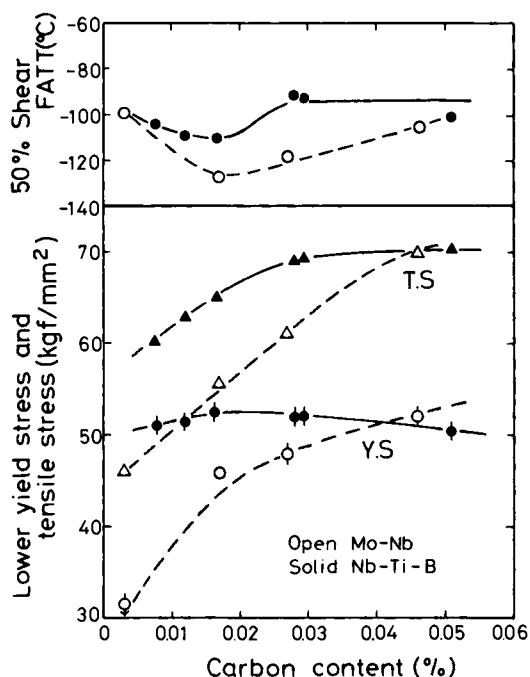


Figure 9.8 Dependence of strength and Charpy transition temperature on carbon content in acicular  $\alpha$  steel and ultra-low carbon-bainite steel

content of less than 0.02%. The starting temperature of the bainite transformation in this steel is very low, e.g. around 630°C in 0.02% C steel, preventing completely the  $\alpha$  formation. The accelerated cooling after controlled-rolling can replace somewhat the content of manganese or molybdenum in both the acicular  $\alpha$  and ultra-low carbon-bainite steels, and the recent progress of steelmaking technology enables us to produce an extremely low-carbon-high-manganese steel economically in high tonnages.

### 9.3 Impurity elements

The major harmful impurities in steel are nonmetallic inclusions, and their detrimental effect on ductility becomes more intense with increasing strength levels in HSLA steels. Among various types of oxide and sulphide inclusions, the manganese sulphides, and also silicates which are not formed in aluminium-killed steel, are deformable at hot-working temperatures; manganese sulphide tends to be more elongated by controlled-rolling, since the relative plasticity difference in manganese sulphide and matrix increases with the decrease of rolling temperatures. These elongated manganese sulphide inclusions in hot-rolled products cause the anisotropy of ductility relative to the rolling direction.

The role of inclusion in ductile fracture has been well documented. The ductile fracture is initiated by the cracking of inclusions and the decohesion of matrix-inclusion interface at low strains or around the onset of plastic instability. The

final fracture takes place by the localized shearing or the void sheet formation between neighbouring cracks. Microfractography on the ductile fracture surface exhibits large cracks including fragments of manganese sulphide and small dimples which may be associated with fine inclusions or other fine second particles such as carbides or nitrides. Since the cracking or decohesion in fine second particles occurs at higher strains, the observed ductility is mostly controlled by the volume fraction, size and shape of large inclusions.

Consequently, the desulphurization technology has been remarkably advanced during the last decade, simultaneously with the progress of thermomechanical processings in HSLA steel.<sup>15,16</sup> The technological developments in the steel desulphurization process, utilizing the gas- or powder-injection method as well as pig-iron desulphurization, enable us to produce an extremely low-sulphur steel with a sulphur level below 0.0010% in mass production. Figure 9.9 demonstrates variations of Charpy upper-shelf energy and the transition temperature with reducing sulphur content in 0.08% C–0.25% Si–1.20% Mn steels. The finishing-rolling temperatures of controlled-rolling are 770 and 720° C, the latter being in the intercritical region. The shelf energy in all the directions is prominently improved by decreasing the sulphur content, and the cross-rolling adopted in this case almost diminishes the anisotropy of the shelf energy, although its values in the short-transverse (short T) direction are relatively lower. On the other hand, the transition temperature in both the longitudinal (L) and transverse (T) directions is not varied by sulphur content, which appears to be the common observation in  $\alpha$ -pearlite steel.<sup>17</sup> It is important to note that the transition temperature

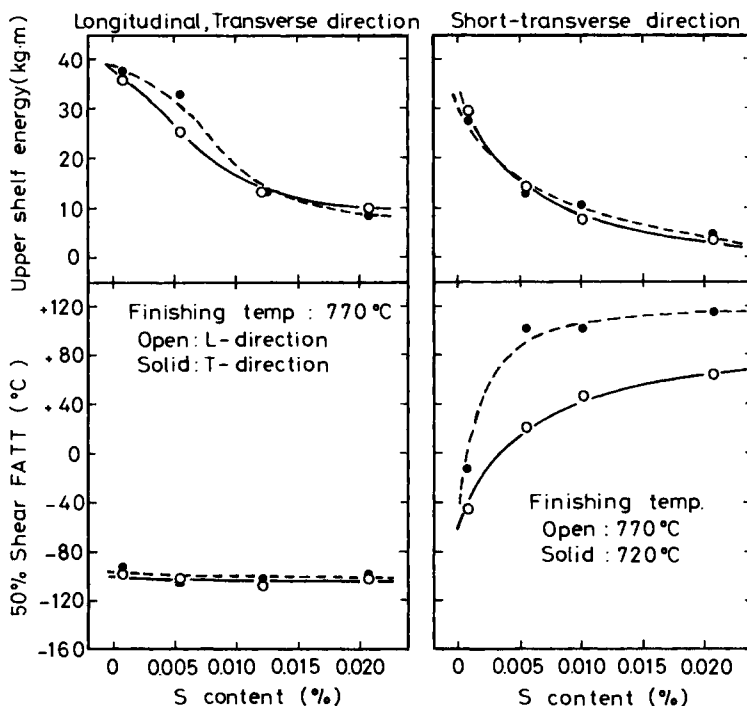


Figure 9.9 The effect of sulphur content on Charpy upper shelf energy and transition temperature in the L, T, and short T directions. 0.08% C–0.25% Si–1.20% Mn steel

in the short-T direction is markedly improved by decreasing the sulphur content to 0.0010%. In general, low-temperature toughness in this direction is worst in controlled-rolled plate,<sup>18</sup> and its deterioration becomes more intense in the intercritical rolling. Although a primary cause for this is presumed to be due to the texture development, the above result indicates that manganese sulphide inclusion may be an origin of brittle crack initiation in the short T direction.

Since the ductility depends on the shape and size of manganese sulphide in a given sulphur content the sulphide shape control, through control of inclusion plasticity as well as cross-rolling, gives the effective means for improvement of ductility in the directions other than longitudinal. This can be achieved by small additions of elements such as the REMs, titanium, zirconium or calcium. Through an actual trial of REM addition in steelmaking, it has been shown that excessive addition of these elements results in contamination in some locations inside ingots or continuously-cast slabs, and that an optimum additional amount for sulphide shape-control additives exists in relation to sulphur level in steel. It is reported, for example, that an addition of REMs of around 0.02–0.04% in the range of sulphur content from 0.005 to 0.010% can yield the maximum improvement of ductility in the T direction.<sup>17</sup> Calcium treatment is applied to an ultra-low sulphur steel which does not normally cause the anisotropy of

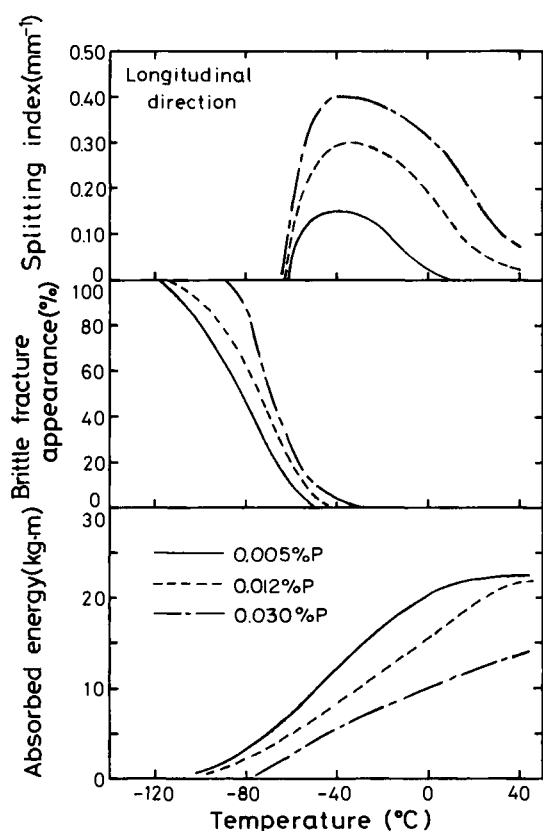


Figure 9.10 The effect of phosphorus content on Charpy transition full curves. The splitting index in the top figure is defined as the total length of splittings divided by fracture surface area of Charpy impact test specimens

the ductility even without a sulphide shape control. The central segregation portion in a continuously-cast slab includes large manganese sulphide inclusions even in a very low-sulphur steel. The treatment by an injection of a small amount of calcium silicate powder can eliminate or shape-control these segregated manganese sulphide inclusions.

Phosphorus, which is well known as a cause of temper embrittlement, does not exert a significantly harmful influence on the mechanical properties of controlled-rolled plates. However, Charpy impact energy in HSLA steels produced by the strip-mill process is deteriorated by phosphorus, since the cooling rate of strip at around 500°C after coiling is slow enough to cause the phosphorus segregation to the  $\alpha$  grain boundary or  $\alpha$ -pearlite interface. This segregation promotes a splitting phenomenon which is observed on the fracture surface in Charpy impact test specimens broken at low temperature, and this in turn, decreases the Charpy impact energy. Figure 9.10 presents the Charpy full curves in 0.04% Nb-0.10% V steel with different phosphorus contents. The strip-mill rolling is simulated by a laboratory mill, which gives accelerated cooling after the finish of rolling, followed by slow cooling at a rate of around 10°C/h from 600°C to ambient temperature. The Charpy impact energy at low temperatures in both the L and T directions is reduced with the increase of the phosphorus content. The fracture mode in the splittings running perpendicularly to the main fracture surface in Charpy specimens is intergranular, and this is a feature which contrasts with the common observation that splittings taking place in controlled-rolled plates have a cleavage mode. Phosphorus and manganese are major elements to segregate in the central location of a continuously-cast slab, and this conjugate effect enhances splittings in HSLA steels from actual strip coil. It is also confirmed that the addition of molybdenum in HSLA steels effectively can suppress splittings, as this element reduces temper embrittlement.<sup>19</sup>

## References

1. IRVINE, K.J., PICKERING, F.B. and GLADMAN, T. *J. Iron and Steel Inst.*, **205**, 161 (1967)
2. GEORGE, T. and IRANI, J.J. *J. Australian Inst. Metals*, **13**, 93 (1968)
3. KOZASU, I., SHIMIZU, T. and KUBOTA, H. *Trans Iron and Steel Inst. Japan*, **11**, 367 (1971)
4. PETKOVIC, R.A., LUTON, M.J. and JONAS, J.J. *The hot deformation of austenite*, American Institute of Metallurgical Engineers, p.68 (1976)
5. LE BON, A., ROFES-VERNIS, J. and ROSSARD, C. *Metal Sci.*, **9**, 36 (1975)
6. WEISS, I. and JONAS, J.J. *Met. Trans.*, **10A**, 831 (1979)
7. YAMAMOTO, S., OUCHI, C. and OSUKA, T. *Thermomechanical processing of microalloyed austenite*, American Institute of Metallurgical Engineers (1981)
8. Le CLERC, J., ARNAUD, C., DUQUAIRE, B. and JEANNEAU, M. *Steel-rolling*, Iron and Steel Institute of Japan, p.1321 (1980)
9. OUCHI, C., OKITA, T. and YAMAMOTO, S. *Trans Iron and Steel Inst. Japan*, **20**, 833 (1981)
10. SERIN, B., DE SALOS, Y., MAITREPIERRE, Ph. and ROFES-VERNIS, J. *Mem. Sci. Rev. Met.*, **75**, 355 (1978)
11. SMITH, Y.E. and SIEBERT, C.A. *Met. Trans.*, **2**, 1711 (1971)
12. OUCHI, C., SAMPEI, T. and KOZASU, I. *Trans Iron and Steel Inst. Japan*, **22**, 214 (1982)
13. NAKASUGI, H., MATSUDA, H. and TAMEHIRO, H. *Steel-rolling*, Iron and Steel Institute of Japan, p.1028 (1980)
14. NIKURA, M., YAMAMOTO, S. and OSUKA, T. *Trans Iron and Steel Inst. Japan*, **22**, B275 (1982)
15. PIRCHER, H. and KLAPDAR, W. *Microalloying 75*, Union Carbide Corp., p.232 (1977)
16. USUI, T., YAMADA, K., MIYASHITA, Y., TANABE, H., HANMYO, M. and TAGUCHI, K. *Proceedings, International conference on injection metallurgy*, SCAN. INJECT II, Sweden, 12, p.7 (1980)
17. KOZASU, I. and TANAKA, J. *Sulfide inclusions in steel*, American Society of Metallurgists, p.286 (1975)
18. SPEICH, G.R. and DABKOWSKI, D.S. *The hot-deformation of austenite*, American Institute of Metallurgical Engineers, p.557 (1977)
19. KUNISHIGE, K., FUKUDA, M. and SUGISAWA, S. *Trans Iron and Steel Inst. Japan*, **19**, 324 (1979)

## Properties of controlled-rolled steels

### 10.1 Strengthening and toughening mechanisms

In controlled-rolled steels, the microstructures range from a recrystallized ferrite ( $\alpha$ ) to a fully cellular dislocation substructure, while strengthening and toughening mechanisms are different, depending on the microstructure.

Steel finished-rolled in the recrystallized austenite ( $\gamma$ ) region gives recrystallized  $\alpha$  grain structure with random crystallographic orientation, in which the yield stress follows the Hall–Petch relation<sup>1</sup>:

$$\sigma_y = \sigma_0 + k_y d^{-\frac{1}{2}} \quad (10.1)$$

where  $\sigma_0$  is the internal stress,  $d$  grain size and  $k$  a constant.

Since  $\sigma_0$  is divided into several terms, lattice hardening  $\sigma_{lh}$ , solid-solution hardening  $\sigma_{sh}$ , dislocation hardening  $\sigma_{dh}$ , and precipitation hardening  $\sigma_{ph}$ , Equation (10.1) is rewritten as follows:

$$\sigma_y = \sigma_{lh} + \sigma_{sh} + \sigma_{dh} + \sigma_{ph} + k_y d^{-\frac{1}{2}} \quad (10.2)$$

As far as deformation in the nonrecrystallized  $\gamma$  region produces a  $\alpha$  grain structure, the microstructure is recrystallized and randomly orientated as shown in Figures 5.6 and 5.7 (pages 107 and 108). In this case, the yield stress is expressed as in Equation (10.2). However, when deformation in the nonrecrystallized  $\gamma$  region produces acicular  $\alpha$  or martensite, the microstructure has a strong crystallographic texture (shown in Figure 5.6), causing anisotropy in mechanical properties. Yield stress is the highest in the transverse (T) direction, followed by the longitudinal (L) direction, while the diagonal (D) direction exhibits the lowest yield stress (shown in Figure 5.8 (page 108)). Therefore, either the texture hardening in the T and L directions or the texture softening in the D direction must be added to Equation (10.2):

$$\sigma_y = \sigma_0 + \sigma_{\text{ext}} + k_y d^{-\frac{1}{2}} \quad (10.3)$$

When deformation is given in the  $\gamma + \alpha$  two-phase region, the microstructure is a mixture consisting of recrystallized  $\alpha$  grains and subgrains and/or cellular sub-

structures.<sup>2</sup> In mixed structures, all boundaries acting as slip barriers must be combined to specify the effective grain size governing yielding. This effective grain size  $d_e$  can be obtained for a mixed structure by:<sup>3</sup>

$$d_e^{-1} = d_r^{-1}(f_r) + d_c^{-1}(1 - f_r) \quad (10.4)$$

where  $d_e^{-1}$  is the number of boundaries per unit length,  $d_r^{-1}$  is the number of high-angle boundaries per unit length,  $d_c^{-1}$  is the number of low-angle boundaries per unit length, and  $f_r$  is the volume fraction of  $\alpha$  recrystallized.

Therefore, the grain-size contribution to yield strength becomes:

$$\Delta\sigma_{gs} = k' d^{-\frac{1}{2}} = k' [d_r^{-1}(f_r) + d_c^{-1}(1 - f_r)]^{\frac{1}{2}} \quad (10.5)$$

Deformation in the two-phase region develops the crystallographic texture, shown in Figure 5.7, which is similar to that developed in an acicular ferritic or martensitic structure. In this case, too, the texture-hardening for the T and L directions and the texture-softening for the D direction, must be considered.<sup>4-6</sup> Therefore, yield stress of steel finished-rolled in the two-phase region is expressed as:

$$\sigma_y = \sigma_0 + \sigma_{\text{ext}} + k' [d_r^{-1}(f_r) + d_c^{-1}(1 - f_r)]^{\frac{1}{2}} \quad (10.6)$$

Bramfitt and Marder<sup>7</sup> proposed that the cell contribution to yield strength could be added by allowing for respective volume fractions of grains and cells in a partly recrystallized structure as follows:

$$\sigma_y = \sigma_0 + K \left[ d^{-\frac{1}{2}}(f_r) + d_c^{-\frac{1}{2}}(1 - f_r) \frac{K_c}{K} \right] \quad (10.7)$$

where  $K$  and  $K_c$  are the experimentally determined values for plots of fully recrystallized structures and fully cellular structures respectively. This model gave an approximate fit to the experimental data (Figure 10.1).<sup>7</sup>

It is to be remembered here that Equation (10.5) is a correct expression of the Hall-Petch relation, while Equation (10.7) is an approximation of it. In Equation (10.5) the high-angle boundary and the low-angle boundary have the same strengthening vector. Whereas, in Equation (10.7) the strengthening effect of the low-angle boundary is distinguished from that of the high-angle boundary.

From a theoretical point-of-view, Heslop and Petch<sup>8</sup> have shown that the ductile→brittle transition temperature is inversely proportional to  $d^{-\frac{1}{2}}$ , where  $d$  is the grain size. Therefore, when polygonal  $\alpha$  grain structure is obtained by the deformation in the recrystallized  $\gamma$  region and/or in the nonrecrystallization region, the transition temperature is given by:

$$T_{rs} = \alpha - \beta d^{-\frac{1}{2}} \quad (10.8)$$

where  $\alpha$  is a constant depending on chemical composition, and  $\beta$  is a constant representing the degree of resistance of grain boundaries to the brittle crack propagation.

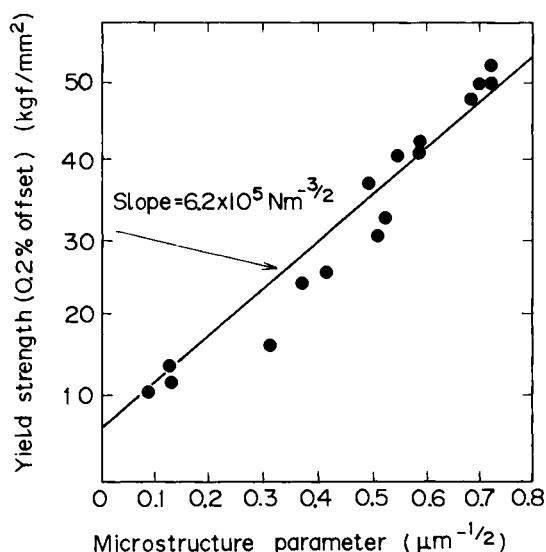


Figure 10.1 Yield strength vs. microstructure parameter, which takes into account contributions from both equiaxed grain size and subgrain or cell size. (After Bramfitt and Marder<sup>7</sup>)

When acicular  $\alpha$  or martensite structure is obtained by the deformation in the nonrecrystallized  $\gamma$  region, two factors governing the transition temperature must be taken into account: (1) effective grain size; and (2) texture development. The effective grain size  $d_e$ , which is equivalent to the mean spacing between grain boundary intersections in polygonal  $\alpha$ , can be defined as the mean spacing between high-angle boundary intersections in the acicular ferritic or martensitic structure.<sup>9</sup>

The texture with  $\langle 110 \rangle // \text{RD}$  (rolling direction) which develops in acicular  $\alpha$  and martensite structures, lowers the transition temperature in the T and the L directions on the one hand and raises that in the D direction on the other, as shown in Figure 5.9 (page 109), while substructure hardening  $\sigma_{\text{subs}}$  and precipitation hardening  $\sigma_{\text{ph}}$  adversely affect toughness. Taking these factors into consideration, the transition temperature of acicular  $\alpha$  structure is given as follows:

$$T_{\text{rs}} = \alpha' - \beta' d_e^{-\frac{1}{2}} + \Delta T_{\text{text}} + k_1 \sigma_{\text{subs}} + k_2 \sigma_{\text{ph}} \quad (10.9)$$

where  $\alpha'$ ,  $\beta'$ ,  $k_1$  and  $k_2$  are constants.

Gladman, Dulieu and McIvor<sup>3</sup> have given the transition temperature of bainitic steel by the equation:

$$T_{\text{rs}} (^{\circ}\text{C}) = -19 + 44 (\% \text{ Si}) + 700 (\% \text{ N}_{\text{free}})^{\frac{1}{2}} + 0.26 (\sigma_0 + \Delta P + \Delta) - 11.5 d^{-\frac{1}{2}} \quad (10.10)$$

where  $\text{N}_{\text{free}}$  is interstitial nitrogen,  $\sigma_0$  is Ashby–Orowan strengthening from dispersed second-phase particles, and  $\Delta P$  and  $\Delta$  are the assumed strengthening contribution from random or forest dislocations and the contribution from dislocations in low-angle boundaries respectively.



TABLE 10.1 Classification of vanadium and/or niobium precipitates formed during the hot-rolling process. (After Kunishige, Hashimoto and Yukitoshi<sup>11</sup>)

| Type | Behaviour and morphology of precipitates |                                       |                | Effect on mechanical properties  |               |             | Remark               |
|------|--|---------------------------------------|----------------|----------------------------------|---------------|-------------|----------------------|
|      | Temperature                              | Sites                                 | Coherency with | Size                             | Strengthening | Embrittling |                      |
| I    | Undissolve at slab soaking               | Matrix ( $\gamma$ )                   | No             | Large ( $\geq 1000\text{\AA}$ )  | No            | No          |                      |
| II   | High temperature ( $\gamma$ region)      | ● Grain boundaries<br>● Dislocations  | No             | Large ( $\sim 1000\text{\AA}$ ?) | No            | No          |                      |
| III  | Low temperature ( $\gamma$ region)       | Dislocations                          | No             | Small ( $100\text{\AA}$ ?)       | Weak          | No          | Dispersion hardening |
| IV   | High temperature ( $\alpha$ region)      | ● Dislocations<br>● Interphase        | No             | Small ( $100\text{\AA}$ ?)       | Weak          | No          | Dispersion hardening |
| V    | Low temperature ( $\alpha$ region)       | ● Matrix ( $\alpha$ )<br>● Interphase | Strong         | Small ( $\leq 100\text{\AA}$ )   | Strong        | Strong      | Secondary hardening  |

TABLE 10.2 Factors governing strength and toughness in controlled-rolled steels. (After Tanaka<sup>12</sup>)

| Factor               | Steel hot-rolled in recrystallization region           | Steel hot-rolled in nonrecrystallization region        | Steel finished-rolled in ( $\gamma + \alpha$ ) region                            |
|----------------------|--|--|--|
| Microstructure       | Equiaxed grain (+ upper bainite)                       | Equiaxed grain   | Equiaxed grain (soft grain) + subgrain (hard grain)                              |
| Grain size           | Coarse   | Fine   | Fine   |
| Strengthening factor | (1) $\alpha$ grain size<br>(2) Precipitation hardening | (1) $\alpha$ grain size<br>(2) Precipitation hardening | (1) $\alpha$ grain size<br>(2) Subgrain hardening<br>(3) Precipitation hardening |
| Toughening factor    | $\alpha$ grain size                                    | $\alpha$ grain size                                    | (1) grain size<br>(2) Separation<br>(3) Subgrain hardening                       |

Deformation in the  $\gamma + \alpha$  two-phase region gives a mixed structure consisting of polygonal  $\alpha$  grains and subgrains and/or cellular substructure. High-angle boundaries increase strength and improve toughness by acting as barriers to crack propagation, while low-angle boundaries contribute to strength and adversely affect toughness since they do not resist crack propagation as they improve strength.

Deformation in the two-phase region develops the crystallographic texture with  $\langle 110 \rangle // \text{RD}$  and  $\langle 001 \rangle // \text{ND}$  (normal direction) orientations as shown in Figure 5.7. The  $\langle 110 \rangle // \text{RD}$  texture causes plane anisotropy, thereby lowering the transition temperature in the T and the L directions and raising that in the D direction as shown in Figures 5.9 and 5.10 (page 109). The  $\langle 001 \rangle // \text{ND}$  texture causes embrittlement in the through-thickness (Z) direction and thereby induces the occurrence of separations. The transition temperature decreases in a linear manner with the number of separations (see Figure 5.15, page 114).

Taking these factors into account, transition temperature in the L, T or D directions of steel finished-rolled in the  $(\gamma + \alpha)$  region is given by:<sup>10</sup>

$$T_{rs} = \alpha'' - \beta d^{-\frac{1}{2}} + \Delta T_{\text{ext}} - \gamma n_s + k_1 \left( \sigma_{\text{ph}} + \frac{k_2}{k_1} \sigma_{\text{dh}} + \frac{k_3}{j_1} \sigma_{\text{sub}} \right) \quad (10.11)$$

where  $d$  is polygonal  $\alpha$  grain size,  $n_s$  the number of separations,  $\sigma_{\text{ph}}$  precipitation hardening,  $\sigma_{\text{dh}}$  hardening due to random dislocations,  $\sigma_{\text{sub}}$  hardening due to subgrain, and  $\alpha''$ ,  $\beta$ ,  $\gamma$ ,  $k_1$ ,  $k_2$  and  $k_3$  are constants.

The precipitation of niobium and vanadium carbonitrides gives a range of strength and toughness. Five types of niobium and vanadium carbonitrides have been observed to form in controlled-rolled steel, as shown in Table 10.1. They are: (1) large, undissolved precipitates that remain during slab-reheating; (2) coarse precipitates formed at high temperatures in the  $\gamma$  region; (3) fine precipitates produced by strain-induced precipitation after rolling in the nonrecrystallized  $\gamma$  region; (4) fine precipitates formed in the high-temperature  $\alpha$  region; and (5) fine precipitates formed during cooling after rolling. Types (3) and (4) nucleate at dislocations and  $\gamma$ - $\alpha$  interfaces, thereby losing coherency with the  $\alpha$  matrix. Type (5) precipitates have coherency with the  $\alpha$  matrix. Because of fine, incoherent precipitates, types (3) and (4) cause weak precipitation hardening without impairing toughness, while type (5) causes much precipitation hardening and embrittlement. Controlled-rolling accelerates the formation of incoherent precipitates, thereby suppressing the formation of coherent ones.

As is clear from the above description, factors governing strength and toughness are different, depending on hot-rolling condition and chemical composition. Table 10.2 gives various factors which control the strength and toughness in hot-rolled steels.<sup>12</sup> In steel rolled in the high-temperature  $\gamma$  region, strength is decided by grain size and precipitation hardening and toughness is governed by  $\alpha$  grain size alone. In steel finished-rolled in the unrecrystallized  $\gamma$  region, strength is decided by grain size and precipitation hardening, while toughness is governed only by  $\alpha$  grain size. In steel finished-rolled in the two-phase region, microstructure is a mixture consisting of soft, equiaxed  $\alpha$  grains and hard subgrains. Strength is governed by  $\alpha$  grain size, subgrain hardening and precipitation hardening, while toughness is governed by  $\alpha$  grain size, subgrain hardening and the number of separations.

### 10.1.1 Interpretation of mechanical properties

The literature on the effect of deformation in the two-phase region on transition temperature has been contradictory. The transition temperature increased with a decrease in finishing temperature in the two-phase region;<sup>13</sup> it reached a minimum at a certain temperature in the two-phase region, and increased again with a further decrease in finishing temperature.<sup>14,15</sup> The transition temperature decreased with decreasing deformation temperature,<sup>15</sup> excessive reduction in the two-phase region raised the transition temperature,<sup>4</sup> and heavy reduction in the two-phase region lowered the transition temperature of plain carbon steel.<sup>16,17</sup> Those contradictory reports are explained consistently by Equation (10.11). In steel deformed in the two-phase region, the fourth term  $\gamma n_s$  and the last term  $k_1(\sigma_{ph} + \frac{k_2}{k_1}\sigma_{dh} + \frac{k_3}{k_1}\sigma_{sub})$  on the right-hand side of the equation have a particularly large influence on transition temperature. If the contribution to the transition temperature from the last term, in particular dislocation hardening  $\sigma_{dh}$ , is larger than that from separations, the transition temperature increases. On the other hand, if the contribution from separation is larger than that from dislocation hardening, the transition temperature decreases.

When deformed just below the  $A_{r3}$  temperature, the cellular dislocation structure changes quickly into a subgrain structure, eliminating large amounts of dislocation hardening. However, when deformed at lower temperatures, insufficient recovery raises  $\sigma_{dh}$ , which exceeds the effect of separations and thereby increases the transition temperature. In niobium steel, conflict between dislocation hardening and separation effect is severe because fine precipitates of strain-induced niobium carbides and nitrides pin down dislocations, and thereby retard recovery and recrystallization of deformed  $\alpha$ . Conversely, in carbon-manganese steel, dislocation hardening is small owing to the rapid progress of recovery and, at the same time, there is a large separation effect due to the development of the  $<100>$  texture, which causes a decrease in transition temperature even when finish-rolled at low temperatures.

## 10.2 Mechanical properties

Figure 10.2 shows schematically the relationship between the required characteristic and metallurgical factors and manufacturing process in high-strength steels. The steel plate is required to possess high strength, good toughness and superior weldability. These three important characteristics are very often contradictory with each other and one characteristic is obtained at the expense of the others. Therefore, in order to produce steel plate having the optimum balance between the three characteristics, the metallurgical *factors*, as well as manufacturing *methods*, shown in Figure 10.2 must be taken into consideration. As is clear from the figure, controlled-rolling can increase strength and toughness through grain refinement and at the same time improve weldability through the decrease in alloy content (carbon equivalent). As a general guide, tensile strength up to 50 kgf/mm<sup>2</sup> is achieved by conventional hot-rolling or normalizing, whereas tensile strength more than 60 kgf/mm<sup>2</sup> is obtained by quenching and tempering. In controlled-rolled steels, however, tensile strength up to 60 kgf/mm<sup>2</sup> can be obtained in ferritic or acicular ferritic structure. Processing variables governing

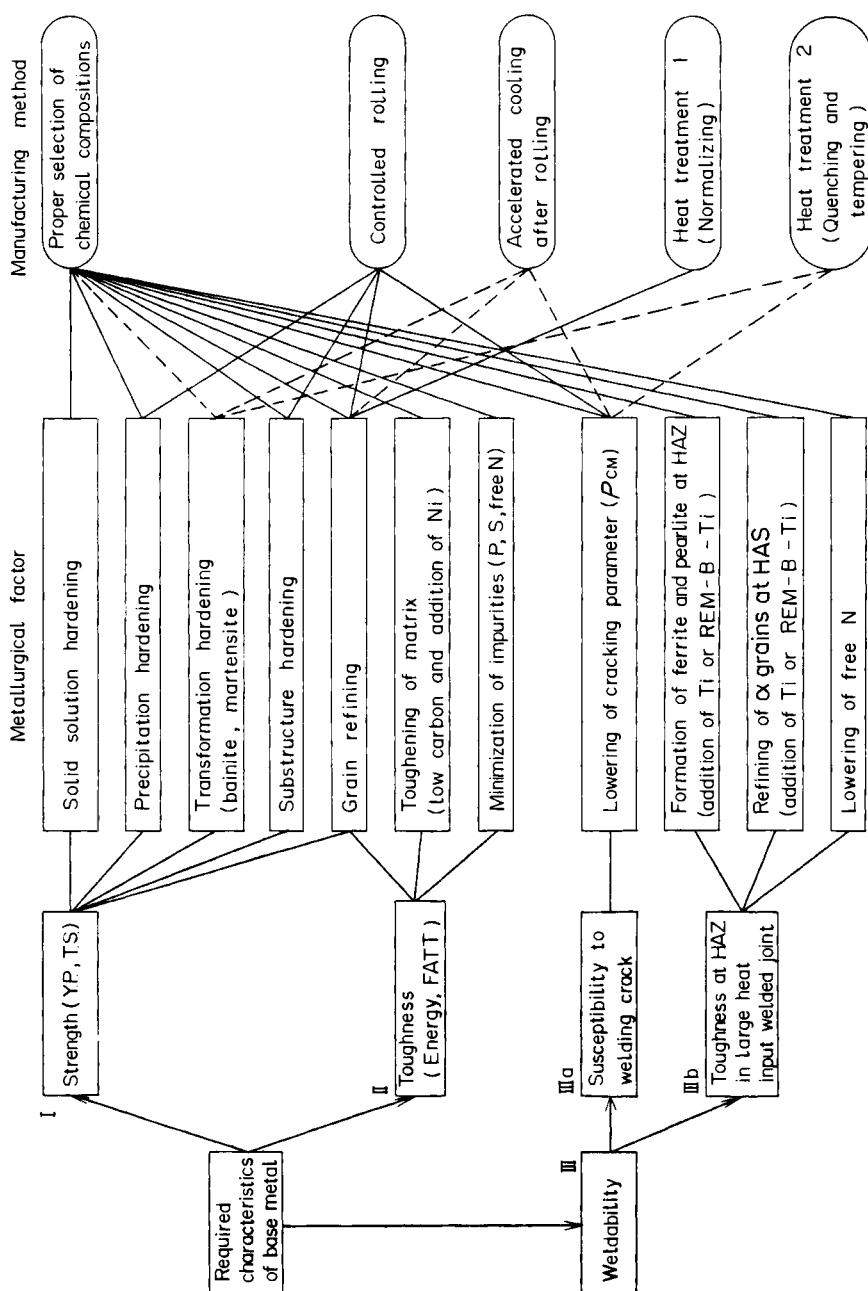


Figure 10.2 Relation between required characteristic, metallurgical factor and manufacturing method in high-strength steel. HAZ = heat affected zone; REM = rare earth metals

controlled-rolling and mechanical properties of structural steel for ships' hulls, line-pipe steel, acicular  $\alpha$  steel and dual-phase steel will be described in detail below.

### 10.2.1 High-tensile strength steel with a tensile strength of 50 kgf/mm<sup>2</sup> (HT-50 steel)

The main objective of controlled-rolling is to attain fine  $\alpha$  grain structure and thereby obtain good toughness and superior weldability as well as high strength. Even though the essence of controlled-rolling is to obtain fine grain structure through heavy deformation of  $\gamma$  at low temperature, actual controlled-rolling practice is different, depending on the properties required for the steel- and millability. Furthermore, accelerated-cooling (the purpose of which is to supplement controlled-rolling on the one hand and to further improve the properties of steel on the other) is being developed.<sup>18,19</sup> Therefore, by the controlled-rolling process, a variety of processes has been proposed as shown in Figure 10.3.<sup>18-21</sup>

Controlled-rolling causes strengthening due to grain refinement, subgrain hardening and precipitation hardening which, in turn, can reduce the alloy contents in steel. In Figure 10.4, tensile strength and 50% shear fracture appearance transition temperature (FATT) are plotted vs. carbon equivalent in plain carbon and niobium steels control-rolled together with conventionally normalized steels. Controlled-rolling can reduce greatly the carbon equivalent, which in turn brings about very beneficial effects on toughness and weldability, as will be described later.

The transition temperature in the Z direction is very high because of the occurrence of separations in controlled-rolled steels and, in particular, in steels finish-rolled below  $A_{r3}$  temperature, though transition temperature is sufficiently low in the L and the T directions. Therefore, properties such as ductility and fracture toughness in the Z direction are of much concern in controlled-rolled steels.

Figure 10.5 depicts a relation between reduction of area in the Z direction and sulphur content in steels finish-rolled above or below  $A_{r3}$ .<sup>20</sup> Reduction of area decreases rapidly with the increase in sulphur content. When sulphur contents are less

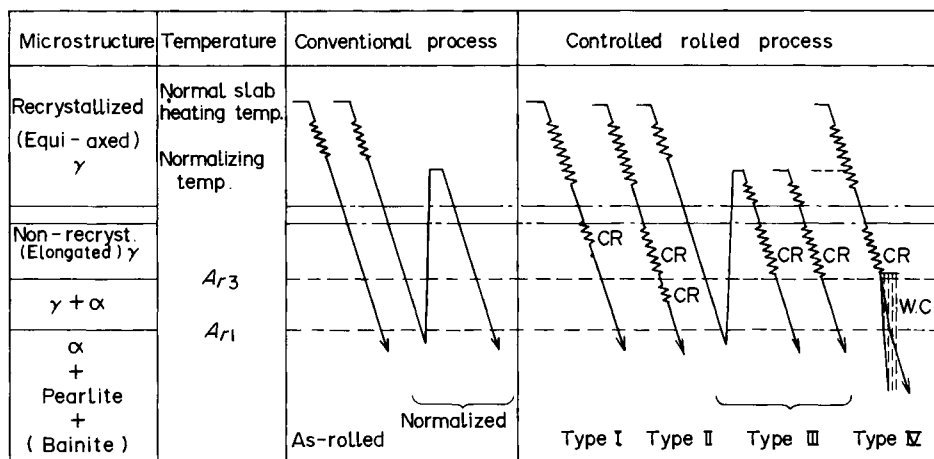


Figure 10.3 Schematic illustration of manufacturing methods of 50-kg/mm<sup>2</sup> grade high-strength steel plate: CR and WC represent controlled-rolling and water-cooling respectively

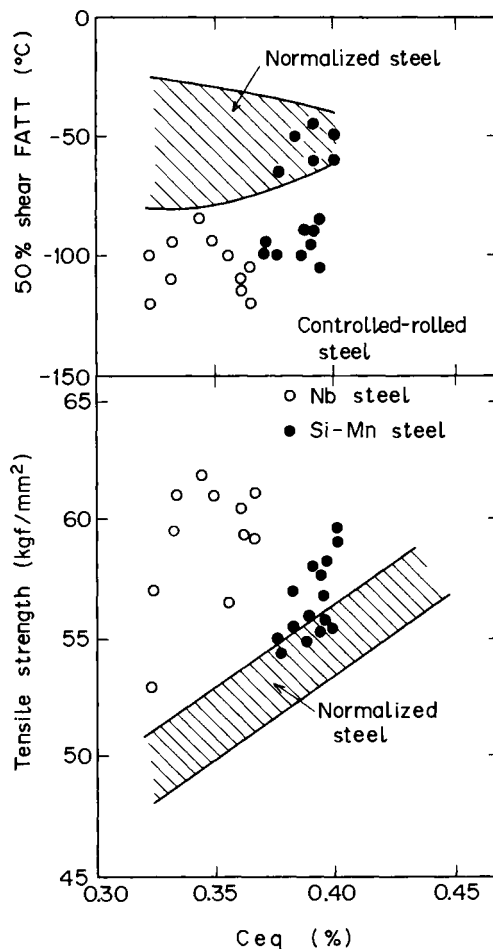


Figure 10.4 Tensile strength and 50% shear FATT are plotted vs. carbon equivalent in control-rolled, and conventionally normalized, steels

than 0.008%, reduction of area is sufficiently high, regardless of controlled-rolling condition, implying that reduction of area is governed mainly by sulphur content, i.e. the amount of manganese sulphide and not by separations.

At welded joints, such as T-joints and fillet joints, tensile stress is induced in the Z direction and thereby enhances the susceptibility to lamellar tearing. A lamellar tear is a stepwise crack occurring in the heat-affected zone or its vicinity in parallel with the plate surface. Lamellar tearing occurs preferentially along brittle zones such as the segregation zone and elongated manganese sulphide. When steel has a high susceptibility to the occurrence of separations, lamellar tearing is of great concern. Figure 10.6 shows a relation between lamellar tearing susceptibility in terms of the percentage of cracking as measured by the Cranfield test and the degree of separations. In controlled-rolled HT-50 steels, no cracks are observed when preheating and interpass temperatures are 50° C. Even in HT-60 steels, the susceptibility is very slight when preheating and interpass temperatures are 50° C. There is no distinct difference in the percentage cracking between separated and nonseparated steel, implying that susceptibility to

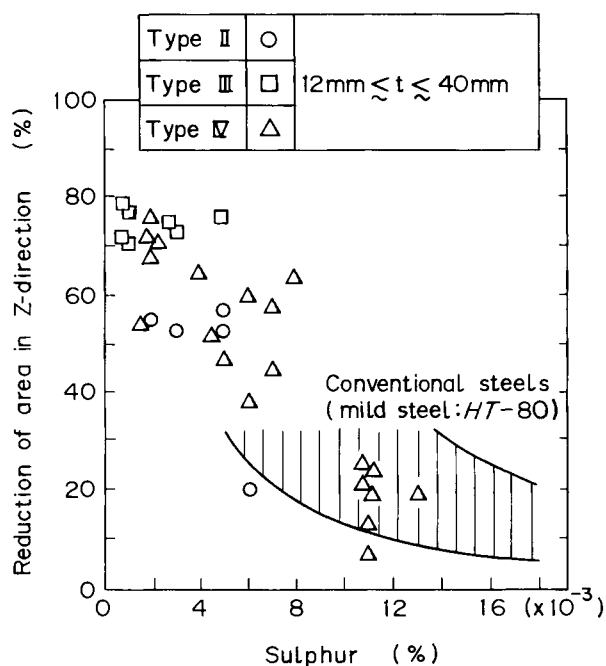


Figure 10.5 Reduction of area in the Z direction is plotted vs. sulphur content in steels finished rolled above or below  $A_{r3}$  temperature where types II, III and IV are exhibited in Figure 10.3. (After Yajima<sup>20</sup>)

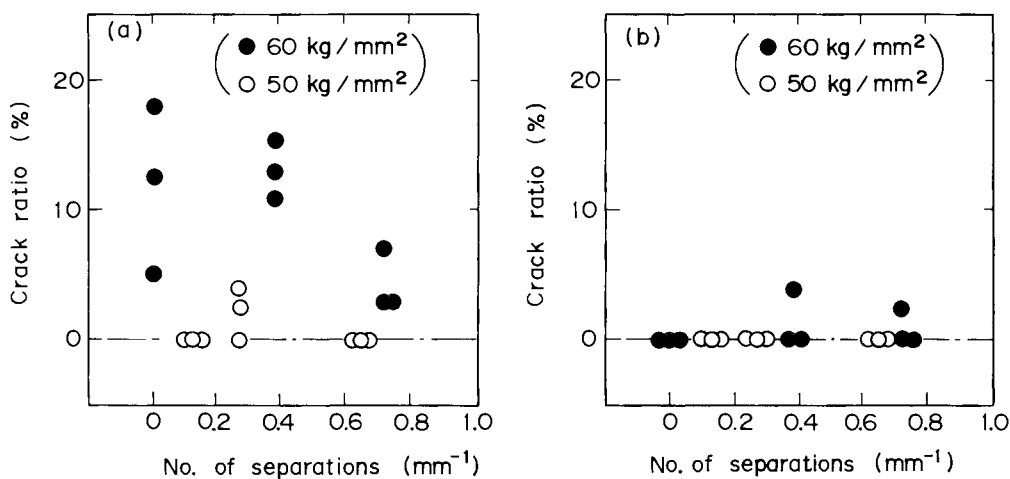


Figure 10.6 Relation between susceptibility to lamellar tearing measured by the Cranfield test and number of separations in controlled-rolled 50-kg/mm<sup>2</sup> grade steels and 60-kg/mm<sup>2</sup> grade steels. Preheating and interpass temperatures are: (a) ambient temperature; and (b) 50°C respectively

lamellar tearing depends more on sulphur content than on the degree of separations.

Figure 10.7 depicts a relation between a critical temperature for brittle fracture initiation in the Z direction (at mid-thickness) and sulphur content.<sup>20</sup> Here, the critical temperature for brittle fracture initiation is taken as a temperature where  $K_{Ic} = 200 \text{ kgf}\sqrt{\text{mm}}/\text{mm}^2$ .  $K_{Ic}$  is obtained from a 400-mm wide, centre-notched tensile test. Critical temperatures are very low, particularly at low sulphur contents, indicating excellent fracture toughness in the Z direction in controlled-rolled steels.

As is clear from Figures 10.5–10.7, controlled-rolled steels exhibit very good properties in the Z direction as far as they have low sulphur contents of less than 0.01%.

The critical crack-opening displacement (COD) is associated with the initiation of a brittle crack from the existing precrack, and is a more rational criterion than the Charpy impact property. The critical COD is plotted vs. temperature in conventionally hot-rolled steel and controlled-rolled steels in Figure 10.8 (COD values are higher for controlled-rolled steels than for conventionally hot-rolled steel). Among controlled-rolled steels, those exhibiting separations give higher COD values than steel exhibiting

|                 |                          |   |                    |
|-----------------|--------------------------|---|--------------------|
| Type II         | HT 50                    | ○ | 25mm ≤ t<br>≤ 40mm |
|                 | HT45 (low temp. service) | ● |                    |
| Type III        | HT 50                    | □ |                    |
|                 | HT45 (low temp. service) | ■ |                    |
| Type IV         | HT 50                    | △ | 25mm ≤ t<br>≤ 35mm |
| Conven. process | HT 50                    | ☆ |                    |

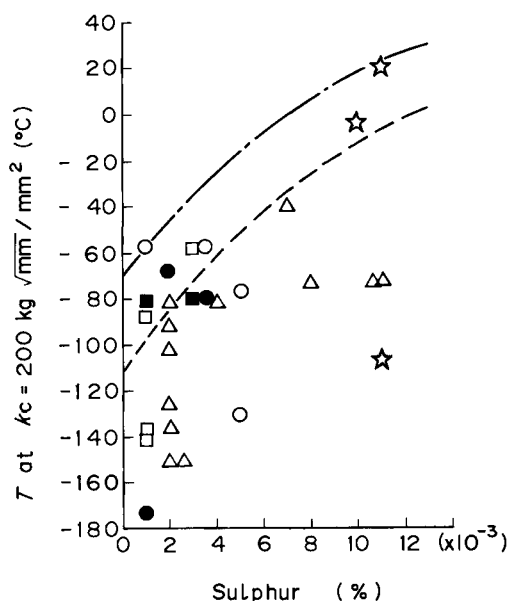


Figure 10.7 Critical temperature for brittle fracture initiation at mid-thickness in the Z direction is plotted vs. sulphur content in control-rolled and conventional steels. Controlled-rolling-types II, III and IV are shown in Figure 10.3. (After Yajima<sup>20</sup>)



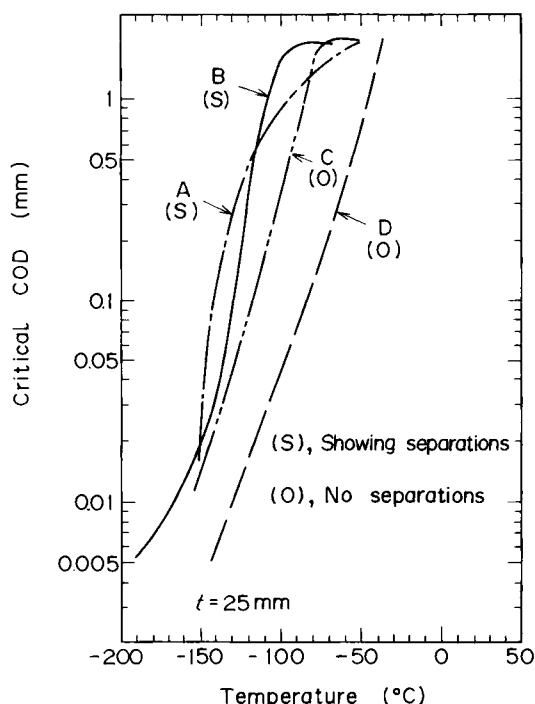


Figure 10.8 Dependence of critical COD on temperature in controlled-rolled 50-kg/mm<sup>2</sup> high-strength steels A, B and C and conventional steel D. S represents steel showing separations; O represents exhibiting no separation

no separation. This is because the occurrence of separations relieves the triaxial stress state and reduces the plate-thickness effect and thereby suppresses brittle-fracture initiation.

Figure 10.9 depicts a relation between 50% shear FATT in the L direction and a brittle-crack arresting temperature.<sup>20</sup> The brittle-crack arresting temperature is taken as a temperature at which  $K_{ca}$  obtained by the 400-mm wide ESSO test or the 500-mm wide double-tension test with temperature gradient, becomes 525–590 kgf√mm/mm<sup>2</sup>. The temperature at which  $K_{ca} = 525\text{--}590 \text{ kgf}\sqrt{\text{mm}}/\text{mm}^2$  is a critical temperature above which the material can arrest a brittle crack with a length of 3000 mm under the applied stress of one-half the yield stress.<sup>20</sup> As is clear from Figure 10.9, both conventional and controlled-rolled steels follow the same relation, but arresting temperatures are much lower for controlled-rolled steels than for conventional ones. Arresting temperatures of controlled-rolled steels are at the same level with, or lower than, that of low-temperature-service steel quenched and tempered.

In summary, controlled-rolled HT-50 steels exhibit excellent low-temperature toughness and superior brittle-crack initiating and arresting properties in the L and T directions. In the Z direction, though transition temperature is very high because of separations, controlled-rolled steel exhibits sufficiently high values for reduction of area, high resistance to the occurrence of lamellar tearing and brittle fracture initiation in so far as they have low sulphur content.

|                    |                        |   |                 |
|--------------------|------------------------|---|-----------------|
| Type II            | HT 50                  | ○ | 25mm ≤ t ≤ 40mm |
|                    | HT45(low temp.service) | ● |                 |
| Type III           | HT 50                  | □ | 25mm ≤ t ≤ 40mm |
|                    | HT45(low temp.service) | ■ |                 |
| Type IV            | HT 50                  | △ | 25mm ≤ t ≤ 50mm |
| Conven.<br>process | HT 50                  | ☆ |                 |
|                    | HT45(low temp.service) | ★ |                 |

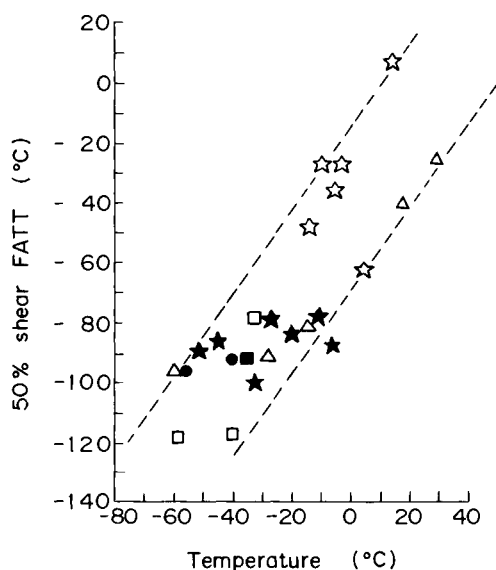


Figure 10.9 Relation between 50% shear FATT and critical temperature for brittle crack propagation arrest in controlled-rolled and conventional 50-kg/mm<sup>2</sup> high-strength steels. Controlled-rolling types II, III and IV are shown in Figure 10.3. (After Yajima<sup>20</sup>)

### 10.2.2 Line-pipe steels

Line-pipe steels have been produced in large quantities by controlled-rolling. In line-pipe, as the stress state is very simple in terms of the hoop stress, the controlled-rolling process is very effective for achieving high strength and excellent low-temperature toughness in the L and T directions, and is the most suitable method for the production of line-pipe steels. However, line-pipe steel must meet two requirements: (1) resistance to brittle fracture initiation measured by the Battelle-type drop-weight tear test (DWTT); and (2) resistance to unstable shear fracture and resistance to hydrogen-induced cracking due to H<sub>2</sub>S. The DWTT characteristic is known to be associated with the FATT of the Charpy impact test<sup>22</sup> and unstable shear fracture property with the Charpy impact energy.<sup>23,24</sup>

The unstable shear fracture is apt to occur in high-pressure gas-transmission pipes. Being assisted by high-energy gas, shear fracture propagates very rapidly in an unstable manner, which can be arrested only when steel possesses sufficiently high-impact energy. Several measures must be taken to ensure high-impact energy. Figure 10.10 depicts the effect of carbon content on the Charpy impact energy in X-60–65 grade niobium–vanadium steels.<sup>25</sup> A decrease in carbon content reduces the volume fraction

of pearlite and bainite, and thereby increases impact energy. The Charpy impact energy is also strongly dependent on sulphur content, as shown in Figure 10.11.<sup>25</sup> A decrease in sulphur content reduces the amount of elongated manganese sulphide, and thereby increases impact energy. Even at very low sulphur contents calcium treatment increases impact energy through the sulphide shape control.

Hydrogen-induced cracking is liable to occur in sour-gas (gas containing hydrogen sulphide) transmission line-pipe. Dissociated hydrogen atoms penetrate from plate surface to such defects as manganese sulphide and cause high pressure there, finally

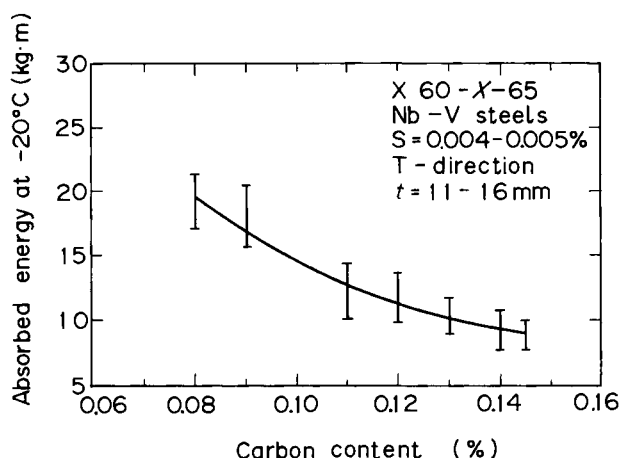


Figure 10.10 Effect of carbon content on the Charpy absorbed energy in controlled-rolled X-60 – X-65 grade, niobium–vanadium line-pipe steels. (After Shiga *et al.*<sup>25</sup>)

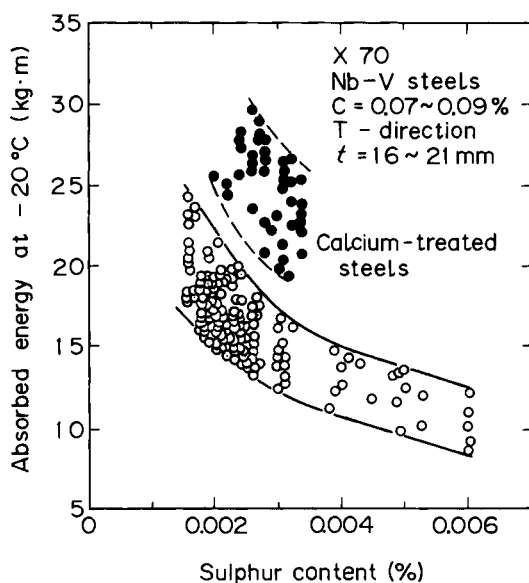


Figure 10.11 Effect of sulphur content on the Charpy absorbed energy in controlled-rolled X-70 grade, niobium–vanadium line-pipe steels. (After Shiga *et al.*<sup>25</sup>)

TABLE 10.3 Chemical compositions of line-pipe steels for Arctic use (percentage weight). (After Shiga *et al.*<sup>25</sup>)

| Steel | C    | Si   | Mn   | P     | S     | Ni   | Mo   | Cu   | Cr   | Nb   | V    | Al    | C <sub>eq</sub> * | Remark      |
|-------|------|------|------|-------|-------|------|------|------|------|------|------|-------|-------------------|-------------|
| C-1   | 0.06 | 0.27 | 1.68 | 0.019 | 0.005 | 0.20 | —    | 0.20 | —    | 0.04 | 0.03 | 0.036 | 0.373             | —           |
| C-2   | 0.05 | 0.29 | 1.74 | 0.016 | 0.004 | —    | —    | —    | 0.18 | 0.05 | —    | 0.040 | 0.376             | —           |
| C-3   | 0.05 | 0.26 | 1.70 | 0.018 | 0.002 | 0.21 | —    | 0.24 | —    | 0.04 | 0.03 | 0.033 | 0.369             | Ca-treated  |
| C-4   | 0.06 | 0.21 | 1.69 | 0.007 | 0.003 | 0.30 | —    | —    | —    | 0.04 | 0.03 | 0.030 | 0.368             | REM-treated |
| C-5   | 0.07 | 0.25 | 1.62 | 0.023 | 0.003 | 0.21 | —    | 0.24 | —    | 0.04 | 0.07 | 0.030 | 0.384             | Ca-treated  |
| Q-1   | 0.07 | 0.25 | 1.35 | 0.004 | 0.003 | —    | 0.18 | —    | 0.19 | 0.03 | 0.04 | 0.034 | 0.377             | —           |

$$* C_{eq} = C + \frac{\text{Mn}}{6} + \frac{\text{Cr} + \text{Mo} + \text{V}}{5} + \frac{\text{Cu} + \text{Ni}}{15}$$

TABLE 10.4 Mechanical properties of line-pipes for Arctic use. (After Shiga *et al.*<sup>25</sup>)

| Steel | Grade<br>(API) | Pipe size<br>Wall thickness<br>× outer dia.<br>(mm) | Tensile properties          |                             |              | Charpy impact properties |                  |                  | Weld portion         |                               |
|-------|----------------|---|-----------------------------|-----------------------------|--------------|--------------------------|------------------|------------------|----------------------|-------------------------------|
|       |                |   | Body                        |                             |              | DWTT                     |                  |                  | Charpy impact energy |                               |
|       |                |   | YS<br>(kg/mm <sup>2</sup> ) | TS<br>(kg/mm <sup>2</sup> ) | YS/TS<br>(%) | at -25°C<br>(kg·m)       | 50% FATT<br>(°C) | 85% FATT<br>(°C) | at -25°C (kg·m)      | Heat-affected<br>zone<br>Weld |
| C-1   | X-65           | 26.9 × 1219   | 47.8                        | 58.8                        | 81.2         | 13.2                     | 7.6              | -135             | 6.5                  | 19.2                          |
| C-1   | X-70           | 21.3 × 1219   | 52.1                        | 60.4                        | 86.2         | 12.9                     | 9.0              | -115             | 9.8                  | 16.8                          |
| C-2   | X-70           | 21.3 × 1219   | 52.2                        | 61.5                        | 84.8         | 14.1                     | 10.0             | -120             | 9.3                  | 7.2                           |
| C-3   | X-70           | 15.2 × 1219   | 51.9                        | 61.7                        | 84.1         | 26.6                     | 18.1             | -112             | 25.2                 | 15.5                          |
| C-4   | X-70           | 18.3 × 1219   | 50.2                        | 60.0                        | 83.8         | 30.0                     | 14.2             | -115             | 21.7                 | 15.8                          |
| C-5   | X-70           | 25.4 × 1219   | 51.2                        | 61.5                        | 80.0         | 30.0                     | 21.3             | -120             | 20.0                 | 16.7                          |
| Q-1†  | X-80           | 19.1 × 1422   | 60.0                        | 70.0                        | 86.0         | 24.0                     | 24.0             | -105             | 20.7                 | 19.0                          |

\*CV100 is the energy at the lowest temperature where shear area is 100%.

† Quenched and tempered.

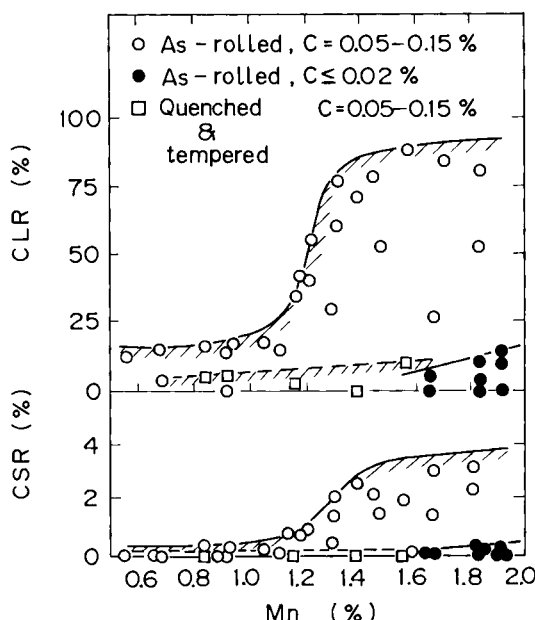


Figure 10.12 Effects of manganese and carbon contents on the susceptibility to hydrogen-induced cracking in controlled-rolled and quenched and tempered steels. (After Taira *et al.*<sup>26</sup>) Crack length ratio (CLR) and crack sensitivity ratio (CSR) are calculated by:

$$\text{CLR}(\%) = \Sigma a_i \div (n \times A)$$

$$\text{CSR}(\%) = \Sigma (a_i \times b_i) \div (n \times A \times B)$$

where  $\Sigma a_i$  = summation of each crack length,  $n$  = number of sections examined,  $A$  = specimen width,  $\Sigma(a_i \times b_i)$  = summation of each stepwise crack area, and  $B$  = specimen thickness

forming stepwise cracks. Several measures have been taken to avoid the occurrence of hydrogen-induced cracking: (1) lowering of sulphur content to an extremely low level to eliminate the initiation sites for hydrogen-induced cracking; (2) inclusion shape control by the addition of calcium and/or rare earth metals; and (3) suppression of micro-segregation of alloy elements and impurities. For those reasons, the susceptibility to hydrogen-induced cracking is reduced with the decrease in carbon and manganese contents as shown in Figure 10.12.<sup>26</sup>

As controlled-rolling can save such alloying elements as carbon and manganese, it can reduce susceptibility to hydrogen-induced cracking, while maintaining high resistance to unstable shear fracture. Tables 10.3 and 10.4 show chemical compositions and mechanical properties for line-pipe steels.<sup>25</sup> Having low-carbon, low-sulphur, and niobium-vanadium as a base composition, these steels exhibit high strength, excellent low-temperature toughness in terms of Charpy test and the DWTT, and high impact energy.

### 10.2.3 Acicular $\alpha$ steel

Controlled-rolled  $\alpha$ -pearlite steels have been produced up to the strength level of API

X-70 grade and up to 40 mm thick. When the thickness is greater than 40 mm, the controlled-rolling effect cannot be spread over the whole thickness because it would cause a coarse grain structure and deteriorating toughness at mid-thickness.

Acicular  $\alpha$  steel, which is produced by the combined effects of controlled-rolling and transformation hardening, can overcome the above difficulty, giving greater thickness and higher strength.

Figure 10.13<sup>27</sup> depicts the effect of the degree of hot-deformation in the nonrecrystallization region on percentage acicular  $\alpha$  volume fraction, and tensile and Charpy impact properties where the amount of reduction in the recrystallization region was fixed at 62.5%. When the amount of reduction is less than 20%, microstructure is fully acicular  $\alpha$  which, being free of polygonal  $\alpha$ , contains a small amount of cementite and martensite, exhibiting rather poor toughness. With further increase in the amount of reduction, steel loses hardenability, and thereby gives a mixed structure of acicular  $\alpha$  and polygonal  $\alpha$ . With the increase in percentage polygonal  $\alpha$  volume fraction, impact energy increases and the transition temperature decreases greatly. Yield strength and tensile strength increase in the initial stage but suddenly decrease at 70% reduction. Therefore, the optimum combination of strength and toughness is obtained at about 15% of polygonal  $\alpha$ .

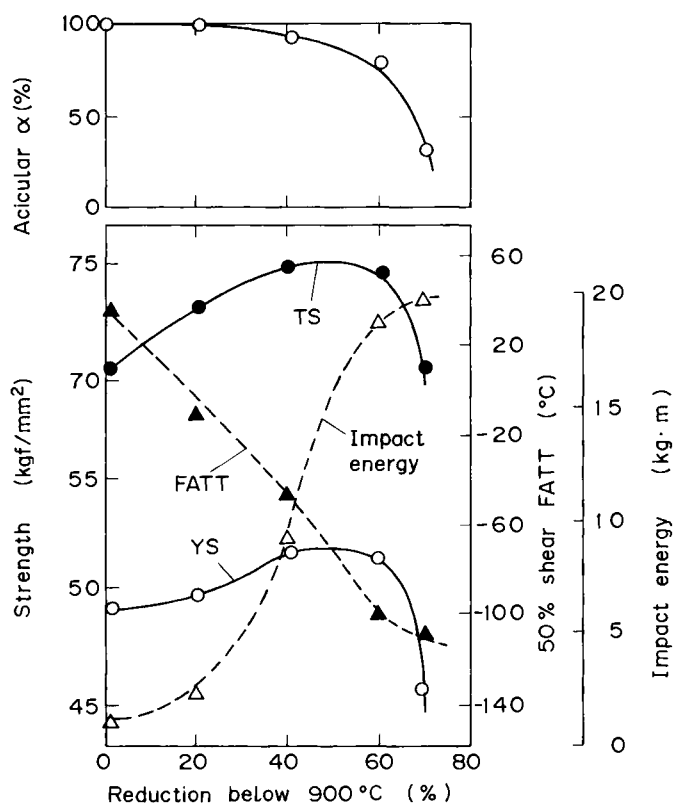


Figure 10.13 Dependence of acicular  $\alpha$  volume fraction, strengths, and the Charpy impact properties on the amount of reduction in nonrecrystallization region in 0.07% C–2.0% Mn–0.06% Nb–0.5% Mo acicular  $\alpha$  steel. (After Tabata *et al.*<sup>27</sup>)

Increase in strength and significant improvement in toughness can be obtained in the mixed structure of acicular plus fine-grained polygonal  $\alpha$  by decreasing recrystallized  $\gamma$  grain size and by increasing the amount of deformation in the nonrecrystallization region. The reason for the improvement is grain refinement in the polygonal  $\alpha$  as well as acicular  $\alpha$ . However, excessive formation of polygonal  $\alpha$  loses strength because of the decrease in the fraction of hard acicular  $\alpha$ .

It is to be noted here that, although the introduction of fine-grained polygonal  $\alpha$  is very effective for the improvement in strength and toughness, the introduction of coarse polygonal  $\alpha$  causes deterioration in strength as well as toughness. Causes of coarse polygonal- $\alpha$  formation are: (1) insufficient hardenability; and (2) inadequate controlled-rolling conditions in terms of finish-rolling temperature and the amount of hot-deformation in the nonrecrystallization region.

Another feature of acicular  $\alpha$  steel is continuous yielding followed by rapid work-hardening, which is paramount to offsetting any loss in yield strength due to the Bauschinger effect,<sup>28</sup> which has a pronounced effect on discontinuous-yielding, polygonal steels.<sup>29</sup> In the process of UOE pipe manufacturing, material is given a complicated strain cycle of bending, unbending, compression and expansion. Because of the strain cycle experienced, the mechanical properties of pipe are much different from those of base plate. In particular, variation in yield strength is large because it suffers both work-hardening and the Bauschinger effect. Difference in yield strength between pipe and plate is plotted against the yield : tensile-strength ratio of plate in various steels in Figure 10.14. Difference in yield strength decreases in a linear manner with increasing ratio. Yield strengths of pipes are larger than those of plates in acicular  $\alpha$  steels which

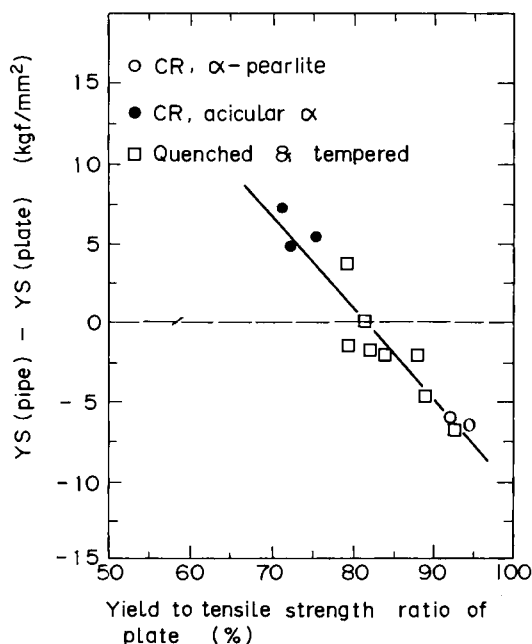


Figure 10.14 Difference in yield strength between pipe and base plate is plotted vs. yield : tensile-strength ratio of plate in controlled-rolled and quenched and tempered steels, exhibiting the beneficial effect of acicular  $\alpha$  steel

TABLE 10.5 Chemical compositions of steels (percentage weight)

| Steel | Type             | C     | Si   | Mn   | P     | S     | V     | Ni   | Cu   | Mo    | Al    | N      | Nb    | C <sub>e</sub> | C <sub>eq</sub> |
|-------|------------------|-------|------|------|-------|-------|-------|------|------|-------|-------|--------|-------|----------------|-----------------|
| 1     | High Ax          | 0.057 | 0.21 | 1.96 | 0.019 | 0.004 | —     | 0.26 | —    | 0.420 | 0.027 | 0.0057 | 0.063 | 0.006          | 0.485           |
| 2     | Medium Ax        | 0.050 | 0.20 | 1.92 | 0.018 | 0.004 | —     | 0.24 | —    | 0.330 | 0.040 | 0.0048 | 0.074 | 0.006          | 0.452           |
| 3     | Low Ax           | 0.049 | 0.10 | 1.59 | 0.013 | 0.004 | —     | 0.25 | —    | 0.330 | 0.020 | 0.0035 | 0.055 | —              | 0.397           |
| 4     | Pearlite-reduced | 0.057 | 0.26 | 1.70 | 0.016 | 0.003 | 0.026 | 0.22 | 0.22 | 0.002 | 0.034 | 0.0039 | 0.043 | 0.036          | 0.383           |
| 5     | QT*              | 0.093 | 0.24 | 1.45 | 0.021 | 0.006 | 0.025 | 0.21 | —    | 0.014 | 0.028 | 0.0038 | —     | —              | 0.356           |

\* Acicular  $\alpha$ 

† Quenched and tempered

TABLE 10.6 Changes in mechanical properties with pipe-forming (transverse direction)

| Steel | Type             | Thickness<br>(mm)<br>(Pipe expansion<br>ratio (%)) | Location | Tensile properties          |                             |              | Charpy impact properties |                    |                  | DWT | Remark           |
|-------|------------------|--|----------|-----------------------------|-----------------------------|--------------|--------------------------|--------------------|------------------|-----|------------------|
|       |                  |  |          | YS<br>(kg/mm <sup>2</sup> ) | TS<br>(kg/mm <sup>2</sup> ) | YS/TS<br>(%) | 50% FATT<br>(°C)         | at -25°C<br>(kg·m) | 85% FATT<br>(°C) |     |                  |
| 1     | High Ax*         | 18.3<br>(1.29)                                     | Plate    | 54.7                        | 75.8                        | 72.2         | -135                     | 11.0               | < -80            |     |                  |
|       |                  |  | Pipe     | 59.5                        | 76.4                        | 77.9         | -128                     | 8.6                | < -80            |     |                  |
| 2     | Medium Ax        | 18.3<br>(1.29)                                     | Plate    | 51.8                        | 69.7                        | 74.3         | -119                     | 8.7                | -80              |     | Yield elongation |
|       |                  |  | Pipe     | 57.1                        | 70.4                        | 81.1         | -110                     | 8.5                | -76              |     |                  |
| 3     | Low Ax           | 18.3<br>(1.29)                                     | Plate    | 40.2                        | 56.3                        | 71.4         | -119                     | 11.2               | < -80            |     | Yield elongation |
|       |                  |  | Pipe     | 47.5                        | 57.4                        | 82.8         | -109                     | 10.4               | -81              |     |                  |
| 4     | Pearlite-reduced | 15.3<br>(1.26)                                     | Plate    | 55.4                        | 60.1                        | 92.2         | -113                     | 19.4               | < -80            |     | Yield elongation |
|       |                  |  | Pipe     | 49.4                        | 61.2                        | 80.7         | -105                     | 19.1               | -71              |     |                  |
| 5     | QT†              | 20.0<br>(1.32)                                     | Plate    | 55.8                        | 63.4                        | 88.0         | -68                      | 10.7               | -30              |     | Yield elongation |
|       |                  |  | Pipe     | 53.7                        | 63.7                        | 84.3         | -53                      | 7.1                | -17              |     |                  |

\* Acicular  $\alpha$ 

† Quenched and tempered



have low yield : tensile-strength ratios because of a parabolic stress-strain curve. The situation is reversed in  $\alpha$ -pearlite steels which have high yield : tensile-strength ratios due to their fine-grained structures.

Table 10.5 shows chemical compositions of acicular  $\alpha$  steels as well as pearlite-reduced steel and quenched and tempered steels which were commercially produced for large-diameter line-pipes. Table 10.6 shows the mechanical properties of plates and pipes. Acicular  $\alpha$  steels exhibit much lower yield : tensile-strength ratios than quenched and tempered steel or pearlite-reduced steel. Although acicular  $\alpha$  steels give almost the same transition temperature with pearlite-reduced steel, they have much lower impact energy than pearlite-reduced or quenched and tempered steel.

#### 10.2.4 As-hot-rolled dual-phase steel

Dual-phase steel has a microstructure consisting of  $\alpha$  grains dispersed with fine martensite islands. It is characterized by continuous yielding followed by rapid work-hardening, which results in low yield but high tensile strength and large elongation. Dual-phase steel can be produced in the as-hot-rolled condition by the combination of suitable chemical composition and rolling conditions.<sup>30-36</sup>

Figure 4.22 (page 99) depicts the continuous cooling temperature diagram of 0.05% C-1.0% Si-1.5% Mn-1.0% Cr steel deformed in the nonrecrystallized  $\gamma$  region,

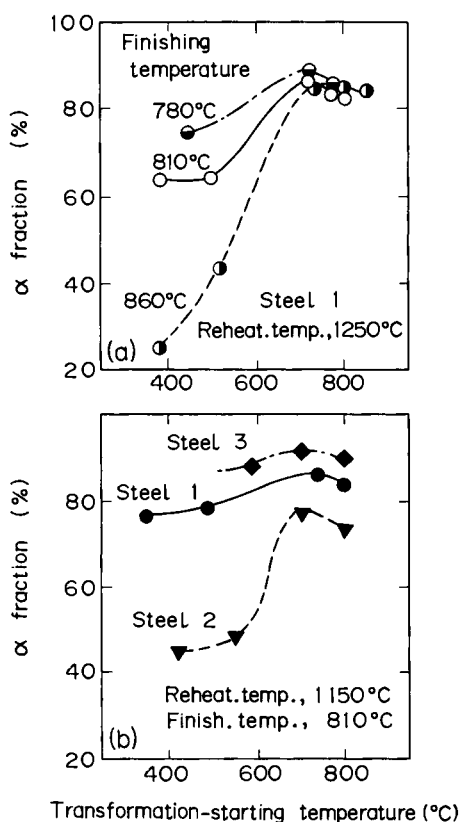


Figure 10.15 Dependence of  $\alpha$  volume fraction on transformation-starting temperature in dual-phase steels where duration of transformation is fixed at 7 s. (After Mano *et al.*<sup>32</sup>)  
Steels 1, 2 and 3 are  
0.05% C-0.99% Si-1.48% Mn-1.09% Cr,  
0.08% C-0.96% Si-1.49% Mn-1.0% Cr and  
0.05% C-1.0% Si-1.54% Mn-0.06% Cr  
respectively

superimposed with three typical cooling patterns for obtaining dual-phase structure.<sup>32</sup> In cooling pattern S, deformed  $\gamma$  is rapidly cooled to a certain supercooling state and held for some time at that temperature in order to accelerate  $\alpha$  transformation as much as possible, and followed by rapid cooling to coiling temperature. In cooling patterns A and B, as the separation of  $\gamma$  into  $(\gamma + \alpha)$  two-phase structure (thereafter abbreviated as separate transformation) does not occur sufficiently, untransformed  $\gamma$  is not fully stabilized, and thereby transforms to upper bainite at higher temperatures. Therefore, the essence of producing dual-phase steel lies in the optimum selection of variables which enhance the separate transformation.

The effect of supercooling temperature, in other words, transformation-starting temperature (see cooling pattern S in Figure 4.22) on percentage  $\alpha$  volume fraction, is shown in Figure 10.15.<sup>32</sup> There is the optimum transformation-starting temperature at about 700° C, which is 20–30° K below  $A_{r3}$ ,<sup>33</sup> where the maximum percentage  $\alpha$  fraction is obtained. Finish-rolling temperature also plays an important role; with the decrease in finishing temperature,  $\alpha$  fraction increases, which is more remarkable at low transformation-starting temperatures. A relation between percentage  $\alpha$  volume fraction and duration of transformation is depicted in Figure 10.16,<sup>32</sup> where transformation-starting temperature is fixed at 700° C. At the optimum temperature of 700° C,  $\alpha$  transformation proceeds very rapidly,<sup>33</sup> though there is large difference in the  $\alpha$  formation rate among the three steels. The effects of coiling temperature on tensile properties are shown in Figure 10.17.<sup>32</sup> In 0.05% C–0.99% Si–1.48% Mn–1.09% C steel, the critical coiling temperature is 550° C below which yield point elongation is suppressed, giving a low yield:tensile-strength ratio while, in 0.05% C–1.00% Si–1.54% Mn steel, the critical temperature is 200° C.

The process of supercooling for  $\alpha$  formation shown in Figure 4.22 could be omitted if a plain carbon steel was finish-rolled at around  $A_{r3}$ , thereby producing a mixed structure of  $\alpha$  and  $\gamma$  at the end of rolling.<sup>34</sup>

Alloying elements play a very important role in producing the dual-phase structure. The addition of silicon accelerates the separate transformation in the early stages of transformation, and thereby enriches untransformed  $\gamma$  with carbon and nitrogen and increases its hardenability. Chromium raises a critical coiling temperature required for the suppression of yield point elongation probably through the increase in harden-

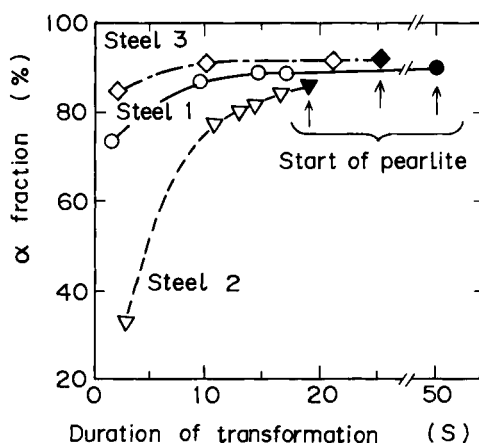


Figure 10.16 Dependence of  $\alpha$  volume fraction on duration of transformation where transformation temperature is fixed at 700° C. Chemical compositions of steels 1, 2 and 3 are shown in Figure 10.15. (After Mano *et al.*<sup>32</sup>)

TABLE 10.7 Chemical compositions and mechanical properties of dual-phase steels produced in the production line. (After Sugisawa *et al.*,<sup>31</sup> Mano *et al.*,<sup>32</sup> Okita, Hosoya and Nakaoka,<sup>33</sup> Furukawa *et al.*,<sup>34</sup> and Tokunaga<sup>36</sup>)

| Steel | C (%) | Si (%) | Mn (%) | Cr (%)        | Thick-<br>ness<br>(mm) | Finish<br>temp.<br>(°C) | Coiling<br>temp.<br>(°C) | YS<br>(kg/mm <sup>2</sup> ) | TS<br>(kg/mm <sup>2</sup> ) | YS/TS<br>(%) | Yield<br>elong.<br>(%) | Total<br>elong.<br>(%) | Reference                                 |
|-------|-------|--------|--------|---------------|------------------------|-------------------------|--------------------------|-----------------------------|-----------------------------|--------------|------------------------|------------------------|---|
| 1     | 0.09  | 0.12   | 1.50   | —             | 2.9                    | >800                    | ~RT                      | 43.5                        | 63.1                        | 69           | 0                      | 31.6                   | Sugisawa<br><i>et al.</i> , <sup>31</sup> |
| 2     | 0.05  | 1.0    | 1.50   | 1.0           | 2.9                    | 810                     | 500                      | 34.7                        | 63.0                        | 55           | 0                      | 33.0                   | Mano <i>et al.</i> , <sup>32</sup>        |
| 3     | 0.05  | 1.0    | 1.50   | —             | 2.9                    | 810                     | 200                      | 40.3                        | 62.0                        | 65           | 0                      | 31.0                   | Mano <i>et al.</i> , <sup>32</sup>        |
| 4     | 0.07  | 1.0    | 1.50   | 0.06          | 2.9                    | 800                     | 200                      | 37.8                        | 63.0                        | 60           | 0                      | 33.0                   | Mano <i>et al.</i> , <sup>32</sup>        |
| 5*    | 0.07  | 0.71   | 1.42   | —             | —                      | 800                     | 200                      | 32.8                        | 67.2                        | 50           | 0                      | 26.0                   | Furukawa<br><i>et al.</i> , <sup>34</sup> |
| 6†    | 0.08  | 0.30   | 1.30   | (Nb)<br>0.035 | 2.67                   | —                       | —                        | 56.1                        | 62.1                        | 90.3         | —                      | 27.6                   | Tokunaga<br><i>et al.</i> , <sup>36</sup> |

\* Hot-rolled by laboratory mill to simulate hot-coil

† Conventionally hot-rolled HSLA steel

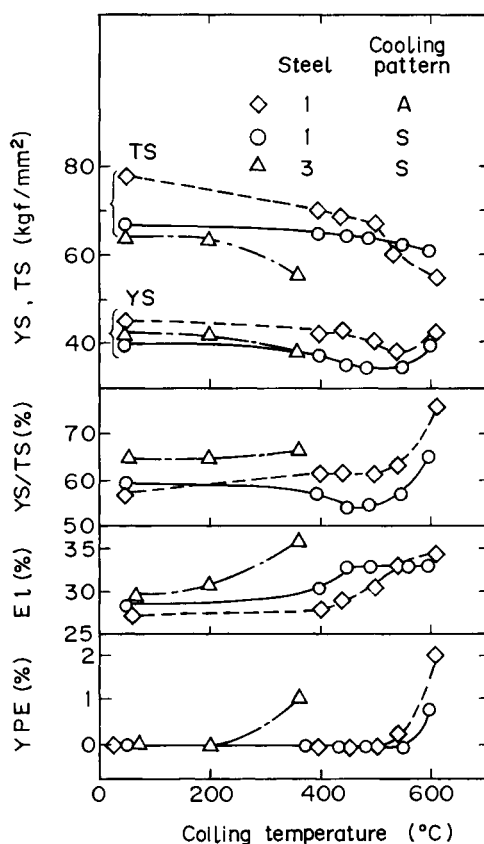


Figure 10.17 Effects of coiling temperature and cooling pattern on tensile properties where slab-reheating temperature and finishing temperature are 1150 and 810°C respectively. Chemical compositions of steels 1 and 3 are shown in Figure 10.15. (After Mano *et al.*<sup>32</sup>)

ability of untransformed  $\gamma$  shown in Figure 10.17. An increase in carbon content not only retards the start of  $\alpha$  transformation, but decreases the  $\alpha$  fraction formed, as shown in Figures 10.15 and 10.16.

Dual-phase steel possesses several features: (1) a parabolic stress-strain curve; (2) a low yield strength but high tensile strength; (3) a large work-hardening rate particularly at the initial stage of stress-strain curve; and (4) large uniform and total elongations. Having those features, dual-phase sheet steel exhibits superior stretch-formability, finding application in the automobile industry and others.

Table 10.7 shows chemical compositions and mechanical properties of dual-phase steels produced by different processes.<sup>32-36</sup> All the steels exhibit lower yield : tensile-strength ratios and larger elongation in comparison with conventionally hot-rolled steels. In general, dual-phase steel with high alloy content and high coiling temperature shows better properties – in terms of low yield : tensile-strength ratios and large elongation – than steel with low alloy content and low coiling temperature.

### 10.3 Weldability

By the term 'weldability', we mean: (1) susceptibility to weld cracking; and (2) toughness at the heat-affected zone. When steel is welded with small heat input, there is a

propensity for cracking to occur at the root of the weld bead (root crack). The susceptibility to weld cracking is conventionally represented by the carbon equivalent which is, however, more directly associated with the maximum hardness at the heat-affected zone. A more suitable parameter is represented by the weld-cracking parameter  $P_{cm}$  which gives contributions from individual alloying elements to the susceptibility to weld cracking, and is expressed by the following equation:

$$P_{cm} = C + \frac{Si}{30} + \frac{Mn + Cu + Cr}{20} + \frac{Ni}{60} + \frac{Mo}{15} + \frac{V}{10} + 5B \quad (10.12)^{37}$$

As the carbon equivalent and  $P_{cm}$  of controlled-rolled steel are lower than those of conventional steel, controlled-rolled steel gives lower maximum hardness and less susceptibility to weld cracking than conventional steel.

The toughness at the heat-affected zone is not influenced by the hysteresis which base metal has experienced, but is governed by: (1) the chemical composition of base metal; and (2) the cooling rate after welding, since the heat-affected zone is heated nearly to melting point, thereby eliminating hysteresis.

With regard to the weldability of controlled-rolled steel, we must take into consideration the effect of alloy elements on the properties of weld metal and weld joint strength besides the two factors mentioned above. As weld metal is diluted by the base metal the properties of the weld metal are influenced by alloy elements of welding material and base metal. The strength of the weld joint is not a problem as in so far as welding heat input is small. With increasing heat input, however, the softened zone becomes wide, decreasing the strength of weld joint.

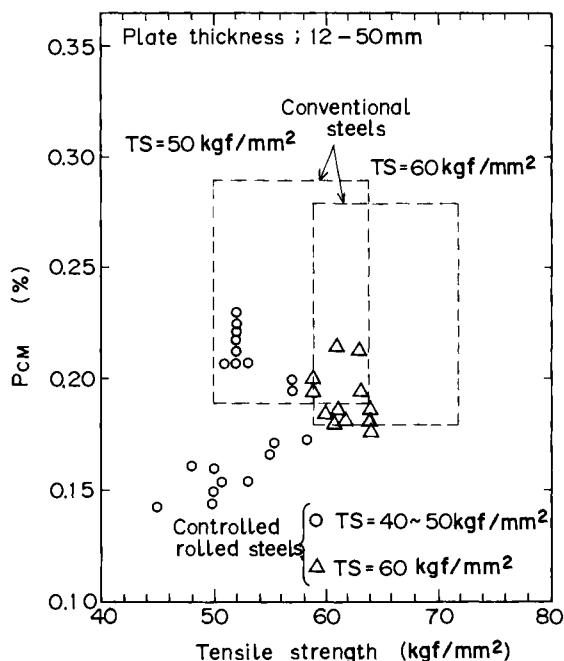


Figure 10.18 Relation between weld cracking parameter  $P_{cm}$  and tensile strength in controlled-rolled and conventional steels

### 10.3.1 Susceptibility to weld cracking

Controlled-rolled steels are less susceptible to weld cracking than conventional ones, since the former have lower values for  $P_{cm}$  than the latter, as shown in Figure 10.18. The susceptibility to weld cracking is usually estimated by the oblique Y-groove restraint cracking test, where a single bead is laid on the oblique Y-groove and three types of cracks – surface, cross-section and root – are measured as shown in Figure 10.19. The percentage of crack is plotted against the preheating temperature in controlled-rolled HT-50 steel with a yield strength of  $36 \text{ kgf/mm}^2$  in Figure 10.20, showing that preheating of  $50^\circ \text{C}$  is necessary to suppress the formation of cracks. The root crack is the most likely to occur, followed by cross-section and surface cracks.

The lowering of the preheating temperature required for the suppression of cracking is very important for the efficiency of welding and the integrity of weld joints. As shown

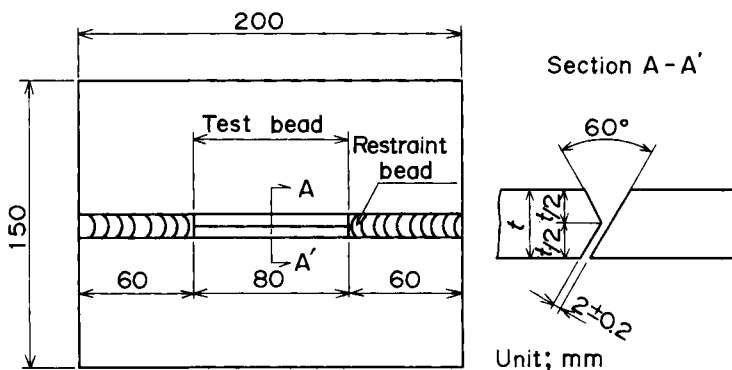


Figure 10.19 Method of Y-groove cracking test (JIS Z3158 (1966))

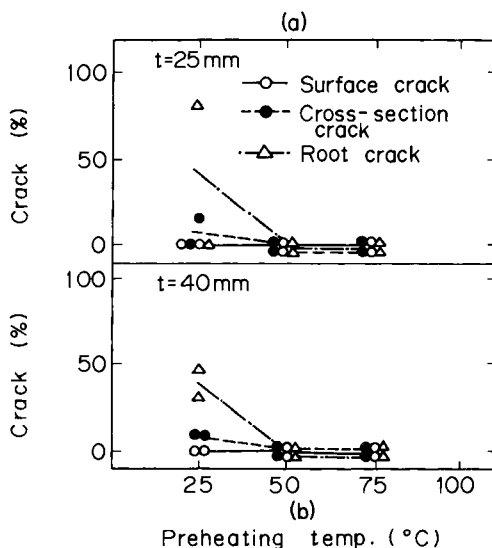


Figure 10.20 Dependence of percentage crack on preheating temperature obtained by the Y-groove restraint cracking test in controlled-rolled 0.14% C-0.26% Si-1.4% Mn steel with yield strength of  $36 \text{ kgf/mm}^2$ : (a)  $t = 25 \text{ mm}$ ; (b)  $t = 40 \text{ mm}$

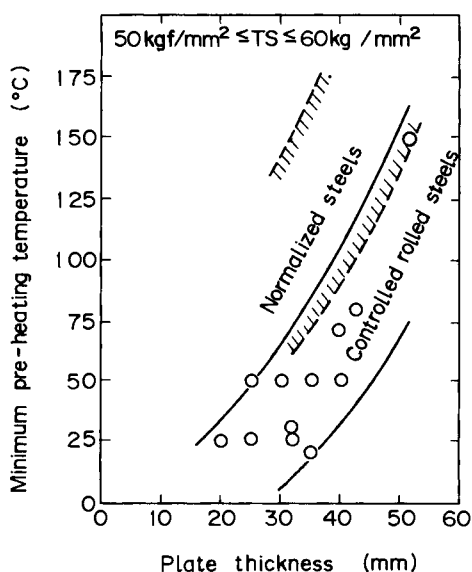


Figure 10.21 Effect of plate thickness on the minimum preheating temperature required for the prevention of crack in control-rolled and normalized steels.

in Figure 10.21, the preheating temperature is much lower for controlled-rolled steels than for conventional ones. Controlled-rolling and subsequent accelerated cooling can further decrease preheating temperature via decrease in carbon equivalent.

### 10.3.2 Toughness at the heat-affected zone

Toughness at the heat-affected zone is another important aspect of weldability. When subjected to the weld thermal cycle, temperatures from melting point to  $A_{r1}$  are given to base metal in a narrow region neighbouring weld metal. The heat-affected zone consists of four regions, depending on temperature: (1) the embrittled region above  $1150^{\circ}\text{C}$ ; (2) the toughened region between  $1000$  and  $850^{\circ}\text{C}$ ; (3) the embrittled region between  $800$  and  $700^{\circ}\text{C}$ ; and (4) the region below  $A_{r1}$ , where toughness remains unchanged, as shown in Figure 10.22 where the heat-affected zone is reproduced by a synthetic thermal cycle.<sup>38</sup>

The fusion line, boundary region between base metal and weld metal which is heated nearly to melting point ( $1250$ – $1500^{\circ}\text{C}$ ) during welding, corresponds to region (1) above. Since the toughness of the heat-affected zone is governed mainly by the toughness of the bond, improvement in the fusion line toughness is most crucial. Figure 10.23 shows the changes in 50% shear FATT and the microstructure with cooling time from  $800$  to  $500^{\circ}\text{C}$  in simulated fusion line where specimens were heated rapidly to  $1350^{\circ}\text{C}$ , held for 5 s and cooled with different cooling rates.<sup>39</sup> Assuming a plate thickness of 25 mm and interpass temperature of  $150^{\circ}\text{C}$ , welding heat-input is also shown in the figure. In HT-50 (tensile strength =  $50\text{ kgf/mm}^2$ ) steel, 50% shear FATT increases monotonously with the increase in cooling time. However, in HT-60–HT-100 steels, 50% shear FATT decreases with increasing cooling time, reaches the minimum, then rises rapidly with a further increase in cooling time, and finally arrives at a steady level. The critical cooling time where FATT becomes the minimum is shifted to a longer time with the increase in alloy content.

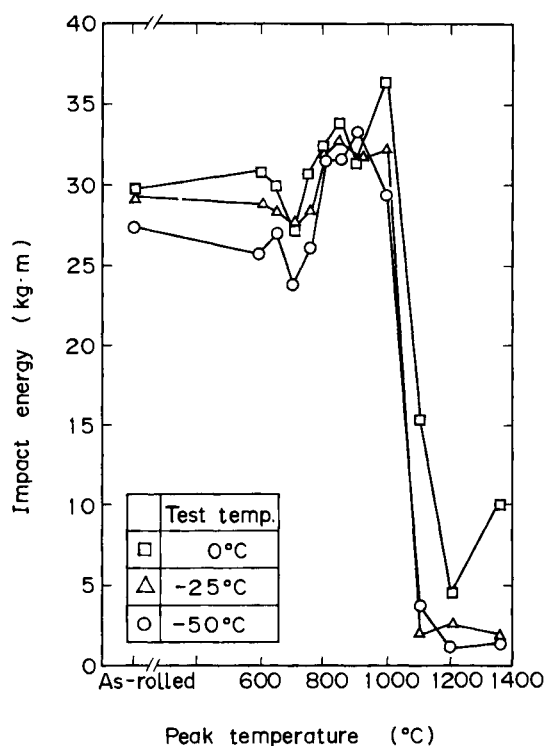


Figure 10.22 Change in the Charpy impact energy of the synthetic heat-affected zone with peak temperature in thermal cycle. (After Shiga *et al.*<sup>38</sup>)

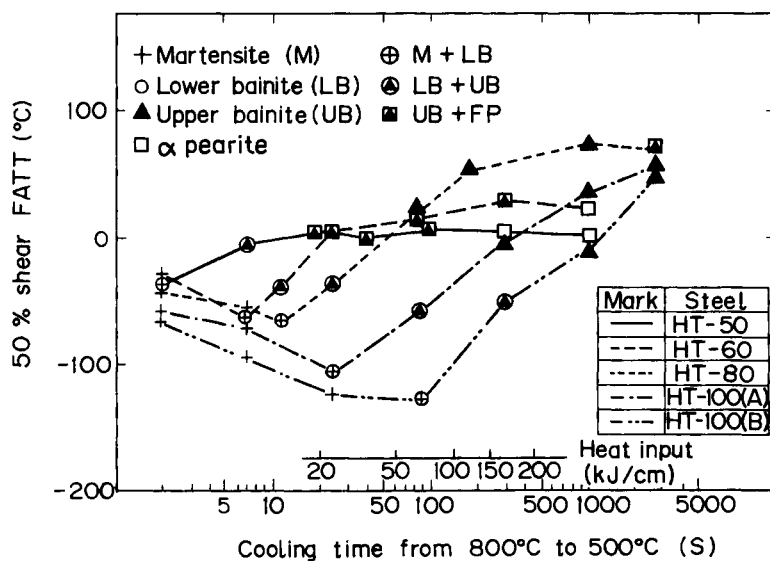


Figure 10.23 Variations in 50% shear FATT and microstructure of synthetic heat-affected zone with cooling rate in HT-50–HT-100 steels. (After Kasamatsu, Takashima and Hosoya<sup>39</sup>)



The behaviour illustrated in Figure 10.23 is more consistently shown in the plot of 50% shear FATT vs. microstructure in Figure 10.24.<sup>39</sup> The toughness at the fusion line consists basically of three regions: (1) with the change in microstructure from martensite to lower bainite, 50% shear FATT is shifted to lower temperature; (2) with the change in microstructure from martensite plus lower bainite to upper bainite, 50% shear FATT increases rapidly, which is more remarkable in high-alloyed steel; and (3) with the change in microstructure from upper bainite to  $\alpha$  plus pearlite, 50% shear FATT remains unchanged or decreases gradually. Increment in 50% shear FATT caused by the change in microstructure from martensite plus lower bainite to upper bainite is dependent on the amount of the martensite- $\gamma$  constituent, and increases with the increase in volume fraction of the martensite- $\gamma$  constituent. The morphology of upper bainite is different depending on the strength level of steel; in HT-50 steel upper bainite consists mainly of cementites formed at  $\alpha$  lath boundaries, while in HT-60–HT-100 steels upper bainite consists of the martensite- $\gamma$  constituent formed at  $\alpha$  lath boundaries.

The embrittled regions above 1150° C and between 800 and 700° C shown in Figure 10.22 are caused mainly by the formation of the martensite- $\gamma$  constituent. The width of embrittled zone increases with the increase in welding heat-input. To make matters worse, large heat-input welding is very often used to increase welding efficiency in such processes as submerged-arc welding and electrogas welding, where by the term 'large heat-input' is usually meant heat input of more than 70 kJ/cm.

In HT-50 steel, with the increase in heat input, toughness decreases rapidly at the initial stage, followed by gradual decrease, as shown in Figure 10.25.<sup>40</sup> In HT-50 steel, deterioration in toughness due to large heat-input welding is attributed mainly to a mixed structure consisting of coarse proeutectoid  $\alpha$  at prior  $\gamma$  grain boundaries and upper bainite in grain interiors, though the martensite- $\gamma$  constituent exerts some effect. If the formation of the mixed structure is suppressed and  $\alpha$  structure alone is formed,

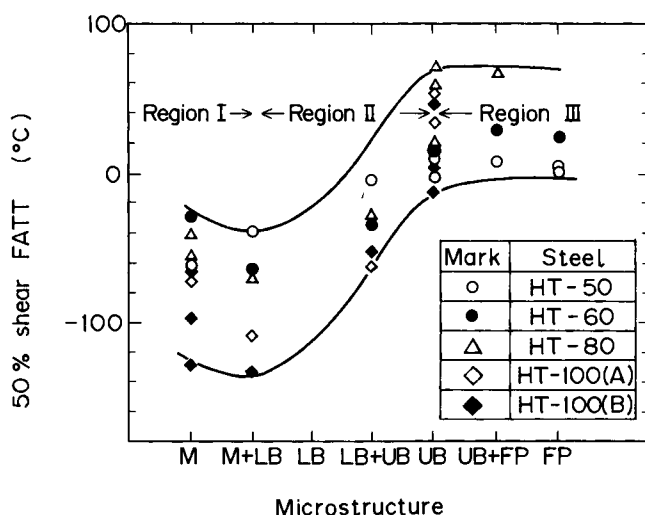


Figure 10.24 Relation between 50% shear FATT and microstructure in synthetic heat-affected zone of HT-50–HT-100 steels. (After Kasamatsu, Takashima and Hosoya<sup>39</sup>)

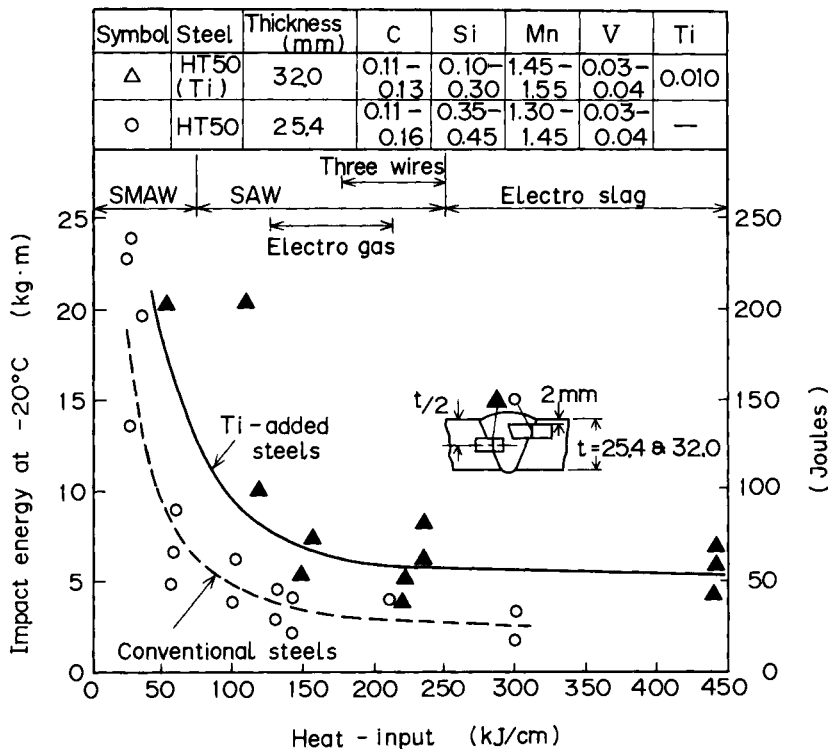


Figure 10.25 Dependence of the Charpy impact energy of the bond on heat-input in conventional and titanium-added HT-50 steels. (After Suzuki<sup>40</sup>)

the toughness at the heat-affected zone will improve markedly. In order to obtain the  $\alpha$  structure alone, two measures have to be taken: (1) suppression of  $\gamma$  grain coarsening during the welding thermal cycle by dispersing fine stable precipitates in base steel and thereby increasing nucleation sites for  $\alpha$  grains in the grain interiors as well as at  $\gamma$  grain boundaries,<sup>41,42</sup> and (2) enhancing  $\alpha$  transformation. To realize this objective, the addition of such elements as titanium,<sup>41</sup> rare earth metal (REM)–boron–titanium,<sup>42</sup> REM–calcium–titanium<sup>43</sup> and low-silicon–boron<sup>44</sup> have been proposed. As shown in Figure 10.25, the addition of titanium improves microstructure and thereby increases impact energy at any level of heat input. Besides the two above-mentioned factors, lowering of carbon, nitrogen and other alloy contents is favourable for the improvement of toughness at the heat-affected zone, because it increases toughness of the  $\alpha$  matrix on the one hand and prevents the martensite– $\gamma$  constituent from forming on the other.

Figure 10.26 shows the degree of deterioration in toughness in controlled-rolled HT-50 steels which were subjected to large heat-input welding, where upper limits of deterioration are shown by solid lines for conventional HT-50 steel and mild steel respectively.<sup>20</sup> The degrees of deterioration in controlled-rolled steels are roughly equal to those in conventional steels. Increments in 50% shear FATT in controlled-rolled and subsequently accelerated-cooled steels are roughly the same with those in mild steels, reflecting the favourable effect of low carbon equivalent in accelerated-cooled steels.

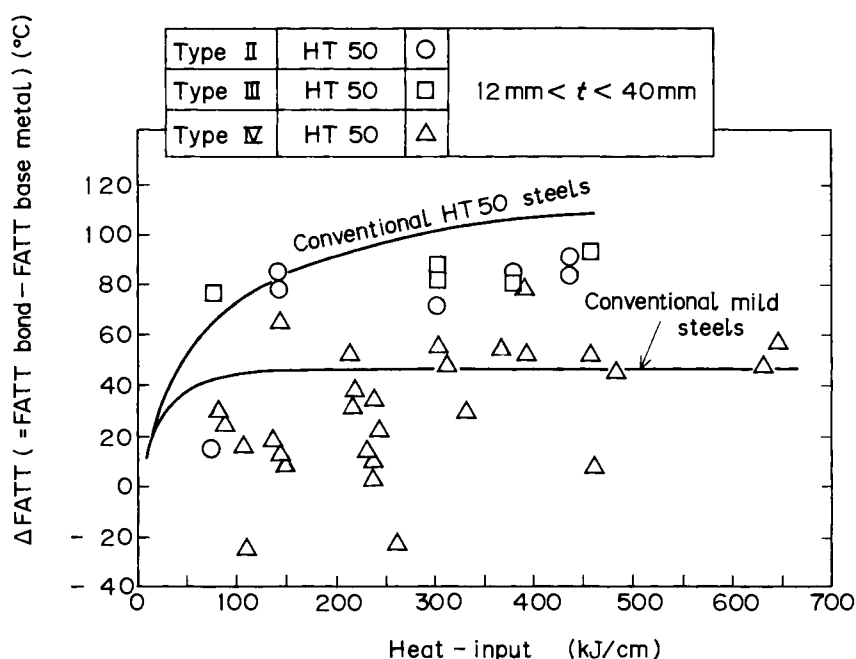


Figure 10.26 Difference in 50% shear FATT between fusion line and base metal is plotted vs. heat-input in controlled-rolled HT-50 steels where solid lines represent upper limits of deterioration for conventional HT-50 and mild steels respectively. Types II, III and IV are shown in Figure 10.3. (After Yajima<sup>20</sup>)

Demand for large heat-input welding has been increasing and controlled-rolled steels containing titanium, REM–boron–titanium, etc. have been produced commercially in large quantity for shipbuilding, storage tanks and other uses. Decrease in carbon equivalent due to controlled-rolling or controlled-rolling and subsequent accelerated-cooling improves both large heat-input weldability in terms of toughness at the heat-affected zone and small heat-input weldability in terms of susceptibility to weld cracking.

As shown in Figure 10.24, in HT-60–HT-100 steels, a decrease in toughness of fusion line with increasing heat input is caused mainly by increasing amounts of the martensite– $\gamma$  constituent. To improve toughness of fusion line, several measures have been taken. (1) lowering of carbon content reduces the amount of martensite– $\gamma$  constituent; (2) the addition of nickel increases toughness of the matrix; and (3) an increase in hardenability avoids the formation of upper bainite. Figure 10.27 depicts the effect of carbon content on a critical temperature where crack opening displacement of the heat-affected zone is equal to 0.1 mm in line-pipe steels.<sup>45</sup> A critical temperature decreases in a linear manner with decreasing carbon content, irrespective of the amount of welding heat-input. When nickel is added, a critical temperature is decreased markedly.

Niobium and vanadium are very frequently used in controlled-rolled steels and in particular in line-pipe steels, the former for the retardation of recrystallization of deformed  $\gamma$  as well as precipitation hardening and the latter for precipitation hardening. Niobium and vanadium have much influence not only on the properties of base

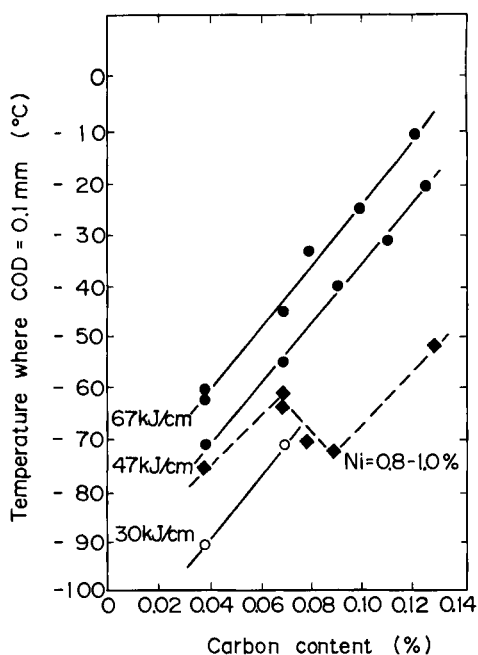


Figure 10.27 Effects of carbon content and heat input on critical temperature in microalloyed steels where COD of the heat-affected zone is equal to 0.1 mm. (After Miyoshi *et al.*<sup>45</sup>)

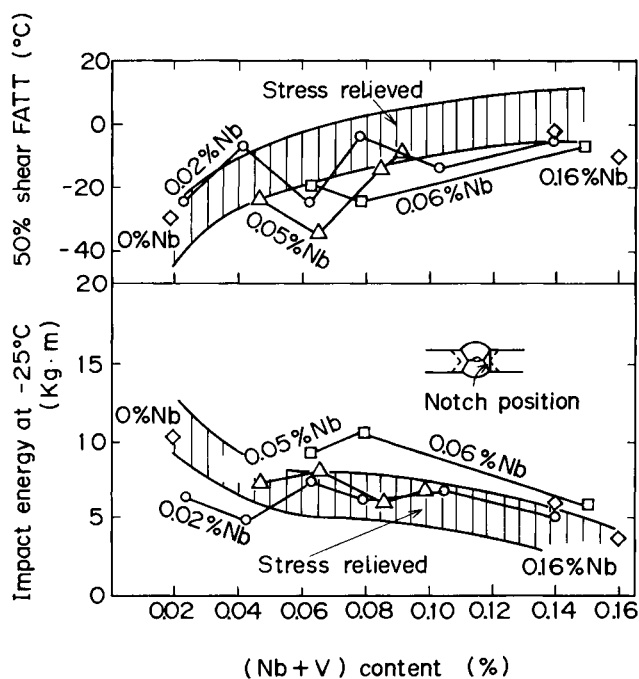


Figure 10.28 Effects of niobium and vanadium on the Charpy impact energy of the heat-affected zone of planar weld with or without subsequent stress-relieving at 600°C for 1 h. (After Shiga *et al.*<sup>38</sup>)

metal but on those of the heat-affected zone and weld metal. Toughness at the heat-affected zone deteriorates with the increase in niobium and vanadium contents both in the as-welded, and stress-relieved, conditions, shown in Figure 10.28.<sup>38</sup> There is a large increase in 50% shear FATT and a large decrease in the impact energy when niobium plus vanadium is raised from 0.02 to 0.04%.

As weld metal is diluted by base metal, the properties of the former are influenced by the chemical composition of the latter. Figure 10.29 depicts the effects of niobium and vanadium contents on the Charpy impact energy and 50% shear FATT of weld metal in the as-welded, and the stress-relieved, conditions. In the as-welded condition, impact energy and 50% shear FATT give maximum and minimum respectively at niobium plus one-half vanadium content of 0.015%, beyond which energy decreases, while 50% shear FATT on its own increases. Stress-relieving causes a large increase in FATT and a large decrease in impact energy. In general, the value for COD of the heat-affected zone is worse in carbon-manganese steels containing niobium and/or vanadium than in carbon-manganese steels. When heat input exceeds 3.5 kJ/mm, the COD value decreases rapidly in niobium-bearing steels as shown in Figure 10.30.<sup>46</sup>

Niobium in solution in  $\gamma$  increases hardenability, and thereby enhances the formation of upper bainite, which in turn deteriorates toughness at the heat-affected zone as well as weld metal, while niobium and vanadium in solution in an  $\alpha$  matrix do not exert any harmful effect on toughness. However, when they exist as coherent precipitates, they cause much hardening and toughness deteriorates markedly. In the as-welded condition, niobium exists as solute atoms in weld metal, having no harmful effect on toughness. However, when stress-relieved, niobium atoms precipitate as coherent pre-

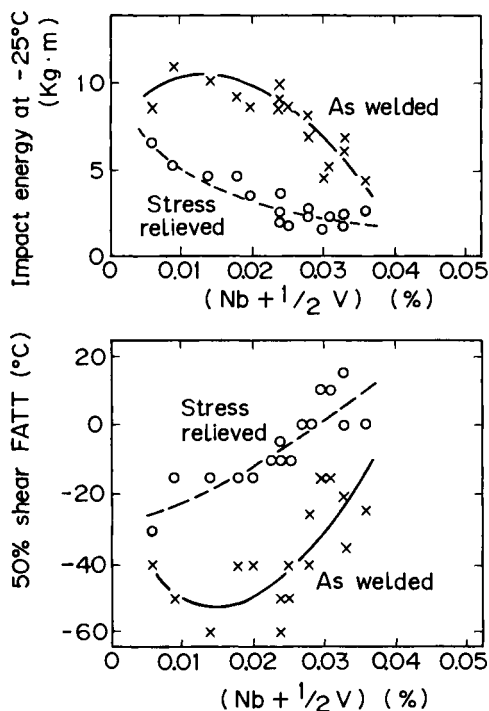


Figure 10.29 Effects of niobium and vanadium contents on the Charpy impact properties of weld metal in as-welded and stress-relieved conditions, where heat input is fixed at 25 kJ/cm

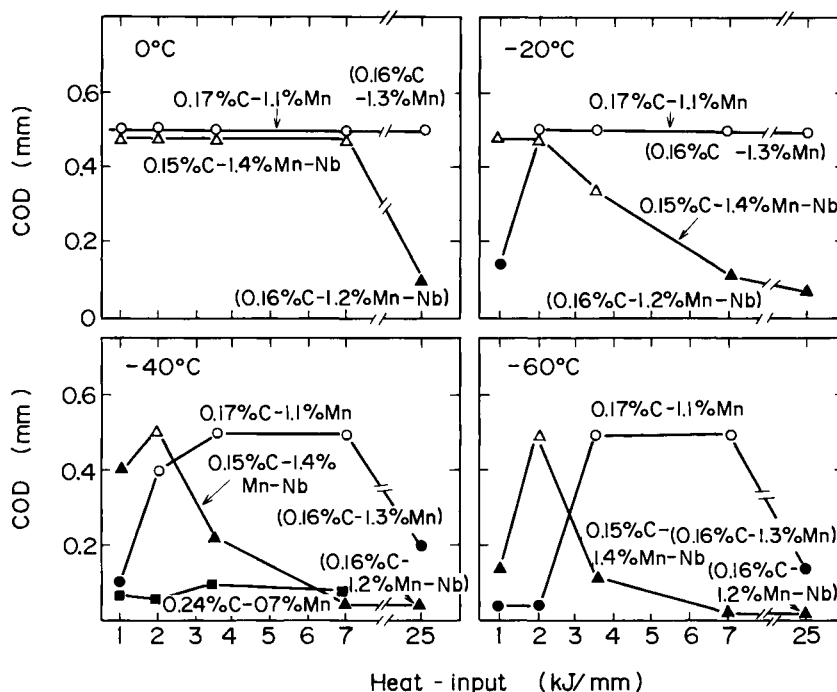


Figure 10.30 Crack-opening displacement data for grain-coarsened heat-affected zone regions of several carbon and carbon-manganese steels as a function of temperature and heat input. Diagram appropriate to 25-mm thick plate, sharp-cracked specimens. Open symbols indicate no cleavage fracture in test, with COD usually 0.5 mm. (After Dolby<sup>46</sup>)

cipitates, thereby markedly increasing strength and deteriorating toughness. When molybdenum coexists with niobium, as is usual in weld metal, it retards the precipitation of niobium carbonitrides, thereby causing more complicated influences on the toughness property in the stress-relieved condition. Taking into consideration the effect of niobium on toughness of the heat-affected zone as well as weld metal, the addition of niobium is desirable only in terms of the least indispensable content of  $\sim 0.02\%$ .

The strength of a weld joint is also an important factor. If welding heat input is small, the strength of a weld joint is more than that of base metal. However, with the increase in heat input, the softened region at the heat-affected zone broadens, thereby decreasing the strength of the weld joint. To attain 100% weld-joint efficiency, steel must have sufficient resistance to the softening which occurs at the heat-affected zone. In order to achieve the strength of more than  $50 \text{ kgf/mm}^2$  at the weld joint in HT-50 grade steel, carbon equivalent must be more than  $0.32\%$ , as shown in Figure 10.31, where welding with a heat input of 110 or  $180 \text{ kJ/cm}$  was employed.<sup>19</sup> From the viewpoint of susceptibility to weld cracking, carbon equivalent needs to be as low as possible while, in terms of strength of the weld joint, the carbon equivalent must be more than a certain critical value. Therefore, the optimum carbon equivalent is in the range of slightly more than  $0.32\%$  in steel. This value is difficult to attain in controlled-rolled HT-50 steel, but can be achieved by a combined process of controlled-rolling and subsequent accelerated-cooling.<sup>18,19</sup>

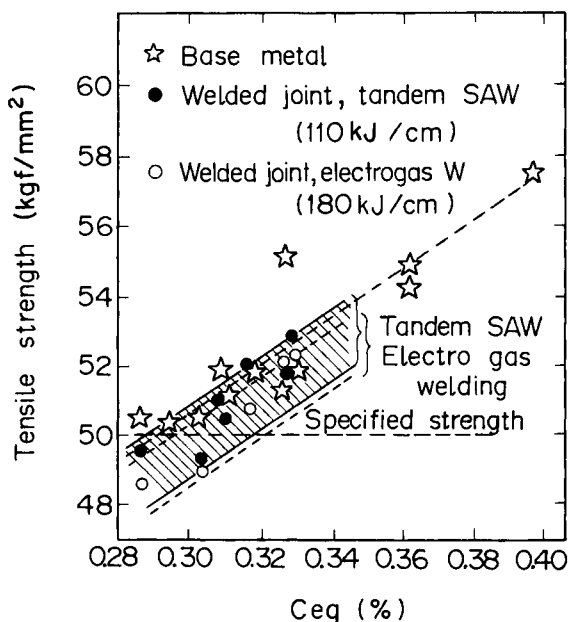


Figure 10.31 Effect of carbon equivalent on the tensile strengths of base metal and welded joint. (After Tsukada *et al.*<sup>19</sup>)

## References

1. HALL, E.O. *Proc. Phys. Soc.*, **64B**, 747 (1951)
2. BAKER, T.N. and MCPHERSON, N.A. *Met. Sci.*, **13**, 611 (1979)
3. GLADMAN, T., DULIEU, D. and MCVOR, I.D. *Microalloying '75*, Union Carbide Corp., p.32, (1977)
4. LITTLE, J.H., CHAPMAN, J.A., MORRISON, W.B. and MINTZ, B. *The microstructure and design of alloys*, Vol. I, The Metals Society p.80 (1974)
5. COLEMAN, T., DULIEU, D. and GOUGH, A. *The microstructure and design of alloys*, Vol. I, The Metals Society, p.70 (1974)
6. TANAKA, T., TABATA, N., HATOMURA, T. and SHIGA, C. *Microalloying '75* Union Carbide Corp., p.107 (1977)
7. BRAMFITT, B.L. and MARDER, A.R. *Processing and properties of low-carbon steel*, American Institute of Mining, Metallurgical and Petroleum Engineers, p.191 (1973)
8. HESLOP, J. and PETCH, N.J. *Philos. Mag.*, **3**, 1128 (1958)
9. KUNITAKE, T., TERASAKI, F., OHMORI, Y. and OHTANI, H. *Toward improved ductility and toughness*, Climax Molybdenum Company (Japan) Ltd, p.83 (1972)
10. TANAKA, T. *International Metals Reviews*, No. 4, 185 (1981)
11. KUNISHIGE, K., HASHIMOTO, T. and YUKITOSHI, T. *Tetsu-to-Hagané*, **66**, 63 (1980)
12. TANAKA, T. *Proceedings, the 7th iron and steel engineering seminar*, Iron Steel Inst. Japan, p.63 (1981)
13. SPEICH, G.R. and DABKOWSKI, D.S. *The hot-deformation of austenite*, American Institute of Mining, Metallurgical and Petroleum Engineers, p.557 (1977)
14. FUKUDA, M., HASHIMOTO, T. and KUNISHIGE, K. *Tetsu-to-Hagané*, **58**, 1832 (1972)
15. MELLOY, G.F. and DENNISON, J.D. *The microstructure and design of alloys*, Vol. I, The Metals Society, p.60 (1974)
16. GOHDA, S., WATANABE, K. and HASHIMOTO, Y. *Tetsu-to-Hagané*, **65**, 1400 (1979)
17. HASHIMOTO, T., SAWAMURA, T. and OHTANI, H. *Tetsu-to-Hagané*, **65**, 1425 (1979)
18. ONOUE, Y., MORIKAWA, H., SOGAWA, Y. and IWANAGA, K. *Tetsu-to-Hagané*, **62**, A231 (1982)
19. TSUKADA, K., YAMAZAKI, Y., MATSUMOTO, K., NIHKURA, M., YAMAMOTO, S., HIRABE, K. and ARIKATA, K. *Tetsu-to-Hagané*, **62**, A235 (1982)
20. YAJIMA, H. *Tetsu-to-Hagané*, **68**, A243 (1982)

21. IKESHIMA, T. *Trans. Iron and Steel Inst. Japan*, **20**, 561 (1980)
22. TAIRA, T., IWASAKI, H. and YAMAGUCHI, T. *Mechanical working and steel processing*, New York, American Institute of Mining, Metallurgical and Petroleum Engineers, p.294 (1975)
23. MAXEY, W.A., KIEFNER, J.F. and EIBER, R.J. *A.G.A. Catalog No. L32176*, American Gas Association (1976)
24. POYNTON, W.A. *J. Eng. Mat. and Tech.*, **96**, 324 (1974)
25. SHIGA, C., HATOMURA, T., KUDOH, J., KAMADA, A., HIROSE, K. and SEKINE, T. *Kawasaki steel technical report, No. 4*, p.97 (1981)
26. TAIRA, T., KOBAYASHI, Y., MATSUMOTO, K., MATSUMOTO, S., TERUNUMA, T. and ARIKATA, K. *Current solutions to hydrogen problems in steel*, American Society for Metals, p.173 (1982)
27. TABATA, N., SHIGA, C., KAMADA, A. and TANAKA, T. *Tetsu-to-Hagané*, **63**, S797 (1977)
28. TITHER, G. and LAVITE, M. *J. Metals.*, **27**, 9, 15 (1975)
29. TANAKA, T. *Microalloying '75*, Union Carbide Corp., p.350 (1977)
30. COLDREN, A.P. and TITHER, G. *J. Metals*, **30**, 4, 6 (1978)
31. SUGISAWA, S., HAMAMATSU, S., KIKUCHI, K. and KUNISHIGE, K. *Tetsu-to-Hagané*, **68**, 1256 (1982)
32. MANO, J., NISHIDA, M., TANAKA, T., KATO, T., AOYAGI, N. and YAMADA, N. *Tetsu-to-Hagané*, **68**, 1297 (1982)
33. OKITA, T., HOSOYA, Y. and NAKAOKA, K. *Tetsu-to-Hagané*, **68**, 1313 (1982)
34. FURUKAWA, T., TANINO, M., MORIKAWA, H. and ENDO, M. *Tetsu-to-Hagané*, **68**, 1323 (1982)
35. HANAI, S., WATANABE, K. and ESAKA, K. *Tetsu-to-Hagané*, **68**, 1306 (1982)
36. TOKUNAGA, Y., YAMADA, M., MIZUYAMA, Y., KURIYAMA, Y., TASHIRO, M. and MIZUI, M. *Tetsu-to-Hagané*, **68**, S1301 (1982)
37. ITOH, Y. and BESSYO, K. *J. Japan Welding Soc.*, **37**, 983 (1968)
38. SHIGA, C., HATOMURA, T., TABATA, N., SHIGA, A., KAMADA, A. and OHASHI, N. *Kawasaki Steel Technical Report, 10, No. 1*, p.1 (1978)
39. KASAMATSU, Y., TAKASHIMA, S. and HOSOYA, T. *Tetsu-to-Hagané* **65**, 1222 (1979)
40. SUZUKI, H. *Weld. in the World*, **14**, 246 (1976)
41. KANAZAWA, S., NAKAJIMA, A., OKAMOTO, K. and KANAYA, K. *Tetsu-to-Hagané*, **61**, 2589 (1975)
42. FUNAKOSHI, T., TANAKA, T., UEDA, S., ISHIKAWA, M., KOSHIZUKA, N. and KOBAYASHI, K. *Trans. Iron and Steel Inst. Japan*, **17**, 419 (1977)
43. KASAMATSU, Y., TAKASHIMA, S. and HOSOYA, T. *Tetsu-to-Hagané*, **65**, 1232 (1979)
44. OHTANI, H., WATANABE, S., KAWAGUCHI, Y. and YAMAGUCHI, Y. *Tetsu-to-Hagané*, **64**, 2205 (1978)
45. MIYOSHI, E., HASEBE, S., BESSYO, K. and YAMAGUCHI, Y. *IIW Doc. 1X-878-74*, Japan Institute of Welding, p.148 (1974)
46. DOLBY, R.E. *Welding J.*, **58**, 225S (1979)



---

## Prediction and control of microstructural change and mechanical properties in hot-rolling

---

The computer-control of hot-rolling combined with the physical metallurgy of hot-working has opened the way to a more rational controlled-rolling process that is still evolving. If temperature change, microstructural change, the degree of strain accumulated during rolling in the nonrecrystallized austenite ( $\gamma$ ) region, the start of ferrite ( $\alpha$ ) transformation, the amount of strain retained in  $\alpha$  and precipitation kinetics of microalloying elements can be predicted accurately and simultaneously during hot-rolling by computer calculation, we are not only able to control, but to adjust, the hot-rolling process to meet more correctly the requirements of the mechanical properties of steel products. As the above parameters cannot be measured directly during hot-rolling, a certain indirect method which enables us to trace changes in these parameters must be considered. Among various processing variables in hot-rolling, the deformation resistance seems to be the most promising way of revealing changes in the above-mentioned parameters.

Deformation resistance is one of the material characteristics and reflects microstructural change occurring during hot-rolling. Therefore, if deformation resistance is measured correctly during hot-rolling, microstructural change accompanying hot-rolling can be predicted from the change in deformation resistance which, in turn, enables us to predict the mechanical properties of rolled products without performing mechanical tests after rolling.

The major microstructural changes accompanying hot-rolling are as follows:

- (1) Grain refinement due to recrystallization and subsequent grain growth in the high-temperature  $\gamma$  region.
- (2) Strain-induced precipitation of niobium carbonitrides during rolling in the low-temperature  $\gamma$  region and in the two-phase region.
- (3) Strain accumulation in the low-temperature  $\gamma$  region.
- (4)  $\gamma \rightarrow \alpha$  transformation.
- (5) Strain accumulation in the ( $\gamma + \alpha$ ) two-phase region.

The effects of the above-mentioned individual factors on hot-deformation resistance have been studied and basic data on the physical metallurgy of hot-working are combined to correlate deformation resistance with microstructural changes.

## 11.1 A model to predict recrystallized $\gamma$ grain size during hot-rolling

In hot-strip-rolling as well as in plate-rolling, grain refinement takes place mostly through static recrystallization. Sellars and Whiteman<sup>1,2</sup> were the first to show a model for the computation of microstructural changes which occur in the processes from slab reheating to  $\alpha$  transformation. The prediction of microstructural change occurring during hot-deformation, based principally on their model, is described below.

The procedure of calculating  $\gamma$  grain size during hot-rolling consists of six steps as shown in Figure 11.1:

- (1) In order to determine recrystallized  $\gamma$  grain size, it is first necessary to know whether dynamic recrystallization occurs in each rolling pass. The occurrence of dynamic recrystallization is judged from strain, strain rate and the Zener–Hollomon (Z) parameter. If the rolling condition satisfies the occurrence of dynamic recrystallization, dynamically recrystallized grain size is calculated.
- (2) Under the condition where dynamic recrystallization does not occur, statically recrystallized grain size is calculated.
- (3) If recrystallization is not completed during the interpass period, the calculations for recrystallized grains and unrecrystallized grains are performed separately in the following passes. As for unrecrystallized grains, strain retained is calculated and added to the strain imposed in the next pass.
- (4) If recrystallization is complete before the next pass, subsequent change resulting from grain growth in the remainder of the interpass period is calculated.

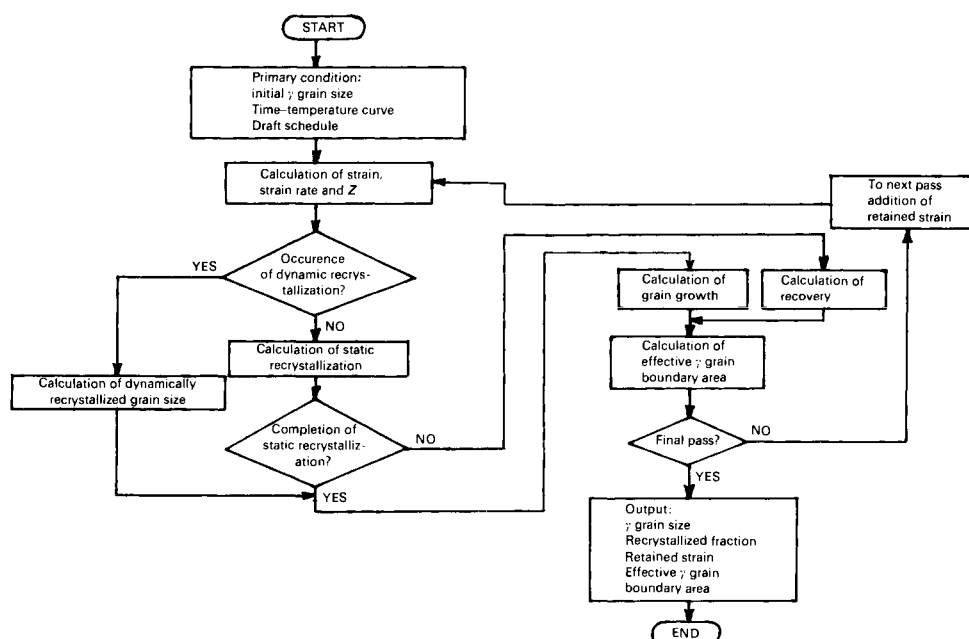


Figure 11.1 Flow chart for the calculation of  $\gamma$  grain size in multipass hot-rolling

- (5) In the mixed structure consisting of recrystallized grains and unrecrystallized grains, the mean grain size is calculated by taking into consideration the recrystallized fraction, where the grain size of unrecrystallized structure is assumed to be the same as that of the recrystallized structure before the previous pass.
- (6) A parameter representing the effective grain boundary area, consisting of grain boundaries and deformation bands, is calculated, which is to express the nucleation sites for  $\alpha$  grains.

Each process is described briefly below.

### 11.1.1 Dynamic recrystallization

As already explained, dynamic recrystallization takes place in the steady-state region beyond the peak strain in the stress-strain curve.<sup>3</sup> The peak strain  $\epsilon_p$  is known to be associated with grain size  $d_0$  and the Zener-Hollomon parameter  $Z$ . Scrutinizing and rearranging available data, Sellars has shown that all the steels follow a similar relationship:<sup>2</sup>

$$\epsilon_p = AZ^m d_0^n \quad (11.1)$$

where  $A$ ,  $m$  and  $n$  are constants.

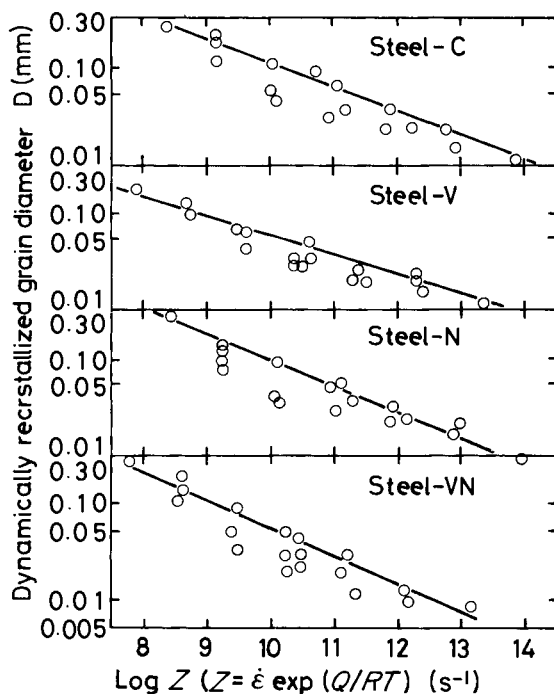


Figure 11.2 Relation between dynamically recrystallized  $\gamma$  grain size and the Zener-Hollomon parameter in carbon, vanadium, niobium and vanadium-niobium steels. (After Horie<sup>4</sup>)

Seeking mean values for constants, Sellars has obtained Equation (11.2) below:<sup>2</sup>

$$\varepsilon_p = 4.9 \times 10^{-4} d_0^{\frac{1}{2}} Z^{0.15} \quad (11.2)$$

The critical strain required for the onset of dynamic recrystallization is much larger for niobium, than for silicon-manganese, steel. In niobium steel, as  $\varepsilon_p$  is different – depending on whether niobium exists as a solute or as a precipitate during hot-rolling – each constant in Equation (11.1) must be distinguished.

As is well known, dynamically recrystallized grain size is solely dependent on  $Z$  value. Figure 11.2 shows dynamically recrystallized grain size as a function of  $\log Z$  in various steels.<sup>4</sup> By using this figure and other available data, we will know the dynamically recrystallized grain size under a specified deformation condition.

### 11.1.2 Static recrystallization

After deformation, softening by static recovery and recrystallization takes place with time at rates which depend on the prior deformation conditions and the holding temperature. The softening curves generally follow the Avrami equation of the form:

$$X_v = 1 - \exp\{-C(t/t_f)^k\} \quad (11.3)$$

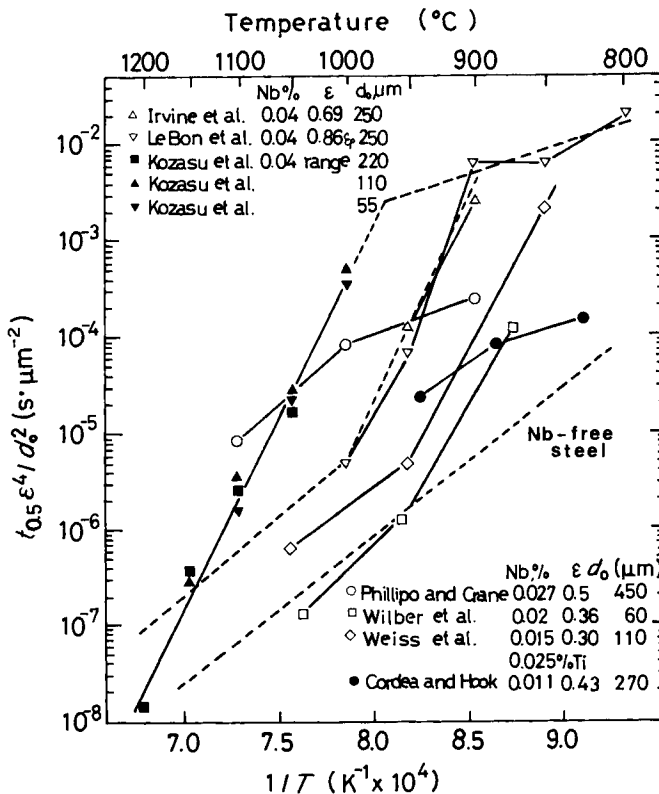


Figure 11.3 Temperature dependence of strain and grain size compensated time to 50% recrystallization or restoration in niobium-treated HSLA steels (grain sizes marked\* are estimated values). (After Sellars<sup>2</sup>)

where  $X_r$  is the fraction recrystallized in time  $t$ ,  $t_f$  is the time for some specified fraction of recrystallization (say 0.5),  $k$  is a constant and  $C = \ln(1-f)$ .

$k$  has been observed to be 2 in steels deformed to strains  $< \varepsilon_c$ , which is a critical strain required for the onset of dynamic recrystallization.<sup>2</sup>

The time to 50% recrystallization for a range of carbon–manganese and low-alloy steels is described in Equations (11.4) and (11.5) below:

$$t_{0.5} = 2.5 \times 10^{-19} d_0^2 \varepsilon^{-4} \exp \frac{300\,000}{RT} \quad (\varepsilon \leq 0.8\varepsilon_p) \quad (11.4)^2$$

$$t_{0.5} = 1.06 \times 10^{-5} Z^{-0.6} \exp \frac{300\,000}{RT} \quad (\varepsilon \geq 0.8\varepsilon_p) \quad (11.5)^2$$

It must be remembered that activation energy for recrystallization of 300 kcal/mol is a mean value obtained from the available data of temperature dependence of time to 50% recrystallization, which differ greatly according to which author is consulted.

For the purpose of establishing a reasonable equation of recrystallization kinetics in niobium steels, time to 50% recrystallization compensated with strain and grain size is plotted vs. the reciprocal of temperature as shown in Figure 11.3.<sup>2</sup> From the figure, Sellars<sup>2</sup> has given the following relationships:

$$t_{0.5} = 2.52 \times 10^{-19} d_0^2 \varepsilon^{-4} \exp \frac{325\,000}{RT} \quad (\varepsilon < \varepsilon_c, T > 1000^\circ \text{C}) \quad (11.6)$$

$$t_{0.5} = 5.94 \times 10^{-38} d_0^2 \varepsilon^{-4} \exp \frac{780\,000}{RT} \quad (\varepsilon < \varepsilon_c, 1000 > T > 890^\circ \text{C}) \quad (11.7)$$

$$t_{0.5} = 9.24 \times 10^{-9} d_0^2 \varepsilon^{-4} \exp \frac{130\,000}{RT} \quad (\varepsilon < \varepsilon_c, T < 890^\circ \text{C}) \quad (11.8)$$

It is important to emphasize that no fundamental meaning is implied by the apparent activation energies below 1000°C and that the initial constants may be altered significantly by different deformation histories altering the kinetics of precipitation.

### 11.1.3 Statically recrystallized grain size

Statically recrystallized grain sizes are given by the following relationships for carbon–manganese and low-alloy steels and for niobium steels respectively:<sup>2</sup>

$$d_{\text{rex}} = D d_0^{0.67} \varepsilon^{-1} \quad (\text{carbon–manganese, } \varepsilon < \varepsilon^*) \quad (11.9)$$

$$d_{\text{rex}} = D' d_0^{0.67} \varepsilon^{-0.67} \quad (\text{niobium, } \varepsilon < \varepsilon^*, T > 950^\circ \text{C}) \quad (11.10)$$

where  $\varepsilon^*$  is a critical strain related to  $\varepsilon_p$ .

All the observations so far are consistent with those forms of relationship but the values of the constants  $D$  and  $D'$  vary considerably from author to author.

As for a recrystallized  $\gamma$  grain size, Ouchi and Okita<sup>5</sup> have given a different formula. They assume that an  $\gamma$  grain size  $d'$  produced by static recrystallization is inversely proportional to one-third of the nucleation frequency of the recrystallized grain per unit volume  $N_v$ .<sup>5</sup>

$$d_\gamma \propto \frac{1}{3N_v} \quad (11.11)$$

$N_v$  is primarily governed by the product of stored energy and the potential nucleation site area for new grains in deformed  $\gamma$ . When the metal is deformed under a uniaxial compression with a strain of  $\varepsilon$  and a stress of  $\sigma_f$ , stored energy is expressed in terms of  $\sigma_f \cdot \varepsilon$ . In the case of rolling,  $\sigma_f$  is replaced by the mill force  $P$  which is, in turn, given by  $K_m \cdot Q$ , where  $K_m$  and  $Q$  are mean hot-deformation resistance and roll pressure function, respectively.  $K_m$  and  $Q$  can be approximated as follows:

$$K_m = A\varepsilon^n \dot{\varepsilon}^m \quad (\text{at a given temperature}) \quad (11.12)$$

$$Q = (\pi + l_d/h_m)/4 \quad (11.13)$$

$$\dot{\varepsilon} = \frac{2\pi N}{60\sqrt{\gamma}} \sqrt{R/h_0} \ln \frac{1}{1-\gamma} \quad (11.14)$$

$$l_d = \sqrt{(h_0 - h_1) \cdot R} \quad (11.15)$$

$$h_m = (h_0 + 2h_1)/3 \quad (11.16)$$

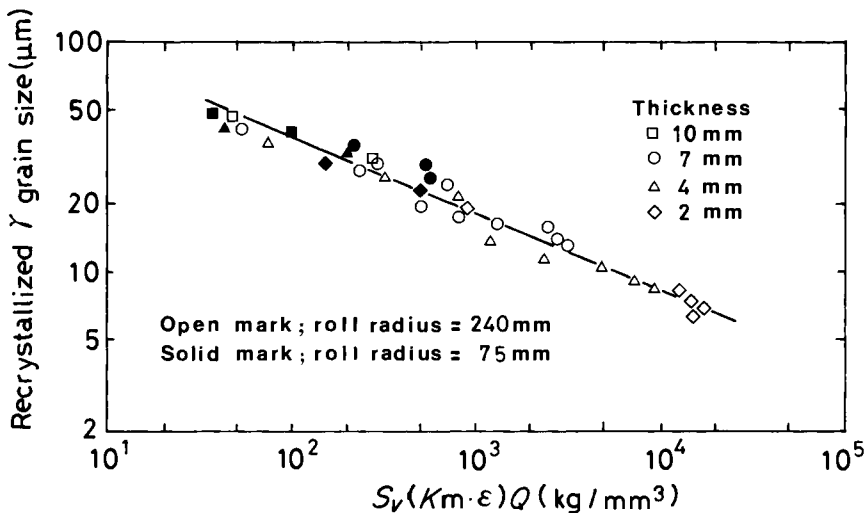


Figure 11.4 Recrystallized  $\gamma$  grain size is plotted vs.  $S_\gamma(K_m \cdot \varepsilon) Q$ , where  $S_\gamma$  is the effective  $\gamma$  grain boundary area,  $K_m$  is mean hot-deformation resistance,  $Q$  is roll pressure function and  $\varepsilon$  is strain. (After Ouchi and Okita<sup>5</sup>)

where  $\dot{\varepsilon}$  is strain rate,  $l_d$  contact arc length,  $R$  roll radius,  $\varepsilon$  pass reduction of rolling, and  $h_0$  and  $h_1$  are entry and delivery plate thicknesses respectively.

With regard to nucleation site area for new grains, the effective interfacial area per unit volume  $S_v$  can be used, which is given by the sum of deformed  $\gamma$  grain boundaries and deformation bands, and expressed in Equation (11.17):<sup>5</sup>

$$S_v = \{1.67(\varepsilon - 0.10) + 1.0\}(2/D_0) + 63(\varepsilon - 0.30) \quad (11.17)$$

where  $D_0$  is the initial grain size.

The first and second terms of the right-hand side in Equation (11.17) represent the interfacial area of the deformed grain boundaries and the deformation band density respectively.

From Equations (11.12) to (11.16), Equation (11.11) is given by:<sup>5</sup>

$$d_\gamma \propto \frac{1}{3\sqrt{S_v(K_m \cdot \varepsilon)Q}} = \frac{C}{3\sqrt{A \cdot S_v \cdot \varepsilon^{n+1} \cdot \dot{\varepsilon}^m \cdot Q}} \quad (11.18)$$

where  $C$  is a constant.

Since mill force  $P (= K_m \cdot Q)$  can be measured during hot-rolling, and  $A$ ,  $n$  and  $m$  can be obtained by laboratory experiment,<sup>5</sup> recrystallized grain size after hot-rolling can be calculated using Equation (11.18). In Figure (11.4)  $\log d_\gamma$  is plotted against  $\log S_v (K_m \cdot \varepsilon) Q$ , where recrystallized grain sizes were obtained by one-pass- and three-pass-rolling experiments, showing the validity of Equation (11.18).

#### 11.1.4 Grain growth

Once recrystallization is complete, further grain growth takes place as a function of time and temperature, represented as:<sup>3</sup>

$$d^{10} = d_{\text{rex}}^{10} + A't \exp - Q_{\text{gg}}/RT \quad (11.19)$$

where  $A'$  is a constant, and  $Q_{\text{gg}}$  is activation energy for grain growth.

Figure 11.5 shows the temperature-dependence of grain growth for carbon-manganese and niobium steels.

The grain-growth kinetics are more generally described by the Miller equation:

$$d_\gamma = Kt^n \quad (11.20)$$

where  $d_\gamma$  is  $\gamma$  grain size,  $t$  the holding time at a given temperature and  $K$  and  $n$  are constants.

Figure 11.6<sup>5</sup> exhibits the change in  $\gamma$  grain size with holding time in silicon-manganese, titanium and niobium steels, which were heated to 1200, 1150 or 1050° C, rolled to 70%

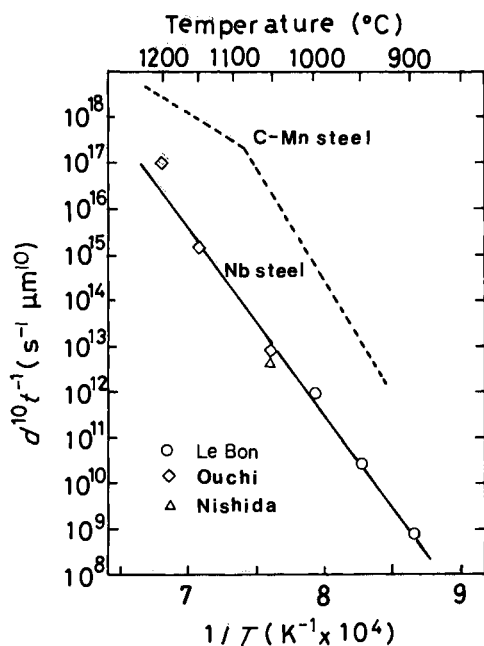


Figure 11.5 Temperature dependence of grain growth after recrystallization in niobium and carbon-manganese steels

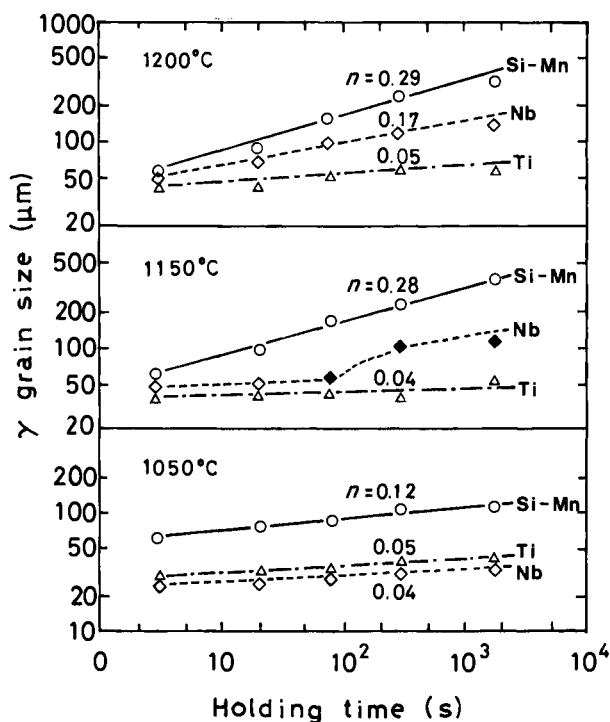


Figure 11.6 Effects of holding time and temperature on  $\gamma$  grain growth in silicon-manganese, niobium and titanium steels which were one-pass-rolled to 70% and subjected to isothermal treatment. (After Ouchi and Okita<sup>9</sup>)



and subjected to various periods of holding. The figure shows that the grain growth kinetics follow the Miller equation and that  $n$  is larger for silicon–manganese steel than niobium and titanium steels. In the case of the holding temperature of 1150°C, the abnormal grain growth takes place in niobium steel. This may be brought about by the loss in the pinning effect of grain boundary migration due to the coarsening of niobium carbonitride precipitates.

### 11.1.5 Static recovery

When deformation is performed at the low-temperature  $\gamma$  region, recovery and recrystallization is not completed in a short time period. In order to measure the fraction of softening, the interrupted deformation technique is used, where a specimen is deformed to a certain strain, unloaded, held for a given time at a specified temperature and again reloaded. From the variation in yield stress, the fraction softened is represented by:

$$X_s = (\sigma_m - \sigma_{II}) / (\sigma_m - \sigma_I) \quad (11.21)$$

where  $\sigma_I$  and  $\sigma_{II}$  are the yield stresses in the first loading and in the second loading respectively, and  $\sigma_m$  is the flow stress at unloading.

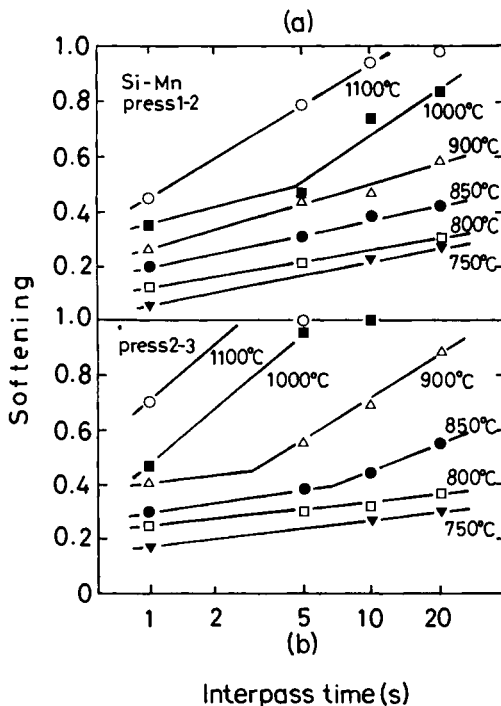


Figure 11.7 Effects of interpass time and deformation temperature on the softening kinetics in silicon–manganese steel which was deformed in three-step compression with strain per step of 0.1: (a) pass 1→2; (b) pass 2→3. (After Ouchi *et al.*<sup>6</sup>)

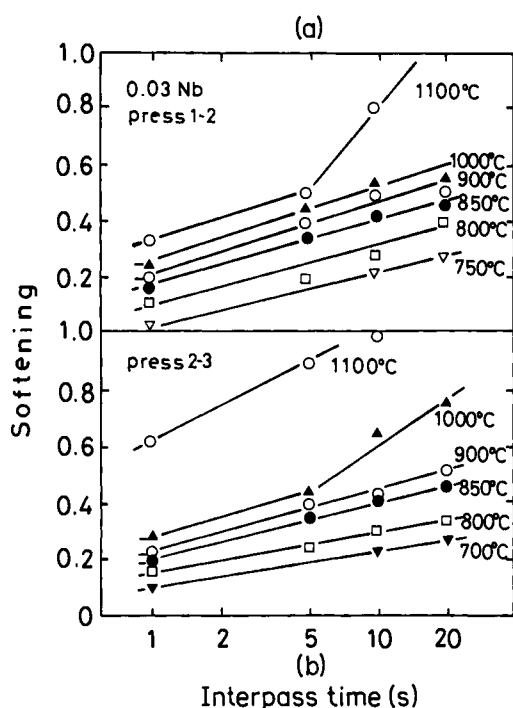


Figure 11.8 Effects of interpass time and deformation temperature on the softening kinetics in 0.03% Nb steel which was deformed in three-step compression with strain per step of 0.1: (a) pass 1→2; (b) pass 2→3. (After Ouchi *et al.*<sup>6</sup>)

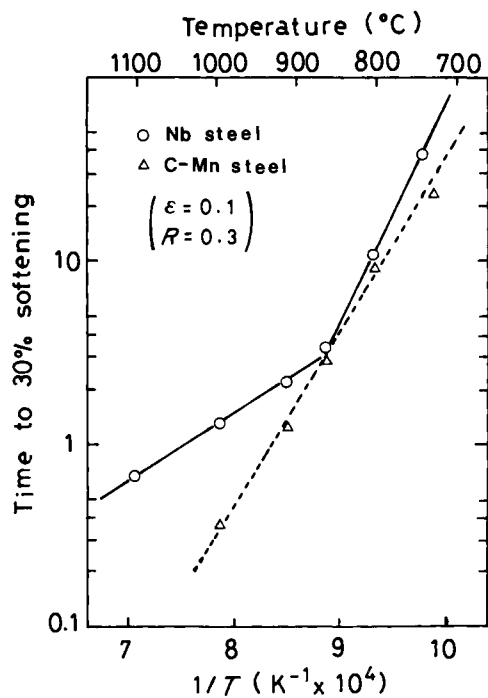


Figure 11.9 Temperature dependence of time for 30% recrystallization or restoration in carbon-manganese and niobium steels which were strained to 0.1 and subjected to isothermal treatment. (After Saeki and Hashimoto<sup>7</sup>)

Figures 11.7 and 11.8 show fraction-softened plotted vs. holding times in silicon–manganese and niobium steels, respectively.<sup>6</sup> In the figures, the beginnings of the steep slopes correspond to the onset of recrystallization. The time to 30% softening is plotted as a function of temperature in Figure 11.9.<sup>7</sup> From Figures 11.7–11.9, softened fraction is represented by:

$$R = \frac{1}{E} \left( \log t = \frac{Q_{\text{rex}}}{2.3 R_g T} - F \right) \quad (11.22)$$

where  $E$  and  $F$  are constants, and  $R_g$  the gas constant.

Strain retained after deformation is given by:

$$\Delta \varepsilon = \varepsilon(1 - R) \quad (11.23)$$

### 11.1.6 Effective $\gamma$ grain boundary area for the formation of $\alpha$ grains

$\gamma \rightarrow \alpha$  transformation behaviour differs greatly in the temperature range between recrystallized  $\gamma$  and deformed  $\gamma$ .  $\alpha$  formation occurs exclusively at  $\gamma$  grain boundaries in recrystallized  $\gamma$ , while it occurs at deformation bands as well as  $\gamma$  grain boundaries in deformed  $\gamma$ . The effects of deformed  $\gamma$  on the site area for  $\alpha$  grains are expressed in terms of effective  $\gamma$  grain boundary area, i.e. deformed  $\gamma$  grain boundary area plus deformation bands, which is expressed by Equation (11.17).

## 11.2 Prediction of $\gamma$ grain size in multipass rolling

The relationships deduced between microstructure and deformation variables can be applied to industrial hot-rolling processes involving multiple hot-deformation passes if the conditions of strain, strain rate, temperature and time are sufficiently well-defined. From these hot-deformation conditions and a knowledge of the temperature and the grain size produced by reheating, the time for recrystallization after the first pass may be calculated from Equations (11.4)–(11.8). Then the grain size produced by recrystallization and the subsequent change resulting from grain growth in the remainder of the interpass period is found from Equations (11.9), (11.10) and (11.19). This then gives the starting structure for calculating the structure produced after the second pass, etc. This procedure will be carried out for the complete rolling schedule.

The structural changes predicted by this computing procedure using the above equations are compared with grain sizes observed in carbon–manganese steel by Sekine and Maruyama<sup>8</sup> during an experimental plate-rolling schedule in Figure 11.10.<sup>2</sup> Saeki and Hashimoto<sup>7</sup> have performed rolling experiments to simulate rougher rolling of hot-strip and compared grain sizes with predicted values, shown in Figures 11.11 and 11.12 for carbon–manganese and niobium steels, respectively. There is very good agreement in grain size between observation and prediction in carbon–manganese steel. There exists, however, some slight disagreement between observation and prediction in niobium steel.

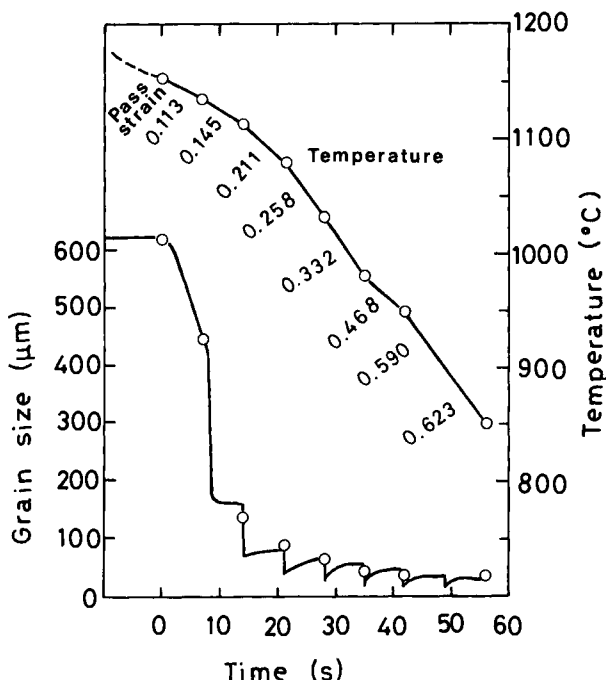


Figure 11.10 Comparison of predicted structural changes with those observed by Sekine and Maruyama<sup>8</sup> during experimental plate-rolling schedule on vacuum-melted carbon-manganese steel (observations shown as points). (After Sellars<sup>2</sup>)

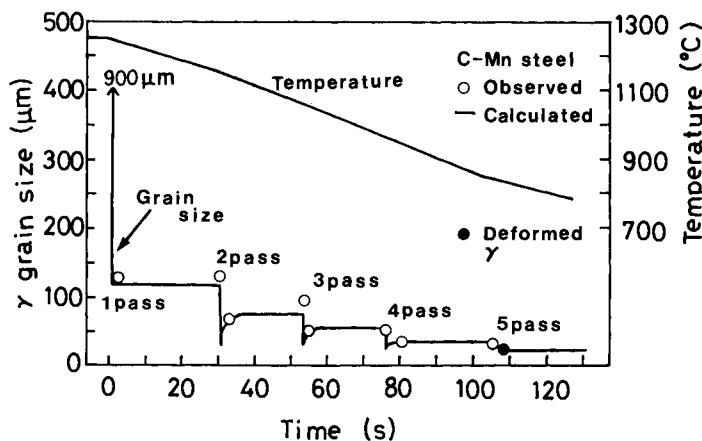


Figure 11.11 Comparison of predicted  $\gamma$  grain sizes with those observed in carbon-manganese steel which was five-pass-rolled with a constant reduction per pass of 30%, to simulate rougher rolling of hot-strip. (After Saeki and Hashimoto<sup>7</sup>)

So far, it has been shown that the expected evolution of microstructure during and after hot-rolling can be computed by combining basic laboratory observations on static recrystallization and subsequent grain growth after hot-deformation with data on temperature, pass reduction, speed and time history of rolling schedules. Since microstructural change is associated with hot-deformation resistance, the evolution of

microstructure during hot-rolling can be predicted from the change in deformation resistance. Saito *et al.*<sup>9</sup> have tried to establish a method which can enable us to predict not only microstructural change but other phenomena occurring simultaneously, and thereby to predict mechanical properties of rolled products by associating deformation resistance with the knowledge of the physical metallurgy of hot-working.

Figure 11.13 shows the change in the mean deformation resistance  $k_m$  strain and temperature with rolling pass in silicon-manganese and niobium steels, where a silicon-manganese and a niobium slab were welded into a composite slab in the longitudinal (L) direction, making possible a correct comparison in deformation resistance between the two steels. In high-temperature rolling after reheating to 1150°C,  $K_m$  values are relatively small reflecting complete recrystallization during the interpass period. The difference in  $K_m$  between the two steels is small and  $K_m$  is about 4% higher in niobium than in silicon-manganese steel, because of solid solution hardening of niobium. Strain-induced precipitation of niobium carbonitrides does not occur in this temperature range. In the high-temperature  $\gamma$  region, it is necessary only to consider the grain refinement by recrystallization as microstructural change.

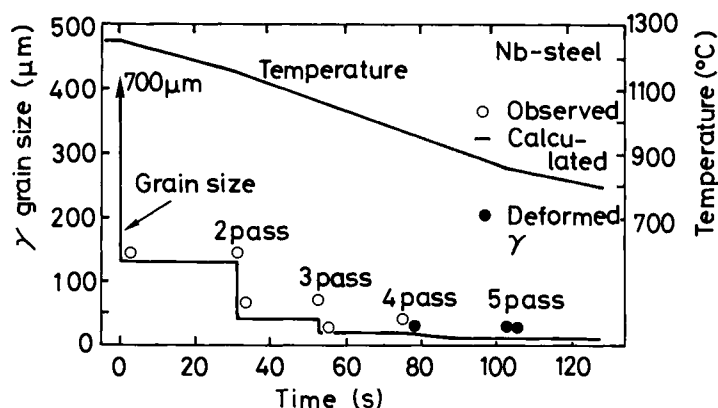


Figure 11.12 Comparison of predicted  $\gamma$  grain sizes with those observed in niobium steel which was five-pass-rolled with a constant reduction per pass of 30%, to simulate rougher rolling of hot-strip. (After Saeki and Hashimoto<sup>7</sup>)

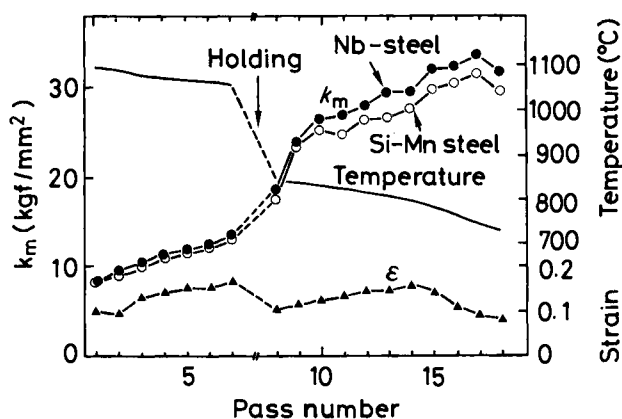


Figure 11.13 Variation in mean deformation resistance, temperature and strain with rolling pass for composite slab which consists of silicon-manganese and niobium steels. (After Saito *et al.*<sup>9</sup>)

In contrast to this, the difference in  $k_m$  between the two steels increases with increasing  $k_m$  value in the low-temperature  $\gamma$  region, which is attributable to insufficient recovery during the interpass period and also to the effect of strain-induced precipitation of niobium carbonitrides in niobium steel. The  $k_m$  value shows a decrease at the last pass in both steels, which is due to the deformation in the  $(\gamma + \alpha)$  two-phase region.

The change in  $k_m$  with a rolling pass in the high-temperature range of Figure 11.13 is correlated with the change in the recrystallized  $\gamma$  grain size, shown in Figure 11.14.<sup>9</sup> (where the result heated to 1250° C is also given). Here, calculation of  $\gamma$  grain size was carried out by using Equation (11.9). In Figure 11.14, the normalized value  $k_m/k_m^c$  is used instead of  $k_m$ . A parameter  $k_m^c$  is a calculated value of the deformation resistance of a certain reference grain size; here the grain size of 150  $\mu\text{m}$  is adopted. This is the deformation resistance obtained under the same deformation condition with hot-rolling by using a mathematical model based on a hot-deformation experiment.<sup>10</sup> As shown in Figure 11.14,  $k_m/k_m^c$  increases with the progress of grain refinement due to recrystallization. Though there is a large difference in  $k_m/k_m^c$  between steel heated to 1150 and that to 1250° C, reflecting a large difference in the initial grain size, the difference becomes small with each rolling pass and finally becomes zero at the sixth pass.

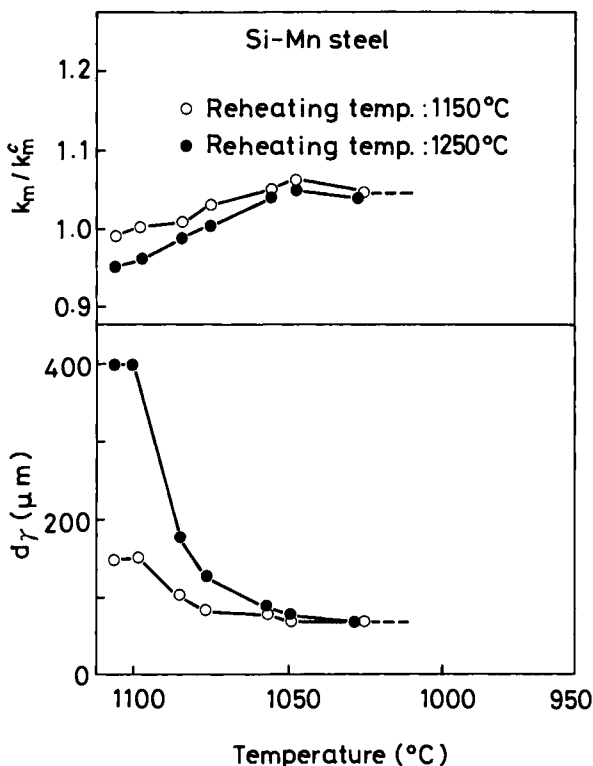


Figure 11.14 Normalized mean deformation resistance  $k_m/k_m^c$  and predicted  $\gamma$  grain size are plotted against temperature in silicon-manganese steel which was heated to 1150 or 1250° C and hot-rolled to plate. (After Saito *et al.*<sup>9</sup>)

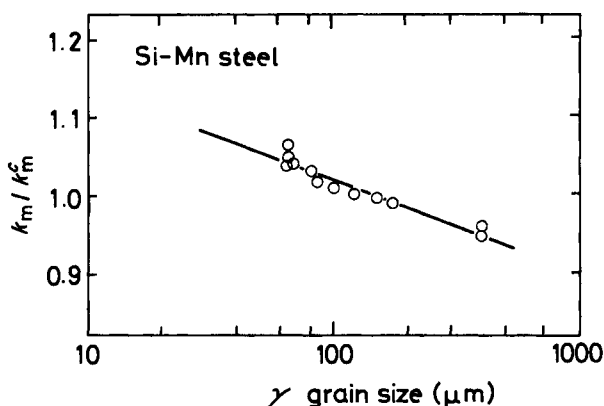


Figure 11.15 Relation between normalized deformation resistance  $k_m/k_m^c$  and  $\gamma$  grain size in silicon-manganese steel. (After Saito *et al.*<sup>9</sup>)

Figure 11.15<sup>9</sup> shows a relationship between recrystallized  $\gamma$  grain size and  $k_m/k_m^c$  in silicon-manganese steel. There is a good relationship, which has also been observed in the hot-deformation experiment,<sup>11</sup> between the two parameters. Therefore,  $\gamma$  grain size can be estimated from deformation resistance provided rolling load and temperature can be measured accurately and, accordingly, deformation resistance predicted with precision.

### 11.3 Strain-induced precipitation of niobium carbonitrides

In the low-temperature  $\gamma$  region, very fine niobium carbonitrides are produced due to strain-induced precipitation in niobium steel. Those precipitates play two very important roles in controlled-rolling, both of which increase deformation resistance: (1) the retardation of recrystallization; and (2) precipitation strengthening. Therefore, it is very important to know the precipitation kinetics of niobium carbonitride and to correlate it with precipitation hardening and thereby deformation resistance.

Though many experimental results have been reported on the precipitation of carbonitrides of niobium accompanying hot-deformation, a quantitative relation between hot-rolling conditions and precipitation hardening has never been established. As precipitation is influenced by temperature, pass reduction, speed, previous strain history and alloy contents, it is quite difficult to describe quantitatively the effect of rolling variables on precipitation kinetics and precipitation hardening. It is also difficult to distinguish precipitation hardening from strain hardening in the temperature range where recrystallization is retarded and the strain introduced by a rolling pass is retained.

### 11.4 Strain accumulation in the low-temperature $\gamma$ region

In the low-temperature  $\gamma$  region, strain is retained and thereby increases deformation resistance in the following rolling passes, as recovery and recrystallization proceeds insufficiently during the interpass period. One approach to the estimation of retained

insufficiently during the interpass period. One approach to the estimation of retained strain has been proposed by Saito *et al.*,<sup>9</sup> as will be described below. The strain retained during the interpass period can be calculated as a function of the observed mean deformation resistance and strain of a given pass by Equation (11.24) below:

$$\Delta\varepsilon = \{(k_m^{(\text{obs})}/k_m^{(0)})^{1/n} - 1\} \cdot \varepsilon \quad (11.24)^9$$

where  $k_m^{(\text{obs})}$  is observed mean deformation resistance,  $k_m^{(0)}$  is a calculated value of deformation resistance for which the effect of retained strain is neglected and  $n$  is the work-hardening coefficient.

Thus, retained strains  $\Delta\varepsilon_{n-1}$  and  $\Delta\varepsilon_n$  for the  $(n-1)$ th pass and the  $n$ th pass respectively are calculated, which enables us to obtain the fraction of retained strain  $\lambda$  during the  $(m-1)$ th pass and the  $n$ th pass by the following relation (see Figure 11.18):

$$\lambda_{n-1} = \Delta\varepsilon_n / (\varepsilon_{n-1} + \Delta\varepsilon_{n-1}) \quad (11.25)$$

Furthermore,  $\Delta\varepsilon_n$  can be represented as a function of strain and the fraction of retained strain in each pass by:

$$\Delta\varepsilon_n = \lambda_{n-1}(\varepsilon_{n-1} + \Delta\varepsilon_{n-1}) = \left( \sum_{i=1}^{n-1} \prod_{j=i}^{n-1} \lambda_j \right) \varepsilon_i \quad (11.26)$$

Equations (11.24)–(11.26) enable us to predict deformation resistance in the low-temperature  $\gamma$  region.

The effect of retained strain will be shown by using Equations (11.24)–(11.26) in the following. Two sets of composite slabs, one consisting of silicon–manganese steel and the other of niobium steel were heated to 1150° C and hot-rolled in the same condition at above 800° C; subsequently, a different rolling schedule was imposed below this temperature. Figure 11.16<sup>9</sup> shows changes in strain-accumulated  $\Delta\varepsilon$  and effective strain  $\varepsilon + \Delta\varepsilon$  with temperature. In niobium steel,  $\Delta\varepsilon$  increases abruptly with decreasing rolling temperature, whereas the increase in  $\Delta\varepsilon$  is moderate in silicon–manganese steel. When a comparison is made between the two kinds of rolling condition, the behaviour of retained strain is almost the same between the two above 800° C, since the rolling schedule is the same. However, the  $\Delta\varepsilon$  value varies greatly, depending on whether rolling is interrupted for holding (experiment 1) or rolling is continued without interruption (experiment 2). In the case of experiment 1,  $\Delta\varepsilon$  decreases markedly during interruption because of the progress of recovery. At temperatures below 740° C,  $\Delta\varepsilon$  value tends to decrease with decreasing temperature, which is attributable to the deformation in the  $(\gamma + \alpha)$  two-phase region.

As will be described below, the strain accumulated just before transformation  $\Delta\varepsilon_r$  has a great effect on  $\alpha$  transformation behaviour and resultant  $\alpha$  grain size. In order to estimate  $\Delta\varepsilon_r$ , it is first of all necessary to know the  $\gamma \rightarrow \alpha$  transformation temperature  $A_{r3}$ . Several methods have been proposed to estimate  $A_{r3}$  (see Section 4.3, pages 93–99). One of them is a method utilizing the Fourier equation of heat conduction, which is indirect but the most practical and useful. At the onset of transformation, such thermal constants as specific heat and thermal conductivity change discontinuously and the latent heat is generated. If the changes in thermal constants are ignored in the



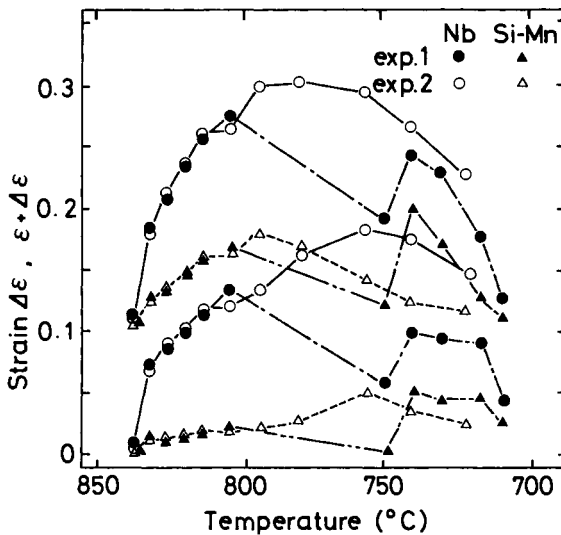


Figure 11.16 Variation in retained strain  $\Delta\epsilon$  and effective strain  $\epsilon + \Delta\epsilon$  with temperature in silicon-manganese and niobium steels, where experiments 1 and 2 represent rolling schedule with interruption prior to transformation and continuous rolling schedule respectively. (After Saito *et al.*<sup>9</sup>)

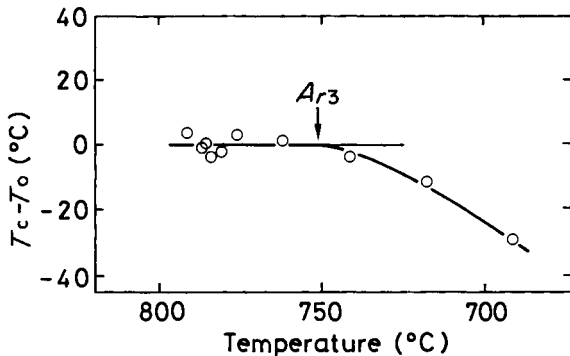


Figure 11.17  $\alpha$ -starting temperature is estimated from disagreement in temperature between observation and calculation. (After Saito *et al.*<sup>9</sup>)

temperature calculation, the difference in temperature between calculation and observation increases monotonously with decreasing temperature below a certain critical temperature, as shown in Figure 11.17.<sup>9</sup> The temperature at which the curve deviates from 0 is  $A_{r3}$ .

Figure 11.18<sup>9</sup> shows schematically how to estimate the strain accumulated prior to the start of transformation  $\Delta\epsilon_t$ . It is assumed that transformation occurs during the interpass period between the  $(n-1)$ th rolling pass and the  $n$ th pass. The recovery of the strain after the  $(n-1)$ th reduction can be described as a function of temperature  $T$ , time  $t$  after the  $(n-1)$ th pass and prestrain  $\epsilon_p$  ( $=\epsilon_{n-1} + \Delta\epsilon_{n-1}$ ) by the following equation:

$$\Delta\epsilon(T, t, \epsilon_p) = \frac{C_2 \cdot \epsilon_p}{\{(C_1 \epsilon_p + C_2) \exp C_2 t \cdot \exp (-Q/RT) - C_1 \epsilon_p\}} \quad (11.27)^{9,12}$$

where  $C_1$  and  $C_2$  are constants and  $Q$  is activation energy of recovery.

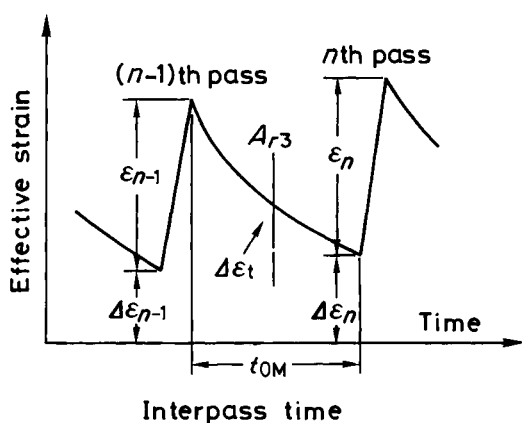


Figure 11.18 Schematic illustration for the estimation of strain retained prior to transformation. (After Saito *et al.*<sup>9</sup>)

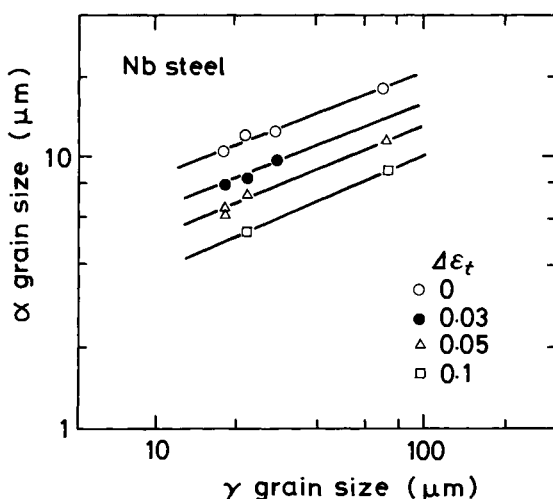


Figure 11.19 Effects of recrystallized  $\gamma$  grain size and strain retained prior to transformation  $\Delta\epsilon_t$  on  $\alpha$  grain size in niobium steel cooled at  $0.2^\circ \text{C/s}$ . (After Saito *et al.*<sup>9</sup>)

As  $T$  and  $\epsilon_p$  are known and  $A_{r3}$  can be predicted, the time to the start of transformation can be determined and  $\Delta\epsilon_t$  can be calculated by using Equation (11.27). The progress of recovery is also predicted by using Equation (11.22).

Since we can predict the strain retained just before the  $\alpha$  transformation  $\Delta\epsilon_t$ , we can also predict the effect of retained strain on transformed  $\alpha$  grain size. Figure 11.19<sup>9</sup> illustrates the effects of retained strain  $\Delta\epsilon_t$  as well as  $\gamma$  grain size on  $\alpha$  grain size, where cooling rate was  $0.2^\circ \text{C/s}$ . At a given  $\gamma$  grain size,  $\alpha$  grain size decreases with increasing  $\Delta\epsilon_t$ . Cooling rate during transformation also plays an important role in governing  $\alpha$  grain size. Figure 11.20<sup>9</sup> shows the influence of cooling rate on  $\alpha$  grain size for the case of  $\gamma$  grain sizes 22 and  $53 \mu\text{m}$ , where  $\alpha$  is transformed from completely recrystallized, strain-free  $\gamma$ . When  $\gamma$  grain size is the same,  $\alpha$  grain size becomes approximately two-thirds of previous size when cooling rate is increased tenfold.

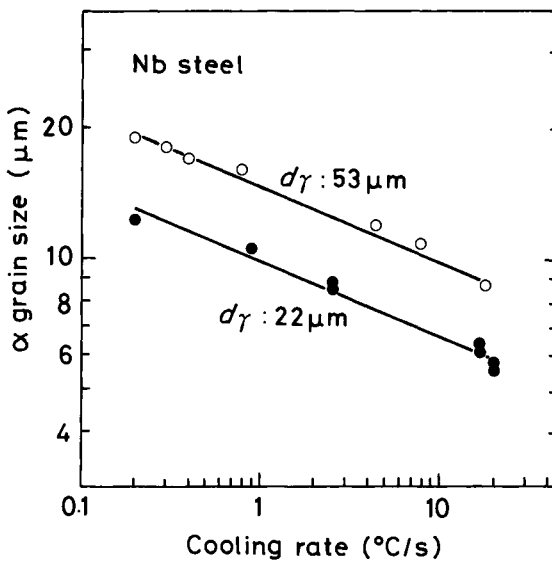


Figure 11.20 Effect of cooling rate on  $\alpha$  grain size in niobium steel transformed from recrystallized, strain-free  $\gamma$ . (After Saito *et al.*<sup>9</sup>)

Using the experimental data shown in Figures 11.19 and 11.20, the effects of recrystallized  $\gamma$  grain size  $d_\gamma$ , cooling rate  $C_R$ , and strain retained just before transformation  $\Delta\epsilon_t$  on  $\alpha$  grain size  $d_\alpha$  is given by the regression Equation (11.28):<sup>9</sup>

$$\ln d_\alpha = 0.92 + 0.44 \ln d_\gamma - 0.17 \ln C_R - 0.88 \tanh(10 \Delta\epsilon_t) \quad (11.28)$$

As for a relationship between  $\gamma$  grain size and resultant  $\alpha$  grain size in carbon-manganese steel with the initial  $\gamma$  grain sizes 20–1000  $\mu\text{m}$  and cooling rates 3.6–120° C/mm, Sellars<sup>2</sup> has given the following equation:

$$d_\alpha(\mu\text{m}) = 11.7 + 0.14d_\gamma + 37.7C_R^{-\frac{1}{2}} \quad (11.29)$$

## 11.5 Deformation in the $(\gamma + \alpha)$ two-phase region

The purpose of hot-deformation in the  $(\gamma + \alpha)$  two-phase region is to increase strength by the strengthening  $\alpha$  grains. This is accomplished by the deformation of transformed  $\alpha$  grains and the formation of substructure within  $\alpha$  grains, by means of the optimum fraction of  $\alpha$  transformed and the optimum amount of deformation in the two-phase region to attain the good combination of strength and toughness. For the quantitative estimation of the effect of rolling in the two-phase region, it is very important to predict the fraction of  $\alpha$  transformation in each pass and the amount of strain retained in  $\alpha$ .

The fraction of transformed  $\alpha$   $R$  depends on chemical composition, temperature, rolling schedule, cooling rate, etc. However, since it is difficult to express  $R$  by a simple equation,  $R$  is estimated using deformation resistance by Saito *et al.*,<sup>9</sup> which will be briefly described below. To investigate a relationship between the fraction transformed and deformation resistance in the two-phase region, an experiment was performed by

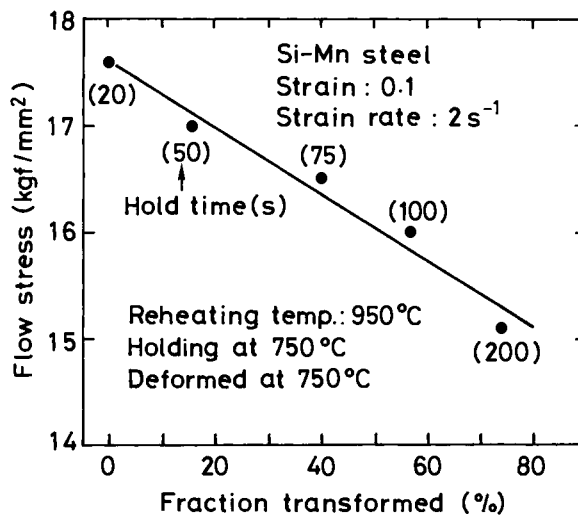


Figure 11.21 Flow stress of  $(\gamma + \alpha)$  two-phase structure is plotted vs.  $\alpha$  fraction in silicon-manganese steel strained to 0.1 in the two-phase region. Digits in parentheses exhibit holding time in the two-phase region. (After Saito *et al.*<sup>9</sup>)

Saito *et al.*<sup>13</sup> while using a hot-deformation simulator. Silicon-manganese steel was heated to 950°C, then cooled to 750°C and held at this temperature. The progress of transformation during holding was measured from the change in thermal expansion, and flow stress was measured by deformation. The result is shown in Figure 11.21,<sup>9</sup> where flow stress decreases in a linear manner with the increasing fraction transformed. This indicates that deformation resistance in the  $(\gamma + \alpha)$  two-phase region obeys the mixed law given by Equation (11.30):

$$k_m^{(\gamma + \alpha)} = (1 - R)k_m^{(\gamma)} + Rk_m^{(\alpha)} \quad (11.30)$$

where  $k_m^{(\gamma + \alpha)}$ ,  $k_m^{(\gamma)}$  and  $k_m^{(\alpha)}$  represent deformation resistances of the  $(\gamma + \alpha)$  two-phase region, and  $\gamma$  and  $\alpha$  in strain-free conditions, respectively.

During deformation in the two-phase region, not only does recovery take place in both  $\gamma$  and  $\alpha$  grains, but also strain release occurs due to transformation. Therefore, a term expressing strain release associated with  $\alpha$  transformation must be added to the formula describing the recovery process (see Equation (11.27)), and recovery kinetics in the two-phase region can be estimated by the modified formula.

Figure 11.22<sup>9</sup> is a flowchart for estimating the fraction transformed using deformation resistance. First of all, deformation resistance of the two-phase region is expressed by the mixed law of deformation resistances  $k_m^{(\gamma)}$  and  $k_m^{(\alpha)}$  respectively. Then the strain retained in the two-phase region  $\Delta\epsilon^{(\text{obs})}$  is obtained from an observed mean deformation resistance  $k_m^{(\text{obs})}$  and a calculated value of  $k_m^{(\gamma + \alpha)}$  in strain-free condition, as described in Equation (11.24). Since the change in the fraction transformed during the interpass period  $\Delta R$  is described as a function of retained strain determined from the observed value  $\Delta\epsilon^{(\text{obs})}$  and retained strain ignoring transformation  $\Delta\epsilon^{(\gamma)}$ , it is possible to estimate  $R$  just before the pass. Starting with  $R = 0$ ,  $R$  in each pass is determined by repeating the above-mentioned procedure until rolling is completed.

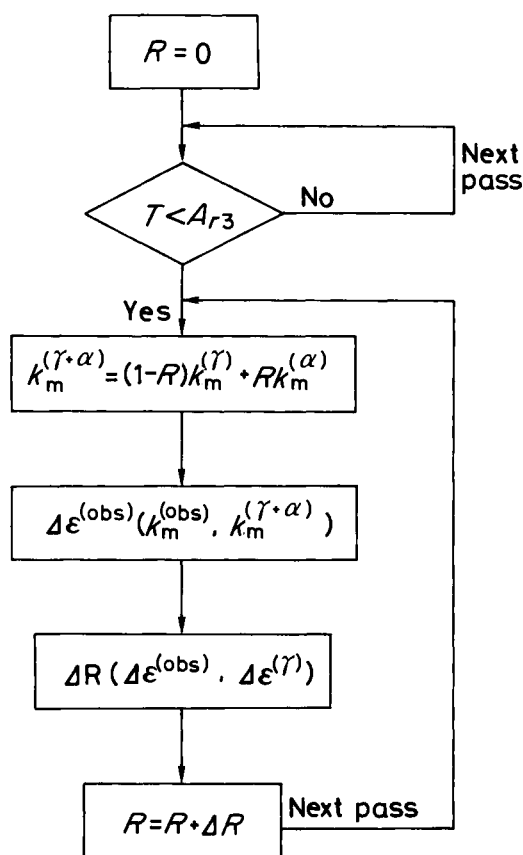


Figure 11.22 Flowchart for the estimation of fraction transformed in the  $(\gamma + \alpha)$  two-phase region. (After Saito *et al.*<sup>9</sup>)

One example of estimating deformation resistance, fraction transformed and retained strain will be shown. Silicon-manganese steel was heated to 1150°C, and rolled in the high-temperature recrystallization region, followed by rolling in the nonrecrystallized  $\gamma$  region and subsequently in the two-phase region. Figure 11.23<sup>9</sup> shows deformation resistance, strain, retained strain and the fraction of transformation plotted against temperature. In the nonrecrystallized  $\gamma$  region, deformation resistance increases with decreasing temperature. In the temperature region below  $A_{r3}$ , increase in deformation resistance becomes very gradual and deformation resistance tends to decrease with further decreases in temperature. This is attributed to the combined effects of increase in the fraction of  $\alpha$  with lower deformation resistance and strain release associated with  $\alpha$  transformation.

Thus, it is possible to predict the  $\alpha$  fraction transformed and the strain retained in  $\alpha$  during rolling in the two-phase region; the effect of rolling in the two-phase region can be expressed by a formula representing the  $\alpha$ -strengthening parameter, which will be described in Section 11.6.

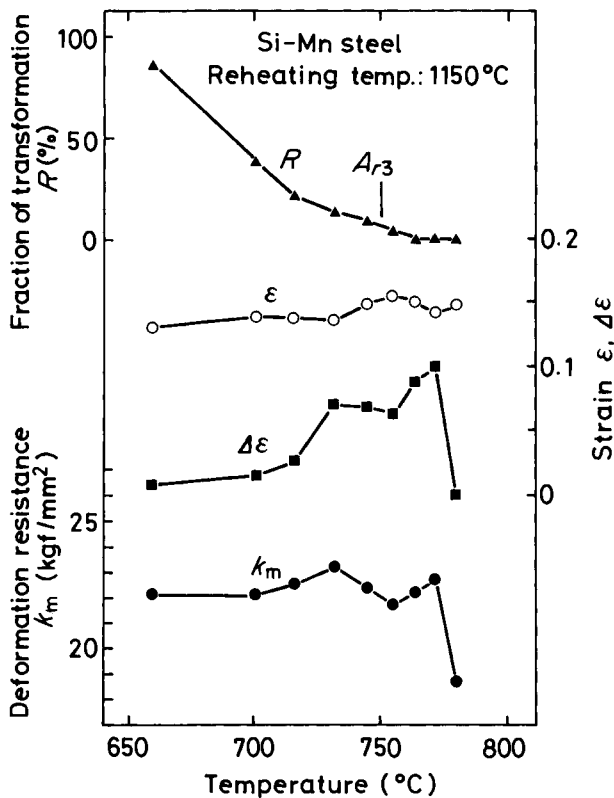


Figure 11.23 Fraction of transformation, strain and deformation resistance are plotted vs. temperature in silicon-manganese steel heated to 1150°C and rolled in the high-temperature region, in the low-temperature region and subsequently in the ( $\gamma + \alpha$ ) two-phase region. (After Saito *et al.*<sup>9</sup>)

## 11.6 Relation between microstructure and strength and toughness

In Section 11.5 it was shown that microstructural changes accompanying hot-rolling can be described by a simple mathematical model and that deformation resistance is closely related to changes in microstructure factors. This implies that it is possible to predict microstructural changes during rolling and to control mechanical properties by measuring deformation resistance in each pass.

As is well known, the yield strength of a polycrystalline solid increases in a linear manner with  $d^{-\frac{1}{2}}$ , and ductile to brittle transition temperature decreases in proportion to  $d^{-\frac{1}{2}}$ . Thus,  $\alpha$ -grain refinement increases both strength and toughness.  $\alpha$  grain size  $d_\alpha$  can be expressed by Equation (11.28) as a function of recrystallized  $\gamma$  grain size  $d_\gamma$  strain-retained just before  $\alpha$  transformation  $\Delta\epsilon_t$  and cooling rate  $C_R$ . When the cooling rate is held constant,  $d_\alpha^{-\frac{1}{2}}$  is proportional to the grain-refinement parameter, which is given by:

$$P_{GR} = d_\gamma^{-0.22} \exp 0.44 \tan h (10 \Delta\epsilon_t) \quad (11.31)$$

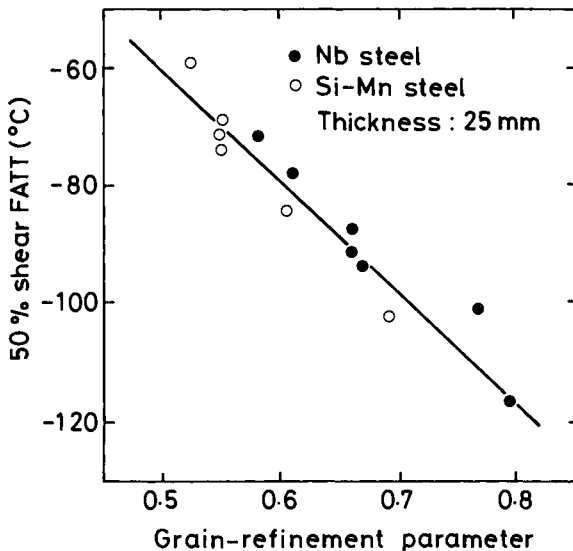


Figure 11.24 Effect of the grain-refinement parameter  $P_{GR}$  on 50% shear FATT in controlled-rolled silicon-manganese and niobium steels. (After Saito *et al.*<sup>9</sup>)

Figure 11.24<sup>9</sup> exhibits a relation between transition temperature and the toughness parameter  $P_{GR}$  of 25-mm thick silicon-manganese and niobium steel plates, which were produced by varying the reheating temperature and the deformation temperature in the nonrecrystallized  $\gamma$  region, thereby varying  $d_\gamma$  and  $\Delta\epsilon_t$ . Figure 11.24 shows that the improvement in transition temperature by controlled-rolling can be described by the toughness parameter  $P_{GR}$ , irrespective of the kind of steel. We have not yet established such a parameter as  $P_{GR}$  which can describe the strength of controlled-rolled material; this is because the strength of controlled-rolled steel is governed by not only  $\alpha$  grain size but precipitation hardening and strain hardening.

The effect on strength of rolling in the two-phase region will be considered. The effect is represented by the amount of strain introduced in the  $\alpha$  matrix. The amount of strain introduced in  $\alpha$  is expressed by a  $\alpha$ -strengthening parameter  $P_F$ , described by the sum of the products of the increment in the fraction of transformed  $\Delta R$  and strain at each pass, as given by Equation (11.32):<sup>9</sup>

$$P_F = \sum_{i=1}^N \epsilon_i \cdot \Delta R_i \prod_{j=i}^N \lambda_j \quad (11.32)$$

where  $N$  is the total pass number.

The fraction of retained strain  $\lambda_j$  between the  $(j-1)$ th pass and  $j$ th pass is introduced in Equation (11.32) in consideration of the effect of recovery in  $\alpha$ .

Figure 11.25<sup>9</sup> exhibits a relationship between the  $\alpha$ -strengthening factor  $P_F$  and tensile strength of niobium steel with grain sizes of 5.3–5.7  $\mu\text{m}$ , where  $P_F$  was varied by changing the amount of deformation in the two-phase region and rolling temperature. Tensile strength increases in a linear manner with  $P_F$ , suggesting that tensile strength can be controlled by controlling  $P_F$  value, when  $\alpha$  grain size is held constant.

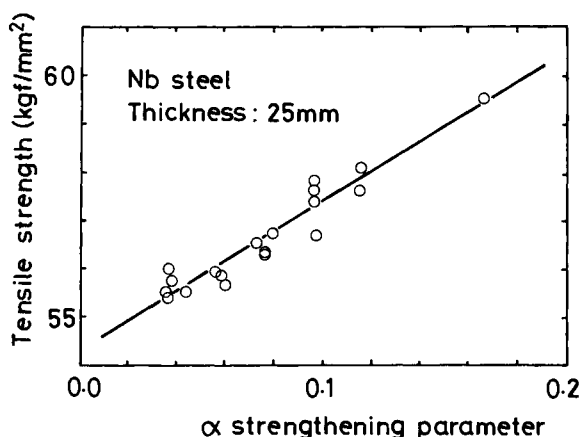


Figure 11.25 Effect of the  $\alpha$  strengthening parameter  $P_F$  on tensile strength of niobium steel rolled in the  $(\gamma + \alpha)$  two-phase region. (After Saito *et al.*<sup>9</sup>)

As shown in Figures 11.24 and 11.25, the  $\alpha$  grain refinement parameter  $P_{GR}$  and the  $\alpha$ -strengthening parameter  $P_F$  are closely related to the strength and toughness of hot-rolled steel.

The evolution of microstructure and prediction of microstructural change in hot-rolling have been described, and results of experiments, and equations, are presented. It must be remembered however, that the results of experiments and the equations derived therefrom have sometimes not been proven, and that many may be only tentative because of insufficient and inconsistent data. The author has tried to describe some experiments which would show the way to the development of a new technology of hot-rolling. The prediction of microstructural evolution and on-line control of microstructure and the mechanical properties of hot-rolled products are the unavoidable trend of hot-rolling in the future. In order to establish the new technology of the on-line prediction and control, however, more comprehensive study of the physical metallurgy of hot-working is required and accurate and consistent data must be accumulated.

## References

1. SELLARS, C.M. and WHITEMAN, J.A. *Metal Sci.*, (March–April) 187 (1979)
2. SELLARS, C.M. *Hot-working and forming processes*, The Metals Society, p.3 (1980)
3. MCQUEEN, H.J. *J. Metals*, (April) 31 (1968)
4. HORIE, S. PhD thesis, Tokyo Institute of Technology (1979)
5. OUCHI, C. and OKITA, T. to be published in *Trans Iron and Steel Inst. Japan*
6. OUCHI, C., OKITA, T., ICHIHARA, T. and UENO, Y. *Trans Iron and Steel Inst. Japan*, **20**, 833 (1980)
7. SAEKI, M. and HASHIMOTO, O. (unpublished)
8. SEKINE, H. and MARUYAMA, T. *Microstructure and design of alloys*, Vol. I, Institute of Metals/Iron Steel Institute, p.85, (1974)
9. SAITO, Y., KIMURA, M., TANAKA, M., SEKINE, T., TSUBOTA, K. and TANAKA, T. *Kawasaki Steel Technical Report*, No. 9, (March) p.12 (1984)
10. SAITO, Y., KOSHIZUKA, N., SHIGA, C., SEKINE, T., YOSHIZATO, T. and ENAMI, T. *Rolling*, Iron and Steel Institute of Japan, p.1063 (1980)
11. SAITO, Y., ENAMI, T. and TANAKA, T. *Physical metallurgy of metal working at elevated temperatures*, Iron and Steel Institute of Japan, p.198 (1982)
12. SAITO, Y., ENAMI, T., TANAKA, T. and INOUE, M. *Tetsu-to-Hagané*, **67**, A45 (1981)
13. SAITO, Y., TANAKA, M., SEKINE, T. and NISHIZAKI, M. *Tetsu-to-Hagané*, **69**, S604 (1983)



---

## Further developments in thermomechanical processing

---

### 12.1 Controlled-cooling after controlled-rolling

The stringent control of whole stages of the hot-rolling process (reheating, rolling and cooling) constitutes the more completed form of thermomechanical treatment for high-strength low-alloy (HSLA) steels. In particular, a combination of controlled-rolling and subsequent accelerated cooling can strengthen the steel while maintaining superior low-temperature toughness under reduced contents of alloying additives or carbon in HSLA steels. The strengthening mechanism operated in accelerated cooling is primarily transformation strengthening due to the duplex microstructure consisting of ferrite ( $\alpha$ ) and bainite. Refinement of  $\alpha$  grain size and precipitation hardening due to carbide or nitride is also enhanced.

Studies of controlled-cooling after hot-rolling, together with the investigation of direct quenching, started in the early 1960s and has been utilized effectively for production of HSLA steels in the hot-strip mill.<sup>1-6</sup> Following the progress of controlled-rolling technology in the 1970s, attention is again being paid to accelerated cooling and direct quenching as means of developing further the advanced thermomechanical treatments which enable us not only to improve mechanical properties but also to save alloying elements and energy. These inline cooling or quenching processes in hot-rolling mills are currently being adopted in the plate-mill, seamless-pipe-mill and bar-mill.<sup>7-10</sup>

The cooling histories in several methods of inline cooling after hot-rolling are superimposed schematically in the continuous cooling temperature diagram shown in Figure 12.1. The major differences of processing parameters in these processes are cooling rate and the temperature range of forced cooling. Accelerated cooling as a controlled-cooling process, in principle, tends to choose the optimum cooling rate applicable to a wide variety of as-hot-rolled steel products without any heat treatment after cooling, whereas direct quenching aims to obtain low-temperature transformed products such as martensite or bainite, which necessitates the subsequent tempering treatment. In the interrupted accelerated cooling or direct quenching, the forced cooling is stopped at a specific temperature, then followed by aircooling.<sup>11-14</sup> Although the stop-temperatures in interrupted direct quenching have to be maintained below those for martensite or bainite,<sup>7</sup> that of interrupted accelerated cooling can be varied widely depending on cooling rate, hardenability of steel and rolling conditions.

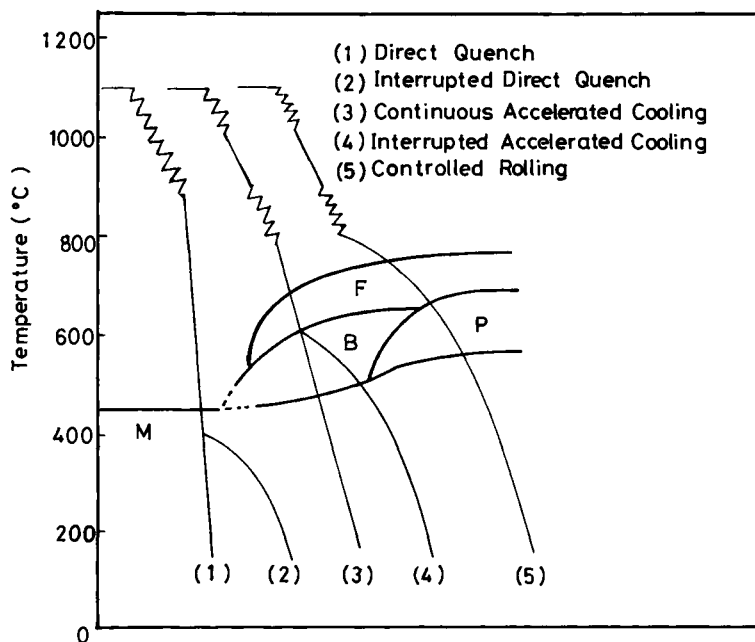


Figure 12.1 Several methods of inline cooling after hot-rolling

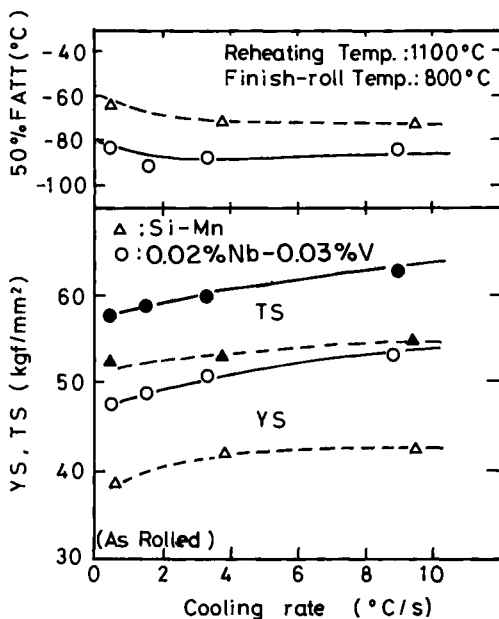


Figure 12.2 Effect of cooling rate on mechanical properties in 0.12% C-0.33% Si-1.38% Mn and 0.14% C-0.27% Si-1.3% Mn-0.023% Nb-0.033% V steels

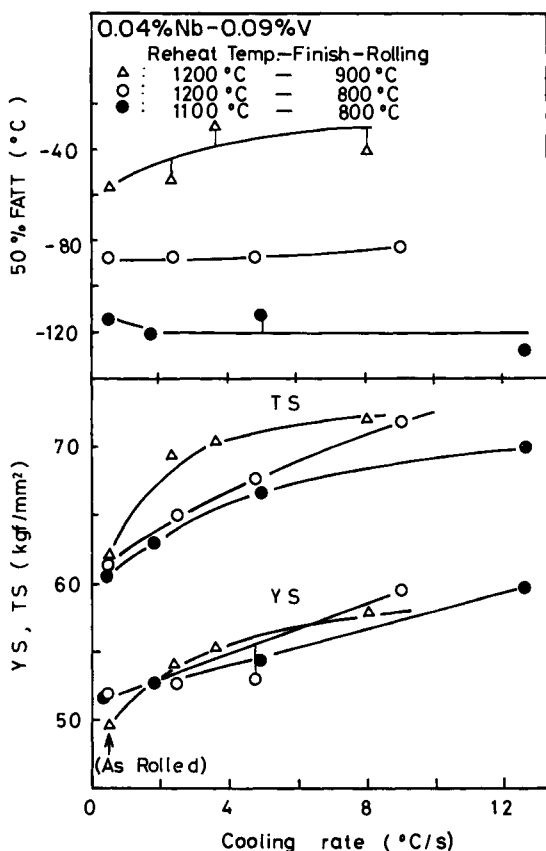


Figure 12.3 Effect of cooling rate on mechanical properties in 0.10% C-0.31% Si-1.50% Mn-0.036% Nb-0.092% V steel

In the following, metallurgical aspects of interrupted accelerated cooling applied to HSLA steel plates are described as an extended processing of controlled-rolling.<sup>8,9,10</sup> The main focus is put on the effects of processing variables and the microstructural features in accelerated-cooled plates.

### 12.1.1 Effects of cooling variables on mechanical properties

The main variables of interrupted accelerated cooling are cooling rate, and the start-and-stop-temperatures of cooling. The optimized conditions of these variables depend on the chemistry of steels and hot-rolling conditions, because hardenability of steel and the austenitic microstructure developed by hot-rolling can influence markedly the transformed microstructure and properties obtained by a specific condition of accelerated cooling. Figure 12.2 represents the effect of cooling rate in silicon-manganese steel and 0.02% Nb-0.03% V steel with a plate thickness of 20 mm. After the finish-rolling at 800°C with a cumulative rolling reduction of 70% below 900°C, accelerated cooling started at 780°C and stopped at 600°C, followed by aircooling. The yield and ultimate tensile strength increased by 3–6 kgf/mm<sup>2</sup> at a cooling rate of 10°C/s com-

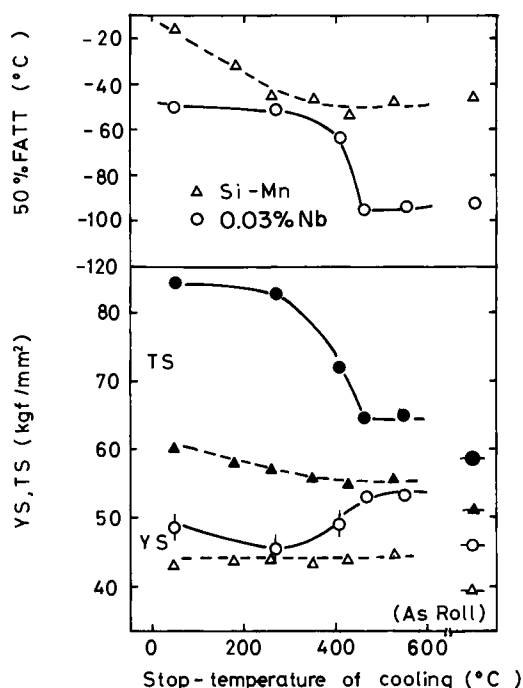


Figure 12.4 Effect of the stop-temperature of cooling in 0.14% C-0.23% Si-1.29% Mn and 0.13% C-0.31% Si-1.62% Mn-0.032% Nb steels

pared with controlled-rolled plates; the increment of strength in microalloyed steel is larger than that of silicon-manganese steel. The fracture appearance transition temperature (FATT) in Charpy impact testing is slightly improved by accelerated cooling.

The dependence of mechanical properties on cooling rate is varied by the condition of controlled-rolling in a fixed steel. This is demonstrated in Figure 12.3. The 0.04% Nb-0.09% V steel was control-rolled with various combinations of the reheating and finish-rolling temperatures, then followed by accelerated cooling. The decrease of strength with cooling rate in this steel, which contains the increased content of manganese and microalloying elements, is much larger than that of steels shown in Figure 12.2. The rolling conditions with higher temperatures of both reheating and finish-rolling resulted in the largest increment of ultimate tensile strength. This is due to the increased hardenability in the coarse austenitic microstructure developed by this rolling condition. The levels of FATT and its dependence on cooling rate were clearly differentiated by rolling variables. The decrease of reheating and finish-rolling temperatures tends to lower FATT with the increase of cooling rate. The transformation from the coarse austenitic microstructure forms the mixed structure of the coarse bainite and  $\alpha$  by accelerated cooling, which decreases toughness with the increase of strength. As a result, it is important to refine the austenitic microstructure by optimization of reheating and rolling variables for both improvement of strength and toughness by accelerated cooling.

It is basically necessary that accelerated cooling starts from above the  $A_{r3}$  transformation temperature. The increment of strength obtained by accelerated cooling reduces as the start-temperature of accelerated cooling approaches  $A_{r3}$  temperature. The ac-

celerated cooling after the finish-rolling below  $A_{r3}$  temperature, i.e. rolling in the  $(\gamma + \alpha)$  region, may strengthen the steel through the suppression of progress of static recovery and recrystallization of deformed  $\alpha$ . Thus, the transformed microstructure obtained by this condition consists of deformed and nondeformed  $\alpha$ , and dispersed pearlite. The effect of the stop-temperature of accelerated cooling on the mechanical properties in silicon–manganese steel and 0.03% Nb steel are shown in Figure 12.4. After being finish-rolled at 800° C, accelerated cooling with a cooling rate of 10° C/s was performed from 780° C to various stop-temperatures. It is observed in niobium steel that ultimate tensile strength increases abruptly with a decrease of the stop-temperature to below 450° C, and this is due to formation of the large amount of bainite. However, both steels exhibited a significant increase of FATT in the stop-temperature below 450° C. Thus, for the continuous-cooling process that accelerates down to ambient temperature, not only the cooling rate, but also the chemistry of steel has to be optimized so that the deterioration of toughness can be avoided. For the stop-temperature above 500° C, the formed bainite may be subjected to self-tempering somewhat during the subsequent aircooling, and the fine precipitation of carbide and nitride on the substructure of bainite is also enhanced. These are favourable conditions for both improvement of strength and toughness by accelerated cooling. The increase of the stop-temperature above 650° C reduces the strengthening effect due to accelerated cooling. It is also important to note that the inadequate increase of cooling rate or too large a reduction of the stop-temperature in a thicker plate tends to expand nonuniform hardness distribution in the through-thickness (Z) direction of the plate. Consequently, variables of accelerated cooling have to be optimized by taking account of the hardenability of the steel, rolling conditions and plate thickness.

### 12.1.2 Transformed microstructure and strengthening mechanism

Examples of microstructural changes with cooling rate are demonstrated in Figure 12.5 for silicon–manganese and 0.02% Nb–0.03% V steels. The increase of cooling rate gives rise to the substantial refinement of  $\alpha$  grain size and to the disappearance of pearlite banding. At cooling of above 4° C/s, bainite is formed in place of pearlite and its volume fraction is much higher in microalloyed steel compared with silicon–manganese steel. That is, the novel role of microalloying elements such as niobium or vanadium revealed by accelerated cooling is the increase of hardenability of steel, and this may be caused by niobium or vanadium dissolved into  $\gamma$ . The quantitative measurements of these microstructural changes with cooling rate in 0.04% Nb–0.09% V steel are shown in Figure 12.6. In the transformation from the coarse austenitic microstructure which is formed by controlled-rolling to the higher reheating and finish-rolling temperatures, bainite formation starts at a relatively lower cooling rate; the volume fraction of bainite at a higher cooling rate is much larger compared with the transformation from very refined  $\gamma$  obtained by the decrease of reheating and finish-rolling temperatures. Conversely,  $\alpha$  grain size obtained in as-rolled conditions was continuously refined with the increase of cooling rate up to and around 5° C/s, and then tended to saturate at higher cooling rate, continuing the differences in grain size achieved by various combinations of reheating and rolling conditions. Strengthening due to accelerated cooling involves three factors: (1) enhanced  $\alpha$  grain refinement; (2) precipitation hardening; and (3) strengthening due to bainite. The

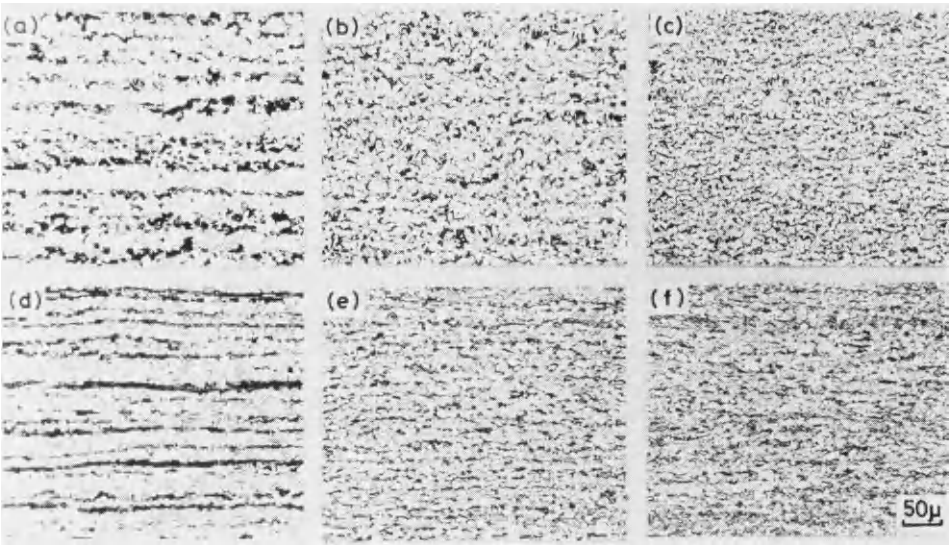


Figure 12.5 The microstructural changes with cooling rate: (a)–(c) silicon–manganese steel; (d)–(f) 0.02% Nb–0.03% V steel; (a), (d) control-rolled plates; (b), (e) cooling rate 4°C/s; (c), (f) cooling rate 10°C/s

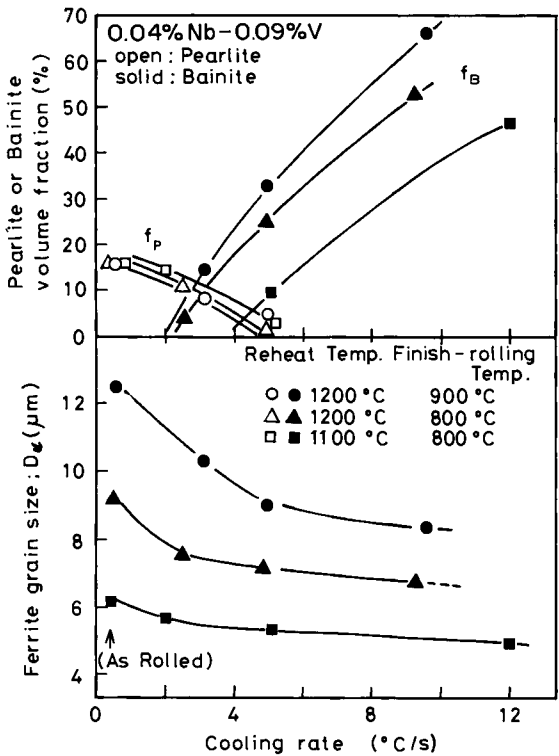


Figure 12.6 The change of  $\alpha$  grain size and bainite volume fraction with cooling rate in 0.04% Nb–0.09% V steel

increment in strength of interrupted accelerated cooled plate compared with the controlled-rolled plate can be approximated by the following equations:

$$\Delta YS = \Delta(K_y d^{-\frac{1}{2}}) + \Delta\sigma_{ppt} + \alpha \quad (12.1)$$

$$\Delta TS = \Delta(K_d d^{-\frac{1}{2}}) + \Delta\sigma'_{ppt} + K_B f_B + \beta \quad (12.2)$$

where  $K_y$  and  $K$  are coefficients for the grain-size dependence of strength in the Petch equation,  $d$  is the  $\alpha$  grain size,  $K_B$  and  $f_B$  are coefficients of strengthening due to bainite and the volume fraction of bainite, respectively,  $\Delta\sigma_{ppt}$  are the increments of precipitation hardening due to accelerated cooling, and  $\alpha$  and  $\beta$  are correction terms.

The contribution of each of the strengthening factors to the overall increment of strength due to accelerated cooling is given in Figure 12.7, where the mechanical properties of 0.04% Nb–0.09% V steel shown in Figure 12.3 were analysed based on quantitative measurements of the transformed microstructure. The values of  $K_y$ ,  $K$  and  $K_B$  used here were 1.8 kgf/mm<sup>3/2</sup>, 0.8 kgf/mm<sup>3/2</sup> and 0.15 kgf/mm<sup>2</sup> respectively. It is seen from Figure 12.7 that the increment of yield strength obtained by accelerated cooling is attributed to enhanced  $\alpha$  grain refinement and precipitation hardening, and that of ultimate tensile strength is mostly based on strengthening due to bainite.

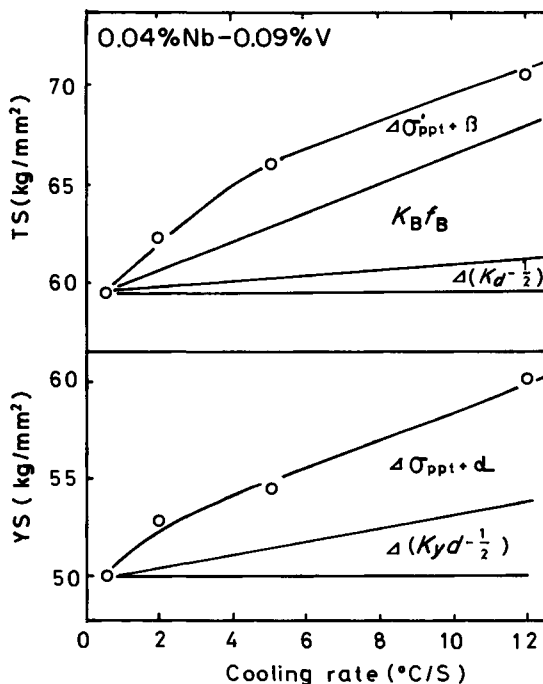


Figure 12.7 Contribution of each of strengthening factors to increment of strength due to accelerated cooling in 0.04% Nb–0.09% V steel. Reheating and finish-rolling temperatures are 1100 and 800°C respectively

## 12.2 Hot-charge rolling and hot-direct rolling

The introduction of continuous casting has made possible an energy saving of 1–1.2 million kJ/t. The charging of hot slabs into reheating furnaces (hot-charge rolling (HCR)) and the direct rolling of hot slabs without reheating (hot-direct rolling (HDR)) further save about 0.4–1.2 million kJ/t respectively.

Although the contribution of the latent heat of  $\gamma \rightarrow \alpha$  transformation to the above amounts of saved energy is considerably smaller compared with that of the specific heat, the metallurgical meaning that slabs have not experienced the transformation is definitely important for controlled-rolling. The  $\gamma$  grain size of slabs reheated from temperatures lower than  $A_{r1}$  to 1250°C is about 0.5  $\mu\text{m}$ , but that of the slabs cast and cooled down to the  $\gamma$  region is about 1–3  $\mu\text{m}$ , i.e. the as-cast  $\gamma$  grains are left coarse down to the  $A_{r3}$  temperature but refined by twice passing the  $\gamma \rightarrow \alpha$  transformation. The  $\gamma$  grains at the start of hot reductions in the HDR of broken-down slabs may be of intermediate size.

The finer the  $\gamma$  grains are before hot-deformation, the easier their refining by recrystallization becomes. The reheating of conventionally broken-down or continuously cast slabs cooled to the environmental temperature has made easy the production of rolled materials having fine transformed structures through the refinement of the  $\gamma$  grains finally being recrystallized by starting hot-reductions from the not-so-coarsened  $\gamma$  grains (Figure 12.8(a)). Extra-low-temperature reheating of slabs, one of the most important technical items in modern controlled-rolling, is the typical utilization of fine-grained  $\gamma$  obtained through twice-transformation by the cooling and reheating of slabs (Figure 12.7(d)). From the viewpoint of saving energy, the HDR of continuously cast slabs is most favourable, but for recrystallization controlled-rolling (RCR) it is the least favourable because of the coarse  $\gamma$  grains at the start of hot-reductions (Figure 12.8(c)). Therefore, HCR should be classified metallurgically into two or three groups according to their charging temperatures. The  $\gamma$  grain sizes before the first reduction are the same as those in HDR when the charging temperatures are higher than their

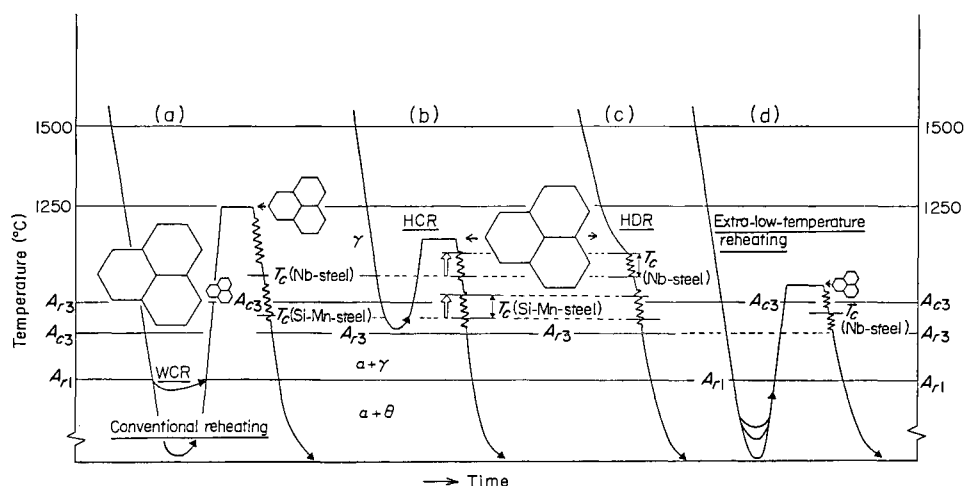


Figure 12.8  $\gamma$  grain sizes at start of reductions and  $T_c$  temperatures in rolling after conventional reheating, WCR, HCR, HDR and rolling after extra-low-temperature reheating



$A_{r3}$ , and almost the same as those in reheating of cold slabs when they are lower than their  $A_{r1}$ . The author would propose to designate the latter hot-charge as the 'warm charge' (Figure 12.8(a)).

There is no problem in the structures and the properties of warm-charge-rolled (WCR) products, as the Sumitomo high toughness (SHT) process explained in Chapter 1 has been its typical positive application. However, the hot-charging of slabs from the temperature higher than  $A_{r3}$  presents the same metallurgical problem as HDR, and the author calls hereafter only this type of hot-charge-rolling HCR in this section (Figure 12.8(b)). The hot-charge from the temperature just below  $A_{r3}$  or just above  $A_{r1}$  may be dealt with almost the same as HCR or WCR products, although preliminary quantitative trials are necessary. The slab charge from the intermediate temperatures between  $A_{r3}$  and  $A_{r1}$  should be avoided for controlled-rolling because of the instability in properties of rolled products except for thinner and low-grade steels.

The comparably coarse  $\gamma$  grains in the conventional reheating of broken-down slabs can be hardly recrystallized only by the first reduction in conventional plate-rolling even in plain silicon–manganese steels, as seen in Chapter 3. However, they and even those of niobium-containing steels by controlled-rolling schedules, are finally recrystallized and refined after successive reductions down to their critical temperatures for recrystallization ( $T_c$  or  $T_p$ ). The temperature range of hot-reductions in HDR is comparably lower than that in conventional rolling according to the not-so-high exit temperature of the continuous casting machine (CCM) and the temperature decrease during the transfer time from the CCM to the rolling-mill, but sufficiently higher than the  $T_c$  of simple silicon–manganese steels or, at least, covers the  $T_c$  in its lower second half (Figure 12.8(b) and (c)). It can recrystallize and refine the coarse starting  $\gamma$  grains and sometimes may improve the properties when the mill capacity is strong enough to complete total reductions at temperatures higher than their  $A_{r3}$ . It might also be possible that the not-so-high exit temperature of slabs from the CCM is also convenient for the accumulation of the deformation strain by successive reductions to recrystallize  $\gamma$  grains. If so, the reheating temperature of HCR slabs should be lowered to below that in the conventional reheating.

In the HCR and HDR of microalloyed steels having high  $T_c$ , e.g. niobium-containing steels hitherto produced by controlled-rolling (including the deformation in the nonrecrystallization region),  $T_c$  is more elevated than in the successive reductions after slab reheating, according to the coarser  $\gamma$  grains before the reduction caused by the coarser starting grains and the temperature range for the reductions in the recrystallization region becomes lower and narrower (Figure 12.8(b) and (c)). Sometimes, the  $T_c$  might be higher than the starting temperature of HCR and HDR, and all the reductions might be carried out only in their nonrecrystallization temperatures. It may barely guarantee the properties of small-size or low-grade rolled products, as shown in Figure 8.7 (page 146). For the controlled-rolling of thicker or higher-grade products through HCR or HDR, it would be necessary to raise the temperature of reheating furnaces or the CCM outlet temperature higher than those for the rolling of plain silicon–manganese steels to ensure the reduction temperature range for the  $\gamma$  grain refinement by recrystallization.

The prolonged transfer time of slabs from the exit of the CCM to the reheating furnace in HCR, causes the precipitation of niobium carbonitride or titanium carbide from supersaturated  $\gamma$ . It reduces the  $T_c$  and the temperature range of nonrecrystalliz-

ation, and further decreases the strength and the toughness of rolled products. In HCR of niobium- or titanium-containing steels, it is necessary to control the transfer time within the prescribed time intervals which should be determined experimentally. For a similar reason, the strict maintenance of four skirt temperatures of slabs over the  $A_{r3}$  of steels is also necessary especially in these steels.

The controlled rolling of high-grade products through HCR or HDR requires the refinement by recrystallization of the coarser  $\gamma$  grains at the start of reductions in nonrecrystallization temperatures whether niobium or titanium is added or not. Extra-low-temperature reheating of cold slabs or the addition of a small amount of titanium, has released controlled-rolling from RCR. Hot-charge rolling and HDR, however, revive the problem of RCR in the further severer manner. The possibility of the refinement of coarse starting  $\gamma$  grains in HCR and HDR would mainly depend on the once-recrystallization by the accumulated strain in the first several successive reductions. At higher temperatures, recrystallization can occur easily but the accumulation of the strain is also difficult by the static recovery during the time interval between successive reductions. The conditions for the once-recrystallization of the coarser  $\gamma$  grains by successive reductions are thought to be comparably easily satisfied at least in the conventional operations of rod- and strip-rolling, which have large total and respective reductions and the very short interpass times in the lower temperatures. The increase in the product thickness becomes out of condition for refinement of the  $\gamma$  grains by recrystallization in plate-rolling, in which the amount of each pass reduction is smaller according to the larger width and thickness of the product, and the interpass time is largely extended by reverse-rolling. The static recovery and the static and dynamic recrystallization by accumulated strain have to be studied on some typical steels. It may determine which grades of steels can be produced by controlled-rolling through HCR and HDR. As seen in Chapter 3, the  $\gamma$  grains at reheating to temperatures lower than the critical temperature for grain coarsening are finer than those recrystallized after any reduction at the same temperature. The author supposes that at least the thicker products hitherto controlled-rolled after extra-low temperature reheating might not be produced through HCR and HDR. The development in the near future of the new CCM having the reduced slab thickness would make it difficult to carry out the controlled-rolling through HCR or HDR, which has to be considered at the choice of the intended slab thickness in the new CCM or at the design of new rolling-mills for the newly developed slabs, even at the layout design of new hot-strip mills.

## References

1. IRANI, J.J. *British Iron and Steel Research Association open report No. MG/A/60/67*, ISMET 3814, FM558 (1967)
2. KLISOWSKI, A.W., LORIA, E.A. and BEISER, C.A. *Trans Am. Soc. Metall.*, **58**, 489 (1965)
3. IRANI, J.J., BURTON, D. and KEYWORTH, F. *J. Iron and Steel Inst.*, **2** (1966)
4. MORGAN, E.R., DANCY, T.E. and KORCHYNSKY, M. *J. Metals*, **17**, 821 (1965)
5. TITHER, G. and MORROW, J.W. *Metals Engrg.*, **42** (1975)
6. GROZIER, J.D. *Microalloying 75*, Union Carbide Corp., p.24 (1977)
7. TSUKADA, K., MATSUMOTO, K., HIRABE, K. and TAKESHIGE, K. *Iron and Steel Mag.*, **21** (1982)
8. LECLERC, J., ARNAUD, C., DUQUAIRE, B. and JEANNEAU, M. *Steel rolling*, The Iron and steel Institute of Japan, p.1321 (1980)
9. HOSTETTER, R.S., KRANENBERG, H. and RONEMUS, D.C. *Iron and Steel Mag.*, **23** (1980)
10. MANGIN, B. and DROUET, F. *Iron and Steel Mag.*, **8** (1979)

11. OUCHI, C., TANAKA, J., KOZASU, I. and TSUKADA, K. *Optimization of processing, properties and service performance through microstructural control*, ASTM Special Technical Publication No. 672, p.105 (1979)
12. MCCUTCHEON, D.W., TRUMER, T.W. and EMBURY, *Rev. Met.* **73**, 143 (1976)
13. HEEDMAN, P. and SJOSTROM, A., *Scand. J. of Met.*, **11**, 233 (1982)
14. OUCHI, C., OKITA, T. and YAMAMOTO, S. *Trans Iron and Steel Inst. Japan*, **22**, 608 (1982)

---

## Conclusion

---

Almost all aspects of the technology for thermomechanical processing of steels have been explained in this book. The microalloying, controlled-rolling and accelerated cooling are the main themes for the thermomechanical processing at the present and in the future.

Ferrous materials are the most important as structural materials and should increase in importance in the future. For this purpose, we should develop more the science and technology of microalloying and thermomechanical treating.

The International Conference on Physical Metallurgy of Thermomechanical Processing of Steels and Other Metals will be held in Tokyo in 1988. In reviewing recent advances and engaging in further development and innovation in thermomechanical processing, the Conference organizing committee considers now is the right time to look into our state-of-the-art knowledge from the viewpoint of physical metallurgy and to clarify the fundamental principles and guidelines for manipulating the desired microstructures and properties through various kinds of thermomechanical processing.

The Conference will focus on the experimental and theoretical bases of physical metallurgy involved in the thermomechanical processing of steels and other metals and alloys. The following categories are covered:

- (1) Deformation behaviour during hot- and warm-working.
- (2) Static and dynamic recrystallization, precipitation and grain growth.
- (3) Diffusional and diffusionless transformations and precipitations from work-hardened phases.
- (4) Interplay of transformation, precipitation and recrystallization, and its applications to structure control and improvement of properties.
- (5) Effects of microalloying on hot-deformation behaviour, recrystallization, grain growth and phase transformation.

This book covers all categories and we hope it will be a turning-point for a new development of thermomechanical processing.

Some parts of this book were written 5 years ago, others more recently. Recent developments are, of course, fully explained in this book.

During these years, Mr Michael Dunn and Mr Stephen J. Snook of Butterworths have been very kind and been most understanding of the authors' situations. The authors thank them for their kindness.

# Index

---

- $\alpha$  grains, *see also* Ferrite grains
  - diameter,  $D\alpha$ , 23–24
  - formation of, 98, 212
  - nucleation of, 142
    - at  $\gamma$  grain boundaries, 39
    - at annealing twin boundaries, 39
    - at deformation bands, 40
    - intragranularly, 40
  - refinement, 144
    - by accelerated cooling, 46–47
    - improvements in, 6
    - by low-temperature finish rolling, 4
    - refining parameter, 225
  - retardation in growth of, 144
  - shape of, 152
  - size, change in, 143–144
    - change with cooling rate, 231
    - estimation, 26
    - expression for, 23–26
    - formed from deformed  $\gamma$  (isothermal), 44–46
    - formed from work-hardened  $\gamma$ , 45
    - refinement of, 230
    - in silicon-manganese steels, 140
    - transformed from  $\gamma$ , 22–30
  - structure, refinement of, 80
- $\alpha$  iron, size of metadynamically recrystallized grains, 55
- $\alpha$  martensite dual-phase steel, 13
- $\alpha$  nucleation, 26, 144
  - frequency at  $\gamma$  grain boundary area, 147
  - sites, 9, 151
- $\alpha$  pearlite steels, controlled-rolled, 182
- $\alpha$  pearlite structure, 141
- $\alpha$  strengthening parameter, 225
- $\alpha$  transformation, 17, 23, 195
- $\gamma$ - $\alpha$  phase transformation, 17–20, 202
  - kinetics in HSLA steels, 125
  - ratio, 151
  - deformation in, 80
- $\gamma$  grain(s), *see also* Austenite grains
  - boundaries, 62, 93, 141
    - $\alpha$  grains nucleated at, 39
    - area, 145, 212
    - lattice distortion in deformed, 43
    - ledges in, 42
  - refinement, 9
    - by recrystallization controlled-rolling, 74
  - shape change of, 41
  - size, 49, 142, 215–216
    - calculation of, 203
    - prediction of, in multipass rolling, 212–216
    - in silicon-manganese steels, 140
  - surface areas, ratio of, before and after rolling, 42
- $\gamma$  recrystallization region, deformation in, 80
- Accelerated cooling, 14, 23, 173, 229
  - $\alpha$  grain refinement by, 46–47
    - after hot-rolling, 46
    - in plate-rolling mills, 13–14
    - after rolling, 145
    - strengthening due to, 230
- Acicular  $\alpha$  steel, 11, 182–186
  - strength of, 162
- Acicular  $\alpha$  structure, 97
  - intensity of, 107
- Acicular transformation, 97
- Activated twin boundaries, 9
  - density of, 148
- Air-cooling transformation, 145
- Alaska, line pipes for, 7
- Alloying, effect of, on  $\gamma$ - $\alpha$  transformation, 18
- Alloying elements, 18, 121
  - and impurities, 154–166
    - effect of, on hot-strength, 123
      - on recrystallized grain size, 75–78
      - on recrystallization behaviour, 74–78
      - on recovery and recrystallization, 82
      - on retardation of recrystallization, 37–39
    - role in producing dual-phase structure, 187
    - substitutional, effects of, 161
- Aluminium,
  - as alloying element, 18
  - as microalloying element, 154
  - nitride, structure of, 155
- Aluminium-killed steels, 12
  - normalizing, 2
- Anisotropy, dimensional, 113
  - in mechanical properties, 106
  - of relative yield strength, 108
  - and texture, 106–110
- Annealing twin(s), 53, 90
  - in  $\gamma$  grains, 32
    - boundaries, 44, 94, 96, 147
      - $\alpha$  grains nucleated at, 39
      - activation of, 145
      - as preferential nucleation sites of  $\alpha$ , 47
      - nucleation at, 41
      - pearlite nucleation at, 93
      - role of, 151
    - effect of reheating temperature on density of, 91, 92
  - formation of, 51
    - in controlled rolling, 92
    - in static recrystallized austenites, 36
- Arctic use, line pipes for, 181
- Arresting temperatures, 178
- ASTM grain size numbers, 61

- ASTM number, 80, 146  
 Ashby-Orowan strengthening, 169  
 As-hot-rolled dual-phase steel, 186–189  
 As-rolled IN-steels, 74  
 Austenite, *see also*  $\gamma$   
   deformation of, in nonrecrystallization region, 80–100  
   in recrystallization region, 49–79  
   to ferrite conversion ratio, relation between  $\gamma$  grain size and, 80  
   and ferrite grain sizes, relationship between, 140  
   to ferrite transformation, 17–48  
   plus ferrite two-phase region, deformation in, 101–116  
   grain structure, pancaked, 86  
   transformation behaviour of, after thermomechanical treatment, 140–153  
 Austenitic microstructure, 229  
 Austenitic recrystallization, retardation of, 157–159  
 Austenitic structure, observation of, 157  
 Automatic quench dilatometer, (Formaster F), 29  
 Automobile industry, use of dual-phase steel, 189  
 Avrami equation, 205
- Bainite, 162, 226, 230  
   banded structure, 113  
   formation, 93–94  
   suppression of, 98  
   fraction, 146  
   lower, 194  
   strengthening due to, 230  
   transformation, 17, 97  
   upper, 93, 96, 148, 187, 194, 198  
   increase in, in niobium-containing steel, 147  
   structure, 97  
   suppression of, 4  
   volume fraction, increase in, 161  
 Bainitic microstructure, 108  
 Bainitic steels, grain size in, 11  
   ultra low-carbon, 13  
 Bainitic structure, 82  
 Bar-mills, 121, 226  
 Battelle-type drop-weight tear test, 179  
 Bauschinger effect, 11, 184  
 BISRA, 150  
 Bond toughness, 196  
 Boron addition, 161, 162  
 Boron as microalloying element, 154  
 Boron, reduction of manganese content using, 11  
 British Iron and Steel Research Association, (BISRA), 150  
 Brittle fracture, initiation, 165, 177–179  
   problems of, 2  
   strength in Z direction, 114  
 Brittle-crack arresting temperature, 178  
 Bulging mechanism, 33
- Calcium,  
   addition of, 11, 154, 165  
   silicate, 166  
   treatment, 165  
   to increase impact energy, 180
- Cam plastometer, use of, 126  
 Carbide-forming elements, 19  
 Carbides,  
   of alloys, 18  
   of niobium, titanium and vanadium, 75  
   of niobium and vanadium, 5  
   structure of, 155  
 Carbon content,  
   effects of, 196, 197  
   on Charpy absorbed energy, 180  
   on hot-strength, 122  
   on softening, 83, 133  
   increase in niobium-bearing steels, 159  
 Carbon equivalent,  
   effect on tensile strengths, 200  
   optimum, 199  
 Carbon steels, stress-strain curves, 126  
 Carbon, strengthening effect of dissolved, 122  
 Carbonitrides, 155  
   niobium and vanadium, 171  
   particle coarsening in, 37  
   in steels, 18  
 Carbon-manganese steels, 85  
   controlled rolling of, 1, 2, 3  
   grain sizes in, 212, 213  
   temperature of rolling operations in, 49  
 Carbon-manganese-niobium steels, 85  
 CCM, 234  
 Cementite, 97, 142, 183  
 Centre-notched (Charpy) tensile test, 177  
 Charpy absorbed energy, 180  
 Charpy impact energy, 166, 179, 180, 193, 195, 197, 198  
   of controlled-rolled steel, 111  
 Charpy impact properties, 102  
 Charpy impact test, 179, 229  
 Charpy shelf energy, 8, 10  
 Charpy specimen, 112, 113  
 Charpy tensile test, 177  
 Charpy tests, 13  
 Charpy transition curves, 110–111, 165  
 Charpy transition temperature, 159, 160, 162, 163  
 Charpy upper shelf energy, 164  
 Charpy V-notch,  
   absorption energy, 149  
   impact testing, 160  
   shelf energy, 150  
   transition temperature, 146, 148  
 Chemical composition of HSLA steels, 154, 185  
 Chromium addition,  
   effect of, 187  
   effect on hot-strength, 122  
 Chromium as alloying element, 18  
 Chromium as substitutional element, 154  
 Chromium, retardation effects of, 75  
 CLR, crack length ratio, 182  
 Classical static recrystallization, 61  
 Cleavage fracture, 110  
 COD, 177, 178, 199  
 Coarse  $\alpha$ , 96  
 Coarse acicular  $\alpha$ , 148  
 Coiling temperature, 145, 187, 188, 189  
 Coils for spiral pipes and electric welded pipes, 13

- Cold-rolled texture, 108  
 Cold-worked grains, 101  
 Commercial production of line pipes for Alaska, 7  
 Compositional change, during diffusional phase transformation, 17  
 Compression, 117  
 Computer simulation for predicting mill load, 135–139  
 Contamination in steelmaking, 165  
 Continuous casting machine, 234  
 Continuous cooling transformation, 26–30  
   diagram, 95, 99  
   kinetics of  $\gamma$ , 21–22  
   relation between isothermal transformation and, 27  
 Controlled-cooling, 226–228  
 Controlled rolling, 157, 173–174  
   bainitic steels and extra-low-temperature reheating, 10–13  
   of carbon-manganese steel, 1, 3  
   before controlled-cooling, 226–228  
   development of, 3  
   in different mills, 2  
   formation of annealing twins, 92  
   and hot-rolling, comparison between, 81, 89  
   for HSLA steels, 75  
   of IN steels, 4  
   of low carbon-manganese-molybdenum-niobium steel, 97  
   of low-carbon niobium-containing steels, 4–9  
   of niobium-containing steels, 3, 9–10, 74  
     early mill trials, 150  
   in nonrecrystallization region, 145  
   outline of, 9–10  
   in a plate mill, 134  
   to produce line-pipe steels, 179–182  
   purpose of, 22–23  
   for refinement of recrystallized  $\gamma$ , 7, 68–74  
   of silicon-manganese steels, 9, 10  
   stages in, 22, 80–81  
   techniques for, 7  
   of thicker plates, 153  
 Controlled-rolled niobium-containing steels, precipitation hardening in, 5  
 Controlled-rolled plates, chemistry and production conditions, 7  
 Controlled-rolled ship's plates, grain refinement in, 141  
 Controlled-rolled steel,  
   Charpy impact energy of, 111  
   embrittlement in, 110  
   properties of, 167–201  
   strength of, 106  
     and toughness in, 170  
   transformation textures of, 107  
   weldability of, 190  
 Controlled-rolled transformation-strengthened steels, 14  
 Controlled-rolled vanadium-containing steels, precipitation hardening in, 5  
 Cooling, 145  
   accelerated, 14  
   rapid, 7  
 (*Cooling, continued*)  
   rate, changes with, 230–232  
     effect on mechanical properties, 227, 228  
   variables, effects on mechanical properties, 228–230  
 Copper,  
   as substitutional element, 154  
   effect on hot-strength, 122  
   size of metadynamically recrystallized grains, 55  
   stacking fault energy of, 31  
 Crack arrestability, 11  
 Crack initiation, 114  
   resistance to, 10  
 Crack length ratio, 182  
 Crack propagation, 10  
 Crack sensitivity ratio, 182  
 Cracking, 175, 190–191  
   hydrogen-induced, 182  
 Crack-opening displacement, COD, 177, 178, 199  
 Cracks, 113  
 Cranfield test, 175, 176  
 Creep deformation, 31  
 Critical crack-opening displacement, 177–178  
 Critical reduction,  
   for metadynamic recrystallization, 69  
   for recrystallization, 61, 62  
   temperature for recrystallization, 62  
   temperatures to refine  $\gamma$  grains by recrystallization, 69  
 Critical strain, 52, 76  
   for metadynamic recrystallization, 53  
   and dynamic recrystallization, 69  
 Critical stress, 112  
 Critical temperature for brittle fracture initiation, 177  
 Cross-rolling, 9  
 Crystallographic texture, 107  
 CSR, crack sensitivity ratio, 182  
 Deformation,  
   in  $\gamma$ - $\alpha$  two-phase region, 80–81, 101–116, 171, 220–223  
     texture developed by, 108–109  
   in  $\gamma$ -recrystallization region, 80  
   of austenite, in nonrecrystallization region, 80–101  
     in recrystallization region, 49–79  
   bands, 8, 9, 81–82, 87, 89, 93, 145, 151  
   definition of, 86  
   density, 87, 148  
   formation and role of, 51, 86–93  
   nature of, 90  
   nucleation of  $\alpha$  grains at, 147  
   nucleation on, 41  
   role in controlled-rolling, 89–90  
   behaviour, of the  $\gamma + \alpha$  two-phase region, 101–106  
     of steels at elevated temperatures, 30–39  
   conditions, factors affected by, 53  
   effect of, on continuous-cooling-transformation diagram, 93–94  
   at high strain rates, 31  
   of inclusions, 149

*(Deformation, continued)*

- in nonrecrystallization region, 80, 88, 96
- at recrystallization temperature range, 22
- resistance, 126, 202, 214, 221–223
  - at elevated temperatures, 117–127
  - formula, strain accumulation in, 133–135
  - parameters affecting, 117
- static restoration processes after, 52
- temperature, effect on softening ratio, 130–131
- at unrecrystallized temperature range, 22
- Deformed  $\alpha$ , 230
- Deformed  $\gamma$ ,
  - $\alpha$  grain size formed from, 44–46
  - grain boundaries, 151
  - grain boundary  $\alpha$  nucleation in, 96
  - growth of  $\alpha$  in, 44
  - pearlite formation in, 95
  - pearlite transformation from, 93
  - transformation behaviour of, 98
- Delay time in rolling reductions, 6
- Density,
  - of activated twin boundaries, 148
  - of annealing twins, 94
  - of deformation bands, 148
- Desulphurization technology, 164
- Diameter, inverse, of statically recrystallized grains, 63
- Diffusional transformation, 17
- Dilatometric methods, 93
- Dimensional anisotropy, 113
- Direct quenching, 226
- Dislocation, 93
  - density, 104
  - hardening, 167
- Dispersed pearlite, 230
- Draught, 9
- Drophammer-type high-speed compression
  - equipment, use of, 126
- Drop-weight tear test, 10, 13, 179
- Dual-phase steel, 98
  - as-hot-rolled, 186–189
- Dual-phase structure, 187
- Ductile fracture, 163
- Ductility, 165
- DWTT *see* Drop-weight tear test
- Dynamic recovery, 31, 105, 118, 119
- Dynamic recrystallization, 31–32, 52, 61, 62, 68, 76, 105, 118–120, 204–205
  - of  $\gamma$ , change in optical microstructure of, 37
  - conditions which favour, 57
  - critical strain for, 69
  - increase in rolling speeds in temperature range of, 73
  - mechanism, 33
  - by rolling hot-deformations, 56–59
- Electric welded pipes, 13
- Electrical capacities of hot-working facilities, 117
- Embrittlement, 109, 110, 113
- Energy,
  - impact, 112
  - saving, 12
  - shelf, 112
- Enhanced nucleation, mechanism of, 42
- Equiaxed  $\alpha$  grains, 101
- European plate-mills, rolling of ship's plates in, 74
- FATT, 101, 114, 174, 175, 179, 192–196, 198, 224, 229
- Failure, intergranular, 113
- Ferrite, *see also*  $\alpha$ 
  - and bainite, 226
  - grain refinement by work-hardening of  $\gamma$ , 39–46
  - grain size, 146
  - nucleation, in deformed  $\gamma$  (isothermal), 39–44
    - on deformation bands, 81
    - potential, 87
- Ferritic region, steels deformed in, 119
- Finish-rolling,
  - in  $\gamma$  region, 115
  - at intercritical temperatures, 7, 11
  - low temperature, 2
- Flow stress, 25, 124, 157
  - dependance on temperature and strain rate, 120
  - in hot-deformation, 123
- Formaster F, 29
- Fractional softening, change in, 35
- Fracture, *see* Cracking
- Fracture appearance transition temperature, *see* FATT
- Fracture toughness in Z direction, 177
- Grain boundary,
  - $\alpha$  nucleation in deformed  $\gamma$ , 96
  - area, 87
  - migration, pinning effect on, 39
    - strain-induced, 72
  - nucleation at, 41
  - sliding, 31
  - surfaces, 44
- Grain coarsening temperature, 13, 156
- Grain growth, 208–210
  - abnormal, by strain-induced grain boundary migration, 52
  - evaluation of, 66
  - rate of, 55
  - retardation of, 75
  - suppression after static recrystallization, 73
- Grain refinement, 174, 184, 202, 203
  - in controlled-rolled ship's plates, 141
  - convergence of, 72–73
  - efficiency of, 73
  - enhancement of, 162
  - and precipitation hardening, 159–161
  - through repeated recrystallization, 81
- Grain size, 121, 169, 170, 204
  - in carbon-manganese steels, 212, 213
  - dependance on strain, 54
  - difference in, with and without niobium, 76
  - dynamically recrystallized, 204
  - effect of, on critical reduction for static recrystallization of  $\gamma$ , 63
    - on hot-strength, 124
    - on recrystallization of silicon-manganese steel, 62
  - factors affected by initial, 53



*(Grain size, continued)*

- initial, 25, 53, 131
  - effect on softening, 130
- of iron and silicon-manganese steels, 57
- limiting, 72
- in multipass rolling, 212
- in niobium steel, 214
- recrystallized, 52, 66, 203
  - dependence on strain and deformation temperature, 64
- starting, 72
- Grain structure, 104
  - inhomogeneity in, 88
- Grain surface nucleation, 25
- Growth of  $\alpha$  in deformed  $\gamma$  (isothermal), 44
- Growth kinetics, 77
- Growth rate of  $\alpha$  in HSLA steels, 44
- Hardenability, 184, 198
- Hardening, 167
- HCR, *see* Hot-charge rolling
- HDR, *see* Hot-direct rolling
- Heat treatment, 173
- High-manganese steels, 148
- High-temperature mechanical testing, 157
- High-temperature tension, 117
- High-tensile strength steel, mechanical properties of, 174–179
- Hillert and Staffanson, regular solution-sublattice model, 28
- Historical survey of thermomechanical processing, 1–14
- Holding time in rolling reductions, 6
- Hoop stress, 179
- Hot-charge rolling and hot-direct rolling, 233–235
- Hot-compression testing, 121
- Hot-deformation, 220
  - of  $\alpha$ , 105
  - with constant strain rate, 52
  - experiments, 129
  - resistance, 213
    - formulae, 126–127
    - resistance of metals, 117
  - restoration during, 30–34
  - rolling, dynamic and metadynamic
    - recrystallization by, 56–59
  - restoration processes during and after, 104
  - temperature, 9
  - texture due to, 39
- Hot-direct rolling, 233–235
- Hot-rolled  $\gamma$  grains, temperature-reduction-recrystallization, 60
- Hot-rolling, 23
  - computer-control of, 202
  - and controlled-rolling, comparison between, 81, 89
  - conventional steels, 74
  - interruption of, 2
  - mills, 226
    - operation of, 117
  - prediction and control of microstructural change and mechanical properties in, 202–225

*(Hot-rolling, continued)*

- prediction of recrystallized  $\gamma$  grain size during, 203
- of ship's plates, controlled low-temperature, 1–4
- softening behaviour after, 128–130
- of thin plates, 3
- Hot-strength,
  - effect of nitrogen on, 122
  - metallurgical factors affecting, 121–125
  - of steel, 117
- Hot-strip mill, 7, 14, 226, 235
  - Misaka mathematical model for, 126
  - prediction of mill load in, 139
- Hot-strip-rolling, 203
- Hot-torsion tests, 75
- Hydrogen-induced cracking, 180, 182
- Impact energy, 112, 179, 180
  - see also* Charpy impact energy
- Impurities and alloying elements, 154–166
- Impurity elements, 163–166
- IN steels, 74
  - controlled-rolling of, 4
- Inclusions, 163
- Inclusion-shape control, 115
- Induced stress, 112
- Inhomogeneity in grain structure, 88
- Initial grain size, 25
  - effect on softening, 132
  - factors affected by, 53
- Inline cooling, 226, 227
- Intercritical rolling, 11
- Intergranular failure, 113
- International Conference on Physical Metallurgy or Thermomechanical Processing of Steels and Other Metals, 237
- Interpass time,
  - effect on softening kinetics, 211
  - effect on softening ratio, 130–131, 133
- Interphase precipitation of niobium carbide, 19
- Iron carbide, 18
- Iron, grain sizes in, 57
- Isothermal and continuous cooling
  - transformation, relation between, 27
- Isothermal holding time, 20
- Isothermally formed  $\alpha$ , 46
- Isotropic strain-free  $\gamma$ , transformation from, 140
- Kinetic control of softening behaviour, 128
- Kinetics, growth and recrystallization, 77
- L-direction,
  - low-temperature toughness in, 114
  - transition temperature in, 164, 174
- Lamellar structure in rolled plates, 142
- Lamellar tearing, 175, 176, 177
- Large-angle grain boundary, 90
- Lath martensite, 17
- Lattice change, 17
- Lattice distortion in deformed  $\gamma$  grain boundaries, 43
- Lattice hardening, 167
- Ledge mechanism of growth, 19

- Ledges in deformed  $\gamma$  grain boundaries, 42  
 Liberty ships, 2  
 Line-pipes,  
     for Alaska, commercial production of, 7  
     for arctic use, 181  
     steel for, 13, 179–182, 196  
 Linear intercept method, 88  
 Low-carbon bainitic steels, 11  
 Low-carbon niobium-containing steels, controlled  
     rolling of, 4–9  
 Low-temperature coiling, 7  
 Low-temperature finish-rolling, 2, 141  
      $\alpha$  grain refinement by, 4  
 Low-temperature reheating of slabs, 7, 9, 11, 12  
 Low-temperature roughing, 9  
 Low-temperature toughness, 178  
  
 Magnesium sulphate inclusions, 166  
 Manganese,  
     addition of, to improve toughness, 8  
     carbon ratio, increase in, 2  
     effect of, on  $\gamma$ - $\alpha$  transformation kinetics, 125  
         on hot-strength, 122  
         on softening, 131, 133  
         on texture intensity, 108  
     increase in content of, 147, 162  
     increase in steel strength due to, 5  
     microstructural changes with addition of, 11  
     molybdenum-vanadium-titanium composition,  
         13  
     retardation effects of, 75  
     as substitutional element, 154  
     sulphide, 8, 163, 175, 180  
         inclusions, 166  
     sulphur, in work-hardened  $\gamma$ , 149  
 Manufacturing methods, 173  
     of high-strength steel plate, 174  
 Martensite, 97, 183, 194, 196, 226  
     intensity of, 107  
     islands, 186  
     transformation, 17, 89  
 Mechanical capacities of hot-working facilities,  
     117  
 Mechanical properties of controlled-rolled steels,  
     172–189  
     interpretation of, 172  
     prediction and control of, in hot-rolling,  
         202–225  
 Mechanism, for dynamic recrystallization, 33–34  
     of grain-refinement by hot-rolling and  
         accelerated cooling, 23  
 Metadynamic recrystallization, 34, 52, 59  
     by rolling hot-deformations, 56–59  
     critical reduction for, 69  
     critical strain for, 53  
     rate of, 52  
 Metadynamically recrystallized grains, size of, 62,  
     65  
 Metallurgical changes during and after hot-  
     deformation, 52–56  
 Metallurgical factors, 173  
     affecting hot-strength, 121–125  
 Microaddition of niobium and titanium, 37  
 Microalloying elements, 154–161  
     effect on hot-strength, 123  
     effects on recrystallization kinetics, 74  
     precipitation hardening of, 161  
 Microalloying, suppression of grain boundary  
     migration due to, 37  
 Microfractography, 164  
 Microstructure, 170  
     change in, 11, 81, 93, 194  
     caused by deformation in the two-phase  
         region, 101  
     control of, in hot-rolling, 202–225  
     with reduction in  $\gamma$ - $\alpha$  region, 103  
     during rolling, 139  
     in stages of controlled-rolling, 23  
     relationship with deformation variables, 212  
     strength and toughness, relation between,  
         223–225  
 Mill(s), *see also* bar-mill, hot-strip mill, rolling  
     mill, plate-mill, shape-mill, strip-mill  
     load, 138  
     computer simulation for prediction of,  
         135–139  
     comparison of measured and calculated, 137,  
         138  
     in controlled-rolling, 136  
     prediction of, in hot-strip mill, 139  
     operation using process computer, 135  
     trials, 6  
 Miller equation, 208  
 Misaka mathematical model, 126  
 Misaka's equation, 137, 138  
 Mixed grain structure, 101  
 Molybdenum,  
     as additional element for controlled-rolling, 77  
     as alloying element, 18  
     carbide, 19  
     -containing acicular  $\alpha$  steels, 12  
     effect of, 166  
         on controlled rolling, 147  
         on hot-strength, 122  
         on grain structure, 76  
     microstructural changes with addition of, 11  
     with niobium, 199  
     steel, yield strength, 106  
     strengthening effect of, 161  
     as substitutional element, 154  
 Multipass rolling, 105, 128, 133  
     prediction of  $\gamma$  grain size in, 212–216  
 Multistage hot-compression testing, 130  
  
 NIC, 3, 13  
 Nickel,  
     addition of, 196  
     effect on texture intensity, 108  
     effect on hot-strength, 122  
     -microalloyed steels,  $\alpha$  grains in, 144  
     retardation effects of, 75  
     size of metadynamically recrystallized grains, 55  
     as substitutional element, 154  
 Niobium, 196–198  
     *see also* Niobium-containing steels  
     affinity with carbon and nitrogen in austenite,

*(Niobium, continued)*

- 154
- as alloying element, 18
- carbide, 20, 155, 156, 160
  - and nitrides, 5, 75, 172
- carbonitride, 171
  - effect on hot-strength, 123
  - strain-induced precipitation of, 84, 104, 202
- drag effect, 104
- effect, 159
- effect of, on controlled rolling, 147
  - on dynamic recrystallization, 205
  - on grain size, 76
  - on hot-strength, 122–123
  - on recrystallization, 82, 85
  - on softening, 82–83, 130
  - on strength, 4
  - stress-strain curves in steels, 118
- improvements in mechanical properties with, 4
- increase in hardenability due to, 230
- microaddition of, 37
  - as microalloying element, 154
- microstructural changes with addition of, 11
- nitride, 155, 156, 160
- precipitates, classification of, 170
- with molybdenum, 199
- Niobium-containing steels, 9, 10, 148, 156, 210, 216–220
  - $\alpha$  grains in, 144
  - change in microstructure of, 103
  - change in transformation behaviour, 141
  - controlled rolling of, 3, 4–9
  - early mill trials of, 150
  - grain size, 61, 155, 214
  - high-strength, 2
  - notch toughness in, 4, 7
  - precipitation hardening in, 5
  - recovery in, 104, 105
  - recrystallization kinetics in, 206
  - recrystallization temperatures of, 8
  - recrystallized grain size, 68
  - rolled in nonrecrystallized region, 149
  - static recrystallization kinetics in, 158
  - stress-strain curve in, 119
  - structure of, 96
  - tensile strength of, 225
  - titanium addition to, 13
  - transformed structure and toughness of, 146
- Niobium-vanadium steels, Charpy impact energy in, 179
- Nippon steel intercritical control, NIC, 3, 13
- Nitride formation, effect on hot-strength, 122
- Nitrides, 18
  - of niobium and vanadium, 5, 155, 156, 160
  - and titanium, 75
  - structure of, 155
- Nitrogen addition to vanadium-containing steels, 7
- Nonmetallic inclusions, 163
- Nonrecrystallization region,
  - deformation of austenite in, 80–101
  - niobium-containing steel rolled in, 149
- Nonrecrystallized  $\gamma$ , transformation from 145–153
- Nonrecrystallized austenitic structure, 128
- Normal rolling, 3, 9
- Normalizing heat treatment, 173
- Notch ductility, 3
  - improvement in, 6, 10, 74
- Notch toughness, 7, 96
  - improvement of, 2, 4, 74
- Nucleated  $\alpha$  grains, retarding growth of, 145
- Nucleation, 20, 61
  - of  $\alpha$  grains, 26, 81, 142
    - on  $\gamma$  grain boundaries, 42
    - at deformation bands, 147
  - at annealing twin boundaries, 41
  - capacity, 87
  - on deformation bands, 41
  - frequency, 47
  - at grain boundaries, 41
  - inside grains, 41
  - rate, 29, 88
    - increase in, 42
    - per unit area of deformation bands and annealing twin boundaries, 44
  - of recrystallization, sites for, 90
  - sites, 44, 151
    - area for new grains, 208
    - density, 47
    - for  $\alpha$  grains, increase of, 89
    - for pearlite, 91, 92
    - increase of, 93, 95
    - of recrystallized grains, 62
- Nucleation-growth mechanism, 33
- Optical micrograph, 33
  - showing effect of  $\gamma$  deformation, 40
    - on number of ferrites on  $\gamma$  grain boundaries, 43
  - showing nucleation, 41
  - showing static recrystallization, 38
- Optical microstructure of dynamically recrystallized  $\gamma$ , change in, 37
- Optical microstructure of work-hardened  $\gamma$ , change in, 36
- Orthoequilibrium, 18
- Ostwald ripening, 37
- Pancaked austenite grain structure, 86
- Pancaking temperature, 51, 62, 147
  - elevation of, 147
- Parabolic rate constant, 30
- Parabolic stress-strain curve, 186, 189
- Peak stress, relation with Z parameter, 120
- Pearlite, 194
  - formation of, 98
    - in deformed  $\gamma$ , 95
  - fraction, 5, 142
  - free steel, 161
  - nucleation, at annealing twin boundaries, 93
    - sites for, 91, 92
  - in tool steel, 94
  - reduced steels, 186
    - improvement of toughness in, 8
  - structure, 113
  - transformation from deformed  $\gamma$ , 93

*(Pearlite, continued)*

- Phase structures, 121
- Phase transformation, classification of, 17–18
- Phosphorus, 154
  - as alloying element, 18
  - content, decrease in, 115
  - effect of, 165, 166
- Pinning effect, 37
  - on grain boundary migration, 39
- Pipe-forming, change in mechanical properties with, 185
- Pipelines for natural gas transportation, 10
- Pipes, in pumping stations, material for, 13
- Plane anisotropy, 109, 110
- Plate mill, 7, 121, 128, 135, 226
  - controlled rolling in, 134
  - plate production in, 14
  - rolling of ship's plates in, 74
- Plate production in heavy plate mills, 14
- Plate-rolling, 203
  - mills accelerated cooling in, 13–14
  - schedule, experimental, 212
- Plate thickness, 10
  - changes in, 136
- Polygonal  $\alpha$ , 183, 184
- Polygonal  $\alpha$ -pearlite, 161
  - intensity of, 107
- Post-dynamic recrystallization, 34
- Precipitation,
  - of alloy carbide from  $\alpha$ , 19–20
  - hardening, 5, 104, 106, 167, 174, 230
    - degree of, due to vanadium and/or niobium carbonitrides, 104
    - and grain refinement, 159–161
  - of niobium and vanadium carbonitrides, 171
  - strain-induced, and solute drag, 159
- Precipitation-hardened controlled-rolled steels, 147
- Precipitation-temperature-time diagram, 84
- Prestrain, effect on softening, 131–132
- Production conditions for controlled-rolled plates, 7
- Proeutectoid  $\alpha$  grains, 89, 194
  - shape of, 151
- Proeutectoid ferrite, 145
- Progress of  $\alpha$  transformation, 23
- Quenching, 61, 89, 90
  - processes, 226
  - and tempering, 173, 186
  - time interval between reduction and, 62
- Rare earth metals, 154, 165, 173, 195
  - addition of, 11
  - boron-titanium addition, 195, 196
  - calcium-titanium addition, 195
- Rate of grain growth, 55
- RCR, 68, 74
- Recovery, 105
- Recovery-retarding effect of vanadium, 86
- Recrystallization behaviour,
  - comparisons of, 64
  - of  $\gamma$  grains after hot-deformation, 4

*(Recrystallization behaviour, continued)*

- of  $\gamma$  in steels, 57
- effects of alloying elements on, 74–78
- Recrystallization controlled-rolling (RCR), 68, 74
- Recrystallization,
  - of  $\gamma$ , in silicon-manganese steels, 8
  - retardation of, 80–86
  - critical temperatures for, 51
  - during diffusional phase transformation, 17
  - dynamic and classical static, 61
  - kinetics, 74–75, 77, 206
    - of carbon, 85
    - of niobium-containing steel, 85
  - region, deformation of austenite in, 49–79
  - retardation, 75
    - effect of titanium, 86
    - with strain-induced precipitation, 84
  - sequence of silicon-manganese steel, 72
  - temperature, 8
    - effect of niobium addition, 9
    - range, deformation at, 22
    - of silicon-manganese steels, 147
  - time diagram, 84
  - time, 52, 53
- Recrystallized  $\gamma$  grain size, 207
  - prediction of, during hot-rolling, 203
- Recrystallized  $\gamma$  grains,
  - controlled rolling for refinement of, 68–74
  - transformation from, 140–153
- Recrystallized grain size, 52, 53, 67
  - dependence on strain and deformation temperature, 64
  - determination of, 61
  - effects of alloying elements on, 75–78
  - for niobium-containing steel, 68, 76
  - relationship with high-temperature strength, 55
  - relation between  $Z$  and, 58
  - of silicon-manganese steels, change in, 71
- Reduction temperature, 67, 73
- Reductions, concentration to nonrecrystallization temperature regions, 153
- Refinement,
  - of  $\alpha$  grains, 2, 80, 144
  - of ferrite grain size, 17–48
  - of recrystallized  $\gamma$  grains, 4, 141
    - by successive hot-reductions, 50
- Reheating temperature, 156
- Residual strain coefficient, 134
- Resistance, deformation, at elevated temperatures, 117–127
- Restoration,
  - during hot-deformation, 30–34
  - and strain hardening, 117–121
  - processes, 104
- Retardation,
  - of austenitic recrystallization, 157–159
  - of crystallization, effect of alloying elements on, 37–39
  - of recrystallization of  $\gamma$ , 80–86
  - strengths, 75
- Rolling experiments, 77
- Rolling hot-deformations, dynamic and metadynamic recrystallization by, 56–59

- Rolling,
  - microstructural changes during, 139
  - mills, 121, 135, 235
    - mill specifications, 136
  - of ship's plates in European plate-mills, 74
  - parameters, 126
  - pass schedule, 138
  - productivity, increasing, 10
  - reduction, change in strain rate during, 57
  - schedule, 50, 126
  - speeds, increase in, 73
  - temperature, 50, 121
    - changes in, 136
    - of plate, 137
  - variables, range of, in various mills, 121
- Root crack, 190
- Roughing controlled rolling, 74
- Scheil's additivity rule, 22
- Seamless-pipe-mill, 226
- Sellers, 67
- Sellers' relations, 66
- Separate nucleation, 20
- Separate transformation, 187
- Separation, 110–114
  - cracks, 113
  - elimination of, 115
- SHT, *see* Sumitomo high-toughness
- Shape change of  $\gamma$  grain, 41
- Shape-mills, 121
- Shelf energy, 112
- Shida's equation, 126, 137, 138
- Shipbuilding,
  - requirements of toughness in, 2
  - steels for, 196
  - thermomechanical processing in, 1
- Ship's plates, rolling of, in European plate-mills, 74
- Silicon, as alloying element, 18
- Silicon,
  - effect of, 187
  - effect on hot-strength, 122
  - effect on softening, 131
  - retardation effects of, 75
  - as substitutional element, 154
- Silicon-manganese steel, 8, 210, 216–218, 221–223
  - change in recrystallized grain size, 71
  - controlled rolling of, 9
  - effect of grain size on recrystallization
    - behaviour, 62
  - grain size, 57, 61, 155
  - microstructural changes with cooling rate, 231
  - recrystallization sequence of, 72
  - recrystallization temperatures of, 147
  - temperature of rolling operations in, 49
  - transformation in, 140
- Site saturation, 21
- Size of metadynamically recrystallized grains, 55, 62
- Size of statically recrystallized grains, 63
- Slab reheating, 153
  - of niobium- or vanadium-containing steels, 74
  - temperature, reduction of, 156
- Slab thickness, 62
- Slip deformation, 31
- Softening,
  - behaviour after rolling and strain accumulation, 128–139
  - change in fractional, 35
  - curves, 205
  - dependence of, on temperature, 83
  - effect of niobium on, 82
  - factors affecting, 130–133
  - kinetics, 82, 211
  - ratio, 130–131, 157
- Solid-solution hardening, 167
- Solubilities of vanadium and niobium compounds,
  - effects of, 6
- Solubility products, 154–156
- Solute dragging effect, 37
  - and strain-induced precipitation, 159
- Sour-gas, 180
- Spiral pipes, coils for, 13
- Stacking fault energy of copper, 31
- Static recovery, 52, 105, 210–212
- Static recrystallization, 62, 205–206
  - critical strain for, 55, 76
  - effects of strain-rate history on, 67
  - grain growth suppression after, 73
  - kinetics in  $\gamma$ , 157, 158
  - kinetics in niobium-bearing steel, 158
- Static restoration during holding after hot-deformation, 34–37
- Static restoration kinetics, 130
- Static restoration processes after deformation, 52
- Static to metadynamic recrystallization behaviour, 64
- Statically recrystallized grain size, 63, 67, 206–208
- Statically recrystallized structures of thin plate, 73
- Steels, chemical composition of, 125
- Storage tanks, steels for, 196
- Strain, 25, 93
  - accumulation, 128–129, 202
    - in deformation resistance formula, 133–135
    - in the low-temperature  $\gamma$  region, 216–220
  - anisotropy, 113
  - critical, 52, 53, 55
  - dependance of statically recrystallized grain size on, 54
  - hardening and restoration, 117–121
  - rate, 56, 57, 67, 119–120
- Strain-enhanced transformation, 93–99
- Strain-induced grain boundary migration, 52, 72
- Strain-induced precipitation, 159
  - of niobium and vanadium carbonitrides, 106
  - of niobium carbonitrides, 84, 202, 214–216
- Strain-induced transformation, 93–99
- Strength, 220
  - of controlled-rolled steels, factors governing, 170, 171
  - high-temperature, 55
  - increase due to manganese, 5
  - of niobium-containing steels, 10
  - and toughness, 13, 182, 183
  - and microstructure, relation between, 223–225

- (*Strength, continued*)  
 of weld joint, 190, 199  
 yield, 106  
 Strengthening, 105  
 due to accelerated cooling, 230  
 factor, 170  
 mechanism, 230–232  
 of steel, 161  
 by addition of niobium or vanadium nitrides, 5  
 and toughening mechanisms, 167–172  
 Stress,  
 critical, 112  
 flow, 120  
 induced, 112  
 peak, 119  
 tensile, 175  
 Stress-strain curves, 32, 117–118, 128–129  
 for carbon steels, 105, 126  
 in dynamic recovery, 119  
 parabolic, 186, 189  
 Strip-mills, 121, 128, 135  
 Subgrain hardening, 81, 174  
 Substitutional alloying elements, 161–163  
 Substitutional elements, 154  
 Sulphur, 154  
 Sulphur content, 176, 177  
 effect on Charpy absorbed energy, 180  
 content, reduction in, 9, 11, 115, 180, 182  
 Sumitomo high toughness process, 3, 12, 234  
 Supercooling temperature, 187  
 Susceptibility to weld cracking, 191–192  
 Synthetic thermal cycle, 192  
 T-direction, Charpy shelf energy in, 8  
 toughness in, 9, 114  
 transition temperature in, 164, 174  
 Tantalum, as alloying element, 18  
 Temper embrittlement, 113, 166  
 Temperature,  
 brittle-crack arresting, 178  
 critical, 51, 69  
 delaying recovery and recrystallization, 82  
 effect of, on density of annealing twins, 91, 92  
 range for conventional rolling, 49  
 for recrystallization, 62  
 and strain rate, dependance of flow stress on, 120  
 Temperature-reduction-recrystallization, 59–68  
 diagrams, 65, 66  
 Tempering, 176, 186, 226  
 Tensile properties of steels and volume fraction of deformed  $\gamma$ , relation between, 103–104  
 Tensile strength, 174, 175, 189, 190  
 change in, with addition of niobium, 4  
 effect of alloying elements on, 161  
 of niobium steel, 225  
 Tensile stress, 175  
 Tetraikadekahedra, 21  
 Texture and anisotropy, 106–110  
 Texture development, 169  
 Texture due to hot-deformation, 39  
 Thermal analysis, 93  
 Thermal cycle, 192  
 Thermomechanical processing,  
 definition of, 1  
 developments in, 226–235  
 historical survey, 1–14  
 Thermomechanical simulation, 117  
 Thermomechanical treatment, transformation  
 behaviour of austenite after, 140–153  
 Three-step compression testing, residual strain in, 134  
 Through-thickness embrittlement, 113  
 Titanium, 156, 159  
 addition, 11, 165, 195, 196  
 effect of, on controlled rolling, 147  
 to improve toughness, 12  
 to niobium-containing steels, 13  
 affinity with carbon and nitrogen in austenite, 154  
 as alloying element, 18  
 carbide, 19–20, 155, 159, 160  
 and nitrides, 75  
 effect on hot-strength, 122, 123  
 effect on softening, 131  
 microaddition of, 37  
 as microalloying element, 154  
 microalloyed steels, 13  
 nitride, 13, 155  
 recrystallization-retarding effect, 86  
 reduction of manganese content using, 11  
 Tool steel, pearlite formation in, 94  
 Torsion testing, 117  
 Toughening factor, 170  
 Toughening mechanisms, 167–172  
 Toughness, 189, 192–200  
 of bond, 194, 196  
 comparison of, in niobium-containing steels, 150  
 of controlled-rolled steels, factors governing, 170, 171  
 deterioration of, 147  
 improvement of, 12  
 in pearlite-reduced steels, 8  
 requirements of, in ship-building, 2  
 of steels, comparison of structures and, 146, 148  
 and strength, 13, 182, 183  
 and microstructure, relation between, 223–225  
 Transformation behaviour of deformed  $\gamma$ , 98  
 Transformation,  
 from nonrecrystallized  $\gamma$ , 145–153  
 from recrystallized  $\gamma$ , 140–145  
 kinetics, 20–22, 47, 99, 125  
 of  $\gamma$ , isothermal, 20–21  
 textures of controlled-rolled steel, 107  
 Transformed microstructure and strengthening  
 mechanism, 230–232  
 Transition temperature, 13, 164, 171, 172, 174, 178  
 decrease in, 2  
 effect of separation on, 114  
 Transverse Charpy energy, 10  
 Transverse direction, *see* T-direction  
 Tungsten, as alloying element, 18  
 Twin bands, 8

- Two-phase region, deformation in, 101–116  
Type-304 austenitic stainless steel, 67
- Unrecrystallized temperature range, deformation at, 22  
UOE pipe manufacturing, 184
- Vanadium, 159, 196–198  
  affinity with carbon and nitrogen in austenite, 154–155  
  as alloying element, 18  
  carbide, 19, 155, 156, 160  
    and nitrides, 5, 75  
  carbonitride, 171  
  effect on hot-strength, 122  
  increase in hardenability due to, 230  
  as microalloying element, 154  
  nitride, 155, 156  
  precipitates, classification of, 170  
  recovery-retarding effect of, 86  
  retardation effects of, 75  
  steel, recovery in, 105  
Vanadium-containing steels, 10, 144  
  nitrogen addition to, 7  
  notch toughness in, 7  
  precipitation hardening in, 5  
Volume fraction of deformed  $\alpha$ , 103
- Wagner approximation, 29  
Warm-charge-rolled products, (WCR), 233, 234  
Weld bead, 190  
Weld cracking, 189–192  
Weld joint, strength of, 199  
Weld thermal cycle, 192  
Weldability, 154, 189–200  
  of controlled-rolled steel, 190  
Weld-cracking parameter, 190  
Widmanstätten  $\alpha$  structure, 17, 18  
Work-hardened  $\gamma$ , change in optical microstructure of, 36  
Work-hardening of  $\gamma$ , ferrite grain refinement by, 39–46  
Work-hardening rate, 189
- Y-groove cracking test, 191  
Yield strength, 106, 110, 168–169, 184  
Yield stress, 167  
Yield: tensile strength ratio, 186
- Z, Zener-Holloman parameter, 25, 32, 53, 57, 121, 203, 204  
  relation between recrystallized grain size and, 58  
  relation with peak stress, 120  
Z dependent relation, 67  
Z-direction,  
  brittle fracture strength in, 114  
  fracture toughness in, 174, 177  
  ductility and, 174  
  tensile stress in, 175  
Zener-Holloman parameter, *see* Z  
Zener's relation, 38  
Zirconium addition, 11, 165  
Zirconium, as alloying element, 18, 154